Acoustical Physics, Vol. 50, No. 5, 2004, pp. 493–495. Translated from Akusticheskiĭ Zhurnal, Vol. 50, No. 5, 2004, pp. 581–584.

Acoustic Remote Sensing of Currents at the Shelf of the Sea of Japan

V. A. Akulichev, V. V. Bezotvetnykh, E. A. Voĭtenko, S. I. Kamenev, A. P. Leont'ev, and Yu. N. Morgunov

Il'ichev Pacific Oceanological Institute, Far East Division, Russian Academy of Sciences, Baltiĭskaya ul. 43, Vladivostok, 690041 Russia

e-mail: akulich@marine.febras.ru; kamenev@poi.dvo.ru

Received July 27, 2003

Abstract—Results of experimental studies of the field of currents in the shelf zone of the Sea of Japan are discussed. The studies were carried out in 2001–2002 near the Gamov Peninsula, in the region of the acoustical-hydrophysical site of the Il'ichev Pacific Oceanological Institute (Far East Division, Russian Academy of Sciences). The purpose of the studies was related to the problems of developing the systems for long-term remote sensing of the climatic variability of the sea medium and for acoustic tomography of the dynamic processes in a shallow sea. In the experiment, combined acoustic transmitting and receiving systems (transceivers) and complex phase-manipulated signals with a carrier frequency of 2500 Hz were used. The velocities of currents calculated from the acoustic data agree satisfactorily with the velocities measured by standard methods of oceanography. © *2004 MAIK "Nauka/Interperiodica".*

Acoustic methods of studying the currents in shallow-water regions of oceans and seas are advantageous for developing systems for a long-term monitoring of the climatic variability of the sea medium. Our previous publications [1–4] reported on the experimental data that were obtained by applying the method of opposite-direction sensing to measuring the velocity of currents in a shallow sea by using phase-manipulated signals. It was shown that the use of complex signals allows one to distinguish and identify the signal arrivals over different trajectories with simple engineering means based on single bottom-moored receiving and transmitting systems. Such an approach provides quantitative estimates of the field of currents in both horizontal and vertical planes. The studies were performed in August and September 2000 at the shelf of the Sea of Japan on a 18-km-long fixed path. For the opposite-direction sensing of the sea medium, phase-manipulated signals (M-sequences) with a carrier frequency of 250 Hz were used. This frequency was chosen to monitor a basin of several hundred kilometers in size. In particular, this method was used in the experimental sensing of the sea medium on a 550-km-long path, which was carried out in cooperation with researchers from the United States and South Korea [5, 6].

In this paper, we discuss the results of studying the field of sea currents by the method of opposite-direction sensing. The data were obtained in September 2001 in the same shelf region of the Sea of Japan as described in [2]. The objective of the studies was the improvement of the accuracy and information output of the measurements on shorter paths. In the measurements on a 3-km path, complex phase-manipulated signals were used with a carrier frequency of 2500 Hz. These signals were orthogonal 511-symbol M-sequences with the field equations $X^9 + X^4 + 1$ and $X^9 + X^5 + 1$, a symbol length of four periods of the carrier frequency, and a bandwidth of 1250 Hz. The improvement of the resolution at higher frequencies was experimentally confirmed in many-hour-long synchronous transmission on fixed paths in the same region of the Sea of Japan. The signal propagation on these paths is governed by multipath and waveguide effects.

Figure 1 shows the layout of the experiment on measuring the velocity of currents by the method of opposite-direction sensing. This figure also shows the vertical profile of the temperature field averaged over the diurnal period. In this experiment, piezoceramic transceivers (combined sound transmitters and receivers) were used that were bottom-moored at depths of 40 and 56 m. Figure 2 presents the results of measuring the velocity and direction of the current by an SM-2 hydrological probe (Japan) at three depths, for ten hours, at the site of the second transceiver. It is shown that the current undergoes substantial time-dependent variations in both its direction and absolute value and depends on the horizon.

The opposite-direction signal transmission was carried out for 15 hours, with 1-min intervals. The signals received by the first and second transceivers were transmitted to the coastal station via a cable and a radio channel, respectively. Then, the cross-correlation processing was performed for the transmitted and received signals propagating in opposite directions relative to each other. The resulting impulse responses of the waveguide were compared. From the time difference in

1063-7710/04/5005-0493$26.00 © 2004 MAIK "Nauka/Interperiodica"

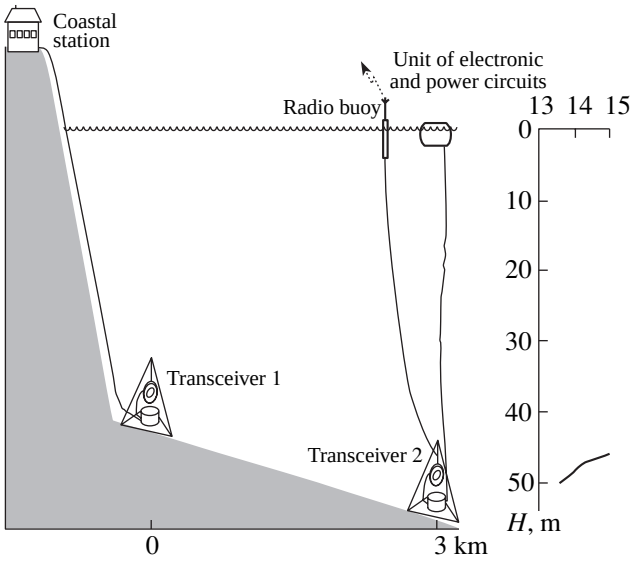

Fig. 1. Layout of the experiment on the opposite-direction sensing and the averaged vertical profile of the temperature field.

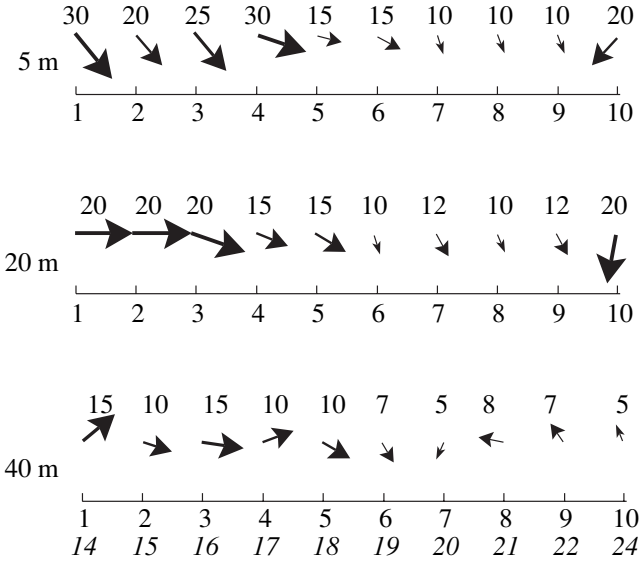

Fig. 2. Velocities (m/s) and directions of the current versus time at depths of 5, 20, and 40 m.

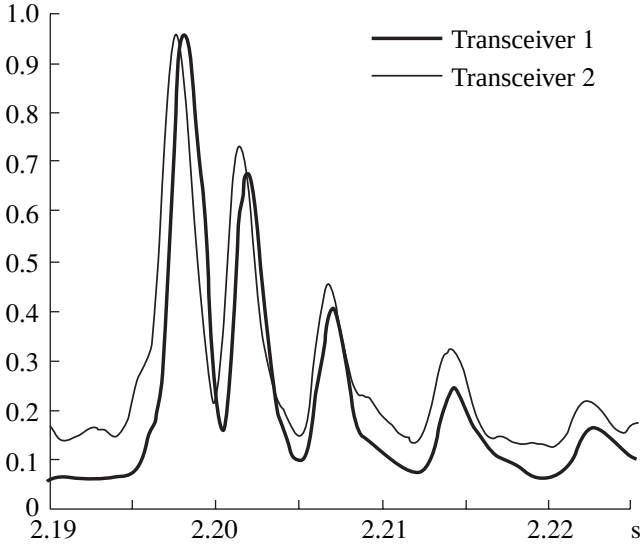

Fig. 3. Impulse responses of the waveguide (low water).

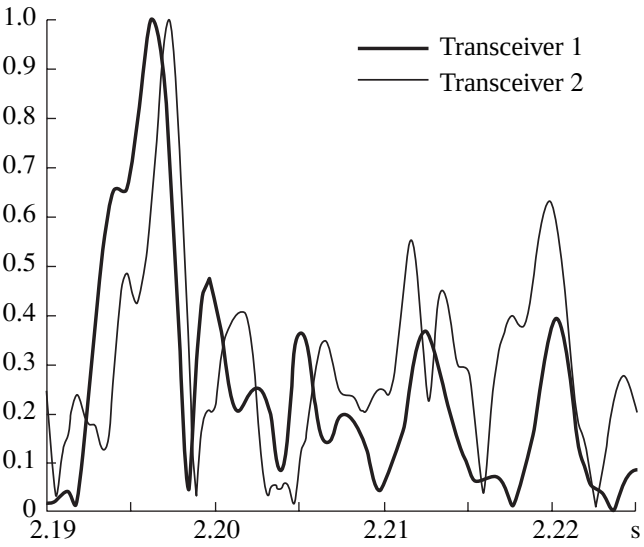

Fig. 4. Impulse responses of the waveguide (high water).

the ray arrivals, the projection of the velocity of current on the propagation path was determined according to the relations taken from [2, 7]. Figures 3 and 4 show the fragments of the waveguide impulse response obtained from the signals received by the transceivers at 15:00, at the time of low water, and at 21:00, at the time of high water, when the near-bottom current changed its direction. Figure 3 shows that the signals of both hydrophones exhibit up to five arrivals that are clearly separated in time and that have time shifts caused by the influence of the sea current on the speed of sound propagation in opposite directions. It is worth mentioning that, by 21:00, the noise level became higher at the second transceiver, and the validity of the reciprocity principle reliably held for only the first and fifth arrivals (Fig. 4).

According to [1–4], when the summer- and autumn-type profiles of the sound speed exist and the sound transmitters and receivers are near the bottom, the first signal arrivals are formed by the rays that propagate within the near-bottom water layer, without touching the sea surface. The thickness of this layer depends on the frequency of sounding and the value of the negative sound speed gradient. The remaining arrivals are

Comparative data on the measured velocity of current (cm/s)

Depth of measurement, m	Data obtained with the oceanographic probe		Data obtained by opposite-direction sensing	
	15 h (low water)	21 h (high water)	15 h (low water)	21 h (high water)
5	18	10	20	12
20	5	12	20	12
40	6	–4	12	–5

formed by the rays that undergo different numbers of reflections from the bottom and surface. Thus, the resolution and identification of the ray arrivals determines the accuracy of reconstructing the vertical structure of the current. The result of measuring the time of the first arrival is especially important, because the complicated dynamics of interaction between the acoustic and hydrodynamic fields in the near-bottom water layer makes it impossible to resolve individual rays in some cases.

To estimate the efficiency of the proposed method, a comparison was performed between the acoustically determined velocities of current and those measured by standard oceanographic means. The table summarizes the projections of the velocities of current onto the propagation path for the measurements performed with the SM-2 probe at 15:00 (the low-water period) and at 21:00 (the high-water period), at depths of 5, 20, and 40 m. The table also presents the velocity projections calculated from the acoustically measured time shifts.

In the high-water phase, the values of the velocity of current reached –10 and 15 cm/s, as measured from the time shift of the first and fifth arrivals, respectively. For the sound profile at hand, the initial signal arrivals correspond to the near-bottom ray trajectories, while other arrivals are formed by the rays propagating through the entire waveguide thickness. Thus, not only the integral variability of the velocity of water current on the path was measured, but also its vertical components were estimated. Some differences between the data obtained with the use of the oceanographic probe and the acoustic method are caused by the fact that the probe measures the velocity of current at a single point while the opposite-direction acoustic sensing yields the velocity averaged over the entire 3-km-long path. In our opinion, an important result is that both methods detected a change in the direction of the near-bottom current after 20:00.

Thus, the experimental results of this study and the results presented in [1, 6] demonstrate the feasibility and good prospects of using the method of opposite-direction sensing for monitoring the field of currents in sea areas of several to several hundred kilometers in size. A possible continuation of this work may consist in the adaptation of the method of matched nonreciprocity [8] to the methodological and technological features of the experimental devices and to the optimization of the characteristics of the probing signals.

ACKNOWLEDGMENTS

This work was supported in part by the Russian Foundation for Basic Research, project no. 03-05-65226, and by the WORLD OCEAN Federal Target Program in the framework of the project “Complex Studies of the Processes, Characteristics, and Resources of the Far Eastern Seas of Russia.”

REFERENCES

1. V. A. Akulichev, V. V. Bezotvetnykh, S. I. Kamenev, *et al.*, Dokl. Akad. Nauk **381** (2), 243 (2001).
2. V. A. Akulichev, V. V. Bezotvetnykh, S. I. Kamenev, *et al.*, Akust. Zh. **48**, 5 (2002) [Acoust. Phys. **48**, 1 (2002)].
3. V. V. Bezotvetnykh, S. I. Kamenev, E. V. Kuz’min, *et al.*, Prib. Tekh. Éksp. **45** (1), 117 (2002).
4. V. A. Akulichev, V. V. Bezotvetnykh, S. I. Kamenev, *et al.*, in *Proceedings of the 7th Western Pacific Regional Acoustics Conference (WESTPRAC VII)* (Japan, 2000), p. 1159.
5. J. Na, in *Proceedings of the 6th Western Pacific Regional Acoustics Conference (WESTPRAC VI)* (Japan, 2000), p. 1165.
6. S. Oh, J. Na, Y.-G. Kim, *et al.*, in *Proceedings of the 8th Western Pacific Regional Acoustics Conference (WESTPRAC VIII)* (Australia, 2003), CD-version.
7. L. M. Lyamshev, Dokl. Akad. Nauk SSSR **138** (3), 575 (1961) [Sov. Phys. Dokl. **6**, 410 (1961)].
8. O. A. Godin, D. Yu. Mikhin, and D. R. Palmer, Izv. Ross. Akad. Nauk, Fiz. Atmos. Okeana **36** (1), 141 (2000).

Translated by E. Kopyl

Acoustical Physics, Vol. 50, No. 5, 2004, pp. 496–500. Translated from Akusticheskiĭ Zhurnal, Vol. 50, No. 5, 2004, pp. 585–589.

Reflection and Refraction of Surface Acoustic Waves by a Periodic Domain Structure

N. L. Batanova, A. V. Golenishchev-Kutuzov, V. A. Golenishchev-Kutuzov, and R. I. Kalimullin

Kazan State Power Engineering University, ul. Krasnosel'skaya 51, Kazan, 420066 Russia

e-mail: adm@kspeu.kcn.ru

Received February 6, 2003

Abstract—Reflection and refraction of surface acoustic waves by a periodic domain structure formed in lithium niobate is studied. A second harmonic generation is observed. A mechanism underlying the linear and nonlinear interactions of acoustic waves with a periodic domain structure is proposed. © *2004 MAIK "Nauka/Interperiodica".*

Characteristic features of acoustic wave propagation in nonlinear media have been attracting the interest of researchers for years because of the unusual physical properties and the possibilities of practical application [1]. Recently, crystals with periodically varying values of some of their physical parameters have become objects of investigation and even actual application in nonlinear acoustics and optics. It was found that such periodic structures possess a number of unusual properties and, in particular, the localization of electron states and optical, elastic, and piezoelectric parameters. The first theoretical publications concerned with the generation and propagation of acoustic waves through grown domain structures appeared as early as the 1970s [2–4]. Then, experimental studies of the reflection and refraction of bulk acoustic waves by grown [5] and induced [6–8] periodic domain structures (PDSs), as well as photoinduced gratings [9], were carried out. However, none of these and the following publications reviewed in [10] reported on the frequency intervals of the total reflection and total transmission of acoustic waves through PDSs or considered the problems of nonlinear interaction of acoustic waves with PDSs. Being motivated by these unsolved problems, we carried out a more comprehensive study of the propagation of surface acoustic waves (SAWs) through a PDS formed in lithium niobate.

The propagation of SAWs through a PDS was studied using an experimental setup schematically represented in Fig. 1. The PDS was formed by the electrical method [7] near the *XZ* surface of a lithium niobate single crystal with the dimensions 20 (*X*) × 2 (*Y*) × 20 (*Z*) mm. The structure consisted of alternating domains of the "head-to-head" type with a period of 50 ± 2 μm and contained 20 periods arranged along the *Z* axis (see object *1* in Fig. 1). Surface acoustic waves in the form of short pulses ($\tau \sim 1$ μs) with a repetition period of 0.1–1 ms were generated by (*5*) a tunable pulser with the use of (*2*) a broadband angular transducer and detected by (*3*, *4*) two similar transducers (transducer *4* for the transmitted pulse and transducer *3* for the reflected pulse). The angle between the wave vector of the incident pulse and the axis of the PDS was 14°. The transmitted and reflected pulses were received by (*6*) a superheterodyne receiver whose resonance frequency was synchronously varied with the pulser frequency.

Experimental results show that, in the frequency range from 20 to 200 MHz, a series of intensity maxima is observed for the acoustic pulses reflected from the PDS (Fig. 2). These intensity maxima observed for the reflected pulses in the frequency bands 32–35, 62–65, 95–100, 125–133, and 192–198 MHz correspond to the intensity minima for the acoustic pulses transmitted through the PDS. At a fixed pulser frequency within 32–35 MHz and with the variation of the frequency of the superheterodyne receiver, in addition to the fundamental frequency signals we also observed signals of acoustic pulses reflected from the PDS in the frequency band of 60–65 MHz, which corresponds to the second harmonic of the initial acoustic pulses. The reflection coefficient for the second harmonic was almost an order of magnitude smaller than that for the fundamental frequency. On the average, it was ~10^{-2}, which is approximately two orders of magnitude greater than the reflec-

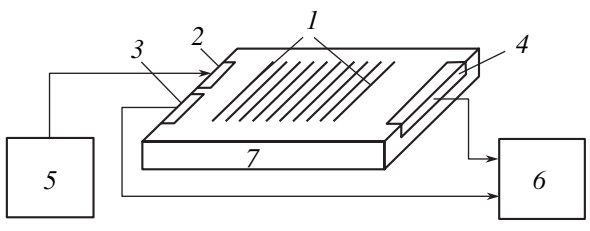

Fig. 1. Block diagram of the experimental setup for studying the propagation of acoustic waves through the PDS: (*1*) domain structure, (*2–4*) end transducers, (*5*) pulser, (*6*) superheterodyne receiver, and (*7*) sample.

1063-7710/04/5005-0496$26.00 © 2004 MAIK "Nauka/Interperiodica"

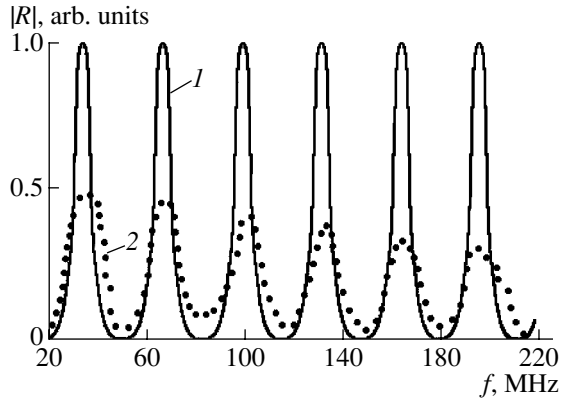

Fig. 2. Spectrum of acoustic pulses reflected from the PDS: (*1*) theoretical and (*2*) experimental spectra.

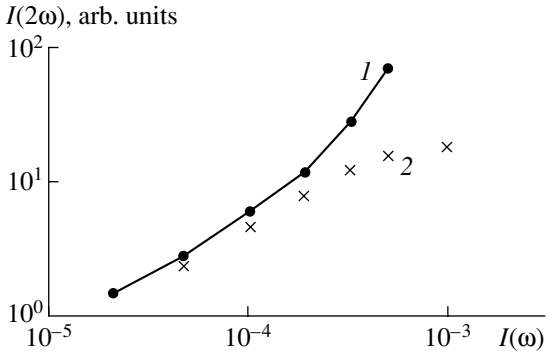

Fig. 3. Dependence of the intensity of the second harmonic of SAWs on the intensity of the first harmonic: (*1*) calculated data and (*2*) experiment.

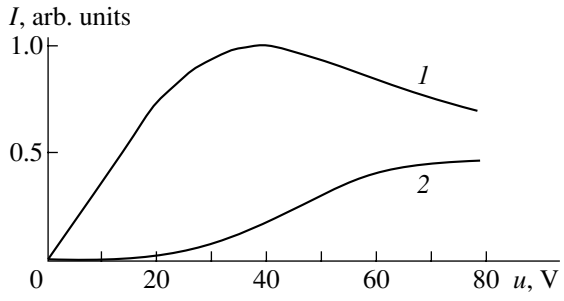

Fig. 4. Dependences of the intensities of the (*1*) first and (*2*) second harmonic of SAWs on the voltage applied to the transducer.

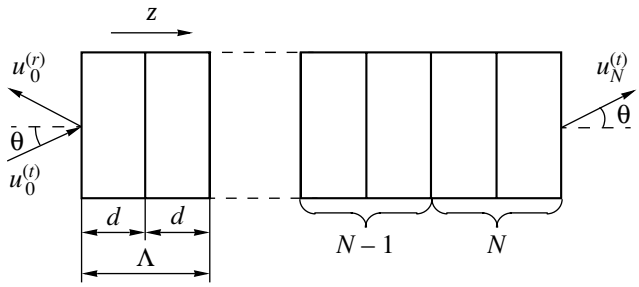

Fig. 5. Geometry of the Bragg reflection for a system consisting of *N* periods.

tion coefficient for a similar transformation with the use of only a homogeneous acoustic nonlinearity in a similar lithium niobate single crystal. With an increase in the pulse amplitude at the fundamental frequency, the second harmonic pulse amplitude exhibited a nonlinear growth (Fig. 3). At the same time, the dependence of the intensity at the fundamental frequency, $I(\omega)$, on the amplitude of the alternating voltage across the transducer, $u(\omega)$ (Fig. 4), exhibits a nonlinear decrease in $I(\omega)$ with increasing $u(\omega)$, which is related to the nonlinear growth of the intensity of the second harmonic, $I(2\omega)$.

A similar intensity behavior was observed for the generation of the second harmonic at frequencies corresponding to higher resonances: $f = 63$ MHz, $2f = 126$ MHz, and so on, at all subsequent harmonics.

The theoretical interpretation of these experimental results is based on a number of characteristic features of the PDSs formed in a ferroelectric-piezoelectric crystal. It is well known that, at any local distortion of the surface characteristics, which manifests itself as a change in the continuity of such physical parameters as the strain and stress components, the electric potential, and the electric induction, a reflection of SAWs from the boundaries of inhomogeneities arises. For PDSs in piezoelectrics, the main feature is the periodic change of signs of the piezoelectric constants e at the domain boundaries while the elastic and dielectric properties remain unchanged.

Thus, the Bragg reflection from the PDS occurs as a result of the interference between the incident wave and the waves reflected from the internal boundaries between the domains. A PDS consisting of N periods (Fig. 5) contains $2N - 1$ boundaries of the types of +/– and –/+, where the plus and minus signs refer to the domains with opposite polarizations. In our experiments, the duration of the SAW pulse exceeded the time of the pulse propagation through the PDS, which means that the interaction of the pulse with the PDS can be considered in a quasi-continuous mode.

The PDS can be compared with a one-dimensional crystal that is invariant with respect to the translations by the lattice constant. Therefore, in describing the propagation of an acoustic wave through the PDS, it is possible to use a formal analogy with the quantum theory of electrons in a crystal and to apply such notions as Bloch waves and allowed and forbidden zones. This model already was used in a number of publications

[13, 14] for a theoretical description of the propagation of acoustic waves or acoustic phonons through periodic structures.

Since the medium is periodic, the tensor e can be expanded into a Fourier series in terms of the PDS wave vectors k:

$$e(z) = \sum_k e_k e^{-ikz}, \quad (1)$$

where $k = 2\pi m/\Lambda$; $\Lambda = 2d$ is the period of the PDS, and d is the domain size. The values of $e_k(m)$ correspond to order m of the Bragg reflection.

A constructive interference occurs when the phase difference between the waves reflected from sequential domain boundaries is equal to an integral number of wavelengths. Thus, the wave vector of the PDS can be put in correspondence with the wave vector of SAWs, $k = \omega/V$, where V is the SAW velocity. The total field inside each domain consists of the fields of the incident and boundary-reflected waves. The complex amplitudes of these two waves have the following form for the mth domain:

$$\begin{aligned} &u_m^{(i)} \exp[-ik_r(r - m\Lambda)] \exp[-i(k_y y - \omega t)]; \\ &u_m^{(r)} \exp[ik_r(r - m\Lambda)] \exp[-i(k_y y - \omega t)], \end{aligned} \quad (2)$$

where the superscripts i and r refer to the incident and reflected waves, respectively.

The wave fields of adjacent domains (1 and 2) are related by the continuity conditions at the boundary between the domain, and, according to [12, 13], these fields can be expressed through each other by the matrix equation

$$\begin{pmatrix} U_i^{(1)} \\ U_z^{(1)} \end{pmatrix} = \begin{pmatrix} A & B \\ C & D \end{pmatrix} \begin{pmatrix} U_i^{(2)} \\ U_z^{(2)} \end{pmatrix}, \quad (3)$$

where $A = \exp(-iK\Lambda) - 2i\exp(-ik_z d)$, $B = 2i\exp(ik_z d)$, $C = 2i\exp(ik_z d)$, $D = i\exp(iK\Lambda) + 2i\exp(ik_z d)$, and K is the Bloch wave number given by the equation

$$K(k_z, \omega) = \frac{1}{\Lambda} \arccos\left[\frac{1}{2}(A + D)\right].$$

The common factor $\exp[-i(k_y y - \omega t)]$ does not depend on the periodic structure and, therefore, is excluded from the consideration.

In a similar way, we can determine the coefficient of reflection, R_N, from the structure consisting of N periods. In this case, R_N is the ratio of the complex amplitude $u_0^{(r)}$ of the reflected wave at the PDS input to the amplitude $u_0^{(i)}$ of the incident wave (Fig. 5). The matrix transformation (3) is replaced with

$$\begin{pmatrix} a_0 \\ b_0 \end{pmatrix} = \begin{pmatrix} A & B \\ C & D \end{pmatrix}^N \begin{pmatrix} a_N \\ b_N \end{pmatrix}. \quad (4)$$

The solution to Eq. (4), which is obtained by raising of the consistent matrix to the Nth power with the use of the Lyapunov exponent [15]

$$\gamma = \lim_{t \to \infty} \frac{1}{t}\left(\frac{D_t}{D_0}\right),$$

has the form [12]

$$\begin{pmatrix} A & B \\ C & D \end{pmatrix}^N = \begin{pmatrix} AU_{N-1} - U_{N-2} & BU_{N-1} \\ CU_{N-1} & DU_{N-1} - U_{N-2} \end{pmatrix},$$

where $U_N = \dfrac{\sin(N+1)KD}{\sin KD}$.

Then, the amplitude reflection coefficient R_N can be represented as

$$R_N = \frac{b_0}{a_0} = \frac{CU_{N-1}}{AU_{N-1} - U_{N-2}}.$$

This yields the expressions

$$|R_N|^2 = \frac{C^2}{C^2 + \left(\dfrac{\sin K\Lambda}{\sin NK\Lambda}\right)^2}, \quad (5)$$

$$K = \arccos\left\{\left[\frac{2}{\Lambda}[\cos(k_z d) - q^2 \sin(k_z d)]^2\right] - 1\right\}, \quad (6)$$

where q^2 is the electromechanical coupling coefficient.

It should be stressed that expression (5) qualitatively coincides with the quantity $|R_N|^2$ obtained by the impedance method for the reflection of SAWs from a system of N equidistant trapezoidal steps [11].

The value of the coefficient C^2 is directly related to the coefficient R_1 of reflection from a single domain ($N = 1$) by the formula

$$|R_1|^2 = \frac{|C|^2}{|C|^2 + 1} \text{ or } |C|^2 = \frac{|R_1|^2}{1 - |R_1|^2}.$$

Since $R_1 = q_2 \tan\theta \ll 1$, the value of $|C|^2$ approaches that of $|R_1|^2$.

The frequency analysis of Eq. (5) shows that the structure of the reflection spectrum is determined by the periodic dependence of the second term in the denominator of Eq. (5) on $K(\omega, k_y)$. The dispersion dependence of K on ω and k_z, which is determined by Eq. (6), allows one to estimate the range of values of k_z for which $|\cos k\Lambda| < 1$ and, hence, K is a real quantity. These

regions, which are also called allowed bands, are characterized by a zero reflection coefficient. The boundaries of these zones are given by the condition $\cos K\Lambda = \pm 1$ or $K\Lambda = \pi m$ ($m = 1, 2, 3, \ldots$), and the reflection coefficient takes the form

$$|R_N|^2 = \frac{|C|^2}{|C|^2 + (1/N)^2};$$

i.e., at sufficiently large values of N, the reflection coefficient tends to unity.

When $|\cos K\Lambda| > 1$, the quantity K is complex. These values correspond to forbidden zones for which $K = \frac{2\pi m}{\Lambda} + iK$. The reflection maximum is realized at the centers of the forbidden zones, and the formula for $|R_N|^2$ takes the form

$$|R_N|^2 = \frac{|C|^2}{|C|^2 + \left(\frac{\sinh K\Lambda}{\sinh NK\Lambda}\right)^2}. \quad (7)$$

For greater values of N, the second term in the denominator of Eq. (7) exponentially tends to zero, as $\exp[-2(N-1)K\Lambda]$. Therefore, the reflection coefficient at the center of a forbidden zone proves to be close to unity.

As follows from the analysis of Eqs. (5) and (6), between two principal reflection maxima given by Eq. (7), $N-2$ subordinate maxima satisfying the condition $K\Lambda = \frac{\pi}{2N}(1 + 2m)$ are present. Thus, from Eq. (5), it follows that the quantity $|R|$ has periodic maxima at $k_z d = 2\pi m$, which correspond to the frequencies

$$f_m = Vm/2d. \quad (8)$$

The values of $|R|$ calculated for $k = 0.32$, $d = 52$ μm, and $N = 20$ (Fig. 2) agree well with the measured spectrum of waves reflected from the PDS. The decrease in the reflected pulse amplitude of the harmonics can be explained by the dependence of the higher Fourier components of the piezoelectric constant tensor e on the number m. Presumably, only for the first order $m = 1$, one can ignore the higher Fourier components, because the experimental value of $|R|^2$ is close to the calculated one. However, this issue requires special consideration.

It is necessary to note the difference between the spectra of waves reflected from the PDS and the spectra of waves generated on the PDS by an alternating electric field [7] or by a laser beam [16]. While the reflection occurs at the interference of waves reflected from the boundaries of one type and their resonance frequencies are described by Eq. (8), the maxima of the generated acoustic waves appear at the interference of waves from the neighboring boundaries and $f_m = Vm/d$; i.e., the resonance frequencies are two times higher than in the case of the reflection.

A nonlinear interaction of two acoustic waves (direct and reflected ones) with a frequency ω on the PDS, which leads to the second harmonic generation (2ω) in the inverse direction, is possible under the phase-matching condition [17] $k_{2\omega} + 2k_\omega - k_z = 0$.

The set of equations describing a three-wave interaction for all point symmetry groups has the general form

$$\frac{\partial A(\omega)}{\partial z} = \Gamma A_\omega A_{2\omega} \exp(ik_z z), \quad (9a)$$

$$\frac{\partial A(\omega)}{\partial z} = -\Gamma A_\omega A_{2\omega} \exp(-ik_z z), \quad (9b)$$

$$\frac{\partial A(2\omega)}{\partial z} = -\Gamma A_\omega A_\omega \exp(-ik_z z), \quad (9c)$$

where Γ is the two-wave interaction factor.

In solving the set of equations (9), we assume that, at the transformation to the second harmonic, the power loss of the input beam (ω) is vanishingly small, so that $\partial A(\omega)/\partial z = 0$ and, upon integration, Eq. (9c) takes the form

$$A_{2\omega} = \Gamma A_\omega^2 \frac{\exp(ik_z L)}{ik_z},$$

where L is the length of the PDS. Using the diffraction approximation, we represent the intensity of the second harmonic as

$$I_{2\omega} = \Gamma^2 I_\omega^2 \frac{L^2}{\Lambda^2} \frac{\sin^2\left(\frac{1}{2}k_z L\right)}{\left(\frac{1}{2}k_z L\right)^2}. \quad (10)$$

Thus, the intensity $I(2\omega)$ exhibits a quadratic dependence on $I(\omega)$, which is observed in Fig. 3. A certain decrease in the intensity $I(\omega)$ with increasing $u(\omega)$ (Fig. 4) can be explained by a nonlinear increase in the intensity of the second harmonic and, hence, an increase in the energy transfer from the first harmonic to the second one.

The attenuation of SAWs (α) in the course of their propagation through the PDS is described by the additional term of the form of $\exp(\alpha N\Lambda)$, which is ignored in Eqs. (2) and (9). This attenuation limits the use of these equations in the case of a large number of periods of the PDS. However, as follows from our previous results [9], for $N < 40$ such an attenuation can be neglected, and formulas (5) and (10) are quite applicable in our case.

Thus, in this study, the reflection and refraction of SAW by a periodic domain structure is observed in the linear and nonlinear regime. The analysis shows that the reflection of SAWs is related to the periodic changes of sign of the piezoelectric constants at the domain boundaries. It is demonstrated that the second

harmonic generation occurs owing to the interaction of the direct and reflected waves in each layer under the phase-matching conditions.

ACKNOWLEDGMENTS

This work was supported by the Russian Foundation for Basic Research, project no. 01-02-16358.

REFERENCES

1. O. V. Rudenko and S. I. Soluyan, *Theoretical Foundations of Nonlinear Acoustics* (Nauka, Moscow, 1975; Consultants Bureau, New York, 1977).
2. G. G. Kessenikh, D. G. Sannikov, and L. A. Shuvalov, Kristallografiya **16**, 350 (1971) [Sov. Phys. Crystallogr. **16**, 287 (1971)].
3. G. L. Gurevich, M. S. Sandler, and Yu. S. Chertkov, Radiotekh. Élektron. (Moscow) **18**, 2609 (1973).
4. J. C. Peusin and M. Tesson, Phys. Status Solidi A, No. 1, 119 (1976).
5. V. V. Belov and O. Yu. Serdobol'skaya, Fiz. Tverd. Tela (Leningrad) **26**, 2624 (1984) [Sov. Phys. Solid State **26**, 1591 (1984)].
6. Y. Zhu, N. Ming, W. Jiang, and Y. Shui, Appl. Phys. Lett. **53**, 2278 (1988).
7. N. L. Batanova and A. V. Golenishchev-Kutuzov, Akust. Zh. **43**, 545 (1997) [Acoust. Phys. **43**, 468 (1997)].
8. D. V. Roshchupkin, M. Brunel, and R. Ticoulou, Appl. Phys. Lett. **64** (2), 164 (1994).
9. N. M. Ushakov and V. V. Kolosov, Pis'ma Zh. Tekh. Fiz. **27** (24), 40 (2001) [Tech. Phys. Lett. **27**, 1044 (2001)].
10. A. V. Golenishchev-Kutuzov, V. A. Golenishchev-Kutuzov, and R. I. Kalimullin, Usp. Fiz. Nauk **170**, 697 (2000) [Phys. Usp. **43**, 647 (2000)].
11. S. V. Biryukov, Yu. V. Gulyaev, V. V. Krylov, and V. P. Plesskiĭ, *Surface Acoustic Waves in Inhomogeneous Media* (Nauka, Moscow, 1991) [in Russian].
12. A. Yariv and P. Yeh, *Optical Waves in Crystals: Propagation and Control of Laser Radiation* (Wiley, New York, 1984; Mir, Moscow, 1987).
13. A. L. Shuvalov and A. S. Gorkunova, Phys. Rev. B **59**, 9070 (1999).
14. S. Tamura and J. P. Wolfe, Phys. Rev. B **36**, 3491 (1987).
15. G. M. Zaslavskiĭ and R. Z. Sagdeev, *Introduction to Nonlinear Physics* (Nauka, Moscow, 1988) [in Russian].
16. A. V. Golenishchev-Kutuzov, V. A. Golenishchev-Kutuzov, and R. I. Kalimullin, Akust. Zh. **46**, 336 (2000) [Acoust. Phys. **46**, 284 (2000)].
17. Y. Ding, J. Kang, and J. Khurgin, IEEE J. Quantum Electron. **34**, 966 (1998).

Translated by E. Golyamina

Acoustical Physics, Vol. 50, No. 5, 2004, pp. 501–511. Translated from Akusticheskiĭ Zhurnal, Vol. 50, No. 5, 2004, pp. 590–602.

False Learning Function of an Acoustic Signal Classifier

A. N. Goncharov

Andreev Acoustics Institute, Russian Academy of Sciences, ul. Shvernika 4, Moscow, 117036 Russia
e-mail: bvp@akin.ru

Received December 25, 2003

Abstract—In works on statistical pattern recognition that use learning and examination, results of the learning depend not only on the feature efficiencies, but also on the proportion between the capacity of the decision rule, length of the learning sample, and number of features. It is usually difficult to calculate the recognition errors, which connect these basic quantities for a particular classifier, while the calculations are approximate and do not clearly characterize the results obtained in the process of the study.

The purpose of this work is to develop a simple, clear, and efficient technique for the experimental estimation of the expected classification errors of the recognition engine employed in learning. The algorithm produces a sample of random noise segments, which is included in the recognition algorithm instead of the features of real signals. Portions of this uniform sample imitate different classes. The false learning function is produced as a result of a successive increase in the number of random features used in the recognition. The corresponding growth of the probability of recognizing artificial classes in such a false learning depends on the length of the learning sample and on the capacity of the decision rule employed.

The main result of this work is the false learning function proposed for any particular classifier. The function is obtained for the same length of the learning sample as that of the one used to recognize real signals. The validity of results obtained in real signals can be estimated by comparing this function with experimental signal recognition probabilities with the same number of features.

The simple false learning function is useful to characterize the validity of any experimental results on the statistical signal recognition in acoustics, seismoacoustics, and hydroacoustics; in speech recognition; in medical and industrial diagnostics; in radar; and in other fields. © *2004 MAIK "Nauka/Interperiodica".*

INTRODUCTION

To develop a new recognition system for a classifier of complex acoustic signals or patterns that consist of a combination of different independent components produced by various processes in the sources [1–4], the designer searches for the most informative set of characteristics that constitute a multidimensional classification space. This search is often performed over a limited amount of learning and examining material. At this stage, it is particularly important to assess the validity of results, because the recognition probability significantly depends on the proportion between the length of the learning sample and the dimension of the feature space of the statistical recognition system. An example for recognizing acoustic signals of a complex structure may, in particular, be the noise inside passenger airplanes [1]. Based on the analysis and classification of the spectrum of this noise, the state of particular mechanisms is tested in order to reduce their noise level or to diagnose their technical condition. Another example: the complex structure of acoustic noise of centrifugal pumps, whose spectrum consists of an irregular continuous part and discrete spectral lines, complicates the problem of timely recognizing the approach of the dangerous cavitation in the liquid [2]. In this situation, the use of a combination of different spectrum features in addition to the most informative discrete component can increase the probability of diagnosing the cavitation. Similarly, spectra of hydroacoustic noise of maritime objects contain many different independent components, and it is necessary in many problems to classify the sources of the received signals based on their spectral structure as accurately as possible [3]. In another topical problem of speech recognition [4], to provide a recognition validity, stringent requirements are imposed on the information content of individual physical and formal features in order to select an efficient combination of classification features with the use of the optimal decision rule.

In many such problems, the amount of raw data is limited; at the same time, domains of the classes being recognized partially overlap in the multidimensional feature space and cannot be satisfactorily separated based on the small number features, while the requirements imposed on the recognition validity are stringent. In such cases, the problems are solved by increasing the number n of features involved and by employing a more complex and stronger decision rule [5, 6]. However, a small length L_{lr} of the learning sample strictly limits the maximum admissible number N of features used simultaneously (i.e., in the statistical recognition, the dimension of the feature space), as well as the acceptable classifier complexity (capacity and number of parameters changed during the learning) [7]. When these con-

1063-7710/04/5005-0501$26.00 © 2004 MAIK "Nauka/Interperiodica"

straints are violated, the results of recognition are overestimated. In this regard, it is very important to have a possibility of rapidly estimating the validity of results obtained in searching for an efficient combination of features. It is mostly for the Gaussian distribution of the feature probability density that various calculation methods exist, which relate the main interdependent quantities: error probabilities α and β of the first- and second-kind classification; lengths of the learning L_{lr} and examining L_{ex} samples; number N of features or dimension of the classification space; and the Mahalanobis distance d between the mean elements of domains of classes in the multidimensional space, which, for features distributed by the Gaussian law and for equal covariance matrices M in classes s_1 and s_2, has the form

$$d^2 = (\mathbf{m}_2 - \mathbf{m}_1)^T M^{-1}(\mathbf{m}_2 - \mathbf{m}_1), \quad (1)$$

where $\mathbf{m}_1$ and $\mathbf{m}_2$ are the mean vectors of multidimensional (n-dimensional) domains of classes s_1 and s_2, M is the common covariance matrix, and the T symbol means transpose. The physical meaning of the quantity d is the distance between the mean elements of classes normalized by the variance of their distributions.

As a result of learning a recognition system by limited-length samples of classes with a successively increasing dimension of the feature space, one usually obtains an increasing function of recognition probability versus the number of features. With samples of a limited length, the recognition probabilities obtained experimentally have a lower statistical validity, the higher the dimension of the decision rule. This is associated with an inevitably increasing requirement on the size of statistics for obtaining multidimensional distributions of a higher dimension in the feature space. The problem arises of assessing the validity and statistical confidence of results on the multidimensional recognition. It is difficult to compare experimental results on the recognition probability of real signals with analytical calculations of these probabilities, because such calculations are complex and mostly refer to the Gaussian feature distributions. Therefore, in order to get an approximate but simple and fast validity assessment of experimental recognition probabilities of real signals, we propose to use for the comparison another recognition function also based on learning. Learning realizations for this second function are obtained from fragments of uniform noise, which imitate samples with class features that are used to learn the same recognition system with similarly increasing dimension of the multidimensional space of random features. For such short noise samples at a high capacity of the decision rule, the probability of recognition of such conditional classes grows rather rapidly with dimension of the feature space and may even approach 1.0 as soon as the number of random features is on the order of 10. Let us call this second function "false learning function." It uses the same sample lengths as those for the real signals. By comparing it with results of learning to recognize real signals, we can quickly assess the possibility of quite randomly selecting real features for the multidimensional set in the current experiment and thereby assess the validity of the achieved probability of recognition based on leaning by real signals with an increasing dimension of the feature space for the length of learning samples used in the recognition system. As we noted above, another possible method of assessing the validity of experimental results from the recognition probability is to compare them with results of analytical calculations of the corresponding probabilities. Although this method is possible, it involves complex numerical methods.

Analytical methods for calculating the classification errors are mostly addressed in theoretical works [7–12, 13]. These works report general theoretical dependences of recognition errors α, $\beta(L_{lr}, L_{ex}, N)$ and give typical examples for particular source data, which are mostly applicable to Gaussian and certain symmetric distributions of ensembles in classes. Also, distributions are observed that are close to Gaussian distributions, and the effect of distribution tails is taken into account in a certain approximation [10]. Nonparametric statistical recognition methods do not consider errors associated with allowance for these tails because of the necessity to have a much greater number of samples to obtain satisfactory estimates. These methods usually consider standard decision-making criteria and typical cases, when either prior distributions or only mean and covariance matrices, as well as their estimates obtained from nonparametric methods with unknown distributions and parameters, are known [8–14].

However, the known theoretical works on methods of statistical recognition in multidimensional space actually imply that not only the general population is distributed by the Gaussian or a symmetric law, but also that initial distributions and their parameters are constant and independent of conditions under which the sources operate, propagation conditions in the medium, etc. But these are the factors that, in real problems (heterogeneous sample), cause both the main parameters of distributions in classes (trend of means, change in variances, etc.) and types of these distributions (specified or being sought) to change, resulting in multimodality and quite atypical distributions of domains of classes in the feature space. These effects make it more difficult to use the above-mentioned analytical methods for calculating the recognition errors.

As for the Gaussian distributions of features and domains of classes, calculations of recognition errors steadily become more complex with increasing uncertainty in the initial data. Below, we will consider typical analytical methods of analyzing the classification errors and show how much the numerical methods of estimating the recognition probability actually rely on the Gaussian distribution of domains of classes and also how they are complex to apply at the critical initial stage of designing a recognition system and in the pro-

cess of searching for the most informative multidimensional feature space. In some cases, we will particularly note the absence of allowance for losses in validity in theoretical estimates of the recognition probability. Further, we will briefly consider several typical calculation methods in order of their increasing complexity.

ANALYTICAL METHODS FOR CALCULATING THE RECOGNITION ERRORS

For the Gaussian distribution of probability densities of domains of two equiprobable classes in a space of n features with different means $\mathbf{m}_1$ and $\mathbf{m}_2$ and equal covariance matrices, with the use of the Bayesian classifier, a general expression was obtained in [8] for estimating the classification errors. A family of curves was calculated for a particular case that relate the recognition error probability p_e to the quantity d defined by formula (1), $p_e(d)$, and to the parameter of the family, namely, the dimension of the feature space: $p_e(d; n)$ for $n = 1, 3, 10$, and 20. The plots were presented on a logarithmic scale (Fig. 5.3 in [8]). Estimates of the mean value and variance of p_e were also obtained for the case when the covariance matrices are not equal and for different lengths of the learning sample $L = 12, 50, 100, 200$, and 400. A more demonstrative dependence $p_e(d)$ was obtained in [9] for a similar simple case of recognizing two equiprobable classes s_1 and s_2, $p(s_1) = p(s_2) = 0.5$ with the Gaussian distribution in a one-dimensional feature space using the Bayesian classifier. This simple example of calculations only illustrates the expressions obtained for a more general case of recognizing several classes $s_{i;j}$ with prior probabilities $p(s_i)$ and $p(s_j)$ when the probability of the recognition error is a sum of errors over class s_i and over class s_j:

$$P_e = P(s_i)\Phi\left(\left(\lambda - \frac{1}{2}d_{ij}\right)/\sqrt{d_{ij}}\right) + P(s_j)\left[1 - \Phi\left(\left(\lambda + \frac{1}{2}d_{ij}\right)/\sqrt{d_{ij}}\right)\right], \quad (2)$$

where $\lambda = \ln[P(s_j)/P(s_i)]$ is the logarithm of the decision taking threshold $\theta = P(s_j)/P(s_i)$ for class s, $P(s)$ is the prior probability of patterns of class s, Φ is the tabulated error function of the Gaussian distribution, and $d_{ij} = (\mathbf{m}_i - \mathbf{m}_j)^T M^{-1}(\mathbf{m}_i - \mathbf{m}_j)$ is the Mahalanobis distance between classes s_i and s_j.

When the prior probabilities of classes are equal, $P(s_i) = P(s_j)$, the threshold is equal to 1 and, accordingly, λ is equal to 0. Then, expression (2) takes the form [9]

$$p_e = 1/2\Phi(-1/2\sqrt{d_{ij}}) + 1/2[1 - \Phi(1/2\sqrt{d_{ij}})] = \int_{(1/2)\sqrt{d_{ij}}}^{\infty} (1/\sqrt{2\pi})\exp(-y^2/2)dy. \quad (3)$$

Using expression (3) for the case of two classes, the function $p_e(d)$ was plotted (Fig. 4.4 in [9]). It is clearly seen from the plots that the region where the main drop of classification errors occurs from the maximum values to 5% or lower is observed in the range of d from the minimal values to 10–15, which corresponds to domains of classes that only weakly overlap, are sufficiently separated, and are clearly distinguished.

Somewhat more generalized theoretical calculations for similar simple cases are reported in [10], where the authors mainly concentrate on the methods for calculating the recognition errors. Addressing the possibility of enhancing the recognition validity by increasing the length of the sample, the classification error α is expressed in terms of the tabulated probability integral as a function of the generalized parameter Ld:

$$\alpha = 1 - \Phi[(c_0 + Ld/2)/\sqrt{Ld}\,],$$

where $c_0 = -\frac{8}{L}\ln(2\alpha_0) \le d$ is the condition for the recognition error to be no higher than a specified level α_0 and α_0 is Chernov's upper bound for classification of Gaussian populations.

For the particular case of recognition of two Gaussian classes in an n-dimensional feature space with different means, the same covariance matrix M, and threshold $c_0 = 0$, the expression for errors α and β is

$$\alpha = \beta = 1 - \Phi(\sqrt{Ld}/2).$$

The monotonically decaying function $\alpha(Ld)$ calculated under these conditions is presented in the form of a plot; as for d in expression (3), recognition errors of less than 5% refer to $Ld > 11$, as is seen from the illustration.

We always focus the reader's attention on the illustrations for the following reasons. The learning sample is normally used for developing the classifier; the examining (test) sample, for estimating its efficiency [9]. We therefore reckon that, at the first stage of designing a recognition system, it is fundamentally important to have a simple procedure for calculating the relationship between the number of features, length of the sample, and classification errors, as well as that the corresponding estimation curves should be clear, which simplifies the rapid assessment of current results.

In somewhat more complex problems than the previous ones, the theoretical analysis of the relationship between classification errors and length of the sample for given N-dimensional Gaussian distributions of classes with different means ($\mathbf{m}_1$ and $\mathbf{m}_2$) and different covariance matrices (M_1 and M_2) appears to be already associated with complex calculations and can be realized with the use of the Monte Carlo statistical modeling method (Section 3.4, Pt. 3 in [10]). In this problem,

the analysis uses dichotomous classification and a likelihood-ratio decision rule

$$\lambda_L = \frac{1}{2}\sum_{l=1}^{L}[(\mathbf{x}_l - \mathbf{m}_1)^T M_1^{-1}(x_l - \mathbf{m}_1) - (\mathbf{x}_l - \mathbf{m}_2)^T M_2^{-1}(\mathbf{x}_l - \mathbf{m}_2)] + (L/2)\ln(\det M_1/\det M_2) \geq \theta, \quad (4)$$

where λ_L is the logarithm of the likelihood ratio; $\theta = \ln c$ is the threshold for choosing between the classes s_1 and s_2, which is defined in compliance with the above quality criterion; L is the number of realizations in the sample, $l = 1, \ldots, L$; $\mathbf{m}_1$ and $\mathbf{m}_2$ are the mean vectors of classes s_1 and s_2; $\mathbf{X} = (\mathbf{x}_1, \ldots, \mathbf{x}_l, \ldots \mathbf{x}_L)$ is the N-dimensional vector of features $\mathbf{x}_l^{(n)}$, $n = 1, \ldots, N$ in sample realizations with indices l, where each realization of the sample with index l is represented by a set of n particular real values $x_{n,l}$ of features; and M_1 and M_2 are the covariance matrices of classes s_1 and s_2.

To obtain analytical results and plots of α_0, $\hat{\alpha}(L_{lr}, L_{ex})$ and β_0, $\hat{\beta}(L_{lr}, L_{ex})$, let us replace the parameters of the Gaussian distributions in (4) with their estimates $\hat{\mathbf{m}}_1$, $\hat{\mathbf{m}}_2$, $\hat{M}_1$, and $\hat{M}_2$ so that the results converge to the limiting values α_0 and β_0 only asymptotically as the lengths of the learning samples taken for both classes grow without limit: $(L_{lr})_1, (L_{lr})_2 \longrightarrow \infty$. Particular plots were calculated from formula (4) at $\theta = 0$, $N = 3$, $(L_{lr})_1 = (L_{lr})_2$,

$$\mathbf{m}_1 = \begin{pmatrix}0\\0\\0\end{pmatrix}; \quad \mathbf{m}_2 = \begin{pmatrix}1\\0.5\\0.5\end{pmatrix}; \quad M_1 = \begin{pmatrix}1 & 0.5 & 0.5\\0.5 & 1 & 0\\0.5 & 0 & 1\end{pmatrix};$$

$$M_2 = \begin{pmatrix}1.5 & 0.75 & 0.75\\0.75 & 1.5 & 0\\0.75 & 0 & 1.5\end{pmatrix}.$$

For this case, the regions of a considerably slower decay in errors of the first and second kind (α and β) for the three-dimensional feature space correspond to sample lengths of $L \sim 15$–30, for which the error probabilities are, respectively $\alpha, \beta \approx 0.05$–$0.02$, these limits for α and β being substantially dependent on lengths of the corresponding samples. For L from 30 to 70, the errors α and β asymptotically tend to zero.

Searching for the recognition error probability function versus the sample length when the type of one-dimensional distribution function in each feature is unknown and, therefore, nonparametric decision rules are used is associated with more complex calculations, which employ experimental estimates of the distribution laws, and uses dedicated programs (Section 5.3 in [10]) even for the two-alternative one-dimensional nonparametric recognition. For the multidimensional nonparametric recognition, the analysis and calculation of error probabilities already becomes relatively complex and intricate.

Methods used in the statistical optimization of the feature space include not only feature decorrelation and sample extension techniques, but also methods that provide a given classification error probability through a justified extension of the number of features n and determine the minimal number of these as a function of generalized parameter ρ (Ch. 5.4 in [10]):

$$\rho = n[\sum_{k=1}^{K}((L_{lr})_k + L_{ex})],\ n' \leq n,$$

where n is the initial number of features, n' is the number of features after the optimization, $(L_{lr})_k$ are the lengths of learning samples for each k of classes s_k, and L_{ex} is the length of the examining sample.

The calculation complexity of such problems of optimizing the characteristics of nonparametric learning is already significantly dependent on the degree of overlap of class regions and on the uncertainty of the effect of feature distribution tails. Note that, to obtain sufficient statistics for the tails, a really representative sample of the general population is necessary, whereas, to assess their effect, information on the recognition validity is necessary. Below, we numerically integrate the expression for errors and replace the Mahalanobis distance with its estimate. If the calculations predict that the length of samples required to obtain the desired level of the recognition error is greater than the available length, the problem should be tackled in a different way; namely, one should try to reduce the errors through increasing the number features n. Publication [10], which is actually devoted to these problems, again reduces the solution (Ch. 5.4) to the use of Gaussian distributions under additional constraints: the means over both classes are unknown, the variances are equal, the common matrix is assumed to be diagonal, and thereby the simplified Mahalanobis distance d of Eq. (1) is replaced with its lower estimate. The accuracy of measuring d is determined by the actual resolution Δd of the system and is particularly assumed to be $\Delta d = 0.1$. Under these conditions, the quality criterion was taken in the form of the conditions $(2L_{lr} + L_{ex})N \longrightarrow \min$ and $\alpha(L_{lr}, L_{ex}, N) \leq \alpha_0$.

The equation for optimization of the error probability with respect to the number of samples and number of features can be solved through successive iterations by the numerical integration technique. The dependence $\alpha(n; L_{lr}, L_{ex})$ was obtained as a function of the dimension of the feature space. The family of curves is presented in the form of a plot (Fig. 5.2 in [10]). In particular, optimization was performed for a set of increasing maximum admissible L from $(L_{lr})_{max} = 20$ and $(L_{ex})_{max} = 50$ to 400 and 200, respectively. These values were chosen in accordance with the given d, α, and N

and also based on sample lengths, which are tightly limited by the admissible learning time. The optimized number N' of features that are necessary to achieve the given error probabilities α from 0.09 to 0.02 for the above set of increasing L steadily decreased from $N' = 7$ to 1, respectively. The optimized length of required learning and examining samples, L'_{lr} and L'_{ex}, also steadily decreased and amounted, for the maximum L'_{lr}, to just 120 instead of the initial value of 400; for L'_{ex}, just 160 instead of 200. Families of curves α were calculated for $N = 1$–14, $L_{lr} = 10$–200, and $L_{ex} = 200$–400. For long samples ($L > 100$–200), the curves rapidly approach the $\alpha \approx (0.01–0)$ level at the number of features of $N \leq 3$–5. On the whole, the theoretical families of curves $\alpha(N)$ with L_{lr} and L_{ex} as parameters, presented as an illustration, together with the data presented above, show that they also actually use weakly overlapping and well-distinguishable domains of classes with the features distributed in these domains by the Gaussian law and with sufficiently long samples. However, if the required sample length is greater than the maximum length available, then, to achieve the given recognition validity, the method of increasing the number of features is used. It should be noted that this is usually performed without estimating the corresponding degradation of the recognition validity.

FALSE LEARNING FUNCTION

Thus, as follows from the above concise analysis of several typical analytical methods for calculating the statistic recognition error probability versus the dimension of the feature space and lengths of the learning and examining samples, all these methods, as a rule, prove to be rather intricate and mostly refer to the Gaussian distributions of domains of the classes and to traditional versions of decision rules. At the same time, when a new recognition system is being developed, it is at this important stage that, on the one hand, the basic approach to the synthesis of the structure is established, but on the other hand, by this time, a sufficient amount of samples is not as yet gathered, neither physical nor formalized features are defined, and satisfactory estimates of their distributions are not obtained. This situation makes it problematic to use such calculations in instant estimates of the validity of results of experimental studies (see [5–7, 11, 12, 14] and Sections 1.3, 2, 7, and 8 in [13]). Also, at the first stage of developing a new recognition system, the decision rule itself, which often has a significant specifics, is chosen either from available possibilities or based on tentative information about the feature distributions in classes, while optimization of the system is only possible at the second stage of the development, when the most efficient collection of features is selected, transformed in an optimal fashion to reduce its dimension, and, finally, a decision rule compatible with the structure of the class boundaries in the multidimensional feature space obtained is chosen.

In this regard, it is clear that it is at the first stage of research that a sufficiently simple method is especially needed for the quick estimation of the maximum admissible number of features used in their multidimensional sets that are tested for the information content. The method must provide a simplified validity assessment of the results on the recognition probability as a function of the number of features and of the actual length of the learning sample of the general population. At the same time, such a method must take into account the capacity of the particular decision rule with allowance for all its practical specific properties added on the basis of heuristic considerations. As for the capacity of the decision rule alone, in particular, the dichotomic capacity C_k of the decision function (unlike the capacity of a criterion) is defined as $C_k = 2(k + 1)$, where k is the number of controlled parameters. For separating boundaries in the form of hyperplanes, C_k equals to $2(n + 1)$, where n is the dimension of the feature space; for hyperspheres, $2(n + 2)$; for quadric surfaces, $(n + 1)(n + 2)$; and for polynomial surfaces of degree r, $2C^r_{n+r}$ (here, C is the number of combinations) (Section 2.5.3 in [9]).

To construct an efficient multidimensional feature space, it is also necessary for such a method of assessing the validity of recognition results to allow for specific properties of procedures that algorithmically form and assess the information content of the classification parameters when analyzing and selecting them for an effective set of features. The complexity of such an allowance for algorithmic properties of the classifier in numerical methods of estimating the recognition errors is clear, in particular, from the theoretical assessment of the relationship between the necessary sample length and the given resolution in measuring the features.

In addition to the dependence of the classification probability on factors of information uncertainty of the source data, on dimension of the feature space, and on lengths of the learning and examining samples, the recognition error and the required sample length depend on the step size $\Delta\theta_n$ in searching for the optimum threshold θ_n, which separates the class domains, in each feature x_n. This step size is calculated in accordance with the feature distributions in classes, with resolution $(\Delta x_n)_\varepsilon \approx (\Delta m_n)_\varepsilon$ in measuring the features x_n and the distance between means in classes for a real system, and with the given cost of the first- and second-kind errors for each of the classes. The error in the distance between mean values of features over classes normalized by the variances (i.e., the Mahalanobis distance d) is not only estimated with allowance for the resolution $(\Delta m_n)_\varepsilon$, but also must be no smaller than it is in the optimal case; in the simplest version,

$$(\Delta d)_{\min} \geq (\Delta m)_\varepsilon/\sigma, \quad (\Delta d)_{\min} > 0. \tag{5}$$

When the recognition problem imposes higher requirements on the accuracy of measuring the distance Δd between the mean values, this actually means that the admissible minimum distance between means over the classes measures a corresponding fraction of the variance. For example, if $\Delta d = 0.01$ is specified, this means that the problem may further be solved with mean values that differ by 0.01σ [10].

Such a problem of optimizing the lengths of the learning and examining samples as a function of the required recognition validity (errors of the first and second find) and in accordance with the given accuracy of the measured normalized difference $(\Delta d)_{\min}$ between the means over the classes was mathematically solved in [10] (Ch. 5.1) for the case of one-dimensional parametric recognition. All equations for this case were derived and solved under the following conditions: the number of classes $K = 2$, the distributions of domains of classes are Gaussian, the means over the classes are unknown and the variances are equal, the decision is taken in terms of the maximum likelihood criterion, and the probabilities of recognition errors α and β are assumed to be equal and are calculated from the probability function. In accordance with these conditions, the following initial expression for the error probability was used:

$$\alpha = \beta = F(-m'/\sigma_2)F(m'/\sigma_1) + F(m'/\sigma_2)F(-m'/\sigma_1), \quad (6)$$

where $m' = (m_2 - m_1)/\sigma$ and $F(z)$ is the probability function: $F(x) = [\Phi(x/\sqrt{2})/2] + \frac{1}{2}$, where $\Phi(x) = (2/\sqrt{\pi})\int_0^X \exp(-z^2)\,dz$ for Gaussian x.

After appropriate substitutions, this expression is used for optimizing the recognition system, i.e., for finding such lengths L_{lr}^* and L_{ex}^* that satisfy the constraints and minimize the chosen criterion ρ in accordance with the expressions

$$\rho = (2L_{lr} + L_{ex}) \longrightarrow \min;$$

$$\alpha = \beta = F(\Delta d/\sqrt{2/L_{lr}})F[-\Delta d/\sqrt{(2/L_{lr}) + (4/L_{ex})}]$$

$$+ F(-\Delta d/\sqrt{2/L_{lr}})F[\Delta d/\sqrt{(2/L_{lr}) + (4/L_{ex})}] \le \alpha_0 = \beta_0.$$

Or, after transformations, the optimization problem takes the form

$$\Delta d^2 = (2L_{lr} + L_{ex}) \longrightarrow \min;$$

$$\Phi(\Delta d/\sqrt{L_{lr}/2})\Phi[-\Delta d/2\sqrt{(1/L_{lr}) + (2/L_{ex})}] \ge 1 - 2\alpha_0, \quad (7)$$

where Φ is the probability function $\Phi(x) = 2/\sqrt{\pi}\int_0^\infty \exp(-z^2)\,dz$ and α_0 is the given upper bound of errors of the first kind, $\alpha_0 = \beta_0$.

To solve this problem is to obtain the optimum values L_{lr}^* and L_{ex}^*. For each particular $\Delta d \equiv \Delta m'$, the optimum lengths L_{lr}^* and L_{ex}^* are determined by solving Eqs. (6), (7) using standard methods of integer programming. The desired sample lengths are expressed in the generalized form as $L_{lr}^*(\Delta d^2)$ and $L_{ex}^*(\Delta d^2)$ and obtained as a function of the given recognition probability $(1 - \alpha_0)$.

Calculations performed for a particular example of this problem in formulation (7) show that, if the required accuracy of measuring the distance between the mean values over the classes increases (i.e., Δd decreases) by a factor of a (for example, for the initial value of 0.1, the new accuracy will be $0.1/a$), the required sample length increases by a factor of a^2 with respect to the initial length L_{lr} (i.e., becomes equal to $L_{lr}a^2$) at least for any recognition probability p higher than 0.9 (Ch. 5.1 in [10]). Because the necessary sample lengths are usually relatively high, such an increase is significant and not always feasible.

It is clear from the analysis of numerical methods for calculation of classification errors why, at initial stages of research, the validity of the experimental results on the multiparameter classification is estimated at the intuitive level. This statement refers to results on both learning and examining. Especially for recognition errors estimated at close to 1.0, the results obtained prove to be too optimistic and their physical interpretation is inadequate due to the statistical learning error associated with the excess dimension of the feature space or with too high a capacity of the decision rule with respect to the insufficient length of the learning sample. Also, real recognition algorithms usually include a series of heuristic operations, which significantly affect the classification errors, but are too complex to be taken into account in calculations.

The experimental probability of the multiparameter classification is known to be very critical to the actual proportion between the sample length and the number of features. It is known in particular that, for the 100% classification of L realizations (patterns) arbitrarily grouped in the L-dimensional feature space, it is sufficient to use L linear separating boundaries (Section 2.5.3 in [9]). Such a classification is possible even when domains of the classes overlap completely. This may not be accompanied by any generalization, i.e., learning in the classification. Let us call such a learning "false learning."

Therefore, experience in solving various recognition problems, in particular, in acoustics, shows that it is necessary to have a simple estimate of validity of the multiparameter classification probabilities obtained in real studies. This is particularly important when the probabilities obtained are close to 1, because such results may to a great extent be caused by too large a number of features used with a sample of a limited length [5–7, 11, 12].

To provide a simpler practical procedure for estimating the classifier's statistical errors in learning or examining, the statistical false learning function (FLF) is proposed.

False learning function is the term that applies to the probability p_r of classification of learning samples of length L_r with random features $x_{l,n}$, $l = 1, \ldots, L_r$, selected from a uniform noise, considered as a function of an increasing number of random features $n_r = 1, \ldots, N_r$ in terms of a multidimensional decision rule at a fixed sample length. Thus, if it is necessary to recognize, for example, two classes A and B of real acoustic signals, two samples of lengths L^A and L^B are formed, which contain particular realizations with sets of features x_n of real signals: $(x_{l,n})^{A;B}$, $l = 1, \ldots, L^{A;B}$; $n = 1, \ldots, N$. To construct the false learning function, one should form noise learning samples of a random process, for example, with a discrete uniform distribution, of lengths L_r^A and L_r^B, whose individual realizations consist of random features $(x_r)_{l,n}^{A;B}$, $l_r = 1, \ldots, L_r^{A;B}$; $n_r = 1, \ldots, N_r$ with corresponding probability distributions.

Experimentally, the FLF $p_r(n_r/L_r)$ is obtained through learning by different portions of a single noise sample, these portions being artificially identified with different classes. Theoretically, the Mahalanobis distance between classes s_i and s_j over all features n_r for an unlimited uniform sample of the random noise process is zero: $d_{ij} \equiv 0$. However, at small sample lengths L_r^A and L_r^B, its estimate $\hat{d}_{ij}$ for some n_r may give a random possibility of false classification at $\hat{d}_{ij}(x_r)_n > 0$, because the smaller the sample, the greater the variance of the sample means over the classes and the higher the probability of finding such $(x_r)_n$ that the difference between the means is significantly greater than zero.

Thus, the FLF is obtained by passing artificially generated noise realizations through the same mechanism of selecting features and classification as the one used to classify the real signals. As the number n_r of random features used in the multidimensional decision rule is increased, the uniform noise sample L_r, artificially divided into "classes," gradually becomes increasingly better to classify.

The rate at which the probability of this false classification increases with the number of features, $p_r(n_r)$, also significantly depends on capacity of the decision rule.

Below, we consider an example of applying the FLF to the development of a recognition system. To facilitate the understanding of the example, we will describe the algorithm used by the classifier and the set of real classification features of a complex acoustic signal.

The algorithm used by the classifier has a comparatively high capacity of the decision rule. It relies on the method proposed in [15–17] (V.A. Fedoseev; V.L. Braĭlovskiĭ; modified versions were realized by A.N. Chernov, Andreev Acoustics Institute). This statistical multiparameter recognition algorithm uses the Bayesian approach to realize the linear division into classes in the selected most informative multidimensional feature subspaces estimated in terms of the likelihood ratio.

Fundamentally, the algorithm consists of two basic parts: preprocessing of features from statistics of the sample and taking a decision in the multidimensional feature space. The source two-dimensional arrays of particular feature values $x_{n,l}$ in realizations of learning samples of lengths L_{lr}^A in the class A: $l^A = 1, \ldots, L_{lr}^A$ and L_{lr}^B in the class B: $l^B = 1, \ldots, L_{lr}^B$ are created separately for each class, $(x_{n,l})^A$ and $(x_{n,l})^B$. Each realization number l of both classes contains N features, $n = 1, \ldots, N$; the index n of each physical feature $x_{n,l}$ is fixed and is the same in all sample realizations of classes A and B.

At first, using the learning sample L_{lr}, the preprocessing procedure finds estimates of one-dimensional distributions of the features $x_{n,l}$, $n = 1, \ldots, N$, in the classes or calculates the means over the classes and divides the interval between them into a number of sections. Our version of the algorithm estimates the information content of the features through projecting the distributions onto the coordinate axes: projection onto random directions is not considered here. Next, optimal thresholds for the pairs of classes for each feature are calculated in terms of a certain decision-taking criterion (the ideal observer, Neyman–Pearson, or maximum likelihood one). Of the total number of features, the most informative features are selected whose number is a factor of 5 to 10 greater than the number that is expected to be used in the ultimately created multidimensional decision rule. Then, the algorithm codes the values of these features according to their thresholds (possibly, in the binary, ternary, quaternary, and so on, notation) and calculates an individual likelihood ratio estimate λ for each element of the multidimensional discrete hypercube feature space. Let us describe the algorithm in more detail.

Let samples of N-dimensional feature vectors, which represent the classes A and B to be recognized (the dichotomy case), be applied to the input of the system:

$$X_l^A = (x_{l,1}^A, \ldots, x_{l,n}^A, \ldots, x_{l,N}^A), \quad l = 1, \ldots, L^A; \quad n = 1, \ldots, N,$$

$$X_l^B = (x_{l,1}^B, \ldots, x_{l,n}^B, \ldots, x_{l,N}^B), \quad l = 1, \ldots, L^B,$$

where L^A and L^B are the numbers of learning realizations (patterns) in classes A and B, respectively, and n is the total number of features.

The samples L^A and L^B for each feature x_n are used to calculate the estimates of minimum, maximum, and

mean values over the classes (or over the source values, or in terms of a robust estimate):

$$(x_n^A)_{\min}, (x_n^B)_{\min}; (x_n^A)_{\max}, (x_n^B)_{\max}; \quad \langle x_n\rangle^A, \langle x_n\rangle^B; \quad n = 1, \ldots, N. \tag{8}$$

If the algorithm relies on the mean values over the classes, the distance between them in each feature, $|\langle x_n\rangle^A - \langle x_n\rangle^B|$, is divided by bounds $\theta_\varepsilon^{(n)}$ in a certain number E of intervals $\Delta_\varepsilon^{(n)}$:

$$\theta_\varepsilon^{(n)} = \inf_{A,B}(\langle x_n\rangle^A, \langle x_n\rangle^B) + (\left|\langle x_n\rangle^A - \langle x_n\rangle^B\right|/E)\varepsilon\Delta_\varepsilon^{(n)}, \tag{9}$$

where $\varepsilon = 1, \ldots, E-1$; $\Delta_\varepsilon^{(n)}(x_n)$ is the step size of discretely changed class boundaries; and $(E-1)$ is the number of segments on the interval $[\langle x_n\rangle^A, \langle x_n\rangle^B]$.

The quantity E may be varied. For each of the bounds, as for the test threshold $\theta_\varepsilon^{(n)}$, which separates the classes A and B by the criterion of, for example, an ideal observer, we further estimate the total recognition error p_e (if prior class probabilities are unknown, $P(A) = P(B) = 0.5$) from the sample. By exhaustively searching through $\theta_\varepsilon^{(n)}$ in expression (9), such ε is finally found that minimizes the total error $p_e = \alpha + \beta$, $\hat{p}_e^{(n)}(\theta_\varepsilon^{(n)}) = \hat{\alpha}^{(n)}(\theta_\varepsilon^{(n)}) + \hat{\beta}^{(n)}(\theta_\varepsilon^{(n)})$ in separating the sample into classes by each feature x_n:

$$\hat{p}_e^{(n)} = \inf_\varepsilon[\hat{p}_e^{(n)}(\theta_\varepsilon^{(n)})], \quad \varepsilon = 1, \ldots, E-1.$$

Here, $\hat{\alpha}$ and $\hat{\beta}$ are the estimates of the recognition errors of the first and second kind, respectively. In the version of the algorithm that we used, estimates $\hat{p}_e^{(n)}(\theta_\varepsilon^{(n)})$ of error probabilities or the corresponding recognition errors $\hat{p}^{(n)}[\theta_\varepsilon^{(n)}] = 1 - p_e^{(n)}[\theta_\varepsilon^{(n)}]$ are determined in terms of Fisher's maximum likelihood criterion with the threshold that corresponds to the minimum mean error:

$$\hat{p}^{(n)}[\theta_\varepsilon^{(n)}] = \sup_\varepsilon[(l_\varepsilon^A + l_\varepsilon^B)/(\mathrm{L}^A + \mathrm{L}^B)],$$

where l_ε^A and l_ε^B are the numbers of recognized elements of the learning samples L^A and L^B in classes A and B, respectively, with the test bound $\theta_\varepsilon^{(n)}$ as the class separation threshold.

Note that the relationship between the resolution $(\Delta x_n)_\varepsilon$ in the measurement of the source features, the distance $(\Delta m_n)_\varepsilon$ between the mean values (or, in accordance with formulas (8), the minimum and maximum values), and the Mahalanobis distance $(\Delta d_{ij}^{(n)})_{\min}$, on the one hand, and the step size $\Delta\theta_n \equiv \Delta_\varepsilon^{(n)}(x_n)$ in searching for the optimum threshold, on the other hand, may significantly affect the probability of recognizing real signals and the FLF. As we have shown above in this section, when the given measurement accuracy Δd is actually high or excessive with respect to the feature measurement accuracy, i.e., when $(\Delta d)_{\min} < (\Delta m_n)_\varepsilon/\sigma$, the required length of the learning sample may significantly increase (expression (5) and further). However, if the actually available samples are short, then, due to the insufficient statistics, the validity of the obtained probabilities, let them even be high, of recognizing real signals in the multidimensional feature space will be much lower and the corresponding FLF will grow faster with the dimension of the solution.

Next, the algorithm used in the experiment fixes the bounds corresponding to the maximum recognition probabilities in each feature x_n as the thresholds θ_n. All features in all sample realizations, $x_{l,n}^A$ and $x_{l,n}^B$, are then coded according to these thresholds in a binary manner (0, below the threshold; 1, above the threshold) to obtain the binary-coded features $y_{l,n}^A$ and $y_{l,n}^B$. Each binary domain (0; 1) of each feature ($y_{l,n} = 0$ or $y_{l,n} = 1$) corresponds to an individual proportion between the numbers of realizations from classes A and B that fall into it and an individual recognition probability

$$\hat{p}_n^A = l_n^A/\mathrm{L}^A; \quad \hat{p}_n^B = l_n^B/\mathrm{L}^B;$$

$$\hat{\lambda}_n = (l_n^A/\mathrm{L}^A)/(l_n^B/\mathrm{L}^B) \text{ or } \hat{\lambda}_n = (l_n^B/\mathrm{L}^B)/(l_n^A/\mathrm{L}^A),$$

where l_n^A and l_n^B are the values of l_ε^A and l_ε^B at the optimum values of $\theta_\varepsilon^{(n)}$. When estimating the information content of features y_n for each domain with respect to the threshold (0; 1), in addition to the total recognition probability, these domains are identified by the class to which they belong.

The binary-coded features y_n are arranged according to their information content ($\hat{p}_n$) and only those of them whose information content is no lower than a certain value are used in the further processing, so that, after this reduction, their number will be N', $N' < N$. Different pairs of features of all realizations of the learning sample are coded anew based on these binary arrays of the selected features. In the new array, each pair of features in the realization is associated with a two-bit binary code, each of whose bits equals to the value (0; 1) of one of the features y_n, y_{n+a} in this realization. A new coded array is obtained consisting of two-bit binary codes for different combinations (C_n^2) of pairs of features y_n, y_{n+a}, and this array forms the following subspaces in the two-dimensional feature space: 00, 01, 10, 11.

A procedure for estimating the conditional distribution probabilities of the sample elements over these subsapaces was described as early as in [15–17]. Here,

we only briefly note that this version of the algorithm performs an exhaustive search through all pairs of features to estimate the information content of the subspaces obtained in terms of the value $\hat{p}_{n;\,n+\alpha}$ for each such pair y_n, y_{n+a}, thereby actually allowing for the relationship between them. In this way, the most informative pair is determined from the learning sample. Its corresponding set of sample estimates λ_n of the classification information content is simultaneously stored for each of the four feature subspaces (00, 01, 10, 11), which correspond to the statistic material of the learning sample. Further, the algorithm supplements the best pair of features selected with an additional (without exhaustively searching through all possible combinations of three features) feature taken from those that have previously been selected as the most informative ones. Here, the algorithm uses a three-bit binary coding for the three features of each realization of the sample, and the method for estimating the information content corresponds to the previous cycles. The example of applying the FLF illustrated in the figure uses a version of the algorithm that supplements the best pair with up to eight additional best features, so that the final quantized recognition feature space is ten-dimensional.

To construct the hyperplane that separates the classes in the multidimensional binary feature space, the algorithm uses not all of its elements (a total of N' hypercubes, which correspond to different multibit code sets of 0s and 1s). Those of them for which the ratio λ for realizations of classes appeared to be relatively close to 1.0 ($\hat{\lambda}_n = (\hat{p}_n^A/\hat{p}_n^B) \approx 1 \pm g$, $g = 0.1$–0.3) are not used, because, otherwise, the recognition probability of the system as a whole may decrease [16, 17]. The domain of each hypercube is identified with the class A or B, and the recognition probability of patterns that fall into this region is determined by the above ratios $\hat{p}_n^A$, $\hat{p}_n^B$, and $\hat{\lambda}_n$.

Subspaces with dimensions of 2–10, consisting of particular sets of informative elementary regions (hypercubes) for each class, are separated by the hyperplane in the total multidimensional feature space. As a result of the synthesis of the decision rule from the learning sample, the main parameters of the total feature space are stored along with parameters of subspaces of each of the classes and of the separating hyperplane. The efficiency of this recognition system is estimated from the statistics of the test (examining) sample.

RESULTS OF THE EXPERIMENT ON APPLYING THE FLF

The figure shows an experimental FLF $p_r(n_r/L_r)$ for the recognition algorithm described above. The most informative features are preliminarily selected by the criterion of an ideal observer, and then a decision is taken in the hypercube space with a separating boundary realized in the form of logical Boolean functions.

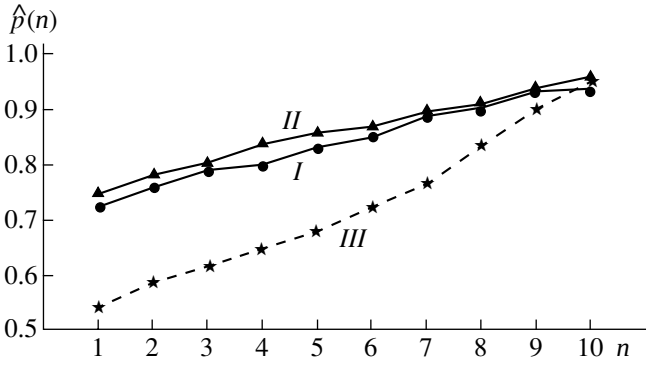

Recognition probability versus the dimension of the feature space: (*I*) real signal, $L_A = 206$, and $L_B = 214$; (*II*) real signal, $L_A = 100$, and $L_B = 100$; and (*III*) noise sample, $L_r^A = L_r^B = 216$.

(This experiment was performed with the classification software developed at the Andreev Acoustics Institute, Moscow.) As seen from the figure (curve *III*), with the use of 9 to 10 random features, this decision rule is capable of separating a uniform finite sample of model noise into artificial classes with the probability of 0.96. This experiment was performed under the following conditions:

(i) The number of realizations (patterns) in the two artificially created classes was $L_r^A = L_r^B = 216$ (the total noise sample of 432 realizations was cut in two).

(ii) The noise generator had a uniform discrete probability density, and the values generated in the range from 0 to 1 were rounded with an accuracy of $(\Delta x_n)_\varepsilon = (\Delta m_n)_\varepsilon = 0.001$; this is a simplified model of the distribution of the normalized components of the signal's averaged energy spectrum, which actually have the β distribution of the probability density.

(iii) 64 random numbers were generated for each realization, which imitated 64 source features $N_r = 64$, from each of which the algorithm described above preliminarily selected $N_r' = 40$ best features, i.e., those that, being taken separately, give the higher probability of separating artificial classes.

(iv) In the search for the optimum threshold for each selected random feature, the algorithm divided the difference between the mean values in the classes into eight segments and analyzed seven test bounds $\theta_\varepsilon^{(n)}$, $\varepsilon = 1, \ldots, 7$, as in the case of estimating the information content of features of real signals; the above rounding of the generated random numbers to the accuracy $(\Delta x_n)_\varepsilon = (\Delta m_n)_\varepsilon$ of 0.001 was not checked by condition (5): $(\Delta d)_{\min} \geq (\Delta m)_\varepsilon/\sigma$.

(v) The most informative random feature allowed the decision rule to tell one half of the noise sample from the other with the probability of $p_r \approx 0.53$.

(vi) The two most informative random features, found through exhaustively searching through all pairs out of 40 features, together (the two-dimensional feature space and the decision rule) gave the probability of false recognition of $p_r \approx 0.58$.

(vii) A gradual increase in the number of additional informative random features increasingly enhances the rate of growth of the false classification probability up to $p_r \approx 0.96$ at the total of ten random features, i.e., with a ten-dimensional decision rule.

The statistical FLF plotted in the figure (curve *III*) corresponds to the decision rule described above at a fixed number of realizations in the classes (216 in each). It is clear that the behavior of the FLF changes with a change not only in the decision rule or sample length but also in the probability distribution function of the model noise, in the number of source or selected features, and in the selection rule.

To use the FLF in practice, it is necessary to compare it with experimental results on the classification based on learning with real signals. A result of applying the FLF is given in the figure.

Curves *I* and *II* refer to experimental results on classification of real acoustic signals. These results were obtained at the early stage of our study aimed at how to find the most efficient set of features for recognizing two classes of these complex signals in the multidimensional feature space. Curve *III* is the FLF for the same preprocessing, the same decision rule, and the same values of the parameters. Curves *I*, *II*, and *III* are obtained for the classification learning with the above statistical recognition algorithm. To construct a real learning sample, the current energy spectrum $G(\omega)$ was first calculated from each realization of the received acoustic signals $x(t)$:

$$G(\omega) = \lim_{T \to \infty} \frac{1}{2\pi} |S_T(\omega)|^2 / T,$$

where $S_T(\omega)$ is the current spectrum, i.e., the Fourier transform of the sample $x_T(t)$:

$$S_T(\omega) = \int_0^T x(t)\, e^{-j\omega t} dt = \int_{-\infty}^{\infty} x(t)\, e^{-j\omega t} dt,$$

where T is the length of the sample of realization of signal $x(t)$.

The spectra were calculated from discrete sample values of the source signal by Cooly and Tukey's fast Fourier transform algorithm.

A special algorithm was used to automatically analyze the spectrum of acoustic signals and construct 64 different spectral features of the signal, which represented together the minimal complete system of the signal's spectral features. One part of the features was associated with different parameters of particular discrete components, i.e., of narrowband spectrum spikes that do not enter harmonic scales. Another part was associated with different parameters of groups of discrete components of multiple frequencies that enter harmonic scales. The third part of the features consisted of parameters of the continuous part of the signal spectra. The number of classes was 2, and they corresponded to different sources of the acoustic signals being studied.

In accordance with the algorithm described above, from the total of 61–64 features, the preprocessing procedure selected the 40 most informative of them for the particular sample of acoustic signals in terms of the maximum likelihood criterion. By exhausting the combinations of 40 features by 2 at a time, the pair was found that minimizes the mean sample classification error in the two-dimensional space. From the 38 remaining selected best features, the best features additional to the first pair were chosen beginning from the best one: at first, one feature was added; then two, three, and so on, for three-, four-, and more-dimensional decision rules, respectively. As we see from the figure, because the feature correlation is strong (the decorrelation is not shown), the probability of classification (curves *I* and *II*) of real signals of two classes slowly grows. Curve *II* corresponds to approximately half the total number of realizations (100 from each class). Curve *I* was obtained from the total amount of the experimental data (216 and 208 realizations in classes *A* and *B*).

Placing the experimental probability $p(n)$ of classification of real acoustic signals from samples L_{lr} together with the FLF curve $p_r(n_r)$ for the noise sample L_r on the same figure allows us to interpret the results of the study much more objectively. For this case, it is clear that no more than a total of five to six formal acoustic features of those that enter the multidimensional set can be used. Then, the probability of random classification based on FLF already appears to be close to $p_r(n_r = 6) \sim 0.7$. With the number of features of $n = n_r > 5$–6, the comparison with the FLF clearly shows the low validity of further selecting real signal features into the set for this decision rule and sample length. This is associated with an inadmissible growth of the probability of actually random selection of further features of the real signal and, consequently, with the false learning. The results obtained on the basis of the FLF were used for designing a multialternative statistical classifier of acoustic signals, which used only three features for carrying out pairwise dichotomies.

Note that nature also avoids decision rules of an increased dimension in its mechanisms of brain operation, although it is lavish with very complex, elaborate, and diverse processing of the same vitally important acoustic signals. For example, the auditory system of dolphins performs the processing of pulsed signals so as to recognize the important characteristics of the received pulsed signals by no more than three features in succession, beginning with the most important one [18]. Studies have also shown that, to take a decision, the human brain represents information mostly in a two-dimensional form; more rarely, in a three-dimensional form.

In contrast to traditional recognition algorithms, for which the FLF is specified in terms of probabilities, for nondeterministic algorithms (neural networks and perceptrons), the FLF may be defined as, for example, the number Q of cycles of the algorithm needed to adaptively solve the problem. In particular, for a three-layer perceptron with error back propagation (from MATHLAB's Neural Networks Tools software package), a rapidly decaying function of the number of adaptive cycles taken to tune the perceptron's structure to a given recognition probability of $p = 0.9$ was obtained as the FLF. The algorithm was slow to recognize two random samples $L_r^A = L_r^B = 20$ from noise with a discrete uniform distribution when it used one or two features (at $n_r = 1$ or 2, it took 300 to 500 cycles: $Q(n_r = 1–2) = 300–500$). The algorithm was much faster when it used $n_r = 3$ to 10 features. In this case, the FLF had the form of an exponentially decaying curve $Q(n_r)$, which was equal to 30–50 cycles at $n_r = 9–10$. Without averaging, the spread with respect to the approximating exponential function was 20–30%, so that the perceptron's FLF had the form of $Q(n_r) \sim Q_0\exp(-n_r a)[1 \pm (0.2 – 0.3)]$.

In conclusion, note that the simplicity of generating the FLF is the basis for its wide application together with the current results on multiparameter recognition. By comparing the results of learning a system to recognize real signals for any particular decision rule, one can approximately but quickly assess the validity of the data obtained with multidimensional sets of features for the signal under study. The FLF proposed above can also be used to properly design the experiment and more unbiasedly interpret the results on multiparameter recognition of real signals when developing a deterministic statistical classifier or a neural-network-based system.

It is clear that, if the recognition system's algorithm is modified, a new FLF adequate to the new version must be generated. Such modifications are changes in the algorithm or parameters of the preprocessing procedure and feature estimation criteria, a change in the decision rule, a change in the normalization of the initial feature space, a change in the step size when searching through the test thresholds, and a change in the number of initial or best features when selecting the most informative of them.

The application of a simple and clear false learning function is useful for characterizing the validity of any experimental results on the automated statistical recognition of signals in acoustics, hydroacoustics, and seismoacoustics; in the recognition of speakers by their pronunciation; in medical diagnostics; in malfunction diagnosis of mechanisms from noise and vibrations; in the recognition of visual patterns; in radar; and in other fields.

ACKNOWLEDGMENTS

I am grateful to L.E. Kazakevich for the assistance in computer experiments and V.A. Baranov for the assistance in calculating the FTF for the perceptron.

REFERENCES

1. V. M. Kuznetsov, Akust. Zh. **49**, 293 (2003) [Acoust. Phys. **49**, 241 (2003)].
2. M. Chudina, Akust. Zh. **49**, 551 (2003) [Acoust. Phys. **49**, 463 (2003)].
3. S. K. Kadashnikov and A. I. Mashoshin, Akust. Zh. **44**, 462 (1998) [Acoust. Phys. **44**, 394 (1998)].
4. E. Chilton and I. Paraskevas, J. Acoust. Soc. Am. **113**, 2271 (2003).
5. S. J. Raudys and A. K. Jain, IEEE Trans. Pattern. Anal. Mach. Intell. **13** (3), 252 (1991).
6. A. K. Jain and B. Chandrasekaran, in *Classification, Pattern Recognition, and Reduction of Dimensionality*, Vol. 2 of *Handbook of Statistics*, Ed. by P. R. Krishnaiah and L. N. Kanal (North-Holland, Amsterdam, 1982), Vol. 2, pp. 835–855.
7. S. J. Raudys and V. Pikelis, IEEE Trans. Pattern. Anal. Mach. Intell. **2** (3), 243 (1980).
8. K. Fukunaga, *Introduction to Statistical Pattern Recognition* (Academic, New York, 1972; Fizmatlit, Moscow, 1979).
9. J. T. Tou and R. C. Gonzalez, *Pattern Recognition Principles* (Addison-Wesley, Reading, Mass., 1974; Mir, Moscow, 1978).
10. Ya. A. Fomin and G. R. Tarlovskiĭ, *Statistical Theory of Pattern Recognition* (Radio and Svyaz', Moscow, 1986), p. 364 [in Russian].
11. L. Devroye, IEEE Trans. Pattern. Anal. Mach. Intell. **10** (4), 530 (1988).
12. S. J. Raudys and R. P. W. Duin, Pattern Recogn. Lett. **19** (5–6), 385 (1998).
13. A. K. Jain, R. P. W. Duin, and Jianchang Mao, IEEE Trans. Pattern. Anal. Mach. Intell. **22** (1), 4 (2000).
14. A. Ruiz, Pattern Recogn. **28** (6), 921 (1995).
15. V. L. Braĭlovskiĭ and A. L. Lunts, Tekh. Kibern. (Moscow), No. 1, 20 (1964).
16. V. L. Braĭlovskiĭ, Tekh. Kibern. (Moscow), No. 2, 30 (1964).
17. V. L. Braĭlovskiĭ and A. L. Lunts, Tekh. Kibern. (Moscow), No. 3, 99 (1967).
18. N. A. Dubrovskiĭ, T. V. Zorikov, O. Sh. Kvizhinadze, and M. M. Kuratishvili, Sens. Sist. **2** (1), 37 (1992).

Translated by A. Khzmalyan

Acoustical Physics, Vol. 50, No. 5, 2004, pp. 512–517. Translated from Akusticheskiĭ Zhurnal, Vol. 50, No. 5, 2004, pp. 603–608.

Electroacoustic Lamb Waves in Piezoelectric Crystal Plates

M. Yu. Dvoesherstov, V. I. Cherednik, and A. P. Chirimanov

Lobachevskii State University, Nizhni Novgorod, pr. Gagarina 23, Nizhni Novgorod, 603950 Russia

e-mail: dvoesh@rf.unn.ru

Received April 3, 2003

Abstract—The main characteristics of various types of plate electroacoustic waves propagating in piezoelectric single-crystal plates of various thickness are numerically studied. A number of piezoelectric plates and orientations in them with record high values of the electromechanical coupling coefficient for transverse plate waves are proposed. © *2004 MAIK "Nauka/Interperiodica".*

As is well known [1–5], a set of plate waves of two classes, Lamb waves and transverse waves, can propagate in a piezoelectric crystal plate. Plate waves propagating in piezoelectric crystal plates provide the basis for developing a variety of acoustoelectronic pressure and temperature sensors, gas and liquid analyzers, and so on [6–8].

The objective of the present study is the numerical analysis of the main parameters of various types of plate waves propagating in plates (whose thickness H is comparable with the wavelength λ) made of piezoelectric single crystals of any crystallographic symmetry class. For various piezoelectric crystal plates, a theoretical search for orientations corresponding to the optimal parameters of plate waves (a high electromechanical coupling coefficient K^2 and a minimal temperature coefficient of delay) is performed.

Figure 1 shows the coordinate system for the problem under investigation. Let the X_1 axis be the direction of wave propagation and the X_3 axis be perpendicular to the plane of a plate of thickness H. For convenience, we place the plane $X_3 = 0$ in the middle of the plate.

As is known [9], acoustic waves propagating in isotropic plates are subdivided into two classes: Lamb waves with vertical-longitudinal polarization and plate waves with transverse polarization (SH waves [1, 5]). In piezoelectric crystal plates, depending on the crystal symmetry class and the specific direction in the crystal, plate waves may have various structures, but they are always accompanied by a quasistatic electric field. The analysis of the properties of plate waves propagating in a piezoelectric plate of any crystallographic symmetry class and any orientation can be performed only by a numerical method. In the analysis, the standard Farnell–Jones technique [10] can be used. The general solution for the mechanical displacements u_i and the electric potential φ can be represented as a sum of eight partial waves:

$$u_i = \sum_{n=1}^{8} A_n \alpha_i^{(n)} \exp(i\kappa\beta^{(n)} X_3) \exp\{i\kappa[X_1 - Vt]\},$$
$$\varphi = \sum_{n=1}^{8} A_n \alpha_4^{(n)} \exp(i\kappa\beta^{(n)} X_3) \exp\{i\kappa[X_1 - Vt]\}. \quad (1)$$

Here, $\alpha_i^{(n)}$ (i = 1, 2, 3) and A_n are the amplitude coefficients, $\beta^{(n)}$ are the attenuation coefficients along the X_3 axis, κ is the wave number, V is the velocity of wave propagation, and t is time. Substituting general solution (1) into the coupled equations of the theory of elasticity for a piezoelectric medium [10], we obtain the Christoffel matrix equation (Eq. (2) below), from which all eight attenuation coefficients $\beta^{(n)}$ (n = 1–8) and the amplitude coefficients $\alpha_i^{(n)}$ can be found:

$$\begin{pmatrix} G_{11} & G_{12} & G_{13} & G_{14} \\ G_{21} & G_{22} & G_{23} & G_{24} \\ G_{31} & G_{32} & G_{33} & G_{34} \\ G_{41} & G_{42} & G_{43} & G_{44} \end{pmatrix} * \begin{pmatrix} \alpha_1 \\ \alpha_2 \\ \alpha_3 \\ \alpha_4 \end{pmatrix} = 0. \quad (2)$$

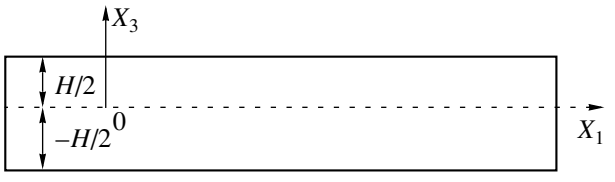

Fig. 1. The coordinate system.

1063-7710/04/5005-0512$26.00 © 2004 MAIK "Nauka/Interperiodica"

Here,

$$\begin{aligned}
G_{11} &= C_{55}^*\beta^2 + 2^*C_{15}^*\beta + C_{11} - \rho^*V^2,\\
G_{12} &= G_{21} = C_{45}^*\beta^2 + (C_{14} + C_{56})^*\beta + C_{16},\\
G_{13} &= G_{31} = C_{35}^*\beta^2 + (C_{13} + C_{55})^*\beta + C_{15},\\
G_{14} &= G_{41} = e_{35}^*\beta^2 + (e_{15} + e_{31})^*\beta + e_{11},\\
G_{22} &= C_{44}^*\beta^2 + 2^*C_{46}^*\beta + C_{66} - \rho^*V^2\\
G_{23} &= G_{32} = C_{34}^*\beta^2 + (C_{36} + C_{45})^*\beta + C_{56},\\
G_{24} &= G_{42} = e_{34}^*\beta^2 + (e_{14} + e_{36})^*\beta + e_{16},\\
G_{33} &= C_{33}^*\beta^2 + 2^*C_{35}^*\beta + C_{55} - \rho^*V^2,\\
G_{34} &= G_{43} = e_{33}^*\beta^2 + (e_{13} + e_{35})^*\beta + e_{15},\\
G_{44} &= -(\varepsilon_{33}^*\beta^2 + 2^*\varepsilon_{13}^*\beta + \varepsilon_{11}),
\end{aligned} \tag{3}$$

where C_{ij}, e_{ij}, and ε_{ij} are the tensors of elastic, piezoelectric, and dielectric constants of the material represented in the contracted matrix form [10] and ρ is the density of the material.

Note that, depending on the crystal symmetry and direction of wave propagation [11], Eq. (2) may be confluent and simultaneously have two independent solutions, because zero terms may appear in it. If the following conditions are satisfied for the elastic and piezoelectric constants of the piezoelectric crystal in the accepted coordinate system,

$$\begin{aligned}
C_{14} = C_{16} = C_{34} = C_{36} = C_{45} = C_{56} = 0;\\
e_{14} = e_{16} = e_{34} = e_{36} = 0,
\end{aligned} \tag{4}$$

one of the independent solutions of Eq. (2) corresponds to piezoactive Lamb modes of the vertical-longitudinal polarization with two components of mechanical displacement and an electric potential (u_1, u_3, and φ), and the other independent solution corresponds to a nonpiezoactive, purely transverse wave with one transverse component of mechanical displacement u_2. If the condition

$$\begin{aligned}
C_{14} = C_{16} = C_{34} = C_{36} = C_{45} = C_{56} = 0;\\
e_{11} = e_{13} = e_{15} = e_{31} = e_{33} = e_{35} = 0
\end{aligned} \tag{5}$$

is satisfied, one of the independent solutions corresponds to a piezoactive plate wave of the transverse polarization with one transverse displacement component and an electric potential (u_2, φ) and the other independent solution corresponds to nonpiezoactive Lamb modes of vertical-longitudinal polarization with two components of mechanical displacement (u_1, u_3).

Thus, if the symmetry conditions (4) and (5) are satisfied, Eq. (2) will always have two independent solutions for Lamb modes of any order, because the symmetry conditions (4) and (5) and their effect on Eq. (2) do not depend on the boundary conditions.

For the most general case of crystal symmetry, Eq. (2) has a unique solution and the modes propagating in the piezoelectric plate have all three components of mechanical displacement and an electric potential (u_1, u_2, u_3, and φ).

To determine the unknown amplitude coefficients A_n, it is necessary to use eight boundary conditions at the upper ($X_3 = H/2$) and lower ($X_3 = -H/2$) boundaries of the piezoelectric plate. These conditions are the zero value of the normal components of the stress tensor at the upper and lower boundaries of the plate

$$T_{31} = 0, \quad T_{32} = 0, \quad T_{33} = 0 \text{ for } X_3 = \pm H/2; \tag{6}$$

the continuity of the normal component of the electric induction at the boundary between the piezoelectric plate and the vacuum (for an open surface)

$$D_3 = D_3^{\text{vac}} \text{ for } X_3 = H/2 \text{ and (or) } X_3 = -H/2 \tag{7a}$$

or the zero value of the electric potential at the boundary when the surface is short-circuited (metallized)

$$\varphi = 0 \text{ for } X_3 = H/2 \text{ and (or) } X_3 = -H/2. \tag{7b}$$

Then, substituting general solutions (1) into boundary conditions (6) and (7), we obtain a set of homogeneous complex boundary equations, the solution of which yields the unknown amplitude coefficients A_n and phase velocities V_k of all modes propagating in the piezoelectric plate.

One of the difficulties arising in the numerical search for the plate wave solutions consists in the fact that, in a piezoelectric plate of a certain thickness H, there is a family of plate modes and each mode has its own phase velocity V_k. Therefore, in the search for every individual mode (search for the zero of the function of boundary equations), it is necessary to choose a sufficiently narrow interval of the velocity search ΔV that would contain only two values of velocity for the same mode: for an open and a short-circuited surface (to calculate the electromechanical coupling coefficient K^2). For a reliable determination of such an interval, we visualized the plot of the function of boundary conditions in the program window.

After finding the phase velocity V_k of some mode, it is possible to determine the electromechanical coupling coefficient (K^2). Usually, the electromechanical coupling coefficient for a surface acoustic wave (SAW) is calculated from the expression [10]

$$K^2 = 2(V_0 - V_S)/V_0, \tag{8}$$

where V_0 and V_S are the phase velocities of the wave at the open and metallized surfaces of the crystal, respectively. For a semi-infinite crystal, this quantity is single-valued for the given orientation. This relation can also be used for calculating the value of K^2 for plate waves.

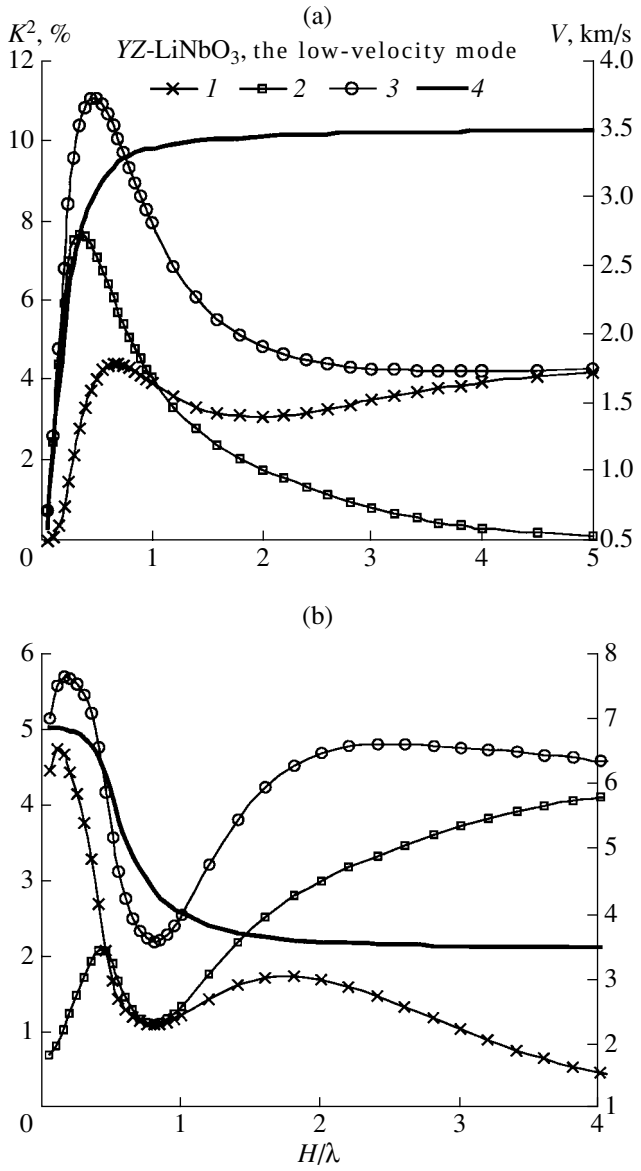

Fig. 2. (*1–3*) Electromechanical coupling coefficient K^2 and (*4*) the velocity of SAW propagation V versus the normalized plate thickness H/λ for the (a) low-velocity and (b) high-velocity zero-order mode. The lower surface is (*1*) open or (*2*) short-circuited; (*3*) both surfaces are either open or short-circuited.

In this case, the electromechanical coupling coefficient K^2 for different modes has a spatial dispersion (it depends on the relative thickness of the piezoelectric plate H/λ).

Note that the phase velocity of plate waves in a piezoelectric plate also depends on the electrical boundary conditions at the lower boundary of the plate (an open or short-circuited surface). Hence, in calculating the electromechanical coupling coefficient K^2 from the relative difference in the velocities along the open and short-circuited surfaces, one should take into account the electrical boundary conditions at the lower surface, which may be either open or short-circuited. If the lower surface is electrically short-circuited, the mode velocities will differ from the velocities for an open lower surface. The electromechanical coupling coefficient K^2 calculated from Eq. (8) will also differ in this case. And, finally, instead of V_0 in Eq. (8), one can substitute the velocity corresponding to both surfaces being open, and instead of V_S, the velocity corresponding to both surfaces being short-circuited. Thus, it is possible to obtain three values of the electromechanical coupling coefficient K_i^2 (i = 1–3), which correspond to three different ways of short-circuiting the electric field at the plate boundaries. Figures 2a and 2b show the three variants of calculated dependences of K_i^2 on H/λ for zero-order Lamb modes propagating in a YZ-cut $LiNbO_3$ plate. From these figures, one can see that the dependence of K^2 on H/λ has a complicated form with maxima at certain values of H/λ (see curves *1–3*). With an increase in the thickness of the piezoelectric plate $H > 3\lambda$, the phase velocities of both zero modes (curves *4*), approach the velocity of a SAW in a semi-infinite medium (V_{SAW} = 3.487 km/s): one from below, starting from the zero value, and the other from above, starting from a value approximately equal to the velocity of the bulk longitudinal wave. However, the value of the electromechanical coupling coefficient K^2 approaches the corresponding value for the SAW ($K^2 \approx$ 4.38%) not in all cases, which is seen from Fig. 2. If the lower surface is open, the value of K^2 for the low-velocity mode (curve *1* in Fig. 2a) approaches the corresponding value for the SAW, while K^2 for the high-velocity mode (curve *1* in Fig. 2b) approaches zero. If the lower surface is short-circuited, the quantities behave conversely (curves *2* in Figs. 2a, 2b). If we calculate K^2 by Eq. (8) from the velocities determined on the condition that both surfaces are either open or short-circuited, then, for both zero modes, as the plate thickness grows, K^2 approaches the value corresponding to the SAW (curves *3* in Figs. 2a, 2b). In addition, in this case, we have the highest value of K^2 equal to about 11% for the low-velocity mode near H/λ = 0.55 (curve *3* in Fig. 2a). The curves in Fig. 2 also show that, for any plate thickness, for both zero-order modes, the condition $K_3^2 = K_1^2 + K_2^2$ is satisfied (here, the subscripts correspond to the curve numbers in Fig. 2). Note that, for the orientation considered, symmetry condition (4) is satisfied and the zero-order Lamb modes have two components of mechanical displacement, u_1 and u_3, and an electric potential φ [11]. Figure 3 demonstrates the calculated distributions of the amplitudes of mechanical displacements u_1 and u_3 (curves u_1 and u_3) over the thickness ($H = 0.5\lambda$) of a YZ-$LiNbO_3$ plate for the high-velocity zero-order mode (here and below, the amplitudes are normalized to $u_0 = \sqrt{|u_{01}|^2 + |u_{02}|^2 + |u_{03}|^2}$,

where u_{0i} are the amplitudes at the surface $X_3 = H/2$). As is seen from Fig. 3, the distribution of the displacement amplitude u_1 over the plate thickness is symmetric and the distribution of u_3 is antisymmetric.

If the symmetry conditions (5) are satisfied, a transverse plate wave (SH wave) propagates in the piezoelectric plate. It is a shear-horizontal high-velocity wave that does not contain the component of mechanical displacement u_3 normal to the plate surface. Owing to this, the SH wave can propagate in a plate contacting a liquid without any radiation loss due to the wave energy leakage into the liquid medium. Another feature of the SH wave consists in the fact that, at a certain plate thickness, the electromechanical coupling coefficient K^2 may be very high. For example, for a lithium niobate plate, the cuts and directions were found [4, 5], in which a quasi-SH wave propagates: although, in the directions found, the symmetry conditions (5) are not satisfied and the wave has all three mechanical displacements, the condition $u_1, u_3 \ll u_2$ is satisfied. For an *XY*-cut $LiNbO_3$ plate with the thickness $H = 0.1\lambda$, the electromechanical coupling coefficient is $K^2 \approx 35\%$ and the phase velocity is $V = 4.372$ km/s.

In the present study, the parameters of SH waves in piezoelectric plates with a strong piezoelectric coupling are theoretically calculated. We considered a potassium niobate crystal ($KNbO_3$) [12] and a lead-treated potassium niobate crystal (PKN) [13] belonging to the rhombic and orthorhombic systems, respectively. In these crystals, symmetry condition (5) is satisfied for the orientations (0°, 90°, 180°*m*), where $m = 0, 1, 2, \ldots$ [14]. Figure 4 displays the calculated velocities *V* (curves *V*1, *V*2, *V*3, and *V*4), which were obtained under the condition that both surfaces were open, and the quantity K^2 (curves *k*1, *k*2, *k*3, and *k*4), calculated under the condition that the lower surface was open, versus the normalized plate thickness H/λ for the crystals (90°, 90°, 0°) $LiNbO_3$, (0°, 90°, 0°) $KNbO_3$, (0°, 90°, 0°) PKN, and (90°, 90°, 0°) $LiTaO_3$. The materials constants for $KNbO_3$, PKN, $LiNbO_3$, and $LiTaO_3$ were taken from [12, 13, 15]. As is seen from Fig. 4, the maximal values of K^2 are as follows: for *XY*-cut $LiNbO_3$, $K^2 \approx 35\%$ and the phase velocity $V \approx 4.35$ km/s at $H/\lambda = 0.06$; for *YX*-cut $KNbO_3$, $K^2 = 99.3\%$ and $V = 4.67$ km/s at $H/\lambda = 0.12$; for *YX*-cut PKN, $K^2 = 54.5\%$ and $V = 3.04$ km/s at $H/\lambda = 0.02$; and for *XY*-cut $LiTaO_3$, $K^2 = 10.7\%$ and $V = 3.75$ km/s at $H/\lambda = 0.06$. Such record high values of K^2 in these crystals open up the possibilities for an efficient control of the SH wave velocity, e.g., by bringing a conducting screen near the plate surface. This feature can be used in developing high-efficiency acoustoelectronic sensors.

We also studied theoretically the temperature properties of Lamb waves in a langasite (LGS) piezoelectric plate with the (0°, 138.5°, 23°) orientation, which is thermostable for a SAW [16]. The calculations showed

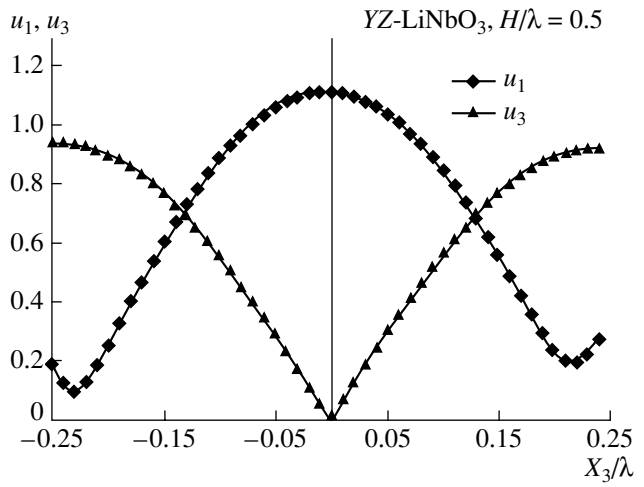

Fig. 3. Distributions of the relative amplitudes u_1 and u_3 over the thickness of a *YZ*-cut $LiNbO_3$ plate for the high-velocity zero-order mode.

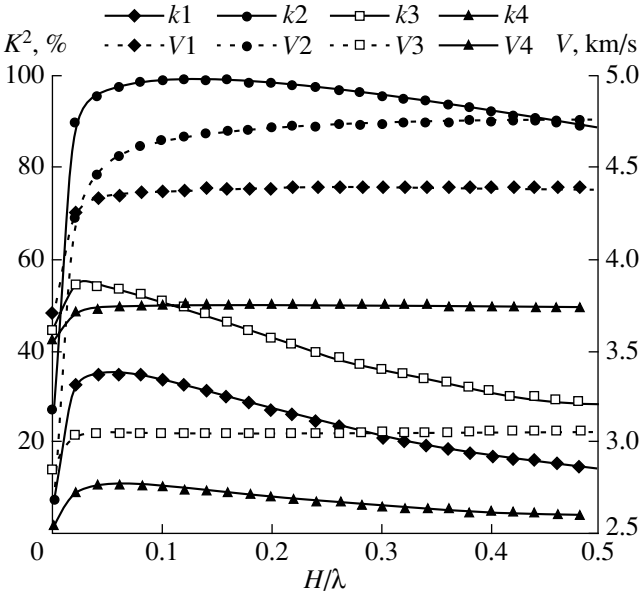

Fig. 4. Velocity of SAW propagation *V* and the electromechanical coupling coefficient K^2 versus the normalized plate thickness H/λ for (*V*1, *k*1) *XY*-cut $LiNbO_3$, (*V*2, *k*2) *YX*-cut $KNbO_3$, (*V*3, *k*3) *YX*-cut PKN, and (*V*4, *k*4) *XY*-cut $LiTaO_3$.

that the value of the temperature coefficient of delay [10] rather strongly depends on the thickness of the piezoelectric plate and on the mode number. Figure 5 shows the computed values of this coefficient for low- and high-velocity zero-order Lamb modes versus H/λ. The value of the temperature coefficient of delay is close to zero for the high-velocity mode at the plate thickness $H \approx 0.6\lambda$, $H \approx 1.3\lambda$, and $H > 1.5\lambda$ (both surfaces are open); for the low-velocity zero-order mode,

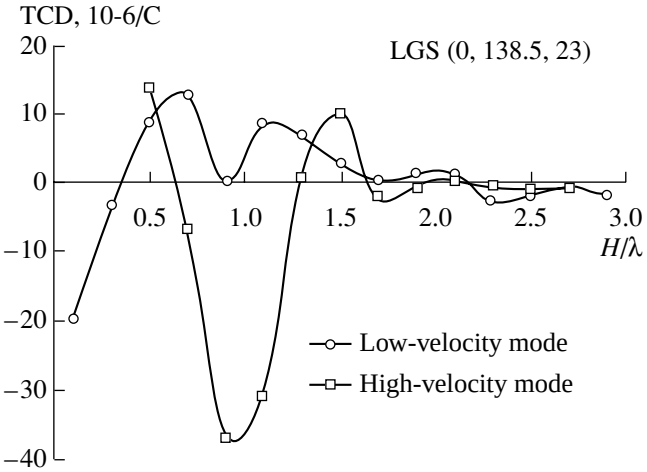

Fig. 5. Temperature coefficient of delay versus the normalized plate thickness H/λ for the low- and high-velocity zero-order Lamb modes in a (0°, 138.5°, 23°) LGS plate.

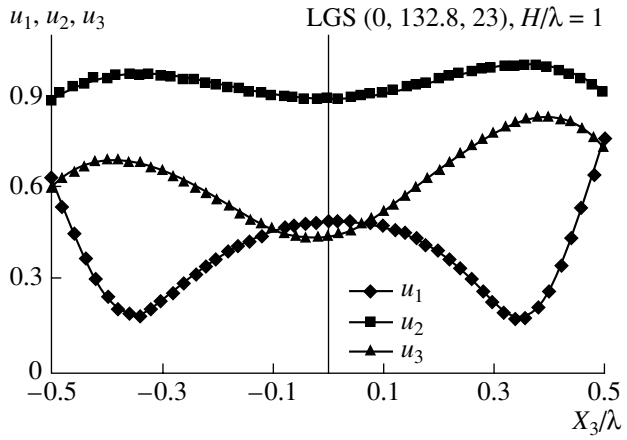

Fig. 6. Distributions of the relative amplitudes U_1, U_2, and U_3 over the thickness of a (0°, 138.5°, 23°) LGS plate. The plate thickness is $H = \lambda$.

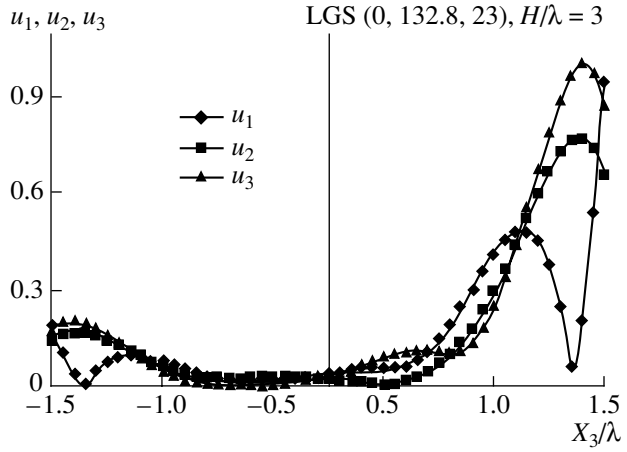

Fig. 7. Distributions of the relative amplitudes U_1, U_2, and U_3 over the thickness of a (0°, 138.5°, 23°) LGS plate. The plate thickness is $H = 3\lambda$.

it is close to zero at $H = 0.35\lambda$, $H \approx 0.9\lambda$, and $H > 1.7\lambda$. The materials constants for LGS were taken from [17].

Now, we consider the distribution of the mechanical displacements u_1, u_2, and u_3 of the Lamb modes for different ratios H/λ. Figure 6 shows the distributions of the normalized amplitudes of mechanical displacements for the low-velocity zero-order mode (velocity V = 2.686 km/s, both surfaces are open) in a (0°, 138.5°, 23°) LGS piezoelectric plate of thickness $H = \lambda$. It is seen from Fig. 6 that the distribution of the amplitudes of mechanical displacements over the plate thickness is of a complex character. There are several characteristic maxima and minima of the displacement values across the plate thickness (curves U_1, U_2, and U_3). At the thickness $H = 3\lambda$ (Fig. 7), the structure of this mode (V = 2.729 km/s) approaches the structure of a common SAW (V = 2.733 km/s). As is seen from Fig. 7, all mechanical displacements are concentrated near the plate boundaries and die out in the middle of the plate (curves U_1, U_2, and U_3).

Thus, in this paper, we calculated the main characteristics of plate waves propagating in $LiNbO_3$, $LiTaO_3$, LGS, $KNbO_3$, and PKN piezoelectric plates. The cuts and directions in which SH waves have record high values of the electromechanical coupling coefficient are determined. In particular, for the *YX*-cut $KNbO_3$ plate, the value of this coefficient is K^2 = 99.3%, and for the *YX*-cut PKN plate, K^2 = 54.5%. It is shown that, at certain plate thickness values, low- and high-velocity Lamb modes propagating in a (0°, 138.5°, 23°) LGS plate have zero values of the temperature coefficient of delay.

REFERENCES

1. E. Adler, IEEE Trans. Ultrason. Ferroelectr. Freq. Control **36**, 223 (1989).
2. Y. Jin and S. G. Joshi, in *Abstracts of IEEE Ultrasonic Symposium* (IEEE, 1993), Vol. 2, p. 847.
3. O. Borovkov and I. Kucherov, Ukr. Fiz. Zh. **17**, 1980 (1972).
4. B. D. Zaitsev, S. G. Joshi, and I. E. Kuznetsova, in *Proceedings of IEEE Ultrasonic Symposium* (1998), p. 419.
5. S. G. Joshi, B. D. Zaĭtsev, and I. E. Kuznetsova, Akust. Zh. **47**, 336 (2001) [Acoust. Phys. **47**, 282 (2001)].
6. I. V. Anisimkin, Yu. V. Gulyaev, and V. I. Anisimkin, in *Proceedings of IEEE Ultrasonic Symposium* (2001), p. 423.
7. F. Teston, G. Feuillard, and L. Tessier, IEEE Trans. Ultrason. Ferroelectr. Freq. Control **45**, 1266 (1995).
8. S. Balandras, J. Briot, and G. Martin, in *Proceedings of IEEE Ultrasonic Symposium* (1996), p. 459.

9. I. A. Viktorov, *Rayleigh and Lamb Waves: Physical Theory and Applications* (Nauka, Moscow, 1966; Plenum Press, New York, 1967).
10. *Surface Wave Filters: Design, Construction, and Use*, Ed. by H. Mathews (Wiley, New York, 1977; Radio i Svyaz', Moscow, 1981).
11. E. Adler, IEEE Trans. Ultrason. Ferroelectr. Freq. Control **36** (2), 223 (1989).
12. M. Zgonik, R. Schlesesser, and I. Biaggio, J. Appl. Phys. **74**, 1287 (1993).
13. R. Sun, S. Fan, and J. Wu, in *Proceedings of IEEE International Frequency Control Symposium* (1996), p. 113.
14. M. Yu. Dvoesherstov, S. G. Petrov, and V. I. Cherednik, Izv. Vyssh. Uchebn. Zaved., Radiofiz. **43** (5), 445 (2000).
15. G. Covacs, M. Anhorn, H. Engan, *et al.*, in *Proceedings of IEEE Ultrasonic Symposium* (1990), p. 435.
16. K. Inoue and K. Sato, Jpn. J. Appl. Phys. **37**, 2909 (1998).
17. Y. Pisarevsky, P. Senyshenkov, B. Mill, and N. Moiseeva, in *Proceedings of IEEE International Frequency Control Symposium* (1998), p. 742.

Translated by A. Svechnikov

Acoustical Physics, Vol. 50, No. 5, 2004, pp. 518–522. Translated from Akusticheskiĭ Zhurnal, Vol. 50, No. 5, 2004, pp. 609–613.

Calculation of the Speed of Sound in Seawater from the Known Ion Concentrations

D. A. Denisov, E. P. Abramova, and A. V. Abramov

Mendeleev University of Chemical Technology, Miusskaya pl. 9, Moscow, 125047 Russia

e-mail: aaabramovs@mail.ru

Received December 17, 2003

Abstract—It is shown that the method proposed earlier for calculating the speed of sound in seawater from the known ion concentrations, in a strict sense, can be applied for computing the sound speed in seas if, as a model of seawater, one uses a solution containing six ions or a solution containing four ions, namely, Na^+, Mg^{2+}, SO_4^{2-}, and Cl^-, with the mole concentration of Na^+ being replaced by the sum of mole concentrations of Na^+ and K^+ and the mole concentration of Mg^{2+} being replaced by the sum of mole concentrations of Mg^{2+} and Ca^{2+}. An algorithm of calculation is proposed. It is demonstrated that, when the seawater is considered as a solution containing six ions, the computed value of the speed of sound does not depend on the choice of the specific ion whose concentration is determined from the condition of electric neutrality. © *2004 MAIK "Nauka/Interperiodica".*

At present, the effect of composition of dissolved components on the speed of sound in seawater u_{mix} is taken into account by using only one variable, namely, the salinity S [1]. This approach is appropriate when the concentration ratios of dissolved components are constant. However, this constancy is often violated, for instance, in passing from oceans and seas connected with the oceans or neighboring seas by wide straits to the inland seas or seas connected with the neighboring seas by narrow straits [1]. We proposed an approach based on considering the seawater as an ideal isopiestic solution, that is, an ideal mixture of binary isopiestic solutions, which makes it possible to calculate the sound speed for arbitrary ratios of concentrations of dissolved components [2]. Isopiestic solutions are the solutions that have the same values of the chemical potential of water μs [3].

The deviations of the computed values of sound speed in seawater u_{mix} from the values found by the interpolation of experimental dependences of sound speed in seawater on S were 0.5–1.0 ms^{-1} [2]. After analyzing the algorithm of calculation, we decided to change the method of approximating the concentration dependences of osmotic coefficients of binary solutions and other properties of these solutions. The polynomials used in [2] to approximate the concentration dependences of binary solutions have the form

$$\tilde{f}_i^{(l)} = \sum_{j=0} A_{ij}^{(l)} \tilde{m}_i^{j/2}, \qquad (1)$$

where $\tilde{m}_i$ is the molality of a binary solution of the ith dissolved component. The superscript in parentheses (l) of the quantity f indicates the specific property of the binary solution that is approximated by polynomial (1).

The value $l = 1$ corresponds to the osmotic coefficient of the binary solution; the value $l = 2$ corresponds to the density of the binary solution, $\tilde{\rho}_i$; $l = 3$ corresponds to the heat capacity of the mass of the binary solution that contains 1 kg of solvent, $C\tilde{p}_i$; $l = 4$ corresponds to the coefficient of thermal expansion of the binary solution, $\tilde{\alpha}_i$; and $l = 5$ corresponds to the sound speed in a binary solution of the ith dissolved component $\tilde{u}_i$. The subscript i indicates the specific dissolved component under consideration. The molality and thermodynamic properties of a binary solution with an arbitrary a_s are marked by the superscript ~ above the corresponding quantity.

All the coefficients $A_{ij}^{(1)}$ were determined by the least squares method. As a result, the values of the first coefficients $A_{ij}^{(0)}$ in Eq. (1) differed from the values of the property f for pure water. (The value of $A_l^{(0)}$ for the osmotic coefficient equals unity) [4].

In the present paper, we propose to approximate the concentration dependences of the properties of binary solutions by polynomials of the form

$$\frac{\tilde{f}_i^{(l)} - f_i^{(l)}\text{H}_2\text{O}}{\sqrt{\tilde{m}_i}} = \sum_{j=0} B_{ij}^{(l)} \tilde{m}_i^{j/2}. \qquad (2)$$

The value of $f_i^{(l)}\text{H}_2\text{O} = 1$ corresponds to the osmotic coefficient of the binary solution, and, for other l,

Table 1. Algorithm of computing the sound speed in a mixed solution containing four ions.

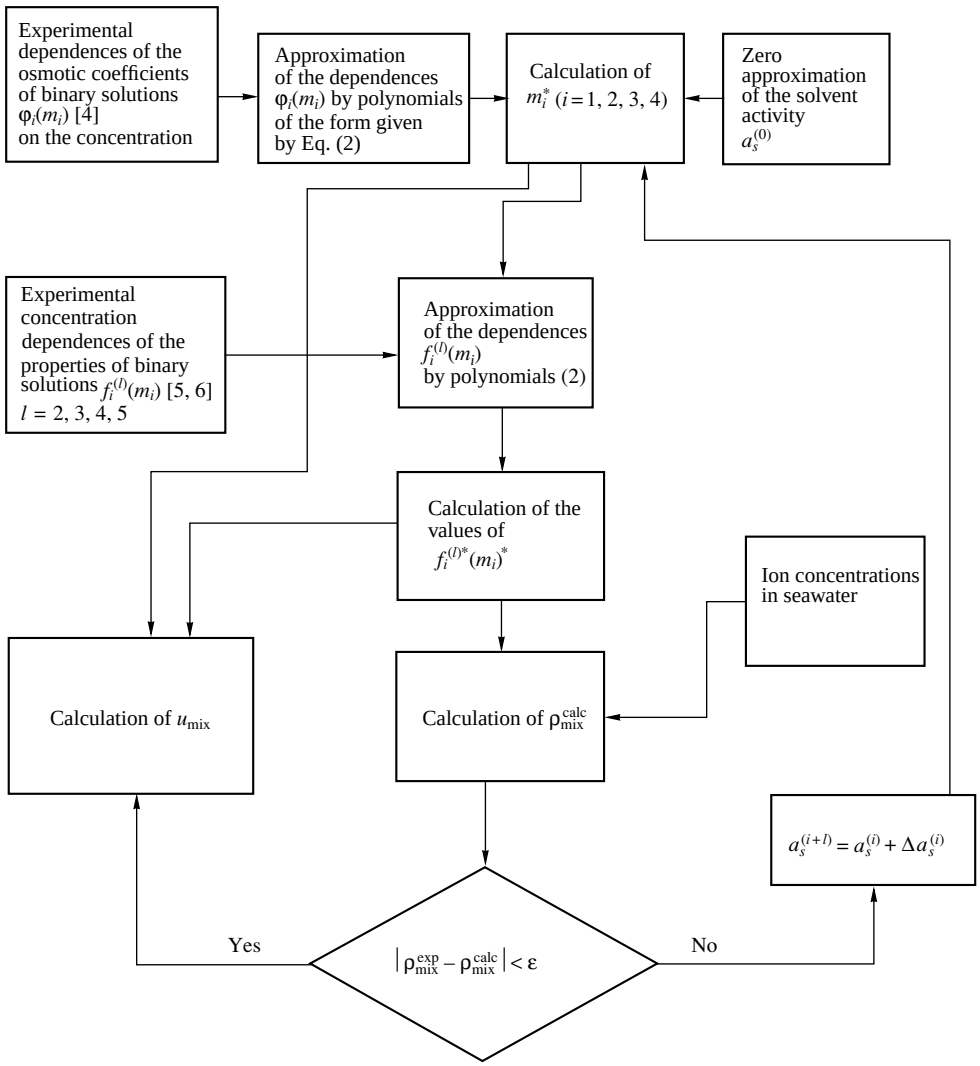

$f_i^{(l)}$ H_2O means the value of the corresponding property for pure water.

Table 1 shows the algorithm of calculation of the sound speed in a mixed solution of four salts serving as a model of seawater.

For a solution containing four ions, Na^+, Mg^{2+}, SO_4^{2-}, and Cl^-, with the molalities of the first three ions equal to their molalities in seawater at $S = 35.004‰$ and the molality of SO_4^{2-} found from the condition of electric neutrality of the considered solution, the following values of molalities of salts in the mixed solution, m_i ($m_1 = 0.484056$, $m_2 = 0.0005118$, $m_3 = 0.026535$, and $m_4 = 0.028753$), and molalities of binary isopiestic solutions, m_i^* ($m_1^* = 0.544983$, $m_2^* = 0.406078$, $m_3^* = 0.370913$, and $m_4^* = 0.737312$), were found. The indices 1, 2, 3, and 4, as in [2], correspond to the salts NaCl, Na_2SO_4, $MgCl_2$, and $MgSO_4$, respectively. For the mixed solution of four salts under consideration, $S = 33.235‰$, the calculated density value is $\rho_{mix} = 1021.846$ kg/m^3, and the value of sound speed computed using the aforementioned values of salt concentrations equals 1532.99 m/s. The value found from the interpolation of the dependence of sound speed in seawater on salinity [1] for $S = 33.235‰$ is equal to 1533.24 m/s.

The molality and thermodynamic properties of a binary solution with the same value of the solvent activity a_s as that of the mixed solution under consideration are marked with the superscript *. Remember that the symbol $\tilde{m}_i$ denotes the molality of the ith dissolved component of the mixed solution.

As is shown above, when the concentrations of all ions but one are equal to the concentrations of these ions in seawater at the salinity $S = 35.004‰$ and the concentration of one ion is found from the condition of electric neutrality of the system, the consideration of

four ions gives a value of salinity of the mixed solution different from the value of S of the seawater and the value of the sound speed u_{mix} in this mixed solution is closer to the sound speed determined by the interpolation of the dependence $u_{mix}(S)$ [1] for the value of S corresponding to this solution, as compared to the sound speed in seawater for $S = 35.004‰$. Therefore, we consider the solution containing four ions for the case when the concentrations of all ions but two, namely, Na^+ and Cl^-, are equal to the concentrations of these ions in seawater at $S = 35.004‰$ and the concentrations of the Na^+ and Cl^- ions are computed from the condition of electric neutrality of the mixed solution and the equality of its salinity to the value of S in seawater. The computed value of sound speed in the solution containing four ions equals 1535.97 m/s. The value of sound speed determined from an experimental dependence of sound speed in seawater on salinity for $S = 35.004‰$ is equal to 1535.00 m/s.

Thus, the use of a solution containing four ions, Na^+, Mg^{2+}, SO_4^{2-}, and Cl^-, makes sense only for testing the proposed method by comparing the computed value of u_{mix} with the value found by the interpolation of an experimental dependence of sound speed in seawater on S [1]. In the initial variant, the concentrations of three out of four ions are taken to be equal to the concentrations of these ions in seawater for $S = 35.004‰$. For this solution, $S = 33.235‰$.

It should be noted that the solution containing the aforementioned four ions with the concentrations equal to the concentrations in seawater at $S = 35.004‰$ has the salinity $S = 33.24‰$ and the value of sound speed u_{mix} calculated for this solution is close to u_{mix} determined by the interpolation of the dependence of sound speed in seawater on salinity [1] for $S = 33.24‰$ rather than to the value of u_{mix} corresponding to the real seawater with the same concentrations of these four ions.

The second variant of using the model of a solution containing four ions is based on the change of the concentrations of at least two out of four ions for reaching the value of $S = 35.004‰$. The use of the second variant is not consistent with the aim of the proposed method, that is, with the calculation of the sound speed from the known concentrations of ions for the systems for which the application of such characteristic as salinity is not quite correct, since the concentration ratios of ions differ from the concentration ratios of the aforementioned ions typical of ocean water.

Obtaining a value of sound speed in seawater close to the value found by the interpolation of the experimental dependence of u_{mix} on S for $S = 35.004‰$, which characterizes the seawater under consideration, by using the model of an ideal isopiestic solution of four salts is possible if the mole concentration of Na^+ corresponding to seawater at $S = 35.004‰$ is replaced by the sum of mole concentrations of Na^+ and K^+ corresponding to the mentioned salinity, and the mole concentration of Mg^{2+} corresponding to seawater at $S = 35.004‰$ is replaced by the sum of mole concentrations of Mg^{2+} and Ca_+^2 corresponding to the aforementioned salinity. The concentration of Cl^- in this solution is equal to the concentration of Cl^- in seawater for $S = 35.004‰$, and concentration of SO_4^{2-} is determined from the condition of electric neutrality of the solution. The salinity of this mixed solution is 34.760‰.

The calculation gives the following values of molalities of the mixed solution: $m_1 = 0.495527$, $m_2 = 0.0000653$, $m_3 = 0.0367397$, and $m_4 = 0.0291997$; and the values of molalities of isopiestic binary solutions are $m_1^* = 0.571140$, $m_2^* = 0.426879$, $m_3^* = 0.388483$, and $m_4^* = 0.775279$. For the solution under consideration, $\rho_{mix} = 1023.045$ kg/m^3 and the computed value of $u_{mix} = 1534.72$ m/s only slightly differs from the aforementioned value of u_{mix} determined from the interpolation of an experimental dependence of sound speed in seawater on S at $S = 35.004‰$, which corresponds to the mass ion concentrations used in the calculation.

For a solution containing six ions, Na^+, Mg^{2+}, K^+, Ca^{2+}, SO_4^{2-}, and Cl^-, with the molalities of the first five ions equal to the molalities of these ions in seawater at $S = 35.004‰$ and the molality of Cl^- found from the condition of electric neutrality of the solution, we determined the molalities of salts in a mixed solution, m_i ($m_1 = 0.44297$, $m_2 = 0.02105$, $m_3 = 0.05229$, $m_4 = 0.00300$, $m_5 = 0.00016$, $m_6 = 0.00521$, and $m_7 = 0.01065$), and in binary isopiestic solutions, m_i^* ($m_1^* = 0.57285$, $m_2^* = 0.42824$, $m_3^* = 0.38963$, $m_4^* = 0.77776$, $m_5^* = 0.57777$, $m_6^* = 0.42993$, and $m_7^* = 0.39297$). The indices 5, 6, and 7 denote the quantities corresponding to the salts KCl, K_2SO_4, and $CaCl_2$, respectively. The value of $u_{mix} = 1534.83$ m/s calculated for this system is close to the value of u_{mix} following from the experimental dependence of u_{mix} on S for $S = 35.004‰$.

The evaluation of the effect of changes in ion concentration on the sound speed in a mixed solution u_{mix} is made by the example of an ideal isopiestic solution of four salts, NaCl, Na_2SO_4, $MgCl_2$, and $MgSO_4$. The quantities corresponding to these salts are denoted by the indices 1, 2, 3, and 4, respectively. We consider a set of solutions containing the four above-mentioned ions. In one of the solutions of this set, the concentrations of Na^+, Mg^{2+}, and SO_4^{2-} ions are equal to the mass concentrations of these ions in seawater for $S = 35.004‰$ [1], which are given in the first line of Table 1. The

Table 2. Molalities of ions and salts in seawater and the sound speed computed by a complete formula [10]

Na^+	Mg^{2+}	SO_4^{2-}	Cl^-	NaCl	Na_2SO_4	$MgCl_2$	$MgSO_4$	u_{mix}	$\frac{u_{mix}-u_{mix1}}{u_{mix}-u_{H_2O}}$
0.485079	0.055288	0.029265	0.537125	0.427185	0.028947	0.054970	0.000318	1533.65	0
0.504482	0.057500	0.030436	0.558610	0.443825	0.030329	0.057393	0.000107	1535.05	+0.038
0.504482	0.057500	0.028094	0.563293	0.448697	0.027893	0.057298	0.000202	1535.00	+0.037
0.504482	0.053077	0.030436	0.549764	0.444101	0.030191	0.052832	0.000245	1534.58	+0.026
0.504482	0.053077	0.028094	0.554447	0.448754	0.027864	0.052847	0.000230	1534.53	+0.024
0.465676	0.057500	0.030436	0.519804	0.404805	0.030436	0.057500	0.0000001	1532.77	−0.024
0.465676	0.057500	0.028094	0.524486	0.409586	0.028045	0.057450	0.000049	1532.71	−0.026
0.465676	0.053077	0.030436	0.510958	0.405366	0.030155	0.052796	0.000281	1532.29	−0.038
0.465676	0.053077	0.028094	0.515640	0.410212	0.027732	0.052714	0.000362	1532.24	−0.039

other solutions of the set differ from the aforementioned one, at least, by the concentration of one of the ions, Na^+, Mg^{2+}, or SO_4^{2-}. The relative deviation of the concentrations of at least one of the aforementioned ions from the concentration of this ion in the solution with the same mass concentrations of Na^+, Mg^{2+}, and SO_4^{2-} as that of the seawater for $S = 35.004‰$ equals ±4%. The concentration of CL^- in all cases is calculated from the condition of electric neutrality of the solution containing four ions.

For the nine possible combinations differing at least by the concentration of one of the ions, using experimental data on the density of the solutions [5, 6] and seawater [1], we calculated by the method reported in [2] the following quantities: the concentrations of NaCl, Na_2SO_4, $MgCl_2$, and $MgSO_4$ in mixed and binary isopiestic solutions; the water activity values corresponding to these concentrations; the values of the properties of binary isopiestic solutions, including the density ρ_i^*, the thermal coefficient of expansion α_i^*, and the isobaric heat capacity of the mass of solution containing 1 kg of pure water; and the values of the sound speed in the mixed solutions under consideration, u_{mix}.

Table 2 represents the ion molalities and the corresponding salt molalities.

The next to last column contains the values of u_{mix} and the last column contains the ratio of the deviation of u_{mix} corresponding to the salt concentrations given in the relevant line from the value of u_{mix} given in the first line to the deviation from the sound speed in pure water $u_{H_2O} = 1497.2$ m/s [7].

Table 3 presents the values of the sound speed u_{mix} and analogous ratios of the sound speed deviations computed using the formula for the sound speed reported in [8] for the case of two dissolved components, this formula being derived by neglecting the difference between the adiabatic and isothermic compressibility.

In the general case, as follows from the formula for u_{mix} [8], the aforementioned assumption leads to the relation

$$u_{mix}^{-2} = \left(\sum_{j=1}^{r} \frac{m_j}{m_j^*} \cdot \frac{1 + m_j^* \times 10^{-3} M_j}{\rho_j^*}\right)^{-2} \times \left(1 + 10^{-3} \sum_{l=1}^{r} m_l^* M_l\right) \cdot \sum_{n=1}^{r} \frac{m_k}{m_k^*} \cdot \frac{1 + m_k^* M_k \times 10^{-3}}{(\rho_k^* u_k^*)^2}, \quad (3)$$

where m_i and m_i^* are the molalities of the ith dissolved component in the mixed and binary isopiestic solutions, r is the number of dissolved components, ρ_k^* is the density of the isopiestic binary solution of the kth component, u_k^* is the sound speed in the binary isopiestic solution of the kth component, and M_k is the mass of a mole of the kth component. Concentration dependences of the sound speed in binary solutions are presented in [9].

As one would expect from the formula given in [10] for computing u_{mix} from the data on binary solutions, a change in the concentration of Na^+ has the strongest effect on the variation of u_{mix}. As is seen from Tables 2 and 3, the simplified formula can be used for evaluating the effect of variations in the ion concentration on u_{mix}.

For the solution containing six ions, we tried to evaluate the effect of the choice of the ion whose concentration is found from the condition of electric neutrality of the solution with given concentrations of the other five ions. The values of molalities of the Na^+, K^+, Mg^{2+}, Ca^{2+}, and Cl^- ions were chosen to be equal to the values corresponding to the seawater at $S = 35.004‰$. The molality of the SO_4^{2-} ion was computed from the condition of electric neutrality. For the solution under consideration, $S = 35.004‰$. The use of the method pro-

Table 3. Molalities of salts in seawater and the sound speed computed by the simplified formula (1)

NaCl	Na_2SO_4	$MgCl_2$	$MgSO_4$	u_{mix}	$\frac{u_{mix} - u_{mix1}}{u_{mix} - u_{H_2O}}$
0.427185	0.028947	0.054970	0.000318	1533.65	0
0.443825	0.030329	0.057393	0.000107	1535.06	+0.039
0.448697	0.027893	0.057298	0.000202	1535.01	+0.037
0.444101	0.030191	0.052832	0.000245	1534.59	+0.026
0.448754	0.027864	0.052847	0.000230	1534.54	+0.024
0.404805	0.030436	0.057500	0.0000001	1532.78	–0.024
0.409586	0.028045	0.057450	0.000049	1532.72	–0.025
0.405366	0.030155	0.052796	0.000281	1532.30	–0.037
0.410212	0.027732	0.052714	0.000362	1532.25	–0.039

posed in [2] gave the following values of molalities of the isopiestic solutions: $m_1^* = 0.57289$, $m_2^* = 0.42827$, $m_3^* = 0.38966$; $m_4^* = 0.77782$; $m_5^* = 0.57782$; $m_6^* = 0.42996$; and $m_7^* = 0.39301$; and it gave the following values of molalities of the mixed solution: $m_1 =$ 044270; $m_2 = 0.02119$; $m_3 = 0.05248$; $m_4 = 0.00280$; $m_5 = 0.00013$; $m_6 = 0.00522$; and $m_7 = 0.01065$. The corresponding value of $u_{mix} = 1534.89$ m/s slightly differs from the value calculated above: $u_{mix} = 1534.83$ m/s. Therefore, it may be concluded that the choice of the ion whose concentration is computed from the condition of electric neutrality for the given concentrations of other ions only slightly affects the computed value of the sound speed.

REFERENCES

1. N. I. Popov, K. N. Fedorov, and V. M. Orlov, *Seawater: Handbook*, Ed. by A. S. Monin (Nauka, Moscow, 1979).
2. D. A. Denisov, E. P. Abramova, and A. V. Abramov, Akust. Zh. **49**, 494 (2003) [Acoust. Phys. **49**, 413 (2003)].
3. J. F. Hu, Bull. Chem. Soc. Jpn. **74** (1), 47 (2001).
4. R. A. Robinson and R. H. Stokes, *Electrolyte Solutions*, 2nd ed. (Butterworths, London, 1959; Inostrannaya Literatura, Moscow, 1963).
5. *Handbook of a Chemist: Main Properties of Inorganic and Organic Compounds*, Ed. by B. P. Nikol'skiĭ *et al.*, 2nd ed. (Khimiya, Moscow, 1964), Vol. 3 [in Russian].
6. V. A. Vasil'ev, *Calculation of the Density and Heat Capacity of Water Solutions of Inorganic Compounds* (Mosk. Khim.–Tekhnol. Inst., Moscow, 1974) [in Russian].
7. *Physical Quantities. Handbook*, Ed. by I. S. Grigor'ev and E. Z. Meĭlikhov (Énergoatomizdat, Moscow, 1991) [in Russian].
8. D. A. Denisov, Akust. Zh. **42**, 777 (1996) [Acoust. Phys. **42**, 684 (1996)].
9. F. J. Millero, V. Vinokurova, M. Fernandes, and P. J. Hershey, J. Solution Chem. **16** (4), 269 (1987).
10. D. A. Denisov, Akust. Zh. **39**, 757 (1993) [Acoust. Phys. **39**, 399 (1993)].

Translated by A. Svechnikov

Acoustical Physics, Vol. 50, No. 5, 2004, pp. 523–527. Translated from Akusticheskiĭ Zhurnal, Vol. 50, No. 5, 2004, pp. 614–618.

Correlation Noise in the Acoustic Wave Front Inversion

V. A. Zverev

Institute of Applied Physics, Russian Academy of Sciences, ul. Ul'yanova 46, Nizhni Novgorod, 603950 Russia
e-mail: zverev@hydro.appl.sci-nnov.ru

Received November 1, 2002

Abstract—Noise that accompanies the wave front inversion of sound signals is considered. It is shown that this noise is a consequence of the interference phenomena occurring in complex media with multiple signal reflections, which lead to a noiselike nature of the spectrum modulus. A method of the wave front inversion that allows one to reduce the interference noise is proposed. The aforementioned phenomena are numerically analyzed. © *2004 MAIK "Nauka/Interperiodica".*

A universal method exists for extracting a signal from noise: the method of matched filtering. The matched filter is the one whose response is complex-conjugate with the signal spectrum. Such a filter is most efficient when the signal with which the filter is matched is a complex signal in the sense that it has a great (much greater than unity) product of its duration and the frequency bandwidth. It is assumed that the modulus of the signal spectrum is approximately constant within the frequency band Δf and vanishes outside this band. Let us denote the signal complexity as N. If the signal duration is T, the complexity is

$$N = \Delta f T. \quad (1)$$

Let the signal spectrum be $G(\omega)$. Then, the response of the matched filter to the signal will be [1]

$$W(t) = \frac{1}{2\pi}\int G(\omega)\overline{G(\omega)}\exp(i\omega t)d\omega. \quad (2)$$

Here and further, the bar over a function means complex conjugation. The function $W(t)$ belongs to the class of so-called positive definite functions. Such functions cannot have complexity (1) greater than unity. At the same time, function (2) has the same spectrum width as the signal. This statement follows from Eq. (2). Hence, function (2) must be shortened in time by a factor of N, where N is given by Eq. (1).

Let us take the signal in the form of a computer-generated noise realization. The signal values are uncorrelated at each pair of points. Let the separations of the adjacent samples of the realization be equal to 1. Then, according to the sampling theorem, the spectrum width is $\Delta\omega = 2\pi$, or $\Delta f = 1$. With the realization length T, the signal complexity is $N = T$. The signal of form (2) will be shortened to a single interval of sampling.

Let us consider the actual result of transformation (1) shown in Fig. 1a. Indeed, there is a sharp peak, with the duration of a single sampling interval at zero delay. But what can be seen in the vicinity of that point? This is just the noise that is the subject of our consideration. The source and nature of this noise can be determined from Eq. (2). According to this expression, the response of the matched filter to the signal is the spectrum of the squared modulus of the signal spectrum. Such a spectrum has a constant component, because it is the spectrum of a quantity that is positive everywhere. The constant component is precisely the narrow peak of a single-sample width that was interpreted by us as the matched filter response to the signal. However, our signal is a realization of random noise. The spectrum modulus is also a random quantity. Hence, the spectrum of the squared signal modulus should not have only one constant component. The spectrum should have components at other nonzero frequencies. It is just what we can see in Fig. 1a: the correlation noise.

Let us consider the level of the correlation noise. For a noise realization, it is characteristic that the level of the constant component of the spectrum is approximately equal to the energy of the varying component, that is, to the energy of the correlation noise. Thus, if the constant component of the spectrum (the response of the matched filter to the signal) is N, the energy of the correlation noise will also be N and its amplitude will be $\sqrt{N}$. In our case, $N = 1024$, which corresponds to a level of correlation noise that is 30 dB lower than the level of the central correlation peak. Earlier (in the 1950s [1]), this fact was used to solve only one problem: to extract a signal from noise. If the signal is combined with noise with which the correlation peak of the signal is still visible (say, 10 to 15 dB lower than the peak), the correlation noise will be fully masked by this noise. That is why one was not interested in the correlation noise: it did not prevent extracting the signal from the masking background. Today, transformation (2) is used not only for extracting weak signals from noise but also for other purposes. In particular, this transfor-

1063-7710/04/5005-0523$26.00 © 2004 MAIK "Nauka/Interperiodica"

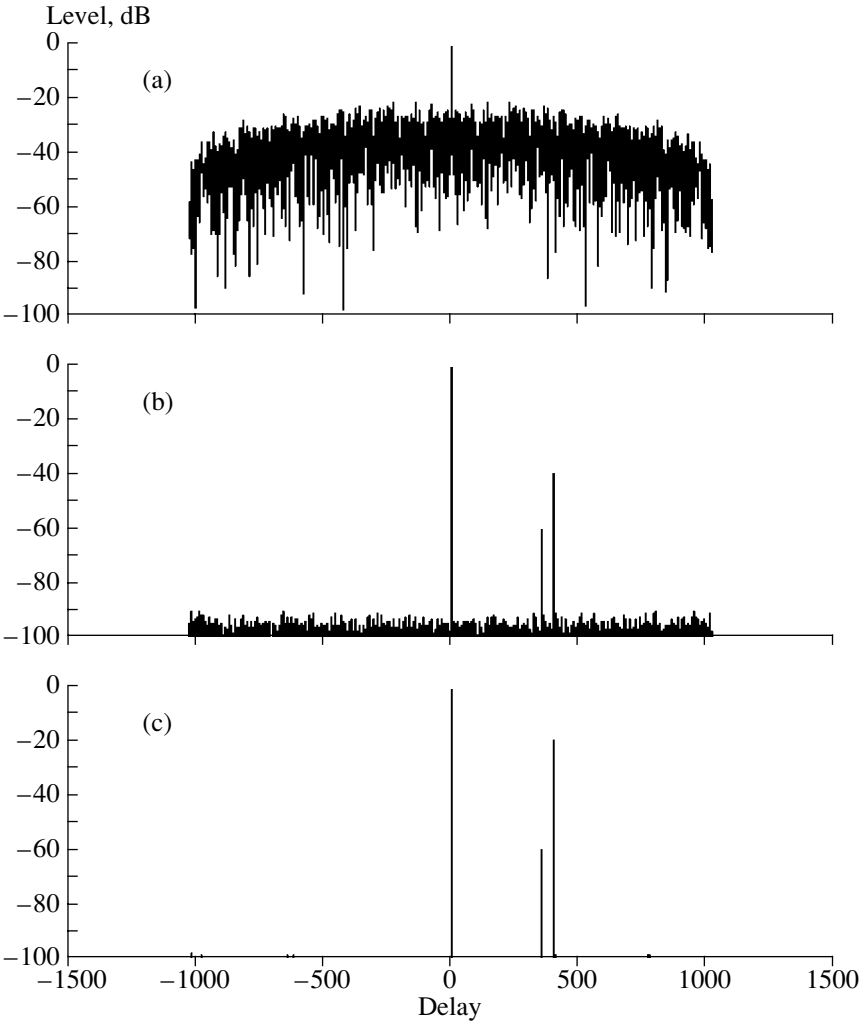

Fig. 1. Correlation function (the output signal of the matched filter) for different processing algorithms: (a) ordinary processing by convolution of the spectrum with or its multiplication by the complex-conjugate spectrum; (b) processing by dividing the spectra of the same signals; (c) processing by dividing the spectra with a special sounding signal whose spectrum does not involve small values.

mation serves for solving the problems of wave front inversion [2].

Suppose that an initially short sound pulse propagates in a complex medium with multiple signal reflections. To implement the wave front inversion (WFI) in acoustics, it is sufficient to receive this pulse, which is now long due to multiple reflections; to store it; and to transmit it again in reverse time with a complex-conjugated spectrum. For real signals, both procedures are equivalent and should not be doubled. For complex signals, both procedures are required [2, 3]. As a result of the WFI, the reradiated signal, upon propagation through the complex medium, will arrive at the transmission point as a short pulse. The latter pulse will be similar to the initial one with a single exception: it will pick up correlation noise. Such a noise can be seen from numerous illustrations given in [2]. Let us clarify the process of the formation of the correlation noise.

Let us introduce the frequency response $k(\omega)$ of the medium [3] with allowance for all signal reflections. The received signal can be represented by combining the Fourier transform $y_\omega(\omega)$ of the initial pulse and the frequency response $k(\omega)$ as follows [3]:

$$y(t) = \frac{1}{2\pi}\int_{-\infty}^{\infty} y_\omega(\omega)k(\omega)\exp(i\omega d)d\omega. \qquad (3)$$

Let the initial pulse be so short that its spectrum is constant in the entire frequency band: $y_\omega(\omega) = 1$. According to Eq. (3), the spectrum of the received pulse has the form of the frequency response $k(\omega)$. Now the same signal, but with the complex-conjugate spectrum, should be sent to the transmission point through the same medium. It is assumed that the frequency response of the medium is the same for both direct and inverse directions of sound propagation:

this is the condition for the WFI to be feasible [2]. For the signal arriving at the transmission point, Eq. (3) takes the form

$$a(t) = \frac{1}{2\pi}\int_{-\infty}^{\infty} \overline{k(\omega)}k(\omega)\exp(i\omega t)d\omega. \quad (4)$$

Relation (4) obtained for the signal arriving at the transmission point after the WFI fully coincides with Eq. (2) characterizing the output of the matched filter. This result is especially emphasized in [2]. As we have already learned, the correlation noise is the consequence of the fact that the squared modulus of the signal spectrum has a noiselike form. In ordinary matched filtering, the noiselike nature of the spectrum modulus is caused by the choice of the signal shape. In the WFI procedure, the frequency response is determined by the interference phenomena in signal propagation. Hence, the correlation noise in the WFI can be explained by the interference. For the signal propagating in a complex medium with multiple reflections, the interference is inevitable and always present. Does it mean that the WFI is always accompanied by the correlation noise? If so, the problem would be complicated, because, in the WFI, the correlation noise is commonly masked by nothing and is quite pronounced [2].

However, a radical method exists to get rid of the correlation noise. This method is effective for the WFI. One should simply replace the traditional algorithm of signal processing by a new one. Let us consider the new algorithm for the matched filter as an example.

It is well known [4] that the matched filter can be obtained by not only constructing its frequency response to be complex-conjugate with the signal spectrum. The frequency response of the matched filter can also be equal to the inverse complex spectrum of the signal. In this case, Eq. (2) takes the form

$$W(t) = \frac{1}{2\pi}\int \frac{G(\omega)\exp(i\omega\tau)}{G(\omega)}\exp(i\omega t)d\omega. \quad (5)$$

This expression accounts for the fact that the signal can be delayed by τ in time. At the filter output, according to Eq. (5), a narrow pulse is obtained whose duration is equal to a single sampling interval. Now, there is no correlation noise. Moreover, a similar narrow pulse will be obtained even if the signal has a highly nonuniform spectrum whose width does not cover all possible frequencies. This fact has been long known. Studies [4, 5] exist that consider the possibility of applying Eq. (5) to the signal processing. However, these studies do not recommend using Eq. (5) in practice. Why is it so?

There are two reasons for transformation (5) to lack popularity. The first one is that this transformation cannot be implemented by analog methods. Nowadays, with commonly used computers for signal processing and constructing filters, this reason fails. However, the second reason still exists. It consists in that the matched filters are used for extracting weak signals from strong noise. Algorithm (5) does not solve this problem. The point is that the procedure of dividing by the signal spectrum does not offer noise immunity. This problem is just the subject of [4, 5].

The signal spectrum can be represented as

$$G(\omega) = |G(\omega)|\exp(i\arg(G(\omega))). \quad (6)$$

The argument of the spectrum has no significant effect on the procedure of division. This is not true for the modulus of the spectrum: it can be very small or even zero-valued at some frequencies. However, Eq. (5) does not lack sense, because both the numerator and the denominator have precisely the same behavior at these frequencies. If the signal is added with noise, the situation changes drastically. At frequencies where the spectrum modulus is small, the noise substantially increases and the noise immunity of Eq. (5) fails [4–6]. The fact that Eq. (5) yields no correlation noise in the case of a high additive noise does not matter.

Figure 1 illustrates the aforementioned statements. All plots correspond to the same ratio of signal to additive noise: 83 dB. With such a signal-to-noise ratio, the correlation noise is quite pronounced. Figure 1b is obtained by using transformation (5) for the signal that is a realization of a random pulse sequence characterized by a normal distribution with a zero mean value and a unit variance. Well-pronounced additional low-level signals that have other delays are also seen in the plot. No such signals can be seen in Fig. 1a, which is obtained by using the "classical" expression (2) for the same signal.

Figure 1c corresponds to the output of the matched filter as given by Eq. (5), but for another signal. This signal was obtained from the signal used in plotting Figs. 1a and 1b in the following way. The spectrum of the signal to be processed was modified depending on the spectrum modulus. If the spectrum modulus was greater than some limiting value, say 0.5, the value of the modulus itself was used in the calculations. If the spectrum modulus was lower than the limiting value, this latter value was used. The resulting modulus of the spectrum was supplemented with an appropriate phase: the spectrum modulus was multiplied by an exponential of the imaginary unit multiplied by the argument of the signal spectrum. The change in the spectrum is illustrated by Fig. 2, which shows the moduli of the spectrum before and after transformation. The signal obtained by the aforementioned transformation is called the signal with truncated spectrum.

Figure 3 shows the signal-to-noise ratio at the output of the matched filter as a function of the same ratio at the filter input for two processing algorithms and two signal types. Number *1* labels the dependence obtained by the classical algorithm of Eq. (2). The figure shows that this dependence tends to the level of the correlation noise as the input noise decreases. Number *2* indicates

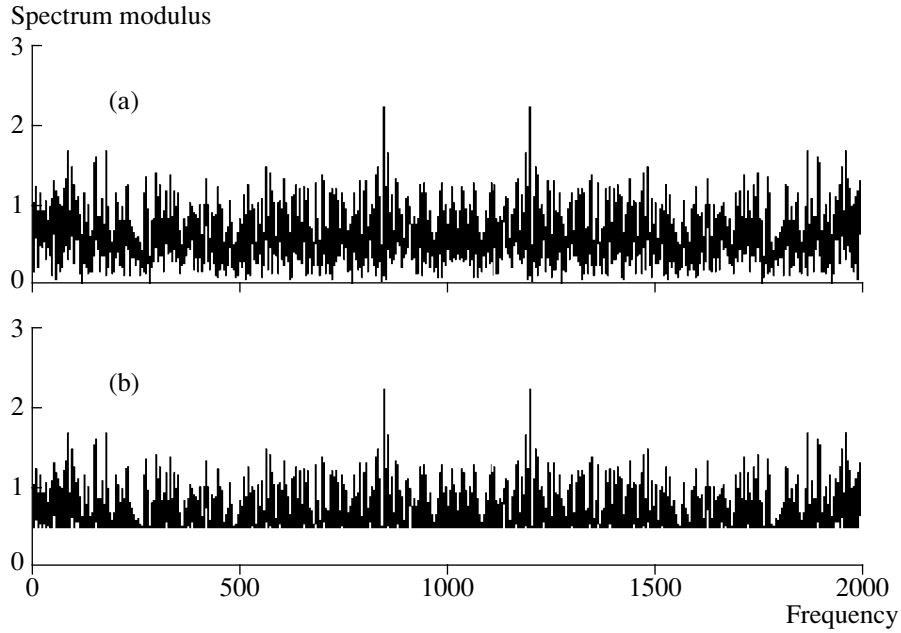

Fig. 2. Moduli of the spectra of a random signal (a) before the transformation and (b) after the truncation of the spectrum.

the dependence for the same signal processed with the new algorithm (5). Here, no correlation noise can be noticed, but the entire curve passes above the values given by algorithm (2) for low signal-to-noise ratios at the filter input. With higher noise levels at the output, the algorithm becomes less efficient in extracting weak signals. The reason is that the effect of noise increases at the frequencies where the modulus of the filter response is minimal. The latter statement is confirmed by the dependence labeled with number *3*. This dependence is obtained with the processing algorithm of Eq. (5) for the signal with a truncated spectrum (Fig. 2b) whose modulus is free of small values. The curve coincides with that labeled with *1* in the band where no correlation noise is noticeable and then passes lower, without any correlation noise. Such a signal is most appropriate for using matched-filtering algorithm (5). Straight line *4* corresponds to the case when the changes in the signal-to-noise ratio remain constant at the input and output. This line is useful for estimating the gain in the signal-to-noise ratio provided by all processing methods used. The distance measured along the vertical from a certain line to line (4) is equal to the gain in the signal-to-noise ratio obtained along this line.

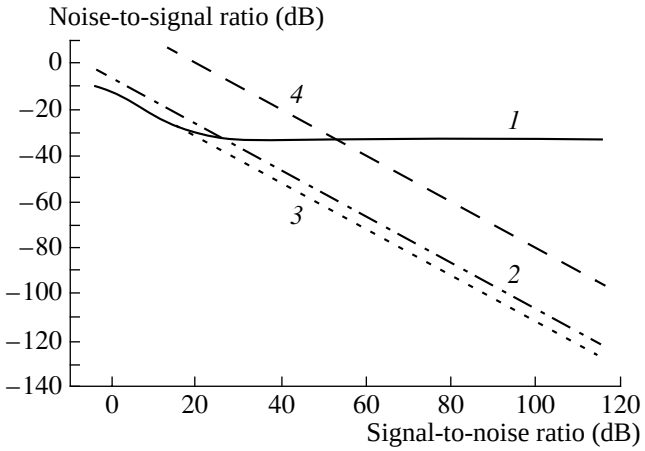

Fig. 3. Noise-to-signal ratio at the output of the matched filter versus the signal-to-noise ratio at the filter input for different processing algorithms and signals: (*1*) ordinary processing with Eq. (2); (*2*) processing with Eq. (5); (*3*) same for the signal with the limited minimal value of the spectrum modulus; and (*4*) the input value of the noise-to-signal ratio.

Now let us consider the wave front inversion. The signal generated by the WFI can involve an additive noise of a rather low level, and the lowest signal level can be governed by the correlation noise. In the WFI-processing, the signal shape cannot be arbitrary. It is advantageous to realize the case number *2* in Fig. 3. By doing so, the effect of the additive noise will be somewhat enhanced but the correlation noise will be fully suppressed. Such a suppression can be quite efficient (see Fig. 3).

Algorithm (5) is recommended for the WFI procedure. In practice, such a procedure can be implemented as follows. One receives the signal and stores it. Then, the Fourier spectrum of this signal is found. The spectrum is reversed by dividing unity by it. The inverse Fourier transform is applied to the inverse spectrum found. The signal obtained is transmitted into the same medium. At the point of transmitting the initial signal, transformation (5) yields a narrow pulse that is free of

correlation noise. Such a transformation is feasible only in acoustics. The author does not know if anybody has ever put the aforementioned algorithm to practice, in spite of the fact that transformation (5) is well known and the correlation noise was actually observed in the WFI [2].

It is useless to introduce changes into the spectrum modulus, because such changes cannot be taken into account in the received signal. Therefore, the two signals will have different shapes, and transformation (5) will not be applicable to them.

ACKNOWLEDGMENTS

This work was supported by the Russian Foundation for Basic Research, project no. 02-02-17056, and a grant from the Ministry of Industry and Science (no. NSh-1641.2003.2).

REFERENCES

1. L. A. Vaĭnshteĭn and V. D. Zubakov, *Extraction of Signals against the Background of Random Noise* (Sovetskoe Radio, Moscow, 1960).
2. M. Fink, D. Cassereau, A. Derode, *et al.*, Rep. Prog. Phys. **63**, 1933 (2000).
3. V. A. Zverev, *Physical Fundamentals of Image Formation by Wave Fields* (Inst. Prikl. Fiz., Ross. Akad. Nauk, Nizhni Novgorod, 1998).
4. T. G. Birdsall and K. Metzger, J. Acoust. Soc. Am. **79**, 91 (1986).
5. J. E. Ehrenberg, T. E. Ewart, and R. D. Morris, J. Acoust. Soc. Am. **63**, 1861 (1978).
6. V. A. Zverev, Izv. Vyssh. Uchebn. Zaved., Radiofiz. **44**, 4 (2001).

Translated by E. Kopyl

Acoustical Physics, Vol. 50, No. 5, 2004, pp. 528–534. Translated from Akusticheskiĭ Zhurnal, Vol. 50, No. 5, 2004, pp. 619–627.

Segmentation of Acoustic Images by Neural Network Processing

S. V. Il'in and M. N. Rychagov

Moscow State Institute of Electronic Engineering (Technical University), Zelenograd, Moscow, 124498 Russia
e-mail: mrychagov@miee.ru

Received July 23, 2003

Abstract—A segmentation method for biomedical acoustic images is reported which efficiently classifies the groups of similar image elements (pixels) and separates them into particular characteristic regions. As the input data, the method uses the pixel intensities of the source image. The classification is performed by learning vector quantization neural networks, which separate the main classes (structures, tissues, artifacts, etc.) present in the image. Because this type of neural network implies that the number of the classes is known and that the network should be trained by instruction, an expert must participate in the process of generating the input data. Results obtained by processing test acoustic (ultrasonic) images demonstrate that the method is capable of effectively solving sonography classification problems. The accuracy of the method is estimated by comparison with the segmentation performed manually. © *2004 MAIK "Nauka/Interperiodica".*

INTRODUCTION

Image segmentation is a process that divides an image into regions with identical characteristics [1]. In recent decades, a variety of approaches have been developed for solving this problem, most of which handle binary or monochrome imagery. The segmentation techniques for such images can conventionally be categorized into the following groups [2]:

(a) segmentation based on the detection of boundaries between the regions (contour segmentation),

(b) clustering,

(c) region growing method, and

(d) split-and-merge method.

The advances in modern means of diagnostics have made it possible to create color and three-dimensional images, which entailed the development of new processing methods. Modifications of the above segmentation techniques may be applied to both color and three-dimensional images. All segmentation methods can also be regarded as belonging to one of two types, binary or fuzzy, depending on what logic, binary or fuzzy, they rely upon. Binary segmentation always gives a definite answer ("yes" or "no") to the question whether or not a pixel belongs to a particular region. Fuzzy segmentation does not necessarily make a unique decision: to each pixel it assigns a probability of belonging to a particular structure.

The methods based on detecting the boundaries of regions deal with digital characteristics of the images by analyzing the range of the local data, as well as the entire two-dimensional vector space, using the gradients calculated in this space. After finding the boundaries, an additional postprocessing is necessary to create objects and segments which characterize the elements present in the image. Other contour segmentation methods also exist, such as the contour-tracing method [1], which uses a certain algorithm to move a point along the object's boundary, thereby tracing its contour, and the edge detection method [3], which relies on the fact that the region of interest is usually separated from adjacent regions of the image by steps in its brightness.

The region-growing and split-and-merge methods mostly operate in terms of threshold brightness values. The first method defines a region by a collection of points, which are "connected" with the "point of growth" and have "similar" values. The algorithm includes pixels in the region that are near the point of growth and whose values are within $m - t$ to $m + t$, where m is the average brightness of the region and t is the threshold value specified by the user. The second method starts with splitting the image into a large number of uniform regions, which are subsequently merged anew to remove the artificial boundaries generated by the splitting procedure. Both the splitting and merging processes use brightness fluctuations across the region as a measure of its uniformity. Although this method is one of the simplest to understand, to obtain acceptable results in practice, one should impose constraints on the growth process, some of them being rather stringent [4].

The most frequently used method of separating different classes in the clustering problem is the "fuzzy c-means" method (or method of fuzzy centers) [5, 6]. The main limitation of this method is that the total number of classes must be known *a priori*.

We should also note the achievements in other statistical methods, such as wavelet analysis [7, 8] and Markov models [9], which are successfully used at present to solve segmentation and pattern recognition problems.

1063-7710/04/5005-0528$26.00 © 2004 MAIK "Nauka/Interperiodica"

Artificial neural networks have found increasing application in various fields, including the signal processing, pattern recognition, medical information science, speech recognition and analysis, and commerce. They form a data processing system, whose structure has much in common with biological neural networks.

The analysis of works associated with application of neural networks in mathematical physics problems shows that the neural-network approach is advantageous over conventional mathematical methods in three cases [10]. First, when the problem, due to its particular features, does not lend itself to adequate formalization, because it contains elements of ambiguity that cannot be formulated in terms of conventional mathematical methods. Second, when the problem can be formalized, but there are presently no tools for solving it. Third, when the problem can be formalized and an appropriate mathematical tool exists, but its implementation by available computers fails to satisfy the requirements in terms of time, size, mass, power consumption, etc. In this situation, one has either to simplify the algorithm, which degrades the quality of the solution, or to apply an appropriate neural network approach if it provides the required quality of solving the problem.

In spite of ample literature devoted to neural networks on the whole and to their specific applications, it was not until quite recently that a steady interest emerged in the study of the potential of applying neural-network approaches to various inverse mathematical physics problems, including the problems of image generation, reconstruction, and interpretation.

Three main directions of the current research efforts in acoustics and related areas of radio-wave physics can be indicated: the application of multilayer perceptrons in data interpretation [11–16], the design of neural networks of a special architecture for solving scalar electromagnetic and acoustic introscopy problems [17], and the solution of linearized versions of tomography and holography problems using Hopfield networks [18–22].

The purpose of this study is to apply the neural network approach to the segmentation of ultrasonic images. The reason why the neural network approach is chosen is that the statistical properties of biological tissues are in most cases known a priori. Therefore, the algorithms that combine learning and self-organization should provide a higher segmentation fidelity. The elements of learning supply the classification process with experience of a diagnostician, while the self-organization enhances the robustness of the method against errors and widens its scope, allowing it to be applied to images of various types.

Let us first detail the topology of the learning vector quantization neural networks, beginning with the self-organizing Kohonen map.

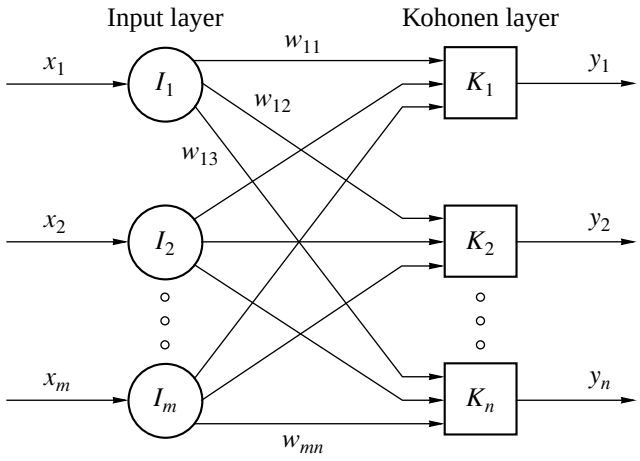

Fig. 1. Self-organizing Kohonen map.

1. SELF-ORGANIZING KOHONEN MAP

Artificial neural networks are computational systems that are similar to biological neural networks, which contain neurons, axons, dendrites, neuron layers, transfer functions, etc. [23, 24]. In general, artificial neural networks can be categorized into two large groups in terms of the amount of information needed for the learning phase: trained (learned by instruction) networks and self-organizing networks.

Trained neural networks use a prior information about the desired network outputs in order to decrease the error between real input and desired output data to a tolerable value. Self-organizing networks themselves determine the distribution of the internal weighting coefficients for the data applied to their inputs and do not require learning by instruction.

Self-organizing networks, also known as Kohonen neural networks, are networks that contain a topology map, i.e., take into consideration the topological arrangement of their elements. Such a neural network has a layer of input neurons and a layer of output neurons. Each neuron of the input layer is connected to each neuron of the output layer. At each stage of the learning phase, the neuron whose weighting coefficients provide the best fit (usually, in terms of the smallest Euclidean distance) with the output signal is declared the winner. This output neuron and neurons of its nearest neighborhood tune their weighting vectors such that they get closer to the input vector. The degree of this tuning is different for different neurons: it is higher near the winning neutron and decreases as the distance from the winner increases.

Figure 1 illustrates the simplest structure of the self-organizing Kohonen map. The output neurons can have an arbitrary spatial distribution; usually, it is a linear or two-dimensional array. A vector X of length m is applied to the input of the network. Neurons I_1, I_2, …, I_m only serve as branching points of the vector X. Each neuron of the input layer is connected to each neuron of

the Kohonen layer through an individual weight w_{mn}. The weights that refer to the nth neuron of the Kohonen layer form the weight vector $W_n = \{w_{1n}, w_{2n}, \ldots, w_{mn}\}$. As the training time passes, the size of the nearest neighborhood of the winning neuron and the degree of tuning of the weighting vector decrease. In general, the number of neurons in the Kohonen layer may be arbitrary and only depends on the parameters of the problem for which the network is used.

2. LEARNING MODE

The Kohonen map is trained through self-learning, which proceeds without a teacher. It is therefore difficult (and unnecessary) to predict what particular Kohonen neuron will be active for a given input vector; it is only necessary to guarantee that, as a result of the self-learning, the neural network will adequately collect similar vectors into separate clusters. Each processing element of the Kohonen layer calculates its input intensity K_n according to the formula

$$K_n = D(X, W_n), \tag{1}$$

where $X = \{x_1, x_2, \ldots, x_m\}$ is the row vector, $W_n = \{w_{1n}, w_{2n}, \ldots, w_{mn}\}$ is the column vector, and D is a certain measure (metric) of the distance between W_n and X.

There are two most general forms of the function $D(X, W_n)$: the Euclidean distance

$$d(X, W) = \|X - W\| = \sqrt{\sum_m (x_m - w_{mn})^2} \tag{2}$$

and the angle between the vectors

$$\Delta(X, W) = \arccos\left(\frac{X \cdot W}{\|X\| \cdot \|W\|}\right), \tag{3}$$

where $X \cdot W$ and $\|X\| \cdot \|W\|$ is the scalar product of vectors X and W.

As the measure of distance, we take the Euclidean distance $d(X, W)$. The Kohonen rule is realized as follows. As soon as each output neuron calculates its function K_n, they start competing in order to find out whose K_n is the lowest. When the winner of this competition is found, its output y_n is set equal to 1, while the outputs of all the remaining elements are set equal to 0.

At this moment, all the weights change according to the Kohonen learning rule [20]:

$$W_n(t+1) = W_n(t) + h_{cn}(t)(X - W_n(t))y_n, \tag{4}$$

where t is the epoch number (discrete time) and $h_{cn}(t)$ is the neuron neighborhood function, which is a function of distance r_c between the winning neuron and neighboring neurons in the network and is nonincreasing with time.

The function $h_{cn}(t)$ can be represented as a product of two functions: a function of distance and a function of time describing the learning rate:

$$h_{cn}(t) = h(\|r_c - r_n\|, t)a(t), \tag{5}$$

where r_n is the neuron coordinate in the network and $a(t)$ is the learning rate, which falls off as a linear or hyperbolic function.

One of the following two functions of distance are commonly used: the rectangular function

$$h(d, t) = \begin{cases} \text{const}, & d \le \sigma(t), \\ 0, & d > \sigma(t) \end{cases} \tag{5}$$

or the Gaussian function

$$h(d, t) = \exp\left(-\frac{d^2}{2\sigma^2(t)}\right), \tag{6}$$

where $\sigma(t)$ is the so-called learning radius.

The Gaussian function usually gives the best result.

Initially, the learning radius is taken to be sufficiently large; then, it is gradually decreased, so that, finally, the winning neuron alone remains learning. Most often, $\sigma(t)$ is a decreasing linear function.

3. FUNCTIONING MODE

In its simplest form, the Kohonen layer functions by the rule "to the victors belong the spoils"; i.e., for a particular input vector, one and only one Kohonen neuron outputs logical 1 (becomes active), while all the rest of the neurons output 0. As in the learning mode, a vector is applied to the input and the Euclidean distance is calculated from Eq. (2). The Kohonen neuron with the smallest $d(X, W)$ becomes the winner. Its output is 1, while all other neurons output 0:

$$y_n = \begin{cases} 1, & d(X, W) = \min\{d(X, W)\}, \\ 0, & d(X, W) \ne \min\{d(X, W)\}. \end{cases} \tag{7}$$

The Kohonen layer classifies the input vectors into groups of similar vectors. This means that, if the input vectors are similar, they activate one and the same output neuron.

It would be ineffective to associate an element of a monochrome biomedical image with a particular biological tissue based on its brightness alone, because such images are often contaminated with noise and show a low contrast. Therefore, when classifying an image element, we consider it not separately but together with its neighborhood. To this end, for each element, we generate a vector whose components are the brightness values of the element and its eight nearest neighbors. Thus, the vector carries information not only about the brightness of one element but also about the structure of the image in its neighborhood.

The vectors obtained were used to train the network so that, as we noted above, similar vectors activate after this training one and the same neuron of the output layer, which is a criterion for the image elements corresponding to these vectors to be ascribed to the same class.

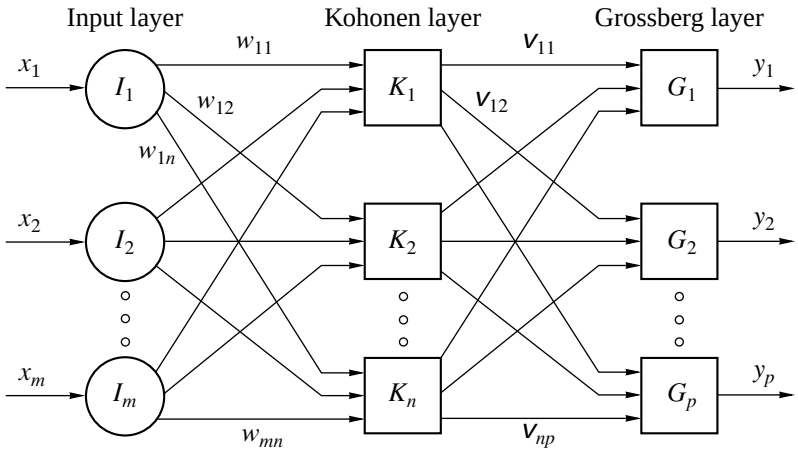

Fig. 2. Learning vector quantization neural network.

Owing to this property, the self-organizing Kohonen map can be used for image segmentation. However, this algorithm sometimes fails to provide a successful segmentation. The reason is that the Kohonen network functions without an instructor. The impossibility of controlling the learning process sometimes causes regions corresponding to different (but similar in their properties) biological tissues to merge into one region. Therefore, although the learning in most cases proceeds successfully, we decided to reject this type of network and use its more complex version, namely, the learning vector quantization network.

4. LEARNING VECTOR QUANTIZATION NETWORK

The learning vector quantization network combines two algorithms: the self-organizing Kohonen map and the Grossberg layer. Figure 2 shows a simplified version of the learning vector quantization network.

When the Kohonen neural network is used, it is doubtful to predict which output neuron will be associated with a particular region of the image. The learning vector quantization network makes such a prediction possible, because training of this network includes elements of learning by instruction.

Consider the learning process in more detail. Let neurons K_1, K_2, and K_3 extract subclasses, which belong to finite class 2 of the Grossberg layer, in the space of input vectors. Then, the neurons K_1, K_2, and K_3 will be connected by unit weights to neuron G_2 and by zero weights to other Grossberg neurons. Thus, neuron G_2 will output 1 if one of the three Kohonen neurons (K_1, K_2, or K_3) becomes the winner and outputs 1. We a priori know the portion of Kohonen layer neurons that must be classified into particular classes of the Grossberg layer; therefore, we can specify the elements of the weight vectors for the Grossberg layer beforehand. Nevertheless, a learning procedure should be executed to obtain a correct classification into subclasses for each of the input vectors.

Learning of the network in the Kohonen layer relies on a set of pairs of input–target vectors: $\{X_1, T_1\}$, $\{X_2, T_2\}$, …, $\{X_q, T_q\}$.

Each target vector has only one 1, the rest of its elements being zero; the 1 indicates the proper classification.

Consider the following pair of vectors:

$$X_1 = \begin{bmatrix} 5 \\ 2 \\ -9 \end{bmatrix}, \quad T_1 = \begin{bmatrix} 0 \\ 0 \\ 1 \\ 0 \end{bmatrix}.$$

Then, the input vector consists of three elements and must be ascribed to one of the four finite classes. Accordingly, the neural network must be trained so as to ascribe the above vector to the third of the four finite classes; i.e., the vector X_1 must activate the third neuron of the Grossberg layer. For the learning vector quantization architecture, the topology of the Kohonen map is not of fundamental importance and the location of the Kohonen neurons that belong to the same class may be arbitrary, because they are grouped into a particular class by the Grossberg layer. Therefore, the Kohonen learning rule can be replaced with its simpler modification: the algorithm of competitive training, which tunes the weight of the winning neuron alone.

To train the network, first, the vector X is applied to its input, after which the winning neuron is found based on the rule given by Eq. (7). Let the ith neuron of the Kohonen layer be the winner. Then, the neuron K_i outputs 1, while all the remaining neurons output 0.

At the next stage, the procedure of finding the winner neuron is applied to the Grossberg layer. As a result, the jth Grossberg neuron wins and outputs 1, thereby ascribing our input vector to the jth finite class. Of course, this classification can be correct or incorrect

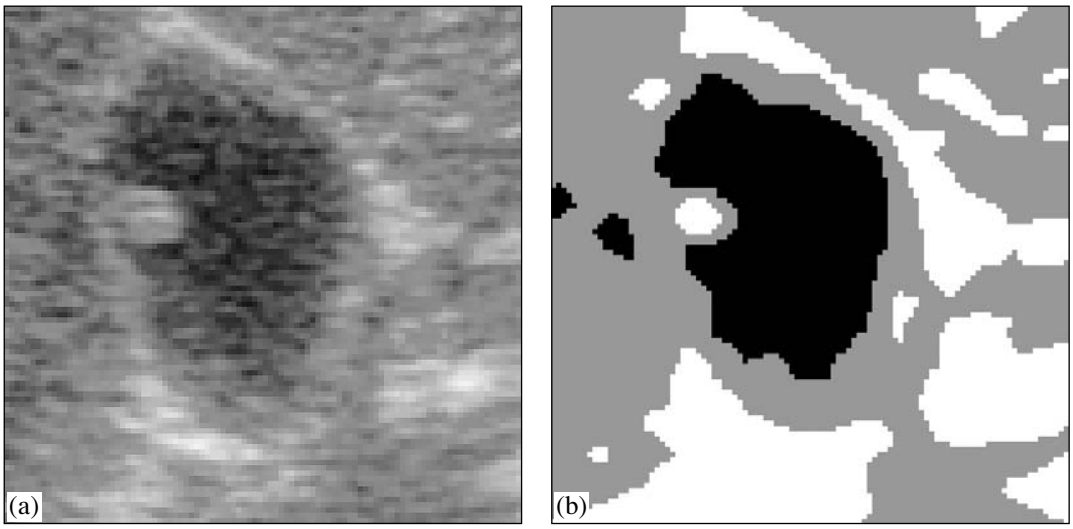

Fig. 3. (a) Original ultrasonic image and (b) the manually segmented reference image.

depending on whether or not the input vector belongs to the *j*th finite class.

If the classification is correct, the vector W_i changes, approaching the input vector by the formula

$$W_i(t+1) = W_i(t) + a(t)(X - W_i(t)); \quad (8)$$

otherwise, the weight vector recedes from the input vector.

The final state of the neural network depends on three main factors:

(a) the initial state of the weighting coefficients,

(b) the data set used to train the network, and

(c) the characteristics (parameters) of the neural network itself.

The initial values of the weighting coefficients are small and are chosen in a random manner; their contribution to the final state of the network decreases with increasing number of test data sets. The parameters of the network, such as the number of neurons in the Kohonen layer, the degree of reducing the size of the winning neuron's neighborhood, and the rule for updating the weighting coefficients, are the basic parameters that determine the final result. It should also be noted that the procedure used for preprocessing the input data plays an important part in training the network and, consequently, in forming its final state. We consider finding the optimal preprocessing procedure as one of the most important lines of further investigation in this area of research.

5. EXPERIMENTAL

Our experiment used ultrasonic images borrowed from the atlas on child and adolescent clinical diagnostics which was issued under the SONO-2000 project [25]. In Fig. 3a, one can distinguish a region of a dark biological tissue surrounded by lighter regions and also the presence of a grain pattern typical of this kind of image.

To create a training sample set from the image, the user selects 45 typical pixels for each of the three tissues. For each of these pixels, an input vector consisting of brightnesses of this pixel and of eight of its nearest neighbors taken sequentially is constructed. As a result, a column vector $X = \{x_1, x_2, \ldots, x_9\}$ is obtained. Thus, each input vector consists of nine elements, which contain information about not only the brightness of the pixel but also the image structure in its neighborhood. Each such vector is associated with the target vector *Y*, which contains information about the finite class it belongs to. As a result, a set of 135 vector–target pairs, which is used to train the network, is obtained. The process of creating the set of input vectors is illustrated in Fig. 4.

A smaller number of training vectors gives a lower accuracy of the method. When the number of input vectors was increased, no noticeable accuracy improvement was observed. Presumably, this is caused by the relatively small size of the initial image.

6. ACCURACY ESTIMATION

The result of the segmentation was quantitatively evaluated by comparing it with the image segmented manually. This reference image is shown in Fig. 3b. After the segmentation, the image obtained was compared with the reference image, pixel by pixel, and the segmentation accuracy was calculated by the formula

$$A = \frac{C}{N} \times 100\%, \quad (9)$$

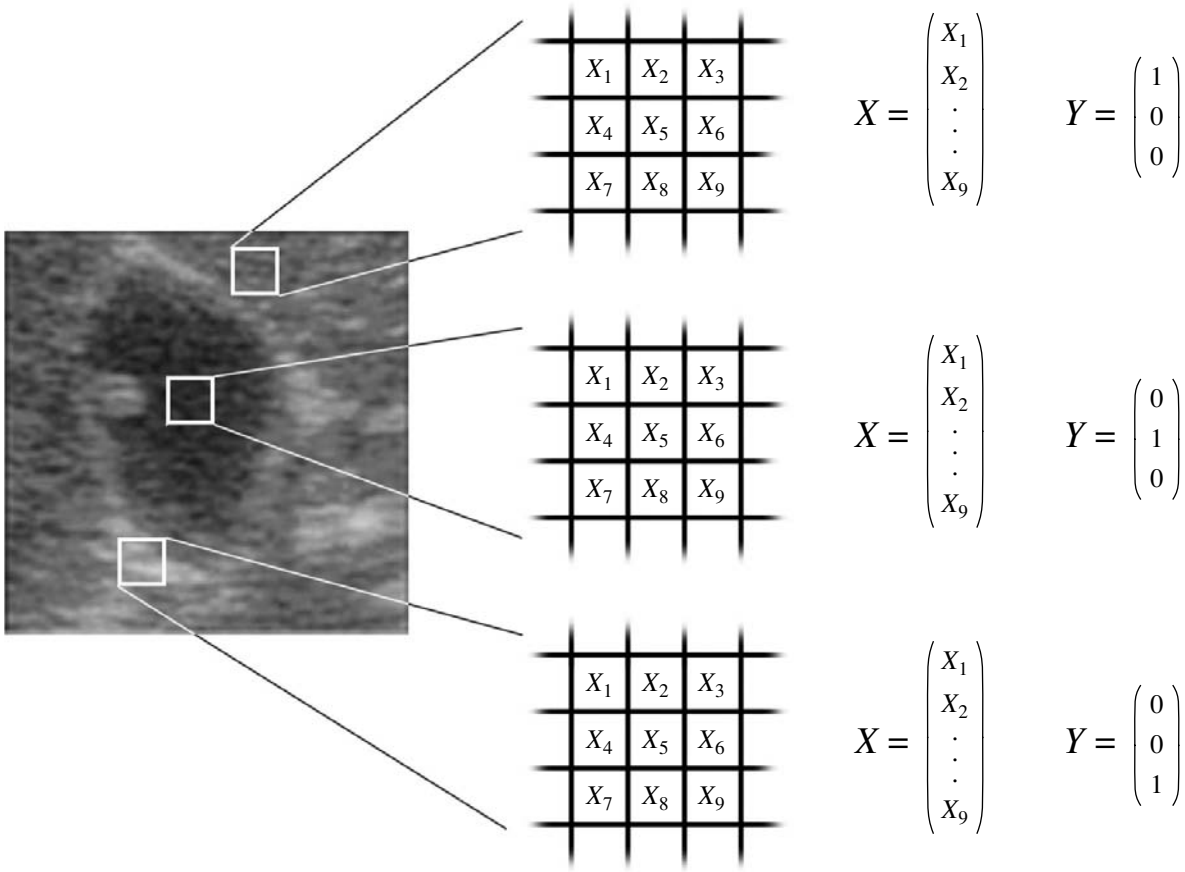

Fig. 4. Generation of the set of input vectors.

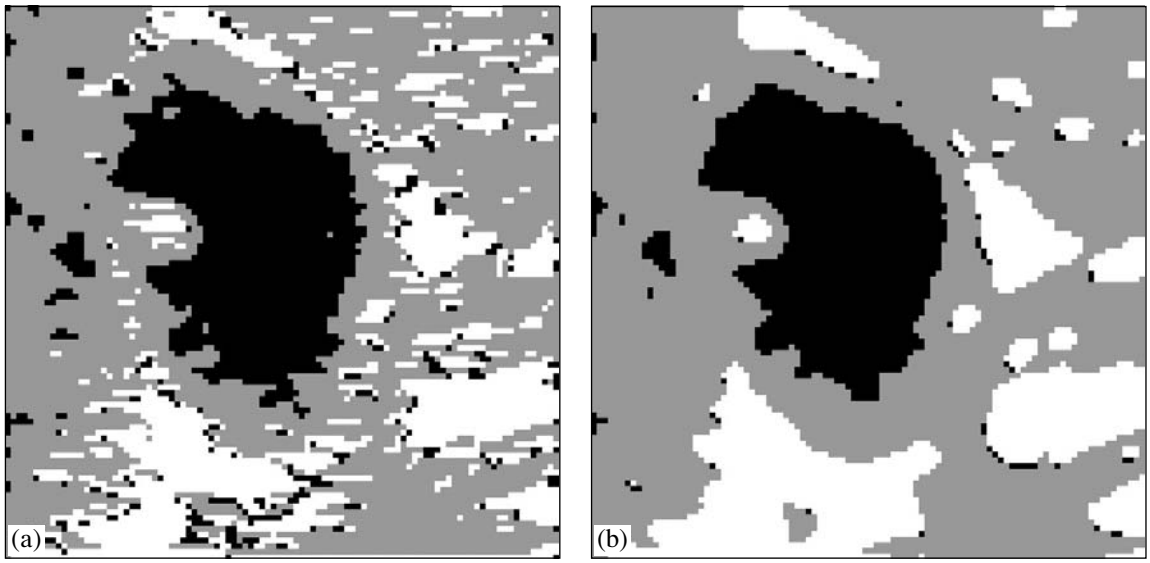

Fig. 5. Segmentation of (a) the original and (b) blurred images.

where A is the segmentation accuracy, C is the number of pixels classified correctly, and N is the total number of pixels in the image.

An example of segmentation by the method described above is shown in Fig. 5a. The segmentation accuracy was on the average 82%. Figure 5b shows the

result of segmentation of the same image subjected to Gaussian blurring to reduce the effect of the grain pattern. The use of this procedure improved the accuracy to 84% and also smoothed the boundaries of the regions and removed the fine features, which is an unavoidable result of the blurring.

CONCLUSION

The segmentation method described in this paper relies on the processing of the image pixel intensity data. The segmentation procedure is performed by the learning vector quantization neural network. The network training vectors are generated from the image pixels selected by the user. After the network is trained, it becomes possible to classify each pixel of the image.

The experimental results prove that the method can be used to clearly recognize the regions in the image, and the accuracy estimates show that the method provides an acceptable robustness.

REFERENCES

1. W. K. Pratt, *Digital Image Processing* (Wiley, New York, 1978; Mir, Moscow, 1982).
2. J. Moreira and L. F. Costa, in *Proceedings of the IX SIBGRAPI'96 Symposium* (Sao Carlos, Brasil, 1996), p. 47.
3. L. G. Roberts, in *Proceedings of Symposium on Optical and Electro-Optical Information Processing, Boston, 1964*, Ed. by J. T. Trippett *et al.* (MIT Press, Cambridge, Mass., 1965).
4. C. R. Brice and C. L. Finnema, in *Integral Robots* (Mir, Moscow, 1975), Vol. 2, p. 136.
5. Y. W. Lim and S. U. Lee, Pattern Recogn. **23**, 935 (1990).
6. R. Medina, M. Garreau, D. Jugo, *et al.*, in *Proceedings of the 17th Annual International Conference of the IEEE Engineering in Medicine and Biology Society* (Montreal, Canada, 1995), p. 405.
7. V. I. Vorob'ev and V. G. Gribunin, *Theory and Practice of Wavelet Transformation* (VUS, St. Petersburg, 1999).
8. A. Yakovlev, *Fundamentals of the Wavelet Transformation of Signals* (SAĬNS-PRESS, Moscow, 2003).
9. S. I. Rodzin, Perspect. Inf. Technol. Intel. Sist., No. 3, 113 (2000), http://pitis.tsure.ru.
10. P. P. Kol'tsov and V. V. Prokhorov, *Neural Processing of Visualized Information* (Nauka, Moscow, 1997).
11. A. Y. Nooralahiyan, B. S. Hoyle, and N. J. Bailey, in *Proceedings of ECAPT*, Ed. by M. Beck (Karlsruhe, 1993), p. 50.
12. A. Adler and R. Guardo, IEEE Trans. Med. Imaging **13**, 594 (1994).
13. E. Coccorese, R. Martone, and F. C. Morabito, IEEE Trans. Magn. **30**, 2829 (1994).
14. A. Roy, P. Barat, and S. K. De, Ultrasonics **33**, 175 (1995).
15. M. N. Rychagov and B. Duchêne, in *Proceedings of IEEE AP-S International Symposium and URSI Radio Science Meeting* (Montreal, Canada, 1997), p. 257.
16. R. Carotenuto, G. Sabbi, and M. Pappalardo, IEEE Trans. Ultrason. Ferroelectr. Freq. Control **49**, 1039 (2002).
17. H.-J. Lee, C.-H. Ahn, C.-S. Park, *et al.*, in *Proceedings of the 9th Conference on the Computation of Electromagnetic Fields, 1993* (1994), p. 74.
18. J.-H. Li, A. N. Michel, and W. Porod, IEEE Trans. Circuits Syst. **36**, 1405 (1989).
19. S.-Y. Lu and J. G. Berryman, Int. J. Imaging Syst. Technol. **2**, 112 (1990).
20. Y. Aoki, Y. Sakamoto, S. Yamaguchi, and R. Mitsuhashi, in *Acoustical Imaging*, Ed. by H. Ermert and H.-P. Harjes (Plenum, New York, 1992), Vol. 19, p. 83.
21. I. Elshafiey, L. Udpa, and S. S. Udpa, IEEE Trans. Magn. **30**, 3629 (1994).
22. M. N. Rychagov and B. Duchêne, in *Proceedings of Progress in Electromagnetic Research Symposium (PIERS-98)* (Nantes, France, 1998), Vol. 3, p. 1202.
23. F. Wasserman, *Neural Computing. Theory and Practice* (Van Nostrand Reinhold, New York, 1989; Mir, Moscow, 1992).
24. R. Callan, *The Essence of Neural Networks* (Prentice Hall, New York, 1998; Vil'yams, Moscow, 2001).
25. *The SONO-2000 Project*, http://www.sono.nino.ru.

Translated by A. Khzmalyan

Acoustical Physics, Vol. 50, No. 5, 2004, pp. 535–543. Translated from Akusticheskiĭ Zhurnal, Vol. 50, No. 5, 2004, pp. 628–637.

Reduction of the Error of Hydrophone Calibration with Respect to the Field in a Hydroacoustic Tank by the Reciprocity Method

A. E. Isaev, A. N. Matveev, V. A. Smelov, and A. I. Shchelkunov

State Metrological Center of Hydroacoustic Measurements, All-Russia Scientific Research Institute for Physical-Technical and Radio-Technical Measurements, Mendeleevo, Moscow oblast, 141570 Russia

e-mail: Isaev@vniiftri.ru

Received October 23, 2002

Abstract—A hydrophone calibration procedure that considerably reduces the error caused by the acoustic field distortions in a hydroacoustic tank is proposed. The procedure is based on the definition of the reduced electric transfer impedances of transducers (i.e., the electric transfer impedances reduced to the spherical wave propagation law) and consists in measuring the electric transfer impedances for different distances between hydroacoustic transducers. The sensitivity of the hydrophone under calibration is calculated from the far-field values of the reduced electric transfer impedances. The latter are determined using a mathematical model of the hydrophone in the form of a system that contains a point sensing element and a finite number of point sources of acoustic signals (point reflectors). A method of determining the number and coordinates of the point reflectors from the analysis of the acoustic "images" of the hydrophone's reflecting surface is proposed. The measuring technique, the algorithms of mathematical processing, and the results of experimental studies are considered. A comparative analysis of the results of the hydrophone calibration with respect to the field by the reciprocity method is performed for the cases of using the conventional technique and the proposed method. © *2004 MAIK "Nauka/Interperiodica".*

In calibrating a hydrophone in a laboratory hydroacoustic tank, it is impossible to provide the far-field conditions, because the casing of the hydrophone and its mounting elements are not acoustically transparent. The interference of the signal produced by the radiator and the signals reflected from the structural and mounting elements of hydrophones leads to distortions of the acoustic field, the degree of the distortions depending on the calibration frequency. These distortions substantially contribute to the measurement errors.

The characteristic size of a measuring hydrophone may considerably exceed the size of its active element. In this case, when the hydrophone is calibrated in a laboratory hydroacoustic tank, it is impossible to provide the conditions with a plane wave incident on the hydrophone. The interference of the direct wave produced by the radiator and the waves reflected from the structural and mounting elements of the hydrophone may introduce considerable distortions into the results of measurements. In this paper, we describe the procedure of calibration in a free field on the basis of using the hydrophone model that consists of a point active element and a finite number of point reflectors [1].

The canonical expression for determining the receiving sensitivity M_H of a measuring hydroacoustic transducer H in a free field by the reciprocity method with the use of auxiliary radiating P and reversible T transducers has the form [2, 3]

$$M_H = \left(\frac{2}{\rho f}\frac{Z_{PH}Z_{TH}}{Z_{PT}}\frac{r_{PH}r_{TH}}{r_{PT}}\right)^{1/2}, \quad (1)$$

where Z_{PH}, Z_{PT}, and Z_{TH} are the values of the electric transfer impedances of the transducers; r_{PH} is the distance between the source P and the transducer H under calibration; r_{PT} is the distance between the source P and the reversible transducer T operating in the receiving mode; r_{TH} is the distance between the transducer H under calibration and the reversible transducer T operating in the transmitting mode; ρ is the density of the medium; and f is the frequency.

The values of the electric transfer impedances Z_{PH}, Z_{PT}, and Z_{TH} are determined from the measured currents I_{PH}, I_{PT}, and I_{TH} flowing through the transducers P and T operating in the transmitting mode and from the open-circuit voltages U_{PH}, U_{PT}, and U_{TH} measured at the outputs of the transducers H and T operating in the receiving mode:

$$Z_{PH} = \frac{U_{PH}}{I_{PH}}, \quad Z_{PT} = \frac{U_{PT}}{I_{PT}}, \quad Z_{TH} = \frac{U_{TH}}{I_{TH}}.$$

Formula (1) is valid for the spherical wave propagation law. Therefore, to obtain acceptable far-field conditions in the measurements, it is necessary that the dis-

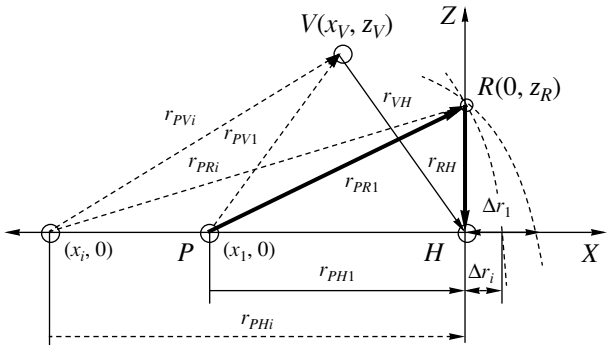

Fig. 1. Simplified model for analyzing the effect of the hydrophone under calibration on the acoustic field.

tances between the transducers be sufficiently large to consider the transducers as point objects [4].

The auxiliary transducers (radiators and reversible transducers), which are used for the calibration by the reciprocity method, are usually designed with minimal dimensions. A measuring hydrophone to be calibrated has a casing and some mounting elements. Their dimensions may be fairly large, so that the criterion of minimal acceptable distance cannot be satisfied under the conditions of a laboratory hydroacoustic tank. As a result, the measurements are performed in a spatial region within which the interference of the direct acoustic signal and the signals reflected from the casing of the transducer to be calibrated and from its mounting elements causes distortions of the acoustic field. Under these conditions, the use of the standard calibration procedure may lead to considerable measurement errors.

To analyze the effect of the hydrophone under calibration on the acoustic field, we consider a simplified model shown in Fig. 1. We assume that the radiator and the hydrophone are separated by a sufficiently large distance, which allows us to represent their respective active elements as a point radiator P characterized by a transmitting sensitivity $\dot{S}'_p$ and a point receiver H characterized by a receiving sensitivity $\dot{M}'_H$. The reflecting properties of the casing and the mounting elements of the hydrophone can be described by a point reflector R with a complex reflection coefficient $\dot{w}_R = w_R e^{-j\varphi_R}$. Elements P, H, and R lie in the XZ plane, as shown in Fig. 1. Receiver H is at the origin of coordinates; radiator P is on the X axis at a point with coordinates $(x_1, 0)$; and reflector R has the coordinates $(0, z_R)$.

The sound pressure acting on the receiver H is a result of interference of two coherent spherical waves: the direct acoustic wave with a complex amplitude expressed as

$$\dot{p}_{PH} = \dot{S}'_P \dot{I}_{PH} \frac{r_0}{r_{PH}} e^{-jk(r_{PH} - r_0)}$$

and the wave reflected from the reflector R with a complex amplitude

$$\dot{p}_{RH} = \dot{S}'_P \dot{I}_{PH} w_R \frac{r_0}{r_{PR} + r_{RH}} e^{-j(k(r_{PR} + r_{RH} - r_0) + \varphi_R)}.$$

Here, r_0 is the reference distance, which usually is taken to be equal to 1 m; $k = \dfrac{2\pi f}{c}$ is the wave number; and c is the sound velocity in water.

The complex amplitude of the voltage at the hydrophone output, $\dot{U}_{PH}$, has the form

$$\dot{U}_{PH} = \dot{M}'_H \dot{S}'_P \dot{I}_{PH} \frac{r_0}{r_{PH}} e^{-jk(r_{PH} - r_0)} \times (1 + w_R y_R(r_{PH}) e^{-j(k\upsilon_R + \varphi_R)}), \quad (2)$$

where $\upsilon_R = r_{PR} + r_{RH} - r_{PH}$ and

$$0 < y_R(r_{PH}) = \frac{r_{PH}}{r_{PR} + r_{RH}} \le 1.$$

The following consideration is based on the definition of the electric transfer impedance reduced to the propagation law of acoustic waves. For radiator P and hydrophone H separated by a distance r_{PH}, we determine the electric transfer impedance reduced to the spherical wave propagation law (below we call it reduced transfer impedance):

$$\dot{Z}_{PH}(r) = \frac{\dot{U}_{PH}}{\dot{I}_{PH}} \frac{r_{PH}}{r_0} e^{jk(r_{PH} - r_0)}. \quad (3)$$

One can easily verify that the reduced transfer impedance of the point radiator P and point receiver H in an unperturbed field of a spherical acoustic wave does not depend on the distance between P and H and is equal to the product $\dot{M}'_H \dot{S}'_P$. We denote the reduced transfer impedance of the point radiator and point receiver in the unperturbed spherical wave field as $\dot{Z}_{PH_0}$.

In the spherical wave field perturbed by the wave produced by a reflector, the reduced transfer impedance depends on the distance between the radiator and the receiver of the acoustic signal. Substituting the expression for the output voltage of the hydrophone into Eq. (3) at $w_R \ll 1$, we obtain an approximate expression for the magnitude of the reduced transfer impedance

$$Z_{PH}(r) = Z_{PH_0} \sqrt{(1 + 2w_R y_R(r_{PH}) \cos(k\upsilon_R + \varphi_R))}, \quad (4)$$

where $Z_{PH_0} = M'_H S'_P$.

Figure 2 shows the spatial dependences of the reduced transfer impedance $Z_{PH}(r)$ measured at frequencies of 30, 40, and 60 kHz for the radiator and the hydrophone manufactured in the form of piezoelectric spheres 7 mm in diameter suspended on thin electric

cables. The impedance $Z_{PH}(r)$ was measured using a reflector, which was made in the form of an empty sphere 30 mm in diameter and fixed to the cable of the hydrophone at a distance of 250 mm along the vertical from the active element. The distance between the transducers was varied from 440 to 1540 mm. The values of $Z_{PH}(r)$ shown in Fig. 2 are expressed in percent of Z_{PH_0}. The latter, in turn, were measured for each frequency without the reflector on the hydrophone cable.

From Figs. 1 and 2, one can see that, as the distance between transducers increases, the difference $\Delta r = r_{PR} - r_{PH}$ between the radiator–reflector and radiator–receiver distances decreases. Hence, the phase difference between the direct and reflected acoustic waves, which are superimposed at the reception point H, varies. As the radiator moves from the initial position to an infinitely distant point, the reduced transfer impedance at a frequency f undergoes $\frac{\Delta r_1}{\lambda}$ oscillations with a decreasing spatial periodicity (λ is the wavelength of the acoustic signal). At $r_{PH} \gg \frac{r_{RH}^2}{\lambda}$, the magnitude of the reduced transfer impedance tends to a constant value:

$$Z_{PH_\infty} = \lim_{r_{PH}\to\infty}(Z_{PH}(r)) = Z_{PH_0}\sqrt{(1 + 2w_R\cos(kr_{RH} + \varphi_R))}. \quad (5)$$

For the receiving sensitivity M_H of the hydrophone as a system consisting of a point active element and a point reflector, we can write the expression

$$M_H = M'_H\sqrt{(1 + 2w_R\cos(kr_{RH} + \varphi_R))}.$$

A similar expression is valid for the transmitting sensitivity S_P of the radiator when the hydrophone is a point receiver and the reflector is concentrated at the radiator:

$$S_P = S'_P\sqrt{(1 + 2w_R\cos(kr_{RH} + \varphi_R))}.$$

The calculation of the sensitivity of the hydrophone with the use of the values of the electric transfer impedances determined at arbitrarily chosen distances between the transducers leads to a considerable error in the result. As seen from Fig. 2, the deviation of the values of the reduced transfer impedance from Z_{PH_∞} may reach a double amplitude of the envelope, which amounts to about 7% at a frequency of 30 kHz and about 6% at a frequency of 40 kHz.

Let us show how the information on the spatial dependence of the reduced transfer impedance $Z_{PH}(r)$ can be used for the determination of Z_{PH_0} and Z_{PH_∞}.

First, we consider the problem of determining the coordinates of the reflector. For this purpose, we use the following approach. Assume that, for a set of distances r_{PH_i} ($i = 1, \ldots, N$), we know the values of the squared

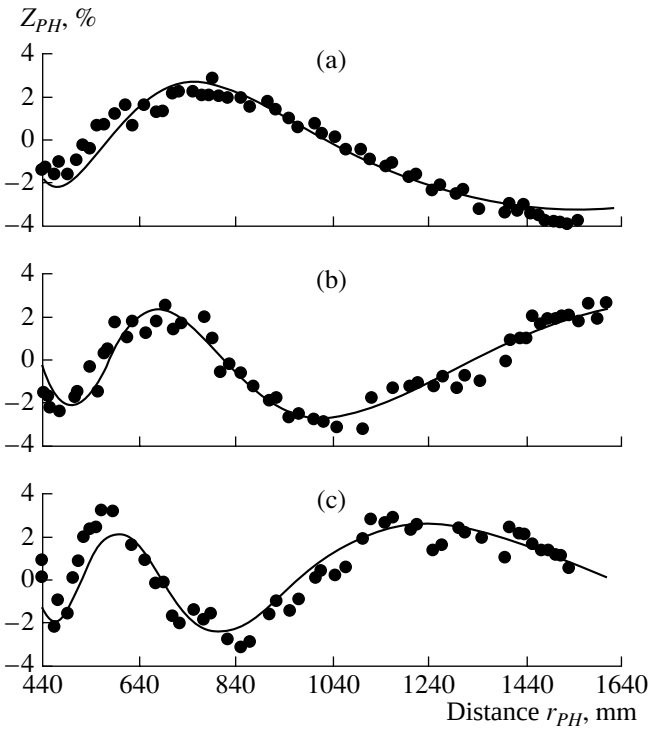

Fig. 2. Spatial dependences of the reduced transfer impedances of a pair of spherical transducers with a single reflector at frequencies of (a) 30, (b) 40, and (c) 60 kHz. The dots represent the experiment, and the lines refer to the model.

magnitude of the reduced transfer impedance $Z^2_{PH}(r)_i$. We place a virtual point reflector V with a unit reflection coefficient at some point of the plane with the coordinates (x_V, z_V) (see Fig. 1). For the virtual reflector V, at the aperture $D \in (r_{PH_i}, i = 1, \ldots, N)$, we determine the functional

$$Q(V, D) = \frac{1}{\|\hbar(V, D)\|}\sqrt{(Q'(V, D))^2 + (Q''(V, D))^2}, \quad (6)$$

where

$$Q'(V, D) = \sum_{i=1}^{N} \aleph_i y_V(r_{RH_i})\cos(k\vartheta_{V_i}),$$

$$Q''(V, D) = \sum_{i=1}^{N} \aleph_i y_V(r_{PH_i})\sin(k\vartheta_{V_i}),$$

$$\aleph_i = \frac{Z^2_{PH}(r)_i}{Z^2_{PH_0}} - 1,$$

$$\vartheta_{V_i} = r_{PV_i} - r_{PH_i} + r_{VH},$$

and (V, D) is the normalizing function.

One can easily see that the functional $Q(V, D)$ has a global maximum at the point with coordinates ($x_V = x_R$,

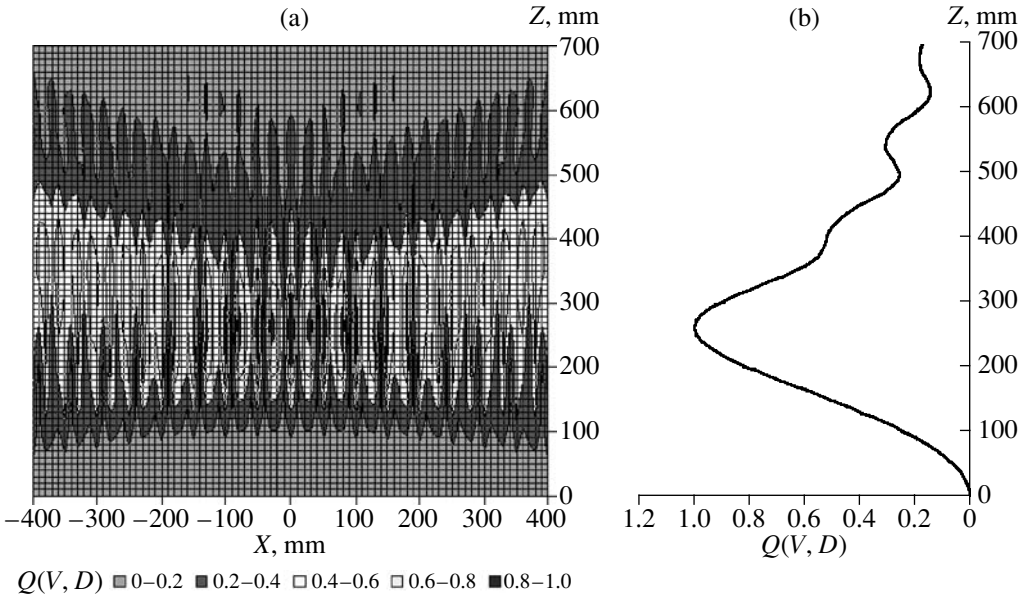

Fig. 3. (a) Acoustic image of the reflector at a frequency of 30 kHz and (b) the values of functional $Q(V, D)$ at $x = 0$.

$z_V = z_R$). Hence, by scanning with the virtual reflector over the area $x_V \in (x_R - a, x_R + a)$, $z_V \in (z_R - b, z_R + b)$ in the expected region of the reflector R and by mapping the values of the functional $Q(V, D)$ by gradations of brightness for each position of reflector V, we obtain an image of the reflector R in the form of a bright spot corresponding to the intersection of two beams at the point with coordinates (x_R, z_R).

Figures 3a–5a show acoustic images of the reflector at frequencies of 30, 40, and 60 kHz. The images were obtained from the spatial dependences of the reduced transfer impedances presented in Fig. 2. In calculating functional (6), we used the approximation

$$Z_{PH_0} \approx \frac{1}{N}\sum_{i=1}^{N} Z_{PH}(r)_i. \qquad (7)$$

The virtual reflector scanned the space within –400 to +400 mm along the X axis and within 0 to 700 mm along the Z axis with respect to the center of the active element of the radiator. Figures 3b–5b show the values of the functional $Q(V, D)$ versus the Z axis. In all three plots, the functional $Q(V, D)$ reaches its maximum in the same spatial region, near the point with the coordinates (0, 250). This result agrees well with the experiment and testifies to the stability of the method.

The proposed method was used to reconstruct the reflecting surface of a hydrophone to be calibrated. In Fig. 6, the dots represent the spatial dependences of the magnitude of the reduced transfer impedance $Z_{PH}(r)$ measured experimentally for a B&K 8104 hydrophone at frequencies of 40, 60, and 120 kHz. The values of $Z_{PH}(r)$ are given in percent of Z_{PH_0}, which was estimated by Eq. (7) for each frequency. The distance between the hydrophone and the radiator was varied from 480 to 800 mm. The hydrophone was placed vertically in a hydroacoustic tank at a depth of 3 m and fixed with its cable to two thin titanium strings by a plastic clamp, whose ρc parameter was close to that of water. The maximal size of the clamp did not exceed 50 mm. The clamp was fixed at a distance of 550–570 mm from the geometric center of the sensing element of the hydrophone. As radiators, we used piezoelectric spheres with diameters of 20 (at a frequency of 40 kHz) and 7 mm (at frequencies of 60 and 120 kHz). The temporal selection of signals reflected from the boundaries of the hydroacoustic tank was provided by radio-pulse measurement mode. The duration of radio pulses was no greater than 50 periods of the carrier frequency. The position of the geometric center of the active element of the B&K 8104 hydrophone was taken to be the origin of coordinates. Experimental dependences of the magnitude of the reduced transfer impedance were used to obtain the acoustic images of the reflecting surface of the hydrophone. The scanning by the virtual point reflector was performed over the area lying within ±400 mm along the X axis and 0 to 700 mm along the Z axis (with respect to the position of the center of the sensing element of the B&K 8104 hydrophone). The resulting acoustic images are shown in Figs 7a–9a, while Figs. 7b–9b represent the values of the functional $Q(V, D)$ within 0 to 700 mm along the Z axis (passing through the casing, cable, and clamp of the hydrophone). From Fig. 7, one can see that, at a frequency of 40 kHz, the casing and the cable of the hydrophone can be considered as acoustically transparent. The bright spot corresponding to the maximum of the functional $Q(V, D)$ at the point (0, 560) is the acoustic image of the

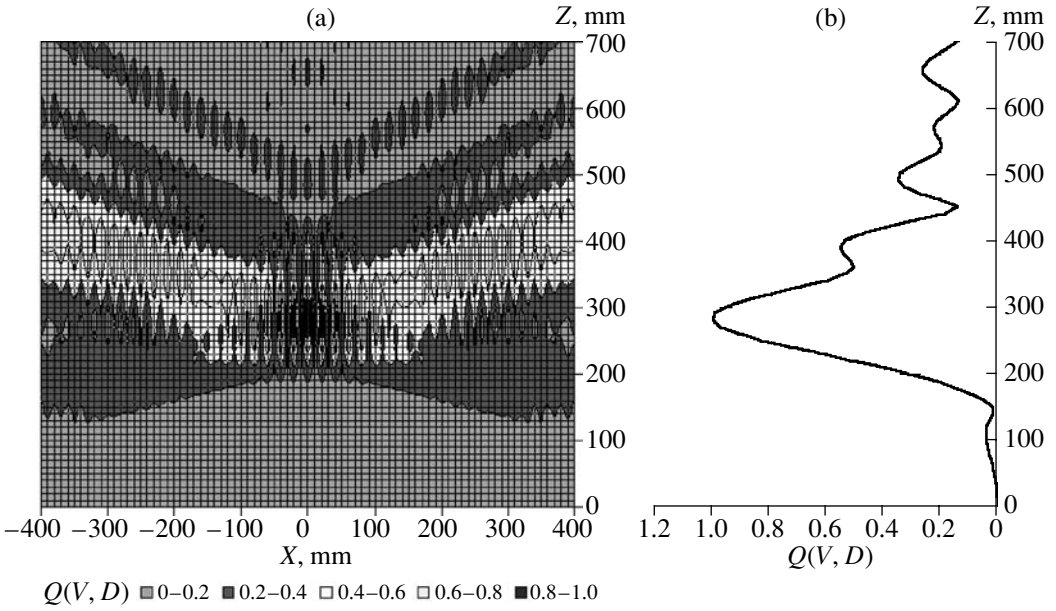

Fig. 4. (a) Acoustic image of the reflector at a frequency of 40 kHz and (b) the values of functional $Q(V, D)$ at $x = 0$.

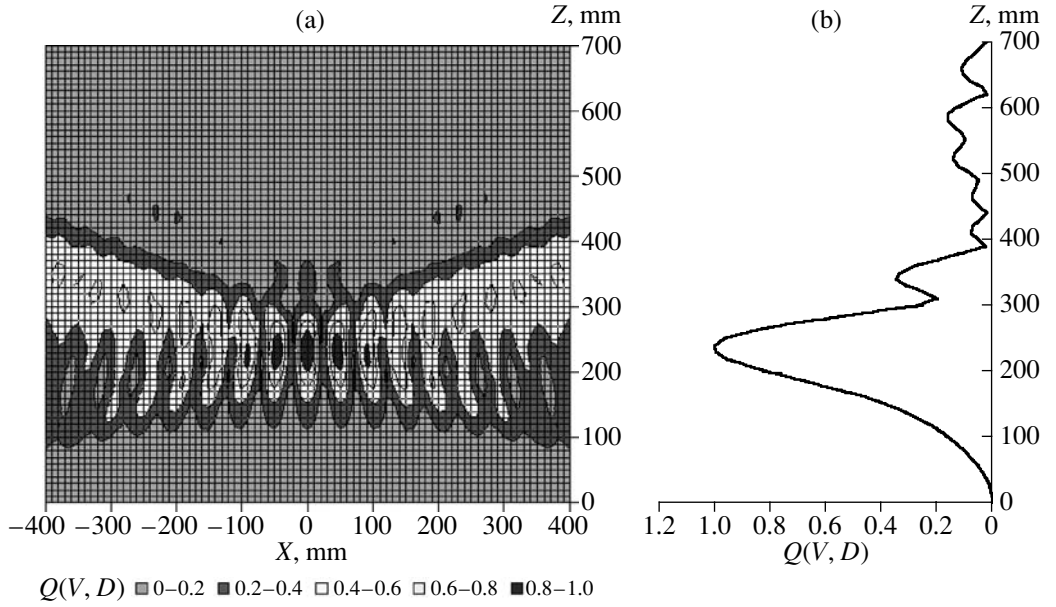

Fig. 5. (a) Acoustic image of the reflector at a frequency of 60 kHz and (b) the values of functional $Q(V, D)$ at $x = 0$.

clamp. As seen from Fig. 8, at a frequency of 60 kHz, the functional retains its extremum at the point (0, 560), but the casing and cable of the hydrophone cease being acoustically transparent and begin manifesting themselves as an additional reflector positioned at a distance of 230 mm from the sensing element. At a frequency of 120 kHz (see Fig. 9), the effect of the casing and cable of the hydrophone can be interpreted as that of a reflector positioned at a distance of 170 mm from the sensing element. The effect of the clamp at a frequency of 120 kHz does not manifest itself because of the temporal selection of the direct signal and the signal reflected by the clamp.

The resulting images can be conveniently approximated by a simplified model in the form of a set of point reflectors. Let us place reflectors at the points corresponding to the maxima of the functional $Q(V, D)$ on the Z axis and, for each frequency, obtain a simplified hydrophone model in the form of a point active element

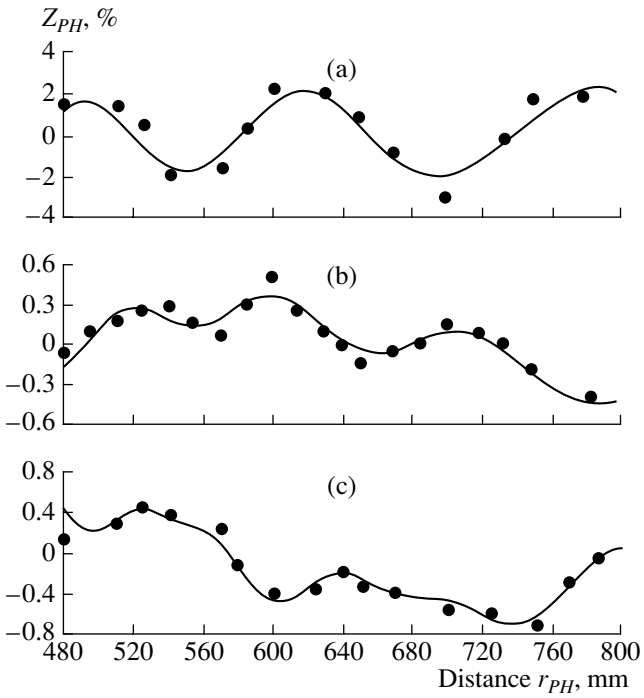

Fig. 6. Spatial dependences of the reduced transfer impedances of a spherical radiator and a B&K 8104 hydrophone at frequencies of (a) 30, (b) 40, and (c) 60 kHz. The dots represent the experiment, and the lines refer to the model.

with a receiving sensitivity of M'_H and a system of M point reflectors with reflection coefficients $\dot{w}_m$ and with known coordinates. When $w_m \ll 1$ ($m = 1, \ldots, M$), the squared magnitude of the reduced transfer impedance can be represented by the following function of $2M + 1$ unknown parameters Z_{PH_0}, w'_1, w''_1, …, w'_M, w''_M:

$$Z^2_{PH}(r) = Z^2_{PH_0}\left(1 + 2\sum_{m=1}^{M} y_m(r_{PH}) \times (w'_m \cos(k\upsilon_m(r_{PH})) - w''_m \sin(k\upsilon_m(r_{PH})))\right), \quad (8)$$

where

$$\upsilon_m = r_{PRm} + r_{RmH} - r_{PH},$$

$$y_m(r_{PH}) = \frac{r_{PH}}{r_{PRm} + r_{RmH}},$$

$$w'_m = \mathrm{Re}(\dot{w}_m), \quad w''_m = \mathrm{Im}(\dot{w}_m), \quad m = 1, \ldots, M.$$

One can easily verify that the problem of determining the unknowns in the expression for $Z^2_{PH}(r)$ is reduced to the well-known problem of optimal linear filtering for the measurement equation

$$\Re_0 + \sum_{m=1}^{M} \Re'_m y_m(r_{PH_i})\cos(k\upsilon_m(r_{PH_i})) - \sum_{m=1}^{M} \Re''_m y_m(r_{PH_i})\sin(k\upsilon_m(r_{PH_i})) = \Im_i + \varepsilon_i,$$

where ε_i is a random error,

$$\Im_i = Z^2_{PH}(r)_i,$$

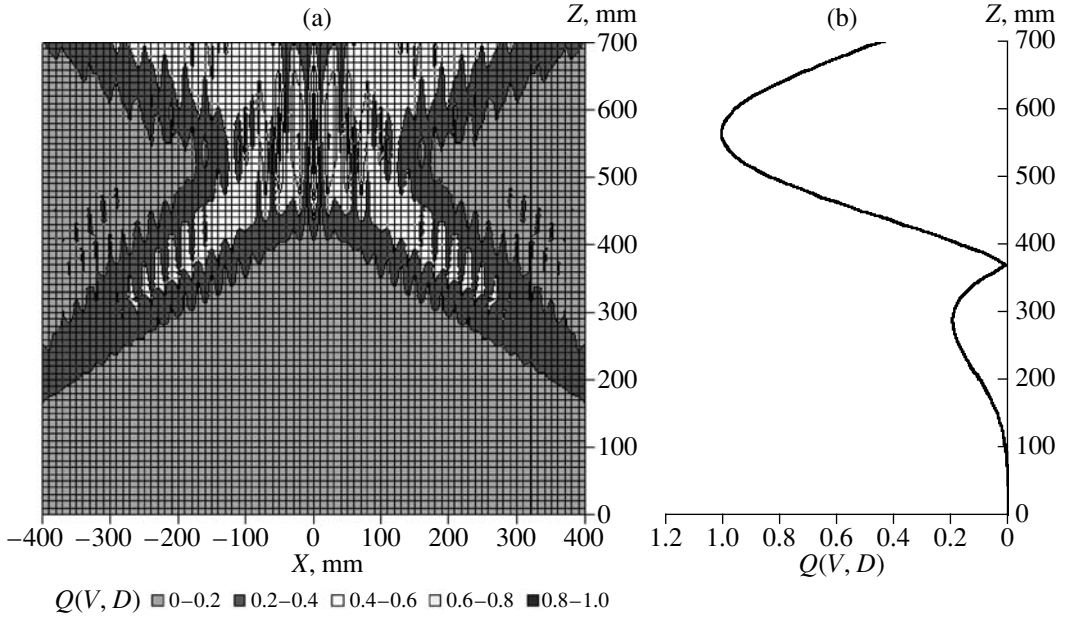

Fig. 7. (a) Acoustic image of the reflecting surface of the B&K 8104 hydrophone at a frequency of 40 kHz and (b) the values of functional $Q(V, D)$ at $x = 0$.

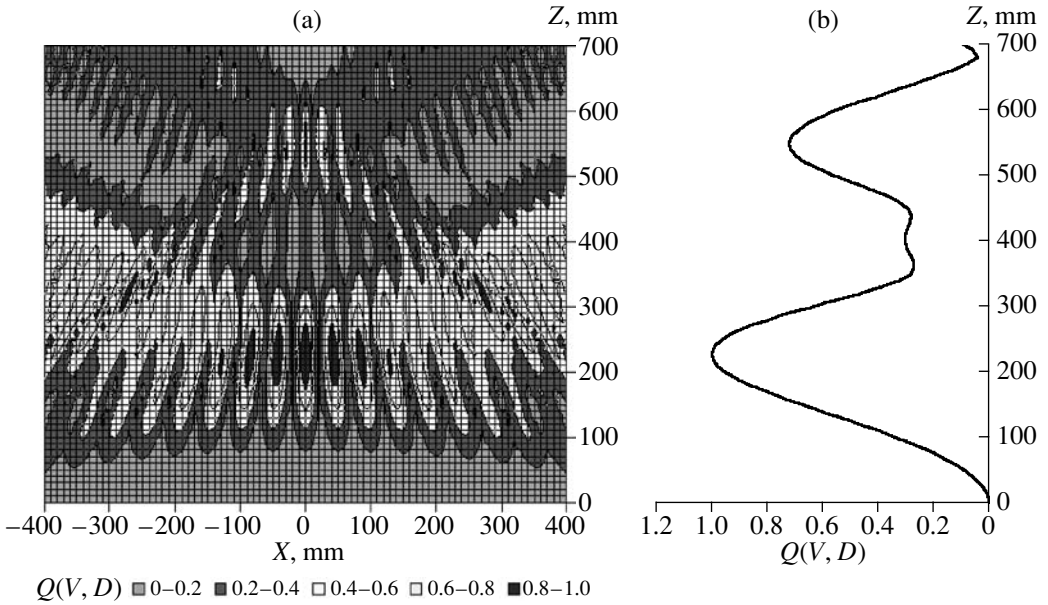

Fig. 8. (a) Acoustic image of the reflecting surface of the B&K 8104 hydrophone at a frequency of 60 kHz and (b) the values of functional $Q(V, D)$ at $x = 0$.

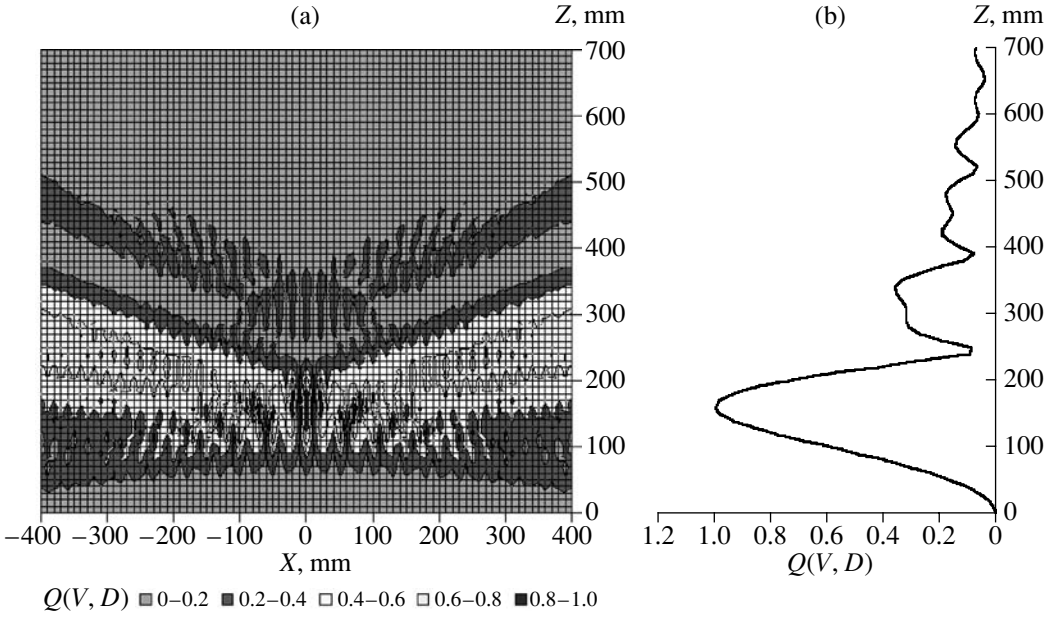

Fig. 9. (a) Acoustic image of the reflecting surface of the B&K 8104 hydrophone at a frequency of 120 kHz and (b) the values of functional $Q(V, D)$ at $x = 0$.

and the components of the vector of unknown parameters have the form

$$\Re_0 = Z_{PH_0}^2,$$

$$\Re'_m = 2w'_m Z_{PH_0}^2,$$

$$\Re''_m = 2w''_m Z_{PH_0}^2.$$

Let us consider more closely the case of estimating the parameters of the reduced transfer impedance with allowance for the indeterminacy δ in distances between the centers of the active elements of transducers, r_{PH_i}. Assume that the transducers are placed at distances d_{PH_i} from each other, and the values of the distances are chosen arbitrarily but are uniquely determined (e.g.,

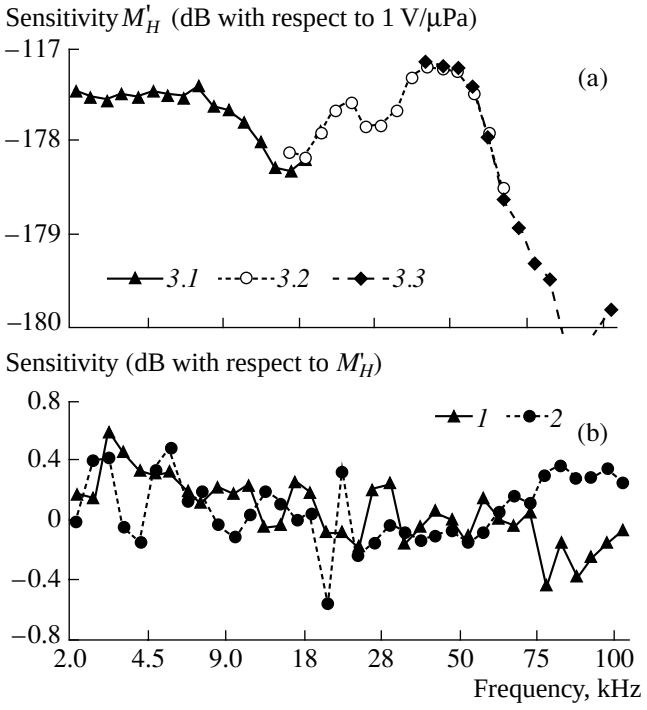

Fig. 10. Results of calibration of the H 52-50 hydrophone in a free field (a) with the use of the proposed procedure and (b) with the conventional technique.

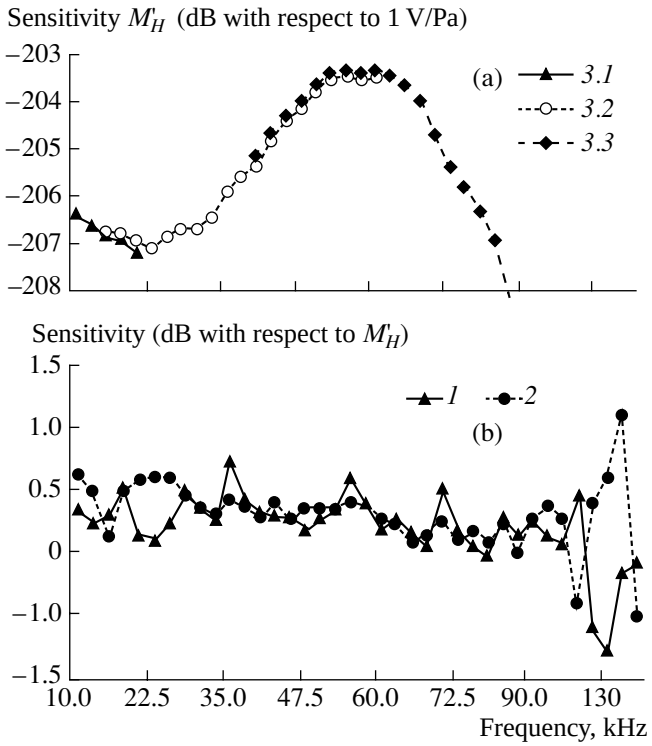

Fig. 11. Results of calibration of the B&K 8104 hydrophone in a free field (a) with the use of the proposed procedure and (b) with the conventional technique.

as the distance between the points of suspension of the hydrophone and the radiator). Taking into account that $\delta = d_{PH_i} - r_{PH_i}$ and assuming that $\delta \ll d_{PH_i}$, we obtain the following expression for $Z^2_{PH}(d)$:

$$Z^2_{PH}(d) = Z^2_{PH}(r) + 2\frac{\delta}{d_{PH} - \delta}Z^2_{PH}(r).$$

Then, the measurement equation can be reduced to the form convenient for solving by the iteration technique:

$$\Re_0 + \sum_{m=1}^{M} \Re'_m y_m(d_{PH_i} - \delta)\cos(k\upsilon_m(d_{PH_i} - \delta))$$
$$- \sum_{m=1}^{M} \Re''_m y_m(d_{PH_i} - \delta)\sin(k\upsilon_m(d_{PH_i} - \delta)) \qquad (9)$$
$$+ \tilde{\delta}\frac{2\Im_i}{d_{PH_i}} = \Im_i + \eta_i,$$

where

$$\Im_i = Z^2_{PH}(d)_i,\ \eta_i = \frac{(r_i - \delta)}{r_i}\varepsilon_i.$$

At the first iteration, the estimates $\Re_0$, $\Re'_1$, $\Re''_1$, …, $\Re'_M$, $\Re''_M$, $\tilde{\delta}$ are calculated under the assumption that $\delta = 0$. At each subsequent iteration, the solutions to Eq. (9) are determined by replacing δ by the value $\tilde{\delta}$ obtained at the preceding iteration. As a simple criterion of termination, we can use the convergence of estimates $\tilde{\delta}$ to a constant value.

After the termination of the iteration procedure, the values of Z_{PH_0} and Z_{PH_∞} are calculated by the formulas

$$Z_{PH_0} = \sqrt{\Re_0},$$

$$Z_{PH_\infty} = \sqrt{\Re_0 + \sum_{m=1}^{M}(\Re'_m\cos(kr_{RmH}) - \Re''_m\sin(kr_{RmH}))}.$$

The reduced transfer impedances Z_{PT_0}, Z_{PT_∞}, Z_{TH_0}, and Z_{TH_∞} are determined in the same way. The proposed method allows one to determine the values of the reduced transfer impedance of the active elements of transducers, Z_{PH_0}, and the reduced transfer impedance of transducers in the far-field zone, Z_{PH_∞}, as well as to calculate the dependence of the reduced transfer impedance on the distance between the transducers, $Z_{PH}(r)$. In Figs. 2 and 6, the solid lines represent the approximations of the spatial dependences of the

reduced transfer impedances, which were obtained from Eq. (8) with the substitution of the estimates of the unknown parameters determined by solving the measurement equation. These approximations based on modeling the reflecting hydrophone surface as a set of point reflectors agree well with the experimental data.

After the values of Z_{PH_0}, Z_{PH_∞}, Z_{PT_0}, Z_{PT_∞}, Z_{TH_0}, and Z_{TH_∞} are determined, the receiving sensitivity of the active element of the hydrophone under calibration, M'_H, can be calculated by the formula

$$M'_H = \left(\frac{2r_0}{pf}\frac{Z_{PH_0}Z_{TH_0}}{Z_{PT_0}}\right)^{1/2}. \quad (10)$$

The formula for calculating the sensitivity of the hydrophone, M_H, with allowance for the effect of its structure takes the form

$$M_H = \left(\frac{2r_0}{pf}\frac{Z_{PH_\infty}Z_{TH_\infty}}{Z_{PT_\infty}}\right)^{1/2}.$$

Figures 10 and 11 show the results of calibrating H 52–50 and B&K 8104 hydrophones in a free field in a laboratory hydroacoustic tank by the method described above. Curves *3.1–3.3* represent the values of M'_H obtained from Eq. (10) in three frequency subbands. In each of these subbands, different types of auxiliary transducers were used, and zones of overlapping of the calibration frequencies were provided (see the regions of overlapping of curves *3.1–3.3*). For the H 52–50 hydrophone, the frequency subbands were 2–20, 16–65, and 40–100 kHz (curves *3.1–3.3*, respectively). For the B&K 8104 hydrophone, the frequency subbands were 10–20, 15–60, and 40–150 kHz (curves *3.1–3.3*, respectively). The overlapping frequencies were chosen to be in the regions where the frequency dependence of the hydrophone's sensitivity had pronounced features. The results of calibration that were obtained with different types of auxiliary transducers differ at the overlapping frequencies by no more than 0.07 dB for H 52–50 and 0.16 dB for the B&K 8104 (in the zones of frequency overlapping, curves *3.1–3.3* in Figs. 10a and 11a practically coincide). The frequency dependences of M'_H obtained for both hydrophones are relatively smooth and exhibit a monotonic behavior. In contrast to the results typical of conventional calibration methods, these dependences exhibit no jumplike fluctuations at neighboring frequencies, which testifies to the reliability of the results of our measurements and to the correctness of the proposed procedure. The results of calibrations performed according to the conventional technique using formula (1) are shown in Figs. 10b and 11b (in decibels relative to the values of M'_H, curves *1* and *2*). Curves *1* and *2* were obtained using two different reference setups realizing the standard procedure of the reciprocity method in a free field. The results represented by curves *2* were obtained with fixed distances between the transducers. Curves *1* represent the results of calibration with the electric transfer impedances being determined as the average values of the results of measurements performed with two different distances between the transducers. The values of hydrophone sensitivity obtained for both setups noticeably differ from the values of M'_H. The difference in the results reaches 0.6 dB for the H 52–50 and 1.2 dB for the B&K 8204. The behavior of curves *1* and *2* in Figs. 10b and 11b is of irregular character and exhibits the influence of measurement errors caused by the distortions of the acoustic field in the hydroacoustic tank. This conclusion is most evident for the H 52–50 hydrophone in the low-frequency region, where the frequency characteristic of sensitivity is almost uniform (see Fig. 10a).

The study described above showed that the proposed procedure makes it possible to considerably reduce the errors caused by the distortions of the acoustic field and by the indeterminacy in the distances between the centers of the active elements of transducers. One can also expect that the proposed procedure should considerably slacken the requirements imposed by the dimensions of hydroacoustic tanks on the calibration of large-size hydroacoustic measurement means.

REFERENCES

1. A. E. Isaev, *Precise Calibration of Hydrophones in Laboratory Water Tank* (Proc. Inst. of Acoustics, UK, 2003), Vol. 25, Part 1.
2. *Calibration of Hydrophones*, IEC STANDARD Publication No. 565 (International Electrotechnical Commission, Geneva, 1977).
3. A. M. Enyakov, S. M. Likhachev, V. A. Platonov, *et al.*, Izmer. Tekh., No. 6, 63 (2000).
4. K. Rasmussen, *Acoustic Center of Condenser Microphones* (Acoustics Laboratory, Technical Univ. of Denmark, 1973), Report No. 5.

Translated by E. Golyamina

Acoustical Physics, Vol. 50, No. 5, 2004, pp. 544–551. Translated from Akusticheskiĭ Zhurnal, Vol. 50, No. 5, 2004, pp. 638–645.

Reflection and Refraction of Acoustic Waves at the Boundary between a Magnetoacoustic Material and a Dielectric

M. M. Karpuk*, D. A. Kostyuk, Yu. A. Kuzavko***, and V. G. Shavrov*****

**Politechnika Koszalinska, ul. Raclawicka 4, Koszalin, 75-620 Poland*

***Brest State Technical University, ul. Moskovskaya 267, Brest, 224017 Belarus*

****Institute of Radioengineering and Electronics, Russian Academy of Sciences, ul. Mokhovaya 18, Moscow, 103907 Russia*

e-mail: kuzavko@newmail.ru

Received September 3, 2002

Abstract—Reflection and refraction of longitudinal and transverse acoustic waves at a plane boundary between an antiferromagnet and a dielectric are studied. The antiferromagnet is assumed to have an easy-plane anisotropy and to be in the state near the orientational phase transition in the magnetic field. A possibility of controlling the angles of the wave-type transformation upon reflection and the refraction angles, as well as all four coefficients of the wave transformation upon reflection and refraction, by the magnetic field is demonstrated. Conditions for the formation of the critical angles of internal reflection and the effect of the magnetic field on their values are specified. A possibility of the radiation of a grazing wave into the material bulk in the vicinity of the phase transition is analyzed. *© 2004 MAIK "Nauka/Interperiodica".*

If a plane acoustic wave is incident on a boundary between two isotropic solids, two waves arise on both sides of the boundary in the general case [1]. In this paper, we study the reflection of an elastic wave at the boundary between a magnet and a dielectric, where both the dielectric and the magnetic crystal are assumed to be isotropic in their elastic and magnetoelastic properties. It is necessary to note that, in magnetically ordered crystals, the magnetoelastic interaction effectively grows as the orientational phase transition is approached and leads to a change in the spectrum of long-wave transverse acoustic oscillations from linear to quadratic at the point of orientational phase transition [2]. In this case, an anisotropy of dynamic elastic moduli, which causes a reduction of the velocity of longitudinal sound and especially the velocity of transverse sound (its experimentally measured change was up to 50% in hematite [3]), arises near the orientational phase transition even for a magnetic material isotropic in its elastic and magnetoelastic properties.

Earlier, the reflection of magnetoacoustic waves from a free surface of a semi-infinite antiferromagnetic crystal with an easy-plane anisotropy, which was in the state near the orientational phase transition in magnetic field $\vec{H}$ applied in the basic *xy* plane of the crystal ($\vec{H} \parallel \hat{y}$, the point of the orientational phase transition is determined by the condition $H = 0$), was studied in [4]. For the aforementioned magnet with a strong decrease in sound velocity near the orientational phase transition and for other magnets with this property, we will use the term "magnetoacoustic materials." The most typical examples of such materials easily grown in the form of massive crystals are antiferromagnets like hematite (α-Fe_2O_3), iron borate ($FeBO_3$), ferromagnets like dysprosium (Dy) and terbium (Tb), and intermetallic compounds with heavy rare-earth elements of the type R–Mn_2Ge_2 (R = Gd, Tb, Dy, Ho, Er, and Tm) [5]. Here, we consider the case where the surface of a magnetoacoustic material borders not the vacuum but a semi-infinite dielectric half-space. In this case, one should expect new specific features of magnetoacoustic wave propagation in such a structure.

Let us give an expression for the elastic component of free energy of the antiferromagnet mentioned above [2]:

$$F_{2y} = \frac{1}{2}\lambda_2 u_{2,ii}^2 + \mu_2 u_{2,ik}^2 - 2\mu_2\zeta u_{2,xy}^2, \qquad (1)$$

where λ_2 and μ_2 are the Lame coefficients for the magnetoacoustic material; $u_{2,ik}$ is the elastic strain tensor; $\zeta = \dfrac{\varepsilon_{me}^2}{\varepsilon_{1\hat{k}}^2}$ is the parameter of magnetoelastic coupling; $\varepsilon_{me} = g\sqrt{2H_E H_{me}}$ is the magnetoelastic gap in the spin wave spectrum; g is the gyromagnetic ratio; $\varepsilon_{1\hat{k}} = \sqrt{\Theta_N^2(ak)^2 + \varepsilon_M^2 + \varepsilon_{me}^2}$ is the energy of low-frequency magnons; $\varepsilon_M = g\sqrt{H(H + H_D)}$ is the magnetic part of the gap that vanishes at the point of orientational phase transition ($H = 0$); H_E, H_D, and H_{me} are the effective exchange, Dzyaloshinski, and magnetostriction fields,

respectively; Θ_N is the Néel temperature; $\vec{k}$ is the wave vector; and a is the lattice constant. The acoustic properties of the dielectric are described by first two terms in Eq. (1).

The values of the material constants for the compound substances of the structure to be calculated are as follows [6]: for quartz, $s_{1l} = 5000$ m/s, $s_{1t} = 3800$ m/s, and $\rho_1 = 2650$ kg/m^3; for hematite, $s_{2l} = 6760$ m/s, $s_{2t} = 4200$ m/s, $\rho_2 = 5290$ kg/m^3, $H_E = 9.2$ MOe, $H_D = 22$ KOe, and $H_{me} = 0.63$ Oe. Proceeding from these data, we estimate the magnetoelastic part of the gap: $\omega_{me} = \varepsilon_{me}/\hbar = 34$ GHz; i.e., within the frequency range $\omega \ll \omega_{me}$ of real ultrasonic transducers, the following approximation is valid: the dynamics of the spin system is not considered in the explicit form and its effect upon the acoustic system is reduced to the respective renormalization of the elastic dynamic moduli or, what is the same, to the renormalization of the velocities of longitudinal (*LA*) and transverse (*TA*) sound, $\tilde{s}_{2l}$ and $\tilde{s}_{2t}$, in the magnetoelastic material. We ignore the attenuation of ultrasonic waves [7, 8].

Using the expressions for the free energy of the dielectric and the magnetoelastic material, it is easy to obtain wave equations for mechanical displacements. Trying the solutions to these equations in the form of plane harmonic waves, we obtain the following expressions for the *TA* and *LA* velocities [4]:

$$\tilde{s}_{2t} = \sqrt{\frac{\mu_2}{\rho_2}(1 - \zeta\cos^2 2\alpha)}, \tag{2}$$

$$\tilde{s}_{2l} = \sqrt{\frac{\lambda_2 + 2\mu_2}{\rho_2}(1 - n\zeta\sin^2 2\alpha)}, \tag{3}$$

where the angle α is measured with respect to the negative direction of the y axis counterclockwise; $s_{2t} = \sqrt{\frac{\mu_2}{\rho_2}}$ and $s_{2l} = \sqrt{\frac{\lambda_2 + 2\mu_2}{\rho_2}}$ are the *TA* and *LA* velocities far from the orientational phase transition, respectively; and $n = \frac{\mu_2}{\lambda_2 + 2\mu_2} = \frac{s_{2t}^2}{s_{2l}^2}$. In the dielectric, $s_{1t} = \sqrt{\frac{\mu_1}{\rho_1}}$ and $s_{1l} = \sqrt{\frac{\lambda_1 + 2\mu_1}{\rho_1}}$, respectively.

Let *LA* be incident under the angle α to the normal to the boundary ($y = 0$) of the dielectric ($y > 0$) from the magnetoelastic material ($y < 0$). It generates two reflected waves (*LA* and *TA*) and two refracted ones (*LA* and *TA*). In the case of plane harmonic waves, the elastic displacements u_i can be represented in the form (see Fig. 1)

$$\begin{pmatrix} u^I_{2l,x} \\ u^I_{2l,y} \end{pmatrix} = u^I_{2l0}\begin{pmatrix} \sin\alpha \\ \cos\alpha \end{pmatrix}\exp[i(k^I_{2l}x\sin\alpha + k^I_{2l}y\cos\alpha - \omega^I_{2l}t)], \tag{4}$$

$$\begin{pmatrix} u^R_{2l,x} \\ u^R_{2l,y} \end{pmatrix} = u^R_{1l0}\begin{pmatrix} \sin\alpha \\ -\cos\alpha \end{pmatrix}\exp[i(k^R_{2l}x\sin\alpha - k^R_{2l}y\cos\alpha - \omega^R_{2l}t)], \tag{5}$$

$$\begin{pmatrix} u^R_{2t,x} \\ u^R_{2t,y} \end{pmatrix} = u^R_{2t0}\begin{pmatrix} \cos\beta \\ \sin\beta \end{pmatrix}\exp[i(k^R_{2t}x\sin\beta - k^R_{2t}y\cos\beta - \omega^R_{2t}t)], \tag{6}$$

$$\begin{pmatrix} u^T_{1l,x} \\ u^T_{1l,y} \end{pmatrix} = u^T_{1l0}\begin{pmatrix} \sin\gamma \\ \cos\gamma \end{pmatrix}\exp[i(k^T_{1l}x\sin\gamma + k^T_{1l}y\cos\gamma - \omega^T_{1l}t)], \tag{7}$$

$$\begin{pmatrix} u^T_{1t,x} \\ u^T_{1t,y} \end{pmatrix} = u^T_{1t0}\begin{pmatrix} -\cos\delta \\ \sin\delta \end{pmatrix}\exp[i(k^T_{1t}x\sin\delta + k^T_{1t}y\cos\delta - \omega^T_{1t}t)], \tag{8}$$

where u_0 and ω are the wave amplitude and frequency.

The boundary conditions, which are the continuity of the normal components of the mechanical stress tensor T_{iy} and the elastic strain tensor u_i, in this case can be written in the form [4]

$$T^I_{2l,iy} + T^R_{2l,iy} + T^R_{2t,iy} = T^T_{1t,iy} + T^T_{1l,iy}, \tag{9}$$

$$u^I_{2l,i} + u^R_{2l,i} + u^R_{2l,i} = u^T_{1t,i} + u^T_{1l,i}. \tag{10}$$

Here, the indices *I*, *R*, and *T* correspond to the incident, reflected, and transmitted waves and $i = x, y$. From boundary conditions (9) and (10) with the substitution of Eqs. (4)–(8) and the stress tensor $T_{ij} = \frac{\partial F}{\partial u_{ij}}$, it follows that, at any time moment t, $\omega^I_{2l} = \omega^R_{2l} = \omega^R_{2t} = \omega^T_{1t} = \omega^T_{1l} = \omega$ and, at any point of the plane $y = 0$, $k^I_{2l,x} =$

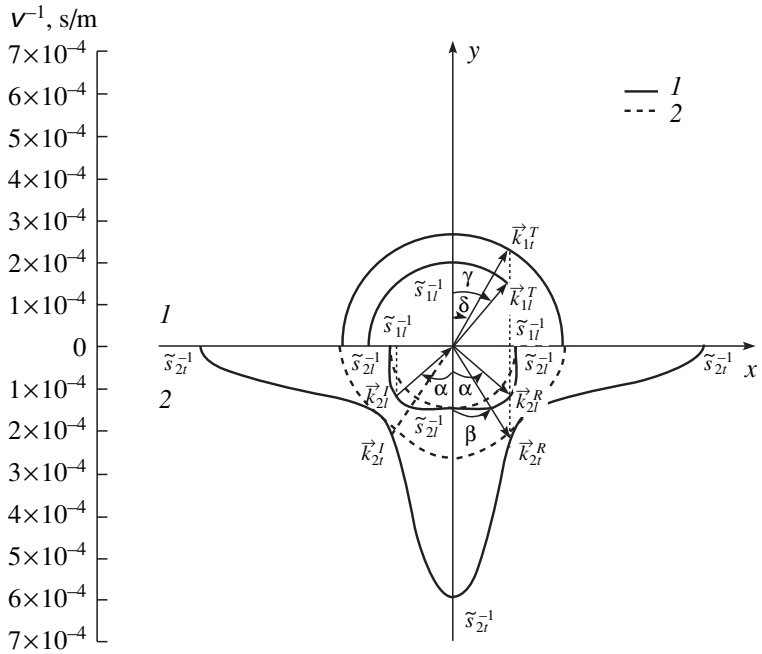

Fig. 1. Geometrical construction of wave vectors for the incident *LA* wave, the reflected *LA* and *TA* waves, and the refracted *LA* and *TA* waves at the hematite–quartz boundary for $H = 0.1$ (solid line) and 2 KOe (dashed line). The vector represented by a dashed line corresponds to the case of incidence of a transverse *TA* wave.

$k^R_{2l,x} = k^R_{2t,x} = k^T_{1l,x} = k_x$. Hence, the directions of wave propagation are determined by the relations

$$\frac{\sin\alpha}{\tilde{s}_{2l}(\alpha)} = \frac{\sin\beta}{\tilde{s}_{2t}(\beta)} = \frac{\sin\gamma}{s_{1l}} = \frac{\sin\delta}{s_{1t}} \qquad (11)$$

and can also be determined graphically on the basis of this expression proceeding from the geometrical construction of the surfaces of inverse phase velocities for all waves, as is demonstrated in Fig. 1.

From Eq. (11), taking into account Eqs. (2) and (3), we determine the expressions for the angles of the wave transformation:

$$\sin^2\beta = \frac{4\zeta n\sin^2\alpha(1+\cos^2\alpha) - 1 + \sqrt{(4\zeta n\sin^2\alpha(1+\cos^2\alpha)-1)^2 - 16\zeta(1-\zeta)n^2\sin^4\alpha}}{8\zeta n\sin^2\alpha}, \qquad (12)$$

$$\sin^2\gamma = b\frac{\sin^2\alpha}{1-\zeta n\sin^2 2\alpha}, \qquad (13)$$

$$\sin^2\delta = c\frac{\sin^2\alpha}{1-\zeta n\sin^2 2\alpha}, \qquad (14)$$

where $b = s^2_{1l}/s^2_{2l}$ and $c = s^2_{1t}/s^2_{2l}$.

According to Eqs. (12)–(14), Fig. 2 gives the dependences of the reflection angle β and the refraction angle γ on the angle of incidence α for different degrees of closeness of the magnetoacoustic material to the point of orientational phase transition. One can see from the figures that, by changing the external magnetic field $\vec{H}$, it is possible to control the reflection angle for the transformed *TA* and also the refraction angles for *LA* and *TA* arising in the dielectric.

After substituting Eqs. (4)–(8) into Eqs. (9) and (10), it is possible to determine the amplitude coefficient of reflection for the incident *LA* wave, $R_{ll} = u^R_{2l0}/u^I_{2l0}$; the coefficient of its transformation into *TA* in the case of its reflection, $R_{lt} = u^R_{2t0}/u^I_{2l0}$; the coefficient of its transmission into the dielectric, $T_{ll} = u^T_{1l0}/u^I_{2l0}$; and the coefficient of its transformation into TA in the case of its refraction, $T_{lt} = u^T_{1t0}/u^I_{2l0}$. All these four parameters can be determined by the Gaussian method

from the system of linear equations corresponding to the boundary conditions given by Eqs. (9) and (10):

$$\begin{cases} \mu_2(1-\zeta)\tilde{s}_{2l}^{-1}(\alpha)\sin 2\alpha R_{ll} \\ +\mu_2(1-\zeta)\tilde{s}_{2t}^{-1}(\beta)\cos 2\beta R_{lt} \\ +\mu_1 s_{1l}^{-1}\sin 2\gamma T_{ll} - \mu_1 s_{1t}^{-1}\cos 2\delta T_{lt} \\ = \mu_2(1-\zeta)\tilde{s}_{2l}^{-1}(\alpha)\sin 2\alpha, \\ -(\lambda_2 + 2\mu_2\cos^2\alpha)\tilde{s}_{2l}^{-1}(\alpha)R_{ll} + \mu_2\tilde{s}_{2t}^{-1}(\beta)\sin 2\beta R_{lt} \\ +(\lambda_1 + 2\mu_1\cos^2\gamma)s_{1l}^{-1}T_{ll} + \mu_1 s_{1t}^{-1}\sin 2\delta T_{lt} \\ = (\lambda_2 + 2\mu_2\cos^2\alpha)\tilde{s}_{2l}^{-1}(\alpha), \\ -\cos\alpha R_{ll} + \sin\beta R_{lt} - \cos\gamma T_{ll} - \sin\delta T_{lt} = -\cos\alpha, \\ \sin\alpha R_{ll} + \cos\beta R_{lt} - \sin\gamma T_{ll} + \cos\delta T_{lt} = -\sin\alpha. \end{cases} \quad (15)$$

Since the solution to Eqs. (15) for R_{ll}, R_{lt}, T_{ll}, and T_{lt} is awkward, we do not give it here. The system of Eqs. (15) was solved numerically for specific layered structures. In particular, Figs. 3 and 4 present the results of calculations for a quartz–hematite structure with different degrees of closeness of hematite to the point of orientational phase transition. Note that, in the cases of normal ($\alpha = 0°$) and grazing ($\alpha = 90°$) incidence of the wave, no wave-type transformations take place.

Analysis of Eqs. (12)–(14) shows that two critical angles of incidence $\alpha_{l,1cr}$ and $\alpha_{l,2cr}$ can exist. Starting from these angles, at $\alpha > \alpha_{l,1cr}$, *LA* begins to propagate along the boundary between the mediua, and at $\alpha > \alpha_{l,2cr}$, *TA* in the dielectric behaves in the same way. The critical angles are determined by the relations following from Eqs. (13) and (14):

$$\alpha_{l,1cr}^{\pm} = \arcsin\sqrt{\frac{b + 4\zeta n \pm \sqrt{(b+4\zeta n)^2 - 16\zeta n}}{8\zeta n}}. \quad (16)$$

The angle $\alpha_{l,2cr}^{\pm}$ is determined by Eq. (16) with the substitution $b \longrightarrow c$. Since $0 \le \alpha_{1,2cr} \le \pi/2$, $0 \le \zeta \le 1$, and $0 \le n \le 1/2$, the existence conditions for the critical angles are rather rigid. For the angles $\alpha_{l,1cr}$ and $\alpha_{l,2cr}$ to exist, the expressions $(b + 4\zeta n)^2 \ge 16\zeta n$ and $(c + 4\zeta n)^2 \ge 16\zeta n$ must be satisfied and the radicand of the arcsin function in Eq. (16) must be nonnegative and must not exceed unity. In the case of the quartz–hematite structure under consideration, the angles $\alpha_{l,1cr}^{-}$ and $\alpha_{l,2cr}^{\pm}$ do not exist. The critical angle $\alpha_{l,1cr}^{+}$ appears starting from $\zeta = 0.277$. It is equal to $\alpha_{l,1cr}^{+} = 49.2°$ and increases with the growth of the magnetoelastic coupling coefficient ζ.

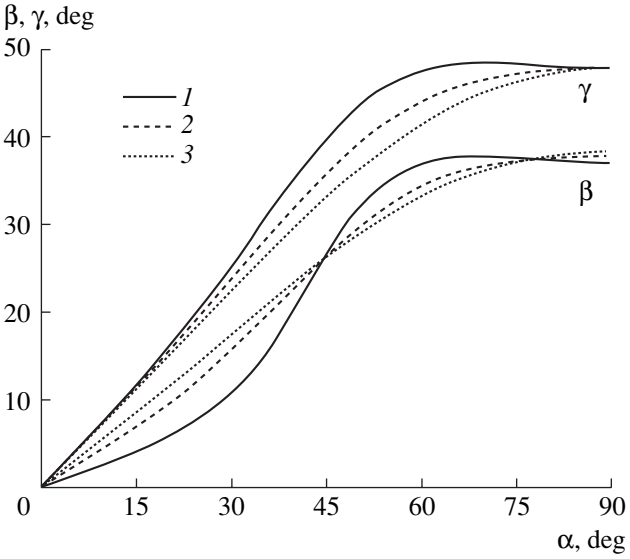

Fig. 2. Dependences of the reflection angle β for the *TA* wave and the refraction angle γ for the *LA* wave on the angle of incidence α of the *LA* wave. Here and in the subsequent figures, H = (*1*) 0.1, (*2*) 0.5, and (*3*) 2 KOe.

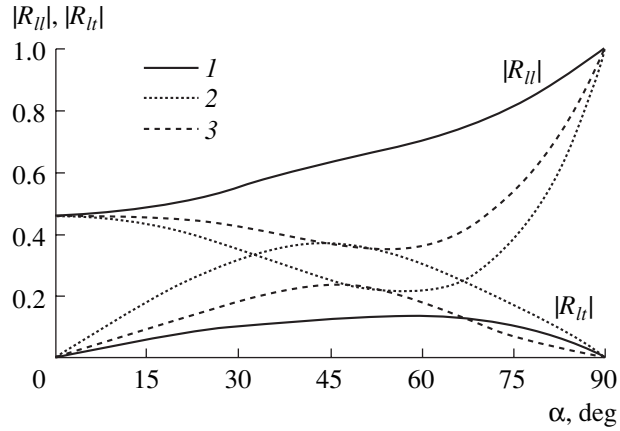

Fig. 3. Dependences of the modulus of the reflection coefficient R_{ll} for the *LA* wave and the modulus of the transformation coefficient R_{lt} of the *LA* wave into the *TA* wave at the hematite–quartz boundary on the angle of incidence α.

The reflected *TA* wave in the case of grazing incidence of the *LA* on the boundary has the following expression for the limiting angle:

$$\beta_{\lim} = \arcsin\sqrt{\frac{4\zeta n - 1 + \sqrt{(4\zeta n - 1)^2 - 16\zeta(1-\zeta)n^2}}{8\zeta n}}. \quad (17)$$

It follows from this expression that, at $\zeta = 0$, $\beta_{\lim} = n$, while, at $\zeta = 1$, $\beta_{\lim} = \arcsin[1 - 4/n]^{1/2}$ ($n > 1/4$) or $\beta_{\lim} = 0$ ($n < 1/4$). At $\zeta = 0$, the limiting angles $\gamma_{\lim} =$

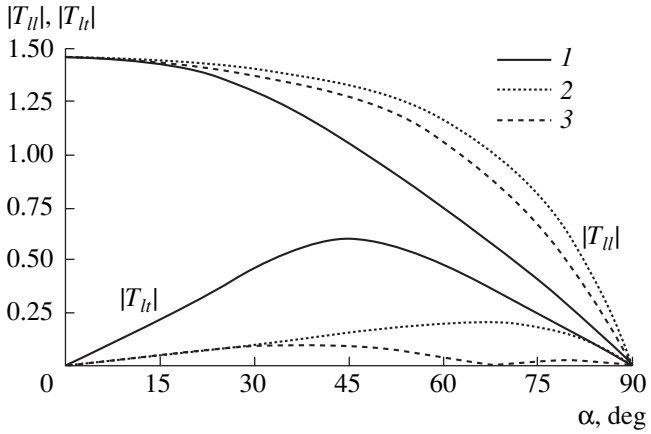

Fig. 4. Dependences of the modulus of the transmission coefficient T_{ll} for the *LA* wave and the modulus of the transformation coefficient T_{lt} of the *LA* wave into the *TA* wave at the hematite–quartz boundary on the angle of incidence α.

$\arcsin b^{1/2}$ and $\delta_{\lim} = \arcsin c^{1/2}$ for *LA* and *TA* also exist in the dielectric. For the example under consideration, $\beta_{\lim} = 42.7°$, $\gamma_{\lim} = 53°$, and $\delta_{\lim} = 38°$.

It is necessary to note that, in the general case, at arbitrary b and c, we formally obtain $\sin^2\gamma = b\sin^2\alpha/(1 - \zeta n\sin^2 2\alpha) \geq 1$ starting from $\alpha > \alpha_{l,\,1cr}$. This means that *LA* becomes inhomogeneous and the phase velocity of its propagation along the boundary is equal to $\tilde{s}'_{1l} = s_{1l}/\sin\alpha$. The inhomogeneity of the wave means that the wave amplitude decreases exponentially ($u_{1l} \sim e^{y/\Lambda_{1l}}$) and the penetration depth can be determined from the expression

$$\Lambda_{1l} = \frac{s_{1l}}{\omega\sqrt{\sin^2\gamma - 1}}. \tag{18}$$

Elastic displacements in the transmitted *LA* are described by Eq. (7) with the corresponding substitution $\cos\gamma = i\sqrt{\sin^2\gamma - 1}$, a phase difference of 90° arising between the projections x and y. The *LA* becomes quasi-longitudinal, since the elastic displacement in it oscillates not linearly but circumscribes an ellipse. It is necessary to note that the reflected and refracted *TA* also have an elliptical polarization. Everything said above is also valid for the *TA* starting from $\alpha > \alpha_{l,\,2cr}$ with the corresponding substitutions in the above expressions.

According to Eq. (15), Figs. 3 and 4 present angular dependences for the moduli of the coefficients R_{ll}, R_{lt}, T_{ll}, and T_{lt} for the quartz–hematite structure for different degrees of closeness of the state of the magnetoacoustic material to its point of orientational phase transition. This demonstrates the possibility of controlling all indicated parameters of wave reflection, refraction, and transformation by the external magnetic field. Since the critical angles (if they exist) also depend on the field, an additional possibility of controlling the total wave reflection at the boundary arises.

In the case of the incidence of a transverse magnetoacoustic wave from the magnetoacoustic material on the boundary with a dielectric, the situation is somewhat different (see Fig. 1). The elastic displacements in the incident wave can be written as

$$\begin{pmatrix} u^I_{2t,\,x} \\ u^I_{2t,\,y} \end{pmatrix} = u^I_{2t0}\begin{pmatrix} -\cos\alpha \\ \sin\alpha \end{pmatrix}\exp[i(k^I_{2t}x\sin\alpha + k^I_{2t}y\cos\alpha - \omega^I_{2t}t)], \tag{19}$$

and in the reflected *LA* and *TA*, they are determined by Eqs. (5) and (6) with the permutation $\alpha \longrightarrow \beta$ and $\beta \longrightarrow \alpha$.

The boundary conditions have the form of Eqs. (9) and (10) with the substitution $T^I_{2l,\,iy} \longrightarrow T^I_{2t,\,iy}$ and $u^I_{2l,\,i} \longrightarrow u^I_{2t,\,y}$. The directions of wave propagation are determined by the expressions

$$\frac{\sin\alpha}{\tilde{s}_{2t}(\alpha)} = \frac{\sin\beta}{\tilde{s}_{2l}(\beta)} = \frac{\sin\gamma}{s_{1l}} = \frac{\sin\delta}{s_{1t}}. \tag{20}$$

Taking into account Eqs. (2) and (3), from Eq. (20) we determine the expressions for the angles of wave transformation:

$$\sin^2\beta = \frac{4\zeta\sin^2\alpha + n(1 - \zeta\cos^2 2\alpha) - \sqrt{(4\zeta\sin^2\alpha + n(1 - \zeta\cos^2 2\alpha))^2 - 16\zeta\sin^4\alpha}}{8\zeta\sin^2\alpha}, \tag{21}$$

$$\sin^2\gamma = \frac{b'\sin^2\alpha}{1 - \zeta\cos^2 2\alpha}, \tag{22}$$

$$\sin^2\delta = \frac{c'\sin^2\alpha}{1 - \zeta\cos^2 2\alpha}, \tag{23}$$

where $b' = \frac{s_{1l}^2}{s_{2t}^2} = \frac{b}{n}$ and $c' = \frac{s_{1t}^2}{s_{2t}^2} = \frac{c}{n}$.

According to Eqs. (21)–(23), Fig. 5 presents the dependences of the reflection angle β and the refraction angle γ on the angle of incidence α of *TA* for various degrees of closeness of the magnetoacoustic material to the point of orientational phase transition. The coefficient of reflection of the incident *TA* wave $R_{tt} = \frac{u_{2t0}^R}{u_{2t0}^I}$, the coefficient of its transformation into a reflected *LA* wave $R_{tl} = \frac{u_{2l0}^R}{u_{2t0}^I}$, the coefficient of its transmission into the dielectric $T_{tt} = \frac{u_{1t0}^T}{u_{2t0}^I}$, and the coefficient of its transformation into *LA* at refraction $T_{tl} = \frac{u_{1l0}^T}{u_{2t0}^I}$ are determined by the Gaussian method from solving the set of equations

$$\begin{cases} -\mu_2(1-\zeta)\tilde{s}_{2t}^{-1}(\alpha)\sin 2\alpha R_{tt} \\ +\mu_2(1-\zeta)\tilde{s}_{2l}^{-1}(\beta)\cos 2\beta R_{tl} \\ +\mu_1 s_{1l}^{-1}\sin 2\gamma T_{tl} - \mu_1 s_{1t}^{-1}\cos 2\delta T_{tt} \\ = -\mu_2(1-\zeta)\tilde{s}_{2t}^{-1}(\alpha)\sin 2\alpha, \\ \mu_2\tilde{s}_{2t}^{-1}(\alpha)\sin 2\alpha R_{tt} \\ +(\lambda_2 + 2\mu_2\cos^2\beta)\tilde{s}_{2l}^{-1}(\beta)R_{tl} \\ +(\lambda_1 + 2\mu_1\cos^2\gamma)s_{1l}^{-1}T_{tl} + \mu_1 s_{1t}^{-1}\sin 2\delta T_{lt} \\ = \mu_2\tilde{s}_{2t}^{-1}(\alpha)\sin 2\alpha, \\ \sin\alpha R_{tt} - \cos\beta R_{tl} - \cos\gamma T_{tl} - \sin\delta T_{tt} = -\sin\alpha, \\ -\cos\alpha R_{tt} + \sin\beta R_{tl} - \sin\gamma T_{tl} + \cos\delta T_{tt} = \cos\alpha. \end{cases} \quad (24)$$

Figures 6 and 7 show the results of the numerical calculation of these coefficients for a hematite–quartz

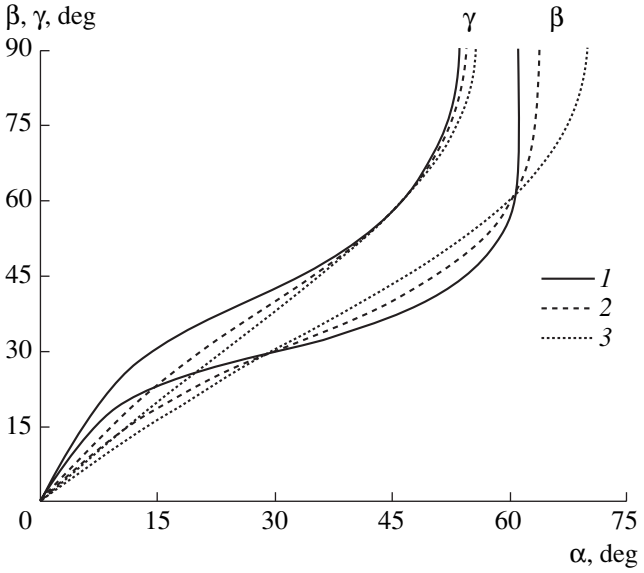

Fig. 5. Dependences of the reflection angle β and the refraction angle γ for the *LA* wave on the angle of incidence α of the *TA* wave.

structure for different degrees of closeness of the magnetoacoustic material to the point of orientational phase transition. In contrast to the case considered first, where the phase is constant, here its behavior is fairly complex (see Fig. 6). Three critical angles of incidence $\alpha_{t,\,cr}$, $\alpha_{t,\,1cr}$, and $\alpha_{t,\,2cr}$ can exist in this case. They are determined by the expressions following from Eqs. (21)–(23):

$$\alpha_{t,\,cr} = \arcsin\sqrt{\frac{4\zeta n - 1 + \sqrt{1 - 8\zeta n + 16\zeta n^2}}{8\zeta n}}. \quad (25)$$

Two angles $\alpha_{t,\,1cr}$ and $\alpha_{t,\,2cr}$ are expressed with the help of Eq. (25) by replacing n with $b' = s_{1l}^2/s_{2t}^2 = b/n$ and $c' = s_{1t}^2/s_{2t}^2 = c/n$, respectively.

At $\alpha > \alpha_{t,\,cr}$, the longitudinal magnetoacoustic wave becomes a grazing wave. Moreover, starting from $\zeta \geq \zeta^* = (n/(4-n))^2$ and for the angles of incidence $\alpha > \alpha_{t,\,cr}^*$, where

$$\alpha_{t,\,cr}^* = \arcsin\sqrt{\frac{\zeta(1+n) - \sqrt{\zeta} + \sqrt{\zeta(1-\sqrt{\zeta}(1+n))^2 + \zeta(1-\zeta)n^2}}{2\zeta n}} \quad (26)$$

(which follows from the negativity of the discriminant in Eq. (21)), the *LA* is again radiated into the bulk. Formally, at $\alpha > \alpha_{t,\,cr}$, $\sin^2\beta > 1$. This means that the *LA* wave becomes inhomogeneous and its phase velocity is directed along the boundary and equal to $s_{2l}' = s_{2l}/\sin\beta$. The depth of penetration of the wave into the magnetoacoustic material is $\Lambda_{2l} = \frac{s_{2l}}{\omega\sqrt{\sin^2\beta - 1}}$. The elastic displacements in the wave are described by Eq. (5) with the substitutions $\alpha \longrightarrow \beta$ and $\cos\beta = i\sqrt{\sin^2\beta - 1}$. In

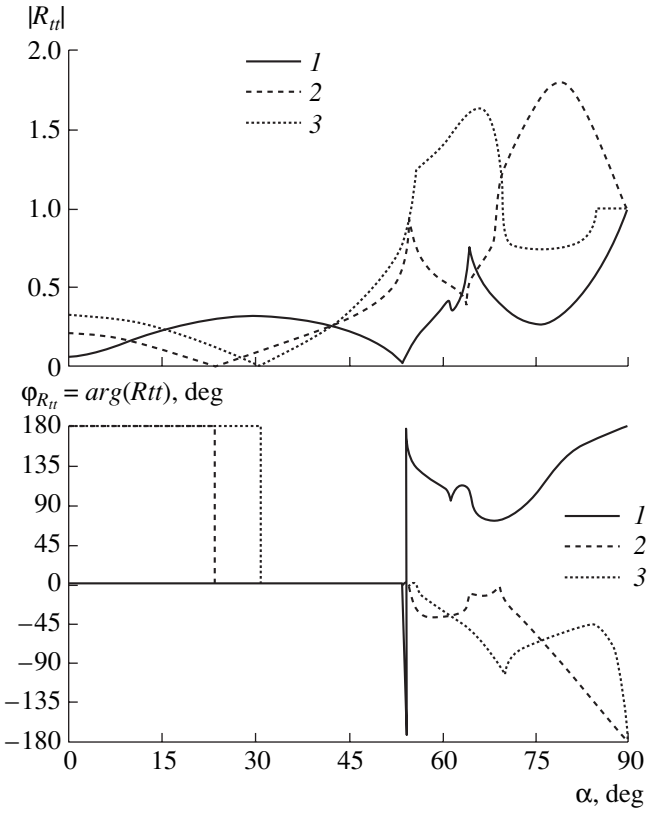

Fig. 6. Dependences of the modulus $|R_{tt}|$ and phase $\varphi_{R_{tt}}$ of the reflection coefficient R_{tt} of the *TA* wave at the hematite–quartz boundary on the angle of incidence α.

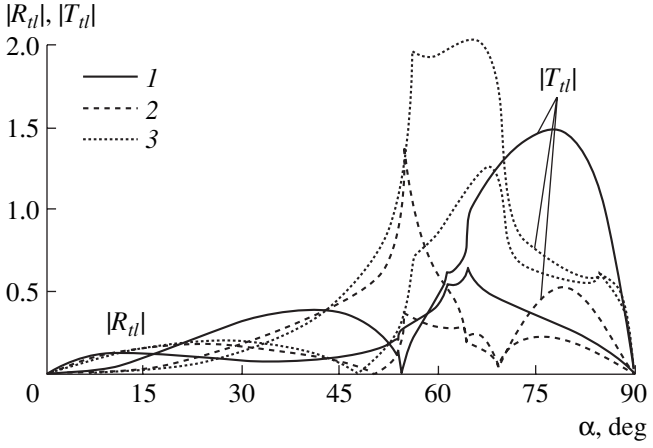

Fig. 7. Dependences of the moduli of the coefficients of transformation, R_{tl} and T_{tl}, of the *TA* wave into the *LA* wave at the hematite–quartz boundary on the angle of incidence α.

this case, a phase shift of 90° arises between them. Further, at $\alpha > \alpha^*_{t,cr}$, $\sin^2\beta$ also becomes complex; i.e., $\sin^2\beta = \bar{x} + i\bar{y} = \sqrt{\bar{x}^2 + \bar{y}^2}\, e^{i\psi_1}$, where $\bar{x} = [4\zeta\sin^2\alpha + n(1 - \zeta\cos^2 2\alpha)]/(8\zeta\sin^2\alpha)$, $\bar{y} = \{[4\zeta\sin^2\alpha + n(1 - \zeta\cos^2 2\alpha)]^2 - 16\zeta\sin^4\alpha\}^{1/2}/(8\zeta\sin^2\alpha)$, and $\tan\psi_1 = \bar{y}/\bar{x}$. Then, $\cos^2\beta = 1 - \bar{x} - i\bar{y} = \sqrt{(1-\bar{x})^2 + \bar{y}^2}\, e^{i\psi_2}$, where $\tan\psi_1 = -\bar{y}/(1 - \bar{x})$. The elastic displacements in the wave are described by the expressions

$$u^R_{2l} = u^R_{2l0}\begin{pmatrix} \sqrt[4]{\bar{x}^2 + \bar{y}^2}\, e^{i\psi_1/2} \\ -\sqrt[4]{(1-\bar{x})^2 + \bar{y}^2}\, e^{i\psi_2/2} \end{pmatrix}$$
$$\times \exp\{k_{2l} - x\sqrt[4]{\bar{x}^2 + \bar{y}^2}\sin(\psi_1/2)$$
$$+ y\sqrt[4]{(1-\bar{x})^2 + \bar{y}^2}\sin(\psi_2/2)\} \qquad (27)$$
$$\times \exp\{ik_{2l}x\sqrt[4]{\bar{x}^2 + \bar{y}^2}\cos(\psi_1/2)$$
$$- y\sqrt[4]{(1-\bar{x})^2 + \bar{y}^2}\cos(\psi_2/2)\}.$$

The first exponent determines the wave attenuation, which increases as the wave propagates, and is dissipation-free (without energy absorption by the media). It characterizes the structure of the new oscillation process, which is also concentrated near the boundary $y = 0$. The second exponent determines the propagation direction of the wave and its velocity:

$$\tan\beta' = \frac{\sqrt[4]{\bar{x}^2 + \bar{y}^2}}{\sqrt[4]{(1-\bar{x})^2 + \bar{y}^2}}\frac{\cos(\psi_1/2)}{\cos(\psi_2/2)},$$
$$s'_{2l} = s_{2l}\frac{\sin\beta'}{\sqrt[4]{(1-\bar{x})^2 + \bar{y}^2}\cos(\psi_2/2)}. \qquad (28)$$

Note that, in contrast to the grazing wave, the phase shift between the elastic components of displacement in the wave is not constant and begins to depend on the closeness of the magnetoacoustic material to the point of orientational phase transition.

The three critical angles indicated above are not always realized in specific structures. For example, for the quartz–hematite structure under consideration, taking into account $b' = 1.417$ and $c' = 0.819$, we determine $\alpha_{t,cr} = 42.7°$ at $\zeta = 0$ and $\alpha_{t,cr} = 40.5°$ at $\zeta = 1$, while the radiation of the grazing wave into the bulk starts at $\zeta > \zeta^* = 0.013$ with the incidence angle $\alpha^*_{t,cr}$ determined from Eq. (26). The critical angle $\alpha_{t,1cr}$ arises in a threshold way at $\zeta \geq 0.417$, reaching the value $\alpha_{t,1cr} = 43.6°$ at $\zeta = 1$. Further, the critical angle $\alpha_{t,2cr}$ exists always: $\alpha_{t,2cr} = 72°$ at $\zeta = 0$ and $\alpha_{t,2cr} = 62.7°$ at $\zeta = 1$.

From Figs. 6 and 7, one can see the possibility of controlling all indicated parameters of wave reflection, refraction, and transformation by the field more efficiently than in the case of the *LA* wave incidence. An interesting feature of the second case in comparison with the first case is the nontrivial behavior of the phase of the transformed wave. Since all three critical angles

depend on the field, additional opportunities arise for controlling the total wave reflection at the boundary.

ACKNOWLEDGMENTS

This work was supported in part by the Russian Foundation for Basic Research and the Belarussian Republican Foundation for Basic Research, project nos. F02R-076 and 02-02-81030 Bel2002_a.

REFERENCES

1. E. Dieulesaint and D. Royer, *Elastic Waves in Solids* (Wiley, New York, 1981; Nauka, Moscow, 1982).
2. E. A. Turov and V. G. Shavrov, Usp. Fiz. Nauk **140**, 429 (1983) [Sov. Phys. Usp. **26**, 593 (1983)].
3. E. A. Andryushchak, N. N. Evtikhiev, S. A. Pogozhev, and V. L. Preobrazhenskiĭ, Akust. Zh. **27**, 170 (1981) [Sov. Phys. Acoust. **27**, 93 (1981)].
4. Yu. A. Kuzavko and V. G. Shavrov, Akust. Zh. **39**, 1088 (1993) [Acoust. Phys. **39**, 572 (1993)].
5. Guo Guanghua, R. Z. Levitin, V. V. Snegirev, and D. V. Filippov, Fiz. Tverd. Tela (St. Petersburg) **43**, 477 (2001) [Phys. Solid State **43**, 496 (2001)].
6. Yu. Kuzavko, H. Roth, and V. Golovko, in *Proceedings of Workshop on Design Methodologies for Signal Processing* (Zakopane, Poland, 1996), p. 131.
7. Y. A. Kuzavko and M. M. Karpuk, in *Book of Abstracts of 17th International Congress on Acoustics* (Rome, 2001).
8. Y. A. Kuzavko and M. M. Karpuk, in *Book of Abstracts of 17th International Congress on Acoustics* (Rome, 2001).

Translated by M. Lyamshev

Acoustical Physics, Vol. 50, No. 5, 2004, pp. 552–561. Translated from Akusticheskiĭ Zhurnal, Vol. 50, No. 5, 2004, pp. 646–656.

On the Feasibility of Normal Wave Selection in a Shallow-Water Waveguide

B. G. Katznel'son*, S. A. Pereselkov*, and V. G. Petnikov**

**Voronezh State University, Universitetskaya pl. 1, Voronezh, 394693 Russia*
e-mail: katz@phys.vsu.ru
***Wave Research Center, General Physics Institute, Russian Academy of Sciences, ul. Vavilova 38, Moscow, 117942 Russia*
e-mail: petniko@kapella.gpi.ru

Received October 28, 2003

Abstract—Long-range propagation of low-frequency narrowband sound signals in the near-bottom acoustic channel with random inhomogeneities caused by internal waves and a rough bottom is investigated in the framework of numerical and field experiments. The feasibility of selecting the signal components corresponding to different normal waves is analyzed. The problem of selecting such components is considered for signals of long duration exceeding the characteristic time of the stationary state of the channel. © *2004 MAIK "Nauka/Interperiodica".*

INTRODUCTION

For the diagnostics of large-scale inhomogeneities on the sea shelf, various methods of low-mode acoustic tomography have been developed [1]. These methods are based on the measurements of propagation times of low-frequency (f = 100–400 Hz) acoustic signals corresponding to individual noninteracting normal waves (modes) of the near-bottom sound channel (acoustic waveguide) typical of the coastal regions of the ocean. The selection of mode signals on the basis of their travel times can be realized using single omnidirectional sources and receivers, i.e., using only the dispersion properties of the propagation channel. As a consequence of these properties, each normal wave propagates with its own group velocity. Such a method of signal selection is promising for practical use because of its simplicity, but its application can meet certain difficulties. The difficulties are related to, first, the high sound attenuation in the near-bottom channel, which leads to the disappearance of some normal waves; second, the specific features of waveguide dispersion in such a channel; and, third, the presence of regular and random inhomogeneities causing interaction and transformation of modes [2, 3]. The regular inhomogeneities are represented by the variations of the general bottom relief and by the changes in the vertical profile of sound velocity, which occur in the regions of frontal zones [2]. The random inhomogeneities are the sound velocity variations caused by internal wave fields. To random inhomogeneities, one should also add the small-scale bottom irregularities with a typical spatial scale of ≤100 m, which are clearly distinguished only with the use of a narrow-beam echo sounder. The sound attenuation, waveguide dispersion, and, especially, channel inhomogeneities have pronounced geographic features; i.e., their characteristics are quite different in different shallow-water regions. In this paper, in the framework of numerical and field experiments, we investigate the specific features of the long-range (several tens of kilometers) propagation of low-frequency narrowband ($\Delta f/f \cong 0.1$) sound signals in the near-bottom acoustic channel with random inhomogeneities, which is typical of the Barents Sea in the summer season.[1] For this channel, we analyze the feasibility of selecting the pulses of individual modes (the signal components corresponding to various normal waves). The problem of selecting these components is considered separately for signals of long duration exceeding the characteristic time T^* of the stationary state of the channel. (During the time T^*, the waveguide parameters can be considered as constant.) Note that the use of such signals for acoustic tomography is of fundamental significance, because it allows one to transmit acoustic signals of a high energy, thus increasing the limiting range of sounding, which is determined by the signal-to-noise ratio at the point of reception. Hence, an increase in energy can be realized not by increasing the radiation power but in a simpler and cheaper way.

[1] Similar investigations for the Barents Sea in the region of the polar front in the presence of regular inhomogeneities are described in [2].

1063-7710/04/5005-0552$26.00 © 2004 MAIK "Nauka/Interperiodica"

1. THE SOUND CHANNEL IN THE BARENTS SEA AND ITS CHARACTERISTICS AFFECTING THE RESOLUTION OF NORMAL WAVES

It is well known that the sound velocity field $c(r, z, t)$ (r is the horizontal coordinate in the cylindrical coordinate system related to the acoustic waveguide, z is the vertical coordinate (depth), and t is time) in the Barents Sea has a considerable space–time variability. It imples the typical changes in the vertical profile of sound velocity from season to season and from region to region. However, for the summer–autumn season, the sound velocity profile has some general features which manifest themselves in the presence of the upper layer of 10–20 m in thickness with a constant sound velocity in depth ($dc/dz = 0$), the thermocline, i.e., an intermediate layer with a considerable negative gradient ($dc/dz \ll 0$), and the lower layer, the thickest one, where the gradient is also negative but smaller in its absolute value ($dc/dz < 0$). These features are associated with the presence of the upper warm mixed layer of seawater, the underlying thermocline, and the basic near-bottom layer of the seawater whose temperature weakly grows as depth decreases. An example of the corresponding sound velocity profile, which was measured in the experiment described below, is shown in Fig. 1.

To describe the processes in such a waveguide, we use the expansion of the field in modes of an unperturbed waveguide with the mean sound velocity profile $c_0(z)$ ($c(r, z, t) = c_0(z) + \delta c(r, z, t)$, where $\delta c(r, z, t)$ is the perturbation of the sound velocity related to internal waves) that is constant along the track and the constant depth along the track H_0 ($H(r) = H_0 + h(r)$, where $h(r)$ is the bottom roughness). After solving numerically the Sturm–Liouville boundary problem for an unperturbed waveguide, it is easy to calculate the group velocities of normal waves $v_m^{gr} = d\omega/dq_m$ (ω is the cyclic frequency and $\xi_m(\omega) = q_m(\omega) + i\gamma_m/2$ is the propagation constant of the mth normal wave). The result of these calculations is shown in Fig. 2. In the calculations, the waveguide parameters correspond to those typical of the Barents Sea: the depth $H_0 = 120$ m, the sound velocity in the sea bottom $c_1 = 1750$ m/s, and the bottom density $\rho_1 = 1.9$ g/cm^3. The sound frequency was equal to $f = 240$ Hz. As indicated in Fig. 2, the sound channel has a group of normal waves with the smallest numbers and with almost the same values of v_m^{gr}. It is important that the group velocities of these waves depend on the number m in a nonmonotonic way. Note that similar dependences of the group velocity on the mode number also occur in other shallow-water regions of the ocean, for example, in the shelf zone near the Atlantic coast of the United States [4]. However, in the Barents Sea, the range of the group velocity variations is much narrower.

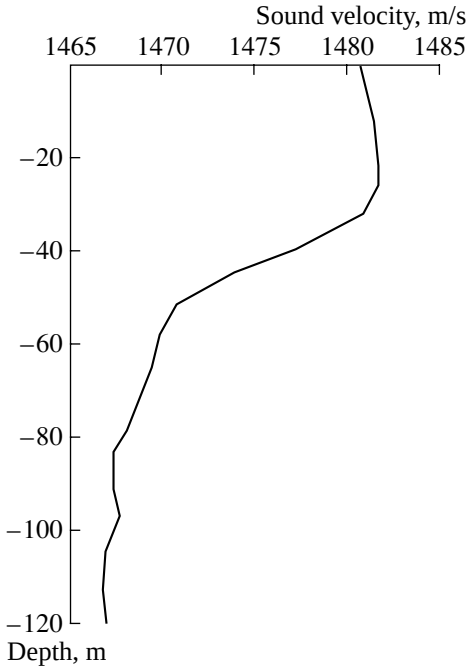

Fig. 1. Depth dependence of the sound velocity.

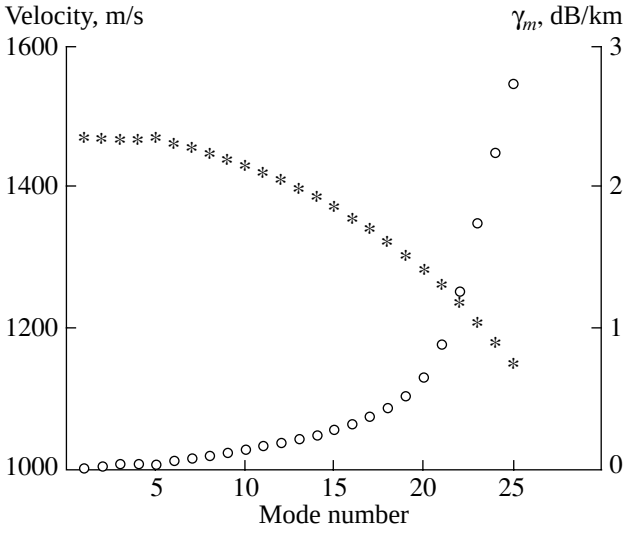

Fig. 2. Dependence of the group velocity (asterisks) and the attenuation coefficient (circles) on the mode number.

The attenuation coefficients of normal waves, γ_m, steeply grow with the mode number, which is caused by sound absorption in the sea bottom. For typical values of the coefficient $\alpha = 0.01$ that describes the imaginary part of the refractive index, n_1, in the sea bottom, $n_1 = \frac{c_0(H_0)}{c_1}\left(1 + i\frac{\alpha}{2}\right)$, and for the same waveguide parameters, the attenuation coefficients of normal waves are shown in Fig. 2.

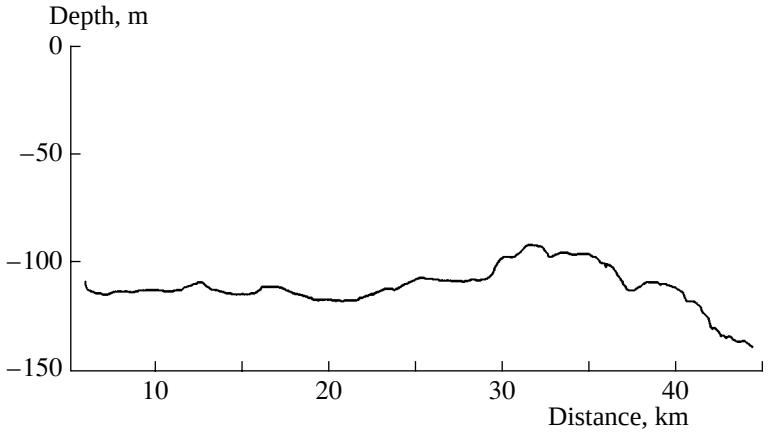

Fig. 3. Experimental dependence of the waveguide depth on distance.

An important parameter for estimating the feasibility of the temporal selection of normal waves in an acoustic waveguide is the interaction coefficient of modes, whose form depends on the transformation mechanism. Generally, this transformation may be caused by the following factors: the presence of volume inhomogeneities in the waveguide; the interaction of the reference modes, which depend on the range as a parameter, because of the insufficiently smooth variation of the general relief; and the presence of relatively small-scale variations of the bottom relief and the ocean surface.

The transformation coefficients corresponding to these mechanisms are different in these cases. For our situation, we consider the influence of only volume inhomogeneities caused by internal waves and the effect of the roughness of the bottom relief.

At present, no comprehensive investigations of random inhomogeneities in the Barents Sea have been carried out. Only results of single experiments are available for different regions of the Barents Sea where typical small-scale roughness of the bottom relief [5] and intense internal waves [6] were observed. These results are used in this paper to study the feasibility of the selection of normal waves in the Barents Sea.

2. FIELD AND NUMERICAL EXPERIMENTS ON THE PROPAGATION OF LOW-FREQUENCY TOMOGRAPHIC SIGNALS IN THE BARENTS SEA

Experimental investigations of the long-range propagation of tomographic signals were carried out at distances of several tens of kilometers in one of the regions of the Barents Sea in the summer season. The sea depth in the test region is shown in Fig. 3. As seen from this figure, the test region is characterized by a very rough bottom relief and a small-scale roughness. The sound velocity profile is shown in Fig. 1. In the course of the experiment, signals with hyperbolic frequency modulation were radiated in a frequency band $\Delta f = 20$ Hz with a carrier frequency $f = 240$ Hz. The duration of a signal was $T = 25.6$ s. The radiation of the signals was performed by a source, which was towed by the research vessel (RV) at a depth of $z_s = 40$ m. The signals were received by a vertical chain of hydrophones lowered from the other RV, as well as by a reference hydrophone fixed at a distance of 1 m from the source. The experimental data, namely, the signal envelopes at the output of an optimal correlation receiver, are shown in Fig. 4 for different depths of reception, z_r, and the distance between the source and the receiver $r_r = 40$ km. Figure 4 also shows the envelope of the signal received by the reference hydrophone. As is seen, due to the intermode dispersion (the difference in the group velocities of individual modes), the total duration of the signal received at a distance of 40 km exceeds the duration of the same signal received by the reference hydrophone. The processing of the experimental data showed that the duration of the received signal weakly depends on distance in the interval $\Delta r \cong 20$–40 km. However, the form of signal envelopes noticeably varies when the distance changes by 1 km. Examples of signal envelopes recorded in this experiment at different distances are given in [7].

For the interpretation of the experimental data, this experiment was modeled numerically. For calculations, the acoustic waveguide model described in Section 1 was used. The basic calculated quantity, as in a real experiment, was the envelope of the correlation function calculated with the use of the following relationship:

$$B(t) \cong \left| \int_{\Delta\omega} \Psi(r_r, z_r, \omega, t) |S(\omega)|^2 e^{-i\omega t} d\omega \right|. \qquad (1)$$

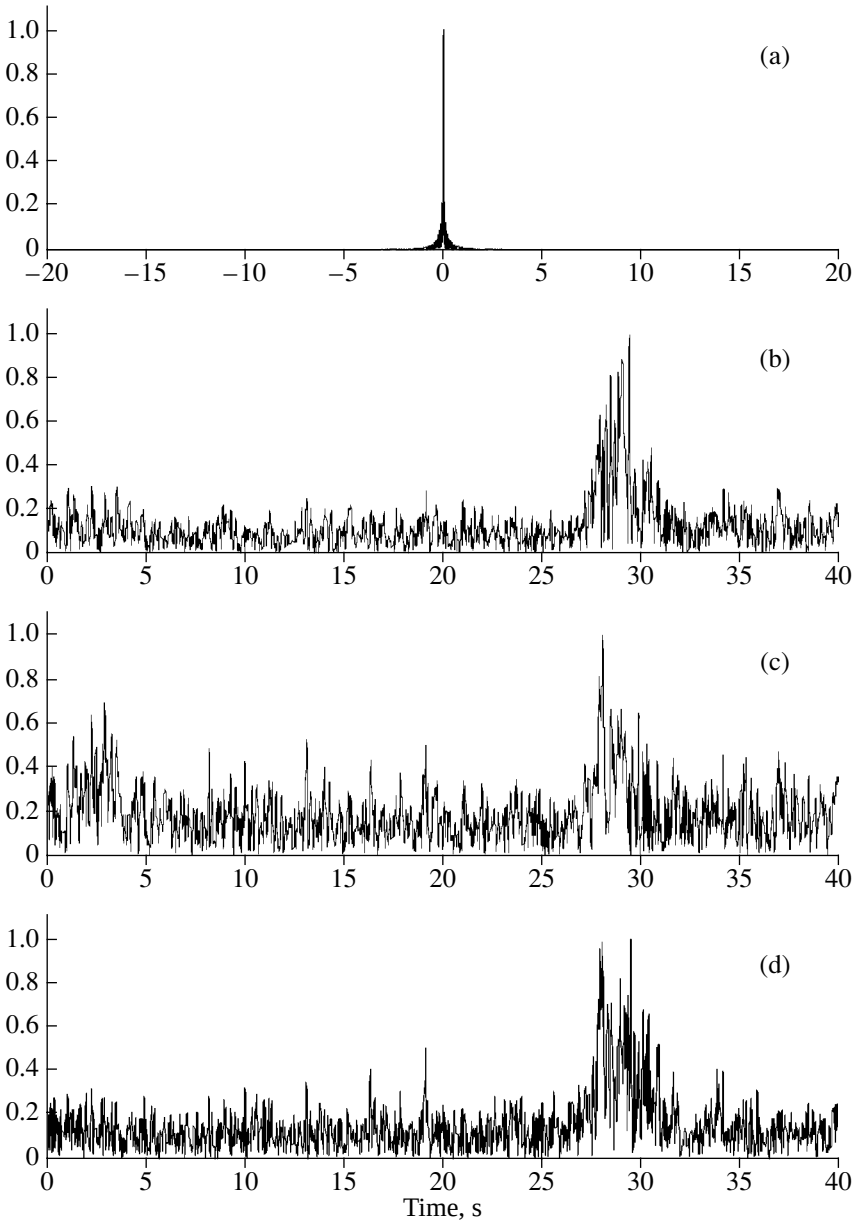

Fig. 4. Experimental results: (a) signal received at a distance of 1 m from the sound source and signals received at a distance of 40 km at the depths of (b) 45, (c) 60, and (d) 78 m.

Here, $\Psi(r, z, \omega, t)$ is the transfer function of the channel (Green's function). The dependence of the transfer function on time in Eq. (1) reflects the variations of the channel in time, which is significant in the modeling of signals of a long duration. However, it should be noted that Eq. (1) is approximate and it can be used for the calculation of the correlation function envelope only for rather slow variation of $\Psi(r, z, \omega, t)$ in time, i.e., for $t_1 \gg 1/\Delta f$, where t_1 is the characteristic time of the variation of the quantity $\Psi(r, z, \omega, t)$.

Now, we derive the basic equations for calculating $\Psi(r, z, \omega, t)$ in the presence of small perturbations $\delta c(r, z, t)$ and $h(r)$ related to internal waves and to the roughness of the bottom relief. In the case under consideration, the refractive index $n(r, z, t)$ of the water medium is determined as

$$\begin{aligned} n^2(r, z, t) &\cong n_0^2(z) + \mu(r, z, t) \\ &= c_0^2(0)/c_0^2(z) - 2\delta c(r, z, t)c_0^2(0)/c_0^3(z). \end{aligned} \tag{2}$$

The Helmholtz equation for a point source with the boundary conditions determines the Green's function in a cylindrically symmetric waveguide and has the form

$$\begin{aligned} \left[\frac{1}{r}\frac{\partial}{\partial r}\left(r\frac{\partial}{\partial r}\right) + \frac{\partial^2}{\partial z^2} + k^2(n_0^2(z) + \mu(r, z, t))\right]\Psi(r, z, \omega, t) \\ = -\delta(z - z_s)\frac{\delta(r)}{2\pi r}, \end{aligned} \tag{3}$$

$$\Psi|_{z=0} = 0; \tag{4}$$

$$\Psi|_{z=H_0+h^-} = \Psi|_{z=H_0+h^+},$$

$$\left.\frac{1}{\rho}\frac{\partial\Psi}{\partial n}\right|_{z=H_0+h^-} = \left.\frac{1}{\rho_1}\frac{\partial\Psi}{\partial n}\right|_{z=H_0+h^+}. \tag{5}$$

It is assumed that the source is located at the point with coordinates $(0, z_s)$, k is the wave number ($k = 2\pi f/c_0(0)$), and $\frac{\partial}{\partial n}$ is the normal derivative. Here and in what follows, the subscript "+" or "–" denotes the limit of a function as the vertical coordinate tends to the bottom surface from the bottom or water column, respectively. For small deviations of the surface, boundary conditions (5) can be rewritten as

$$\Psi^- - \Psi^+ = h\left(\frac{\partial\Psi^+}{\partial z} - \frac{\partial\Psi^-}{\partial z}\right),$$

$$\frac{\partial\Psi^-}{\partial z} - \eta\frac{\partial\Psi^+}{\partial z} \tag{6}$$

$$= -\frac{dh}{dr}\left(\frac{\partial\Psi^-}{\partial r} - \eta\frac{\partial\Psi^+}{\partial r}\right) - h\left(\frac{\partial^2\Psi^-}{\partial z^2} - \eta\frac{\partial^2\Psi^+}{\partial z^2}\right),$$

where $\eta = \rho/\rho_1$ (ρ is the density of seawater). Thus, instead of the boundary conditions on the curved surface, we have the boundary conditions at $z = H_0$.

We seek the transfer function as the expansion of interacting modes

$$\Psi(r, z, \omega, t) \approx \sum_{m=1}^{M} a_m(r, t)\frac{\psi_m(z, \omega)}{\sqrt{r}}, \tag{7}$$

where M is the number of normal energy waves and $\psi_m(z, \omega)$ are the eigenfunctions of the Sturm–Liouville boundary-value problem corresponding to the unperturbed conditions (without internal waves and with a flat bottom):

$$\frac{d^2\psi_m}{dz^2} + [k^2 n_0^2(z) - \xi_m^2]\psi_m = 0 \tag{8}$$

with the boundary conditions $\psi_m(0) = 0$, $\psi_m^- = \psi_m^+$, $\frac{\partial\psi_n^-}{\partial z} = \eta\frac{\partial\psi_n^+}{\partial z}$.

Substituting expansion (7) into Eq. (3) and taking into account Eqs. (6), we obtain a system of coupled equations describing the interaction of the normal waves at long distances from the sound source:

$$\frac{d^2 a_m}{dr^2} + \xi_m^2 a_m + \sum_l \frac{da_l}{dr}\frac{dh}{dr}(\eta - 1)\psi_l^-\psi_m^-$$

$$+ \sum_l \frac{d^2 a_l}{dr^2}h(1-\eta)\psi_l^-\psi_m^- \tag{9}$$

$$+ \sum_l a_l k^2 \int_0^\infty \psi_l \mu(r, z, t)\psi_m dz + \sum_l a_l h$$

$$\times\left\{\left(\frac{1}{\eta} - 1\right)\frac{\partial\psi_l^-}{\partial z}\frac{\partial\psi_m^-}{\partial z} + \psi_n^-\psi_m^-(k^2 n_0^2(H_0) - \eta k_1^2)\right\} = 0.$$

Here, k_1 is the wave number in the bottom ($k_1 = 2\pi f/c_1$). Note that the main problem in deriving system (9) is that we cannot differentiate term by term the field expansion in an infinite set of eigenfunctions. More precisely, in the term by term differentiation of series (7) with respect to z, an error is introduced which tends to zero with $h \longrightarrow 0$. Thus, the derivation of system (9) is not trivial, because it is necessary to take into account the terms of the order of h.

In the forward scattering approximation, the modal amplitudes can be represented as $a_m = C_m q_m^{-1/2} e^{iq_m r}$ assuming that coefficients $C_m(r, \omega, t)$ slowly vary with distance r. In this case, for calculating $\Psi(r, z, \omega, t)$, it is sufficient to solve the system of equations of the first order for the coefficients $C_m(r, \omega, t)$:

$$\frac{dC_m(r, \omega, t)}{dr} = -\frac{\gamma_m}{2}C_m(r, \omega, t)$$

$$+ i\sum_l^M \nu_{lm}(r, \omega, t)C_l(r, \omega, t)\exp[i(q_l - q_m)r] \tag{10}$$

with the initial conditions $C_m(0, \omega) = \psi_m(z_s, \omega)$.

In the case of a rough bottom, we have

$$\nu_{lm}(r) = \frac{h(r)}{2\sqrt{q_l q_m}}\left\{\left(\frac{1}{\eta} - 1\right)\frac{\partial\psi_l}{\partial z}(H_0)\frac{\partial\psi_m}{\partial z}(H_0)\right.$$

$$\left. + [(k^2 n_0^2(H_0) - q_l^2) - \eta(k_1^2 - q_l^2)]\psi_l(H_0)\psi_m(H_0)\right\} \tag{11}$$

$$+ \frac{i(dh/dr)q_l(1-\eta)}{2\sqrt{q_l q_m}}\psi_l(H_0)\psi_m(H_0).$$

Here and in what follows, the subscript "–" of the functions $\psi_{l,m}$ is omitted. For the numerical experiment, we use the realizations of $h(r)$ that were recorded in the field experiment (Fig. 3).

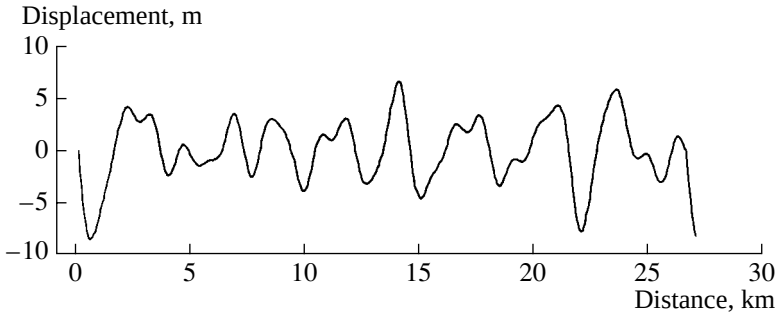

Fig. 5. Fragment of a realization of vertical displacements of liquid under the action of IWs.

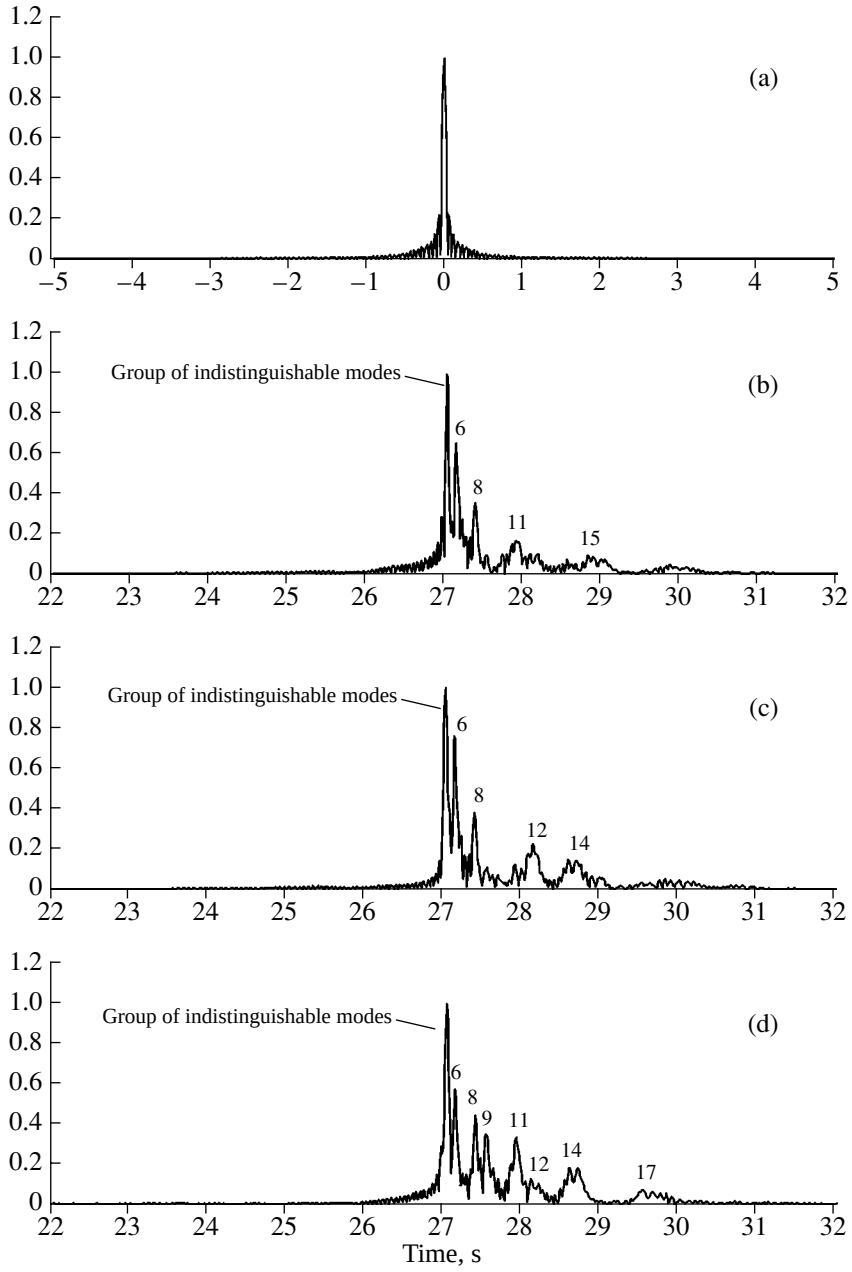

Fig. 6. Dependence $B(t)$ normalized by its maximal value in the absence of random inhomogeneities: (a) the autocorrelation function of the emitted signal; the distance is 40 km and the depth is z_r = (b) 45, (c) 60, and (d) 75 m.

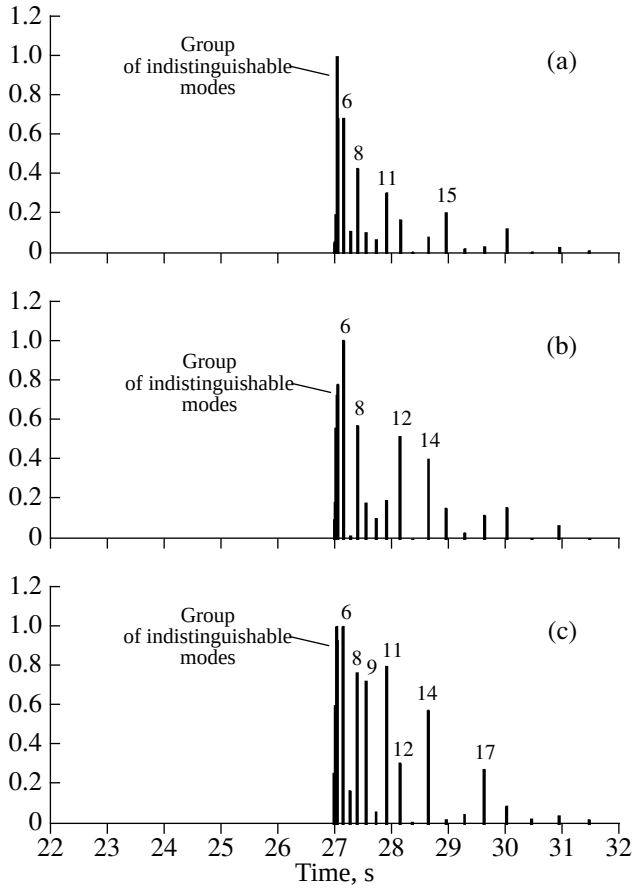

Fig. 7. Results of the numerical modeling of the mode signal propagation. The distance is 40 km, and the depth is z_r = (a) 45, (b) 60, and (c) 75 m.

For inhomogeneities related to internal waves, the coefficients are calculated by the formula

$$v_{lm}(r, \omega, t) = \frac{k^2}{2\sqrt{q_l(\omega)q_m(\omega)}}\int_0^H \mu(r, z, t)\psi_m(z, \omega)\psi_l(z, \omega)dz. \quad (12)$$

The quantity $\mu(r, z)$ is directly determined by the field of internal waves and is expressed as [2]

$$\mu(r, z, t) = -2QN^2(z)\varsigma(r, z, t), \quad (13)$$

where Q is the coefficient depending on the physical parameters of water (for the ocean, $Q \cong 2.4$ s^2/m), $N(z)$ is the buoyancy frequency, and $\varsigma(r, z, t)$ represents the vertical displacements of the particles of liquid in the field of internal waves (IWs). In the numerical experiment, the vertical displacements were calculated on the basis of the known experimental data [6] on the characteristics of internal waves in the Barents Sea. We used the realizations of trains of nonlinear intense IWs recorded in the experiment, as well as the calculated realizations of background internal waves with statistical characteristics obtained by analyzing the aforementioned data. In particular, in these calculations, we took into account that, in the Barents Sea, the spectrum of the background IWs decays with frequency as $\Omega^{-1.6}$. The vertical displacements caused by both intense nonlinear internal waves and background IWs at a depth of 40 m are shown in Fig. 5. It was assumed that such displacements exist along the whole acoustic track between the sound source and the receiver. It was also assumed that the field of the vertical displacements moves along the track toward the sound receiver with the speed v = 0.5 m/s typical of internal waves. At the same time, the displacements are assumed to occur synchronously over the whole depth, and the depth dependence of the displacement amplitude is described by the eigenfunction of the first mode of IWs. The latter assumption corresponds to the model of quasi-plane single-mode internal waves moving in a definite direction.

The results of the numerical experiment are shown in Figs. 6–10. Figure 6 exhibits the envelope of the correlation functions of signals at different depths in the absence of random inhomogeneities. As shown in Fig. 6, the structure of the envelope varies depending on the depth of reception. To determine a one-to-one correspondence between separate maxima of the curves in Fig. 6 and the numbers of normal waves in the waveguide, the propagation times of mode signals, $t_m = r/v_m^{gr}$, and their amplitudes $p_m = \left|\frac{\psi_m(z_s)\psi_m(z_r)}{\sqrt{\xi_m r}}\right| \exp(-\gamma_m r/2)$ were calculated. Separate vertical lines in Fig. 7 show the results. The length of each line corresponds to p_m, while its position on the time axis corresponds to t_m.

The envelopes of the correlation functions of signals are shown in Figs. 8–10. Figures 8 and 9 are calculated for distances of 40 and 200 km between the sound source and the receiver in the presence of internal waves. Figure 10 corresponds to the situation when a small-scale bottom roughness occurs along the track (r = 40 km).

3. A COMPARATIVE ANALYSIS OF EXPERIMENTAL AND CALCULATED RESULTS

A comparison of Figs. 6 and 7 shows that, in the absence of random inhomogeneities in the sound channel, at a distance of 40 km, a selection (by the propagation time) of mode signals corresponding to normal modes with sufficiently high numbers, from 7 to 17, is possible. The modes with the smallest numbers are indistinguishable when the relative band of emitted sig-

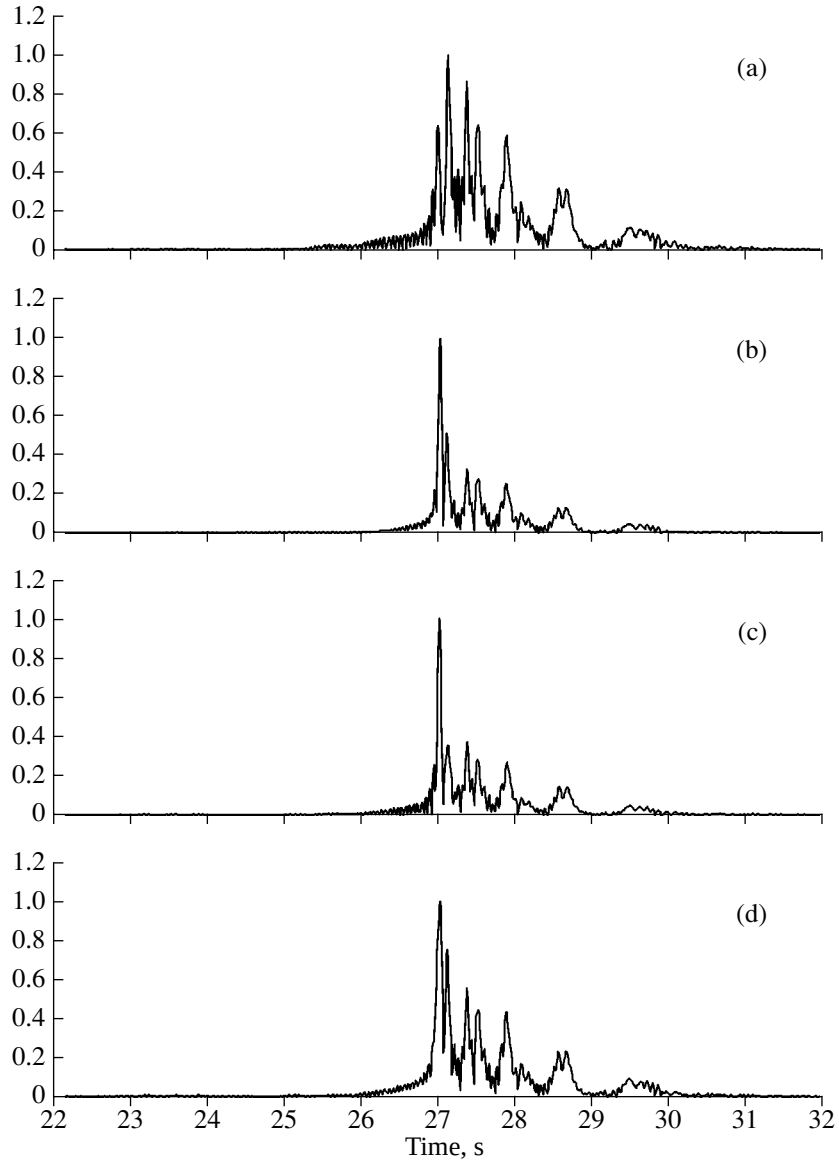

Fig. 8. Dependence $B(t)$ normalized by its maximal value in the presence of internal waves. The distance is 40 km, and the depth is z_r = 75 m. The instant of time is t = (a, d) 0, (b) 2000, and (c) 4000 s; the signal duration is (a–c) 25.6 and (d) 2×10^4 s.

nals is $\Delta f/f \cong 0.1$.[2] The signals of higher modes should most likely be covered with noise because of their small amplitudes. This is related to high attenuation of normal waves with high numbers (Fig. 2).

The presence of random inhomogeneities caused by internal waves at the same distance 40 km does not qualitatively perturb the signal structure (Fig. 8). This attests to the fundamental feasibility of mode acoustic tomography at such distances when the random inhomogeneities are only associated with the field of internal waves.

However, the situation changes as the distance increases. The results of the numerical experiment for a distance of 200 km are shown in Fig. 9. The rest of parameters of the experiment in these calculations were the same. As follows from Fig. 9, in the absence of random inhomogeneities, the selection of the mode signals at a distance of 200 km is possible, but only for the first five modes with small and approximately equal attenuation coefficients (see Fig. 2). The modes of higher numbers will hardly be seen at such distances against the noise background. In the presence of the internal waves, the structure of the envelope of the correlation

[2] Note that sufficiently intense low-frequency sound sources radiating signals with a relatively wide frequency band are difficult to manufacture and fairly expensive. Therefore, such signals are rarely used in acoustic tomography.

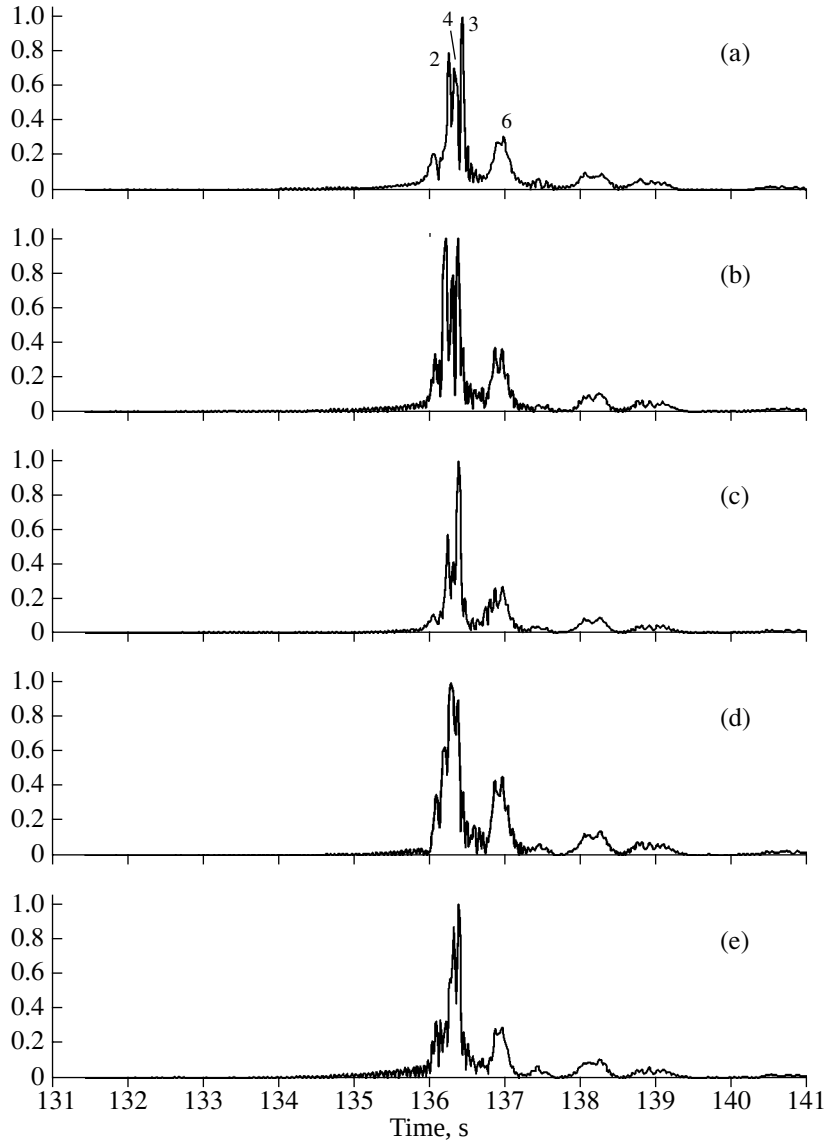

Fig. 9. Dependence $B(t)$ normalized by its maximal value at a distance of 200 km and a depth z_r = 75 m: (a) in the absence of random inhomogeneities and (b–e) in the presence of internal waves; the instant of time is t = (b, e) 0, (c) 2000, and (d) 4000 s; the signal duration is (b–d) 25.6 and (e) 2×10^4 s.

function of the received signal at these distances drastically changes. The separated mode signals become indistinguishable, and, therefore, mode tomography is impossible in this case.

The numerical modeling also showed (see Figs. 8d and 9e) that internal waves do not destroy the mode structure of the envelope of the correlation function at short distances of ~40 km for signals of large duration $T = 2 \times 10^4$ s either. For greater distances of ~200 km, the mode structure is violated, as for short signals.

The small-scale bottom roughness in the experiments under consideration had a much greater influence on the received signal than the internal waves (see Fig. 10). Due to the transformation of the normal waves even at small distances ~40 km, the signal structure changes drastically. As for the identification of individual components in the signal structure corresponding to the separate waveguide modes, it proves to be impossible. A superposition of individual components takes place, and the signal structure is complicated by the intermode interference and becomes difficult to interpret.

Precisely this situation occurred in the field experiment, the results of which are shown in Fig. 4. Although the total duration of signals at the output of the optimal correlation receiver was almost the same in the experiment and in the calculations (see Figs. 4 and 10), the structures of the signal envelopes noticeably differed.

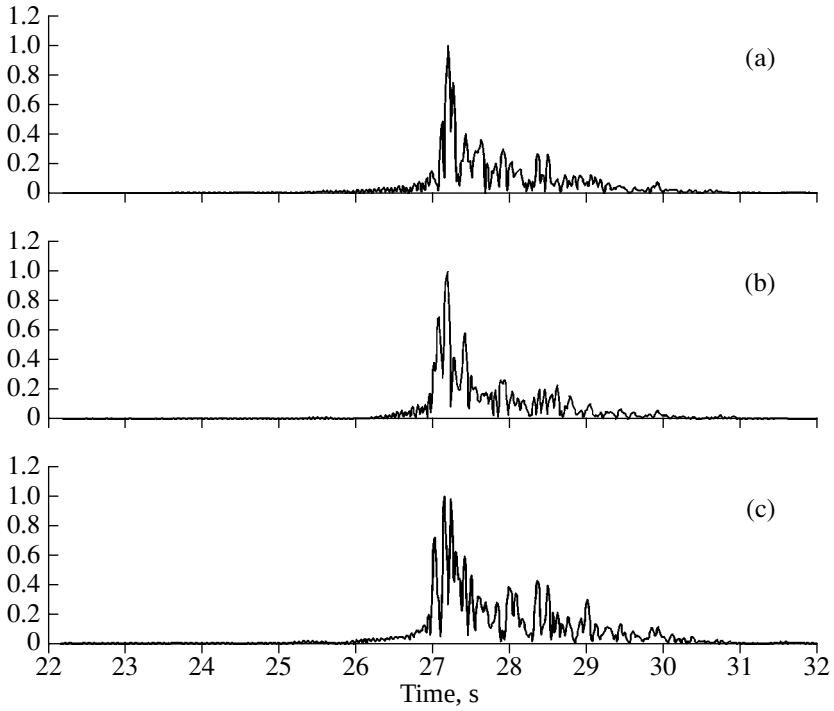

Fig. 10. Dependence $B(t)$ normalized by its maximal value in the presence of a rough bottom. The distance is r = 40 km and the depth is z_r = (a) 45, (b) 60, and (c) 75 m.

This difference is mainly unrelated to ambient noise, which is absent in the numerical experiment. The origin of the difference is the lack of exact data on all acoustic characteristics of the waveguide, including the characteristics of the sea bottom along the acoustic track. Without such data, it is impossible to reproduce all interference maxima in the structure of the signal envelope observed in the experiment.

4. CONCLUSIONS

The results obtained in this study allow one to hope for successful tomographic experiments only in certain regions of the Barents Sea with a relatively smooth bottom. The limiting distances of acoustic probing will depend not only on the sound attenuation but also on the parameters of internal waves in these regions. It is important to note that, using single omnidirectional sound sources and receivers for acoustic tomography, one can use only a few mode signals. The composition of these signals (the set of numbers of the corresponding modes) also depends on the probing distance. These circumstances limit the feasibility of acoustical monitoring in the water area under consideration.

ACKNOWLEDGMENTS

This work was supported by the Russian Foundation for Basic Research, project no. 02–02–16509.

REFERENCES

1. A. G. Nechaev and A. I. Khil'ko, Preprint No. 178, IPF AN SSSR (Inst. of Applied Physics, USSR Academy of Sciences, Nizhni Novgorod, 1987).
2. G. Jin, F. Lynch, C. S. Chiu, and J. H. Miller, J. Acoust. Soc. Am. **100**, 193 (1996).
3. B. G. Katsnel'son and V. G. Petnikov, *Acoustics of a Shallow Sea* (Nauka, Moscow, 1997).
4. J. R. Apel, M. Badiey, C. S. Chiu, *et al.*, IEEE J. Ocean Eng. **22** (3), 465 (1997).
5. B. G. Katsnel'son, V. M. Kuz'kin, S. A. Pereselkov, and V. G. Petnikov, in *Acoustics of the Ocean: Proceedings of the School–Seminar of Academician L. M. Brekhovskikh* (GEOS, Moscow, 1998), p. 273.
6. G. I. Kozubskaya, K. V. Konyaev, A. Pludeman, and K. D. Sabinin, Okeanologiya (Moscow) **47** (4), 476 (1999).
7. V. A. Grigor'ev, V. M. Kuz'kin, and V. G. Petnikov, Akust. Zh. **50**, 44 (2004) [Acoust. Phys. **50**, 37 (2004)].

Translated by Yu. Lysanov

Acoustical Physics, Vol. 50, No. 5, 2004, pp. 562–570. Translated from Akusticheskiĭ Zhurnal, Vol. 50, No. 5, 2004, pp. 657–665.

Structure of Acoustic Domains in a Cholesteric Liquid Crystal under the Effect of Ultrasound

E. N. Kozhevnikov

Samara State University, ul. Akademika Pavlova 1, Samara, 443011 Russia

e-mail: kozhev@ssu.samara.ru

Received July 22, 2003

Abstract—On the basis of the nonequilibrium hydrodynamics of a cholesteric liquid crystal (CLC), the properties of acoustic domains arising in a CLC layer under a normally incident ultrasonic wave are considered. The geometry and size of domains and the degree of deformation of the CLC structure are analyzed by the perturbation method for sound intensities exceeding the threshold value. Scaling dependences of the domain size and the deformation amplitude on the intensity of external action and the preliminary tension of the layer are plotted. It is shown that, as the effect advances beyond the threshold, the size of domains decreases. © *2004 MAIK "Nauka/Interperiodica".*

Nematic and cholesteric liquid crystals exhibit a variety of spatially modulated dissipative structures (domains), which may arise in them as a result of periodic deformations under oscillatory flows, viscous waves, and sound fields [1–4]. The form of domains depends on the initial orientation of a crystal, on the geometry of the liquid-crystal cell, and on the type and frequency of the external action. The theoretical description of dissipative structures under a low-frequency action (see, e.g., [5–9]) is based on the Leslie–Ericsen hydrodynamic equations [10, 11]. To describe the domains at high frequencies, it is necessary to consider the structural relaxation processes and also the nonlinear relaxation phenomena, which give rise to stationary stresses and moments that are quadratic in the compression of a crystal in a sound field. This approach has made it possible to describe the formation of domain structures in a cholesteric liquid crystal layer under the effect of a normally incident ultrasonic wave in a wide frequency range (covering more than four orders of magnitude) [12, 13].

In all previous publications, the theoretical analysis of domains formed under a periodic deformation of nematic and cholesteric crystals is reduced to the determination of the threshold at which the moments caused by the external action and destabilizing the initial crystal structure become equal to the elastic moments arising in the deformed structure and stabilizing it. This analysis ignores the geometry of domains beyond the threshold, where the intensity of the external action exceeds the threshold value, and does not determine the degree of deformation of the crystal. At the same time, recent experimental studies have shown that, as the external action advances beyond the threshold, the size of domains may vary considerably (see, e.g., [14]). Experimental and theoretical studies of such variations are important for understanding the nature of dissipative structures arising in anisotropic liquids under a dynamic action.

This paper theoretically describes the domain structure formed in a cholesteric liquid crystal (CLC) layer under a normally incident ultrasonic wave whose intensity exceeds the threshold value. The degree of deformation of the cholesteric structure and the size of domains are determined as functions of ultrasonic intensity.

Let us consider the effect of ultrasound of frequency ω with a compression amplitude ε on a planar CLC layer of thickness h. In the unperturbed state of the crystal, the axis of the cholesteric helix is directed along the normal to the layer (the z axis), while the cholesteric layers are parallel to the boundaries of the CLC layer ($z = 0$, h). Assuming that the first boundary encountered by the sound wave ($z = 0$) is acoustically transparent and the second boundary ($z = h$) is rigid, we represent the compression of the crystal in the sound wave as a standing wave:

$$\varepsilon(t, z) \approx 2\varepsilon\cos[k_s(h - z)]\sin\omega t,$$

where $k_s = \omega/c$ is the wave number of sound in the layer and c is the velocity of sound.

The degree of sound action on the crystal is determined by the period-average (denoted by the overbar) square of the compression of liquid in the sound field, $\overline{\varepsilon^2(t, z)}$. In analyzing the effect, we limit our consideration to the frequencies at which the sound wavelength in the cholesteric crystal is greater than the helix pitch. In the equations for the perturbations of the cholesteric structure, we replace $\overline{\varepsilon^2(t, z)}$ by its value averaged over the layer thickness: $\overline{\varepsilon^2(t, z)} = \varepsilon^2[1 + \sin(2k_sh)/(2k_sh)]$.

In addition, let us limit the frequency by the inequality $\omega > \omega_0 = 2.25\tau^{-1}h/P_0$, where P_0 is the pitch of the cholesteric helix and τ is the relaxation time of the crystal alignment. In this case, the destabilization of the initial structure of the crystal is caused by the effect of the nonlinear relaxation stresses $\sigma_{ij}^{(2)}$ and moments $\Gamma_i^{(2)}$ described as

$$\sigma_{ij}^{(2)} \sim \overline{\left\{ \mathrm{Re}\left[\frac{\delta\alpha}{\delta\varepsilon_{pq}}\varepsilon_{pq}\right] v_{ij}\right\}},$$

$$\Gamma_i^{(2)} \sim \overline{\left\{ \mathrm{Re}\left[\frac{\delta(\gamma_2/\gamma_1)}{\delta\varepsilon_{pq}}\delta\varepsilon_{pq}\right] v_{ik}\right\}} n_k,$$

where ε_{pq} are the components of the strain tensor; $v_{pq} = \dot{\varepsilon}_{pq}$; and α, $\gamma_1 = \alpha_3 - \alpha_2$, and $\gamma_2 = \alpha_3 + \alpha_2$ are the Leslie coefficients of viscosity [11]. In this study, we consider only the destabilizing factors specified above and ignore the role of vortex oscillatory flows.

To describe the domains, we assume that the z axis is directed along the normal to the layer, the x and y axes lie in the lower boundary plane $z = 0$, and the unperturbed cholesteric layers are parallel to the xy plane. We consider a crystal with a small pitch of the cholesteric helix: $P_0 \ll h$.

The equations describing the motion of the cholesteric liquid and the rotation of the director under the effect of ultrasound were formulated in [13]. From them, we select the equations for stationary flows and the equilibrium condition for the director in the flows:

$$\nabla \times [\nabla \cdot \hat{\sigma} + \nabla \cdot \hat{\sigma}^{(2)} + \mathbf{F}] = 0,$$
$$\frac{1}{2}(\mathrm{curl}\mathbf{v} \times \mathbf{n}) + \frac{\gamma_2}{\gamma_1}[\hat{v} \cdot \mathbf{n} + (\mathbf{n} \cdot \hat{v} \cdot \mathbf{n})\mathbf{n}] + \frac{1}{\gamma_1}\boldsymbol{\Gamma} + \boldsymbol{\Gamma}^{(2)} = 0. \quad (1)$$

Here, n is the director; $\hat{\sigma}$ is the Leslie viscous stress tensor

$$\sigma_{ij} = \alpha_1 v_{\alpha\beta} n_\alpha n_\beta n_i n_j + \alpha_2 N_i n_j + \alpha_3 N_j n_j + \alpha_4 v_{ij} + \alpha_5 v_{ik} n_k n_j + \alpha_6 v_{jk} n_k n_i;$$

$\mathbf{N} = \dot{\mathbf{n}} - 1/2\,\mathrm{curl}\mathbf{v} \times \mathbf{n}$; $\boldsymbol{\Gamma}$ and $\mathbf{F}$ are the Frank elastic moments and the force arising in the deformed cholesteric structure, which are determined through the Frank elastic energy; and $\boldsymbol{\Gamma}^{(2)}$ and $\hat{\sigma}^{(2)}$ are the nonlinear moments and stresses caused by the relaxation of the liquid crystal structure in the sound field. By analogy with nematic crystals, the viscosity coefficients α_1 and α_3 are assumed to be small and set to be equal to zero in the following calculations, while the torsional viscosity coefficients are $\gamma_1 = -\gamma_2 = \gamma$.

The nonlinear moments and stresses are determined by the intensity of the ultrasonic action and by the direction of oscillations m in the sound wave. In the chosen geometry, $\mathbf{m} = (0, 0, 1)$ and the director $\mathbf{n}$ has the form $\mathbf{n} = (n_x, n_y, \sin\theta)$, where θ is the angle between the director and the xy plane. The vector $\boldsymbol{\Gamma}^{(2)}$ and the components of the stress tensor $\hat{\sigma}^{(2)}$, which are necessary for the formulation of the equation of motion, were determined in [15] as

$$\boldsymbol{\Gamma}^{(2)} = \frac{1}{2}\omega_2 F\varepsilon^2 m_1(\mathbf{m} - m_1\mathbf{n}),$$
$$\sigma_{z\alpha}^{(2)} = -2\gamma\omega_1^+ F\varepsilon^2 \sin\theta\cos\theta n_\alpha^0, \quad (2)$$
$$\sigma_{\alpha z}^{(2)} = 2\gamma\omega_1^- F\varepsilon^2 \sin\theta\cos\theta n_\alpha^0, \quad \alpha = x, y.$$

Here, $m_1 = \mathbf{mn} = \sin\theta$ is the projection of $\mathbf{m}$ on the director; ω_2 and $\omega_1^\pm$ are parameters with the dimension of frequency,

$$\omega_1 = \frac{1}{\tau\langle P_2\rangle}\left[1 + \frac{\sin(2k_s h)}{2k_s h}\right](K\beta_S^{-1} - R)$$
$$\times\left\{\frac{1}{7}\left(R_{22} + \frac{16}{5}R_{24}\right) - \frac{1}{6}(\langle P_2\rangle + 2 - 10T/d)\right\},$$
$$\omega_1^\pm = \frac{nT}{2\gamma}\beta^{-1}\left[1 + \frac{\sin(2k_s h)}{2k_s h}\right](K\beta_S^{-1} - R) \quad (3)$$
$$\times\left\{\frac{3}{2}\langle P_2\rangle \mp [R_{22} + \langle P_2^2(P_2 - \langle P_2\rangle)\rangle]\right\};$$

$n_x^0 = \cos qz$ and $n_y^0 = \sin qz$ are the unperturbed director components; $q = 2\pi/P$; and P is the cholesteric helix pitch.

The stresses $\sigma_{xy}^{(2)}$ are symmetric with respect to the permutation of subscripts, and the diagonal elements of the stress tensor contain no terms nonlinear in perturbations; these components are not involved in the equations of motion.

In Eqs. (2) and (3), β_S is the adiabatic compressibility; $R = 1 - d_T/7 + 12d_T R_{24}/35R_{22}$; $R_{nm} = \langle P_n P_m\rangle - \langle P_n\rangle\langle P_m\rangle$; $d_T = d\langle P_2\rangle/T$; d is the molecular field constant; $P_n = P_n(\cos\chi)$ are the Legendre polynomials; χ is the angle between the longer axis of a molecule and the director; the angular brackets denote averaging over the angular distribution of orientations of the longer axes of molecules; the parameters K and β have the form

$$K = \beta d_T \frac{1}{T}\left(\frac{\partial T_c}{\partial p} - \frac{\alpha TV}{C_p}\right), \quad \beta = \left(1 + nR_{22}\frac{d_T^2}{C_p} - R_{22}\frac{d}{T}\right)^{-1};$$

T_c is the orientational melting temperature of the crystal; α is the coefficient of thermal volumetric expansion; V is the volume; C_p is the specific heat at constant pressure; and the function $F = F(\omega\tau)$ determines the relaxation dependence of the angular distribution per-

turbation on the frequency of the ultrasonic action, $F = F(\omega\tau) = \omega^2\tau^2/(1 + \omega^2\tau^2)$. The formula for $\omega_1^{\pm}$ was obtained in [15] on the assumption that $\alpha_1 \approx 1$ and $\alpha_5 + \alpha_6 \approx -1$.

The Frank elastic moments $\mathbf{\Gamma}$ in the equation of rotation and the force $\mathbf{F}$ in the equation of motion are determined by the differentiation of the free energy density of the crystal g with respect to the director rotation in the first case and with respect to the displacement $\mathbf{u}$ in the second case:

$$\mathbf{\Gamma} = -\frac{\partial g}{\partial \mathbf{n}} + \nabla_i \frac{\partial g}{\partial \nabla_i \mathbf{n}},$$

$$\mathbf{F} = -\frac{\partial g}{\partial \mathbf{u}} + \nabla_i \frac{\partial g}{\partial \nabla_i \mathbf{u}} - \Delta \frac{\partial g}{\partial \Delta \mathbf{u}}.$$

In the two-constant approximation, the elastic energy G has the form [11]

$$G = \int_V g dV$$

$$= \frac{1}{2} K_{33} \int_V \{(\mathrm{div}\mathbf{n})^2 + \lambda(\mathbf{n}\,\mathrm{curl}\mathbf{n} + q_0)^2 + (\mathbf{n} \times \mathrm{curl}\mathbf{n})^2\} dV,$$

where $K_{11} = K_{33}$, K_{22} are the Frank elastic constants; $\lambda = K_{22}/K_{33}$; $q_0 = 2\pi/P_0$; and P_0 is the cholesteric helix pitch in the equilibrium cholesteric structure. When the CLC layer is stretched along the helix axis by $\delta' \ll 1$, the helix pitch in it is determined as $P = P_0(1 + \delta')$, and the equilibrium and actual wave numbers of the helix, which are denoted by q_0 and q, respectively, are related by the formula $q_0 = q(1 + \delta')$.

Let us represent the director using the angular variables θ and $\Phi = qz + \varphi$, where θ is the angle between the director and the xy plane and φ is the angle of the director deviation from the equilibrium orientation in the layer plane:

$$n = (\cos\theta\cos\Phi, \cos\theta\sin\Phi, \sin\theta).$$

In terms of the variables θ and Φ, the elastic energy takes the form

$$G = \frac{1}{2} K_{33} \int_V \{(\nabla\theta)^2 + \cos^2\theta(\nabla_\perp\Phi)^2 + \lambda(\Phi_{,z})^2$$
$$- 2\lambda q_0 \cos^2\theta\Phi_{,z} + 2q\lambda(n_x^0\theta_{,y} - n_y^0\theta_{,x})$$
$$+ 2\lambda q_0 \sin\theta\cos\theta n_\alpha \Phi_{,\alpha}$$
$$+ (\lambda - 1)[(n_x^0\theta_{,y} - n_y^0\theta_{,x})^2 + \cos^4\theta(\Phi_{,z})^2 \qquad (4)$$
$$+ \sin^2\theta\cos^2\theta(n_s^0\Phi_{,s})^2 - \cos^2\theta(n_x^0\theta_{,y} - n_y^0\theta_{,x})\Phi_{,z}$$
$$+ 2\sin\theta\cos\theta n_s\Phi_{,s}(n_x^0\theta_{,y} - n_y^0\theta_{,x})$$
$$- 2\sin\theta\cos^3\theta n_s^0\Phi_{,s}\Phi_{,z}]\} dV.$$

Here and below, the subscript α runs through $\alpha = x, y$.

Consider small deformations of the cholesteric structure, when the angles θ and φ are small. Expanding the trigonometric functions involved in Eq. (4) in powers of θ and φ and transforming the expression for the energy G, we retain the powers up to the fourth inclusive in Eq. (4). The resulting full expression for the energy proves to be cumbersome, and we will consider its simplified version under the assumption that $|\theta| \ll |\varphi|$:

$$G = \frac{1}{2} K_{33} \int_V \{(\nabla\theta)^2 + (\nabla_\perp\varphi)^2 + \lambda(\varphi_{,z})^2$$
$$+ q^2\theta^2(1 + 2\lambda\delta') + 4q\theta n_\alpha\varphi_{,\alpha}(1 + \lambda\delta') \qquad (5)$$
$$+ (\lambda - 1)(n_x^0\theta_{,y} - n_y^0\theta_{,x})^2\} dV.$$

Here,

$$n_x = n_x^0 - n_y^0\varphi - \frac{1}{2}n_x^0\varphi^2,$$

$$n_y = n_y^0 + n_x^0\varphi - \frac{1}{2}n_y^0\varphi^2.$$

The third and fourth powers of the perturbation appear in the cross term containing n_x, n_y.

In a structure with a small helix pitch, where $P_0 \ll h$, the inequality $|\theta| \ll |\varphi|$ is justified by the higher energy of the helical deformation of the structure due to the exit of molecules from the CLC planes, as compared to the energy of the displacement of layers due to the rotation of molecules in the CLC planes. The relation between the angles θ and φ that is obtained below confirms this inequality.

Note that the choice of the new variables $\theta' = \theta(1 + \lambda\delta')$ and $\varphi' = \varphi(1 - 1/2\lambda\delta')$ reduces the elastic energy to the form

$$G = \frac{1}{2} K_{33} \int_V \{(\nabla\theta')^2 + (1 - \lambda\delta')(\nabla_\perp\varphi')^2 + \lambda(\varphi'_{,z})^2$$
$$+ q^2\theta'^2 + 4q\theta' n_\alpha\varphi'_{,\alpha} + (\lambda - 1)(n_x^0\theta'_{,y} - n_y^0\theta'_{,x})^2\} dV,$$

which was used earlier in [12, 13] in the energy representation quadratic in perturbations.

Using Eqs. (2) for nonlinear moments and stresses and the free energy given by Eq. (5), we separate from Eqs. (1) a self-consistent set of equations for the angles θ and φ and the stationary flow velocity v_z:

$$\gamma\omega_2 F\varepsilon^2\sin\theta\cos\theta - K_{33}[\Delta\theta - q^2\theta(1 + 2\lambda\delta')$$
$$- 2qn_\alpha\varphi_{,\alpha}(1 + \lambda\delta')$$
$$+ (\lambda - 1)(n_x^2\theta_{,xx} + n_y^2\theta_{,yy} - 2n_x n_y\theta_{,xy})] = 0,$$
$$\gamma(qv_z - \Omega) - K_{33}[\varphi_{,zz} + \Delta_\perp\varphi + 2q(n_\alpha\theta)_{,\alpha}(1 + \lambda\delta')] = 0,$$
$$q(qv_z - \Omega) + \omega_1^+ F\varepsilon^2(n_\alpha\sin\theta\cos\theta)_{,\alpha} = 0.$$

Eliminating the velocity, we obtain the equations for θ and φ:

$$K_{33}[\Delta\theta - q^2\theta(1 + 2\lambda\delta') - 2qn_\alpha\varphi_{,\alpha}(1 + \lambda\delta') + (\lambda - 1)(n_x^2\theta_{,xx} + n_y^2\theta_{,yy} - 2n_xn_y\theta_{,xy})] - \gamma\omega_2 F\varepsilon_0^2\theta(1 - 2/3\theta^2) = 0, \quad (6)$$

$$K_{33}[\varphi_{,zz} + \Delta_\perp\varphi + 2q(n_\alpha\theta)_{,\alpha}(1 + \lambda\delta')] + \gamma q^{-1}\omega_1^+\varepsilon^2[n_\alpha\theta(1 - 2/3\theta^2)]_\alpha = 0.$$

We seek the solution to Eqs. (6) in the form of an angle θ rapidly varying along the helix axis and a slowly varying angle φ. Such a solution corresponds to the minimum of the elastic energy in the deformed cholesteric structure and, hence, to the maximal distortion under the external action. Assuming that the angles θ and φ are equal to zero at the boundaries of the layer and periodically vary in the layer plane, we represent them as

$$\theta = \sin k_z z[\psi_x n_x^0 \sin k_x x\cos k_y y + \psi_y n_y^0 \cos k_x x\sin k_y y], \quad \varphi = \psi_2 \sin k_z z\cos k_x x\cos k_y y, \quad (7)$$

where ψ_x, ψ_y, and ψ_2 are constant coefficients and $k_z = \pi/h$. Taking into account that the pitch of the cholesteric helix is small compared to the thickness of the CLC layer, we assume that the following inequalities are valid:

$$k_z = \pi/h \ll k_\alpha \ll q = 2\pi/P. \quad (8)$$

Substituting expressions (7) for the angles into Eqs. (6), we separate from them a set of equations for the coefficients ψ_2, ψ_x, and ψ_y. For this purpose, we multiply the first of the equations by $n_x^0 \sin k_x x\cos k_y y$ and then multiply the same equation by $n_y^0 \cos k_x x\sin k_y y$; then, we multiply the second of the equations by $k_z z\cos k_x x\cos k_y y$; and then, we integrate the resulting products over $z \in [0, h]$, $x \in [0, 2\pi/k_x]$, and $y \in [0, 2\pi/k_y]$. Expanding the results of integration in powers of $k_z/q \ll 1$ and limiting our consideration to the second power of k_z/q, we arrive at the following set of equations:

$$[2q^2(1 + \lambda\delta') + k^2]\psi_x - 2qk_x\psi_2\left(1 - \frac{27}{128}\psi_2^2\right) - \frac{\lambda - 1}{4}[(3k_y^2 + k_x^2)\psi_x - 2k_xk_y\psi_y] - f_2\varepsilon^2\psi_x\left[1 - \frac{27}{128}\psi_2^2 - \frac{3}{128}(3\psi_y^2 + \psi_x^2)\right] = 0,$$

$$[2q^2(1 + \lambda\delta') + k^2]\psi_y - 2qk_y\psi_2\left(1 - \frac{27}{128}\psi_2^2\right) - \frac{\lambda - 1}{4}[(3k_x^2 + k_y^2)\psi_y - 2k_xk_y\psi_x] \quad (9)$$

$$- f_2\varepsilon^2\psi_x\left[1 - \frac{27}{128}\psi_2^2 - \frac{3}{128}(3\psi_x^2 + \psi_y^2)\right] = 0,$$

$$(\lambda k_z^2 + k^2)\psi_2 - qk_\alpha\psi_{,\alpha}\left(1 - \frac{9}{128}\psi_2^2\right)(1 + \lambda\delta') - q^{-1}f_1\varepsilon^2\left\{k_\alpha\psi_\alpha\left(1 - \frac{9}{128}\psi_2^2\right) - \frac{3}{128}[k_x\psi_x(9\psi_x^2 + \psi_y^2) + k_y\psi_y(9\psi_y^2 + \psi_x^2)]\right\}.$$

Here, we introduced the notation

$$f_1 = \gamma\omega_1^+/K_{33}, \quad f_2 = \gamma\omega_2/K_{33}, \quad k^2 = k_x^2 + k_y^2, \quad \alpha = x, y.$$

When ultrasound is normally incident on the CLC layer, its effect on the crystal is isotropic in the plane of the layer. In this case, the cholesteric structure is least stable to perturbations with the geometry corresponding to the minimal elastic energy. In layered systems, including CLCs, such perturbations have the form of square grids when the external action is isotropic in the layer plane. Indeed, in the long-wave approximation, the free energy G of a layered structure [16] with a layer displacement given as $w_z = w_0\sin(k_z z)\cos(k_x x)\cos(k_y y)$ is reduced to the form

$$G = \frac{VB}{2048}[(k^4 + 24(k_x^2 - k_y^2)^2]\omega_0^4 + \frac{V}{8}[Bk_z^2 + K'k^2]\omega_0^2.$$

This energy is minimal at $k_x = k_y$ (here, B and K' are the elastic constants and V is the volume). Therefore, we consider the formation of a square grid-type structure in the CLC layer and assume that $k_x = k_y = k/\sqrt{2}$ and $\psi_x = \psi_y = \psi_1$. Let us select the equations for ψ_1 and ψ_2 from the set of equations (9):

$$\left[2q^2(1 + \lambda\delta') + \frac{3 + \lambda}{4}k^2\right]\psi_1 - 2qk_x\psi_2\left(1 - \frac{9}{128}\psi_2^2\right)(1 + \lambda\delta') - f_2\varepsilon^2\psi_1\left[1 - \frac{3}{32}\psi_1^2 - \frac{9}{128}\psi_2^2\right] = 0, \quad (10)$$

$$[\lambda k_z^2 + k^2]\psi_2 - 2qk_x\psi_1\left(1 - \frac{9}{128}\right)(1 + \lambda\delta') - 2f_1q^{-1}\varepsilon^2k_x\psi_1\left[1 - \frac{15}{64}\psi_1^2 - \frac{9}{128}\psi_2^2\right] = 0.$$

Introducing a vector $\boldsymbol{\psi}$ as

$$\boldsymbol{\psi} = \begin{pmatrix}\psi_1\\ \psi_2\end{pmatrix},$$

we separate the terms that are linear in the deformation on the left-hand side of the set of equations (10) and represent the latter in the form

$$\hat{D}\cdot\boldsymbol{\psi} = Q, \tag{11}$$

where $\hat{D}$ is the matrix with the components

$$\begin{aligned} D_{11} &= 2q^2(1+\lambda\delta') + \frac{3+\lambda}{4}k^2 - f_2\varepsilon_0^2,\\ D_{12} &= -2qk_x(1+\lambda\delta'),\\ D_{21} &= -2qk_x(1+\lambda\delta') - 2\frac{k_x}{q}f_1\varepsilon_0^2,\\ D_{22} &= \lambda k_z^2 + k^2; \end{aligned} \tag{12}$$

Q is the vector of the right-hand sides of set (10), which are nonlinear in the deformation of the structure, with the components

$$\begin{aligned} Q_1 &= f_2(\varepsilon^2-\varepsilon_0^2)\psi_1 - \frac{9}{64}qk_x(1-\lambda\delta')\psi_2^3\\ &\quad - \frac{3}{128}f_2\varepsilon^2(4\psi_1^2+3\psi_2^2)\psi_1,\\ Q_2 &= 2\frac{k_x}{q}f_1(\varepsilon^2-\varepsilon_0^2)\psi_1 - \frac{9}{64}qk_x\psi_1(1-\lambda\delta')\psi_2^2\\ &\quad - \frac{3k_x}{64q}\varepsilon^2 f_1(5\psi_1^2+3\psi_2^2)\psi_1; \end{aligned} \tag{13}$$

and ε_0 is the threshold compression determined below for the domain structure with the wave number k.

Let us analyze Eqs. (11) by the perturbation method. Taking into account that the equations contain the first and third powers of the angles ψ_1 and ψ_2, we represent these angles and the square of compression ε^2 in the form

$$\begin{aligned} \psi_k &= \psi_k^{(1)}\zeta + \psi_k^{(3)}\zeta^3 + \ldots, \quad k = 1, 2,\\ \varepsilon^2 &= \varepsilon_0^2 + E_2\zeta^2 + \ldots, \end{aligned} \tag{14}$$

where $\zeta \ll 1$ is a small parameter. Substituting expansions (14) into Eqs. (11) and separating the terms that contain the first and third powers of ζ, we obtain the equations for $\boldsymbol{\psi}^{(1)}$ and $\boldsymbol{\psi}^{(3)}$

$$\hat{D}\cdot\boldsymbol{\psi}^{(1)} = 0, \tag{15}$$

$$\hat{D}\cdot\boldsymbol{\psi}^{(3)} = \mathbf{Q}^{(3)}, \tag{16}$$

in which $\mathbf{Q}^{(3)}$ is the coefficient multiplying ζ^3 in the expansion of the vector **Q**:

$$\begin{aligned} Q_1^{(3)} &= f_2E_2\psi^{(1)} - \frac{9}{64}qk_x(1-\lambda\delta')(\psi_2^{(1)})^3\\ &\quad - \frac{3}{128}\varepsilon_0^2 f_2[4(\psi_1^{(1)})^2 + 3(\psi_2^{(1)})^2]\psi_1^{(1)},\\ Q_2^{(3)} &= 2\frac{k_x}{q}f_1E_2\psi_1^{(1)} - \frac{9}{64}qk_x(1-\lambda\delta')\psi_1^{(1)}(\psi_2^{(1)})^2\\ &\quad - \frac{3k_x}{64q}\varepsilon_0^2 f_1[5(\psi_1^{(1)})^2 + 3(\psi_2^{(1)})^2]\psi_1^{(1)}. \end{aligned}$$

Let us solve Eq. (15). Equating the determinant of the set to zero, we determine ε_0^2. Taking into account relations (8) and the smallness of the elongation δ', we obtain

$$\begin{aligned} \varepsilon_0^2 &= \varepsilon_0^2(k)\\ &\approx \frac{1}{2f_1+f_2}\frac{\frac{3+\lambda}{4}k^4 + 2\lambda q_0^2k_z^2 - 2q_0^2k^2\lambda\delta'}{k^2}. \end{aligned} \tag{17}$$

Introducing the notation

$$k_0^4 = \frac{8\lambda}{3+\lambda}q_0^2k_z^2, \quad \delta = \lambda\delta'\frac{4}{3+\lambda}\frac{q_0^2}{k_0^2},$$

we represent ε_0^2 in the form

$$\varepsilon_0^2 \approx \frac{3+\lambda}{4(2f_1+f_2)}\frac{k^4+k_0^4-2k^2k_0^2\delta}{k^2}. \tag{18}$$

The quantity ε_0 has the meaning of the threshold amplitude of compression in the sound wave, which corresponds to the beginning of the formation of the structure with the wave number k. The parameter δ is equal to the ratio of the layer tension δ' to the threshold one δ_0 at which the domain structure is formed in the CLC layer without the external action: $\delta = \delta'/\delta_0$.

The eigenvector of problem (15), $\boldsymbol{\psi}^{(1)}$, with allowance for inequalities (8) has the form

$$\boldsymbol{\psi}^{(1)} \approx \begin{pmatrix}1\\ q/k_x\end{pmatrix}a, \tag{19}$$

where a is the amplitude determined below.

The amplitude a and its dependence on the wave number k is found from the condition of solvability of Eqs. (16) with respect to $\psi_1^{(3)}$ and $\psi_2^{(3)}$. This condition has the form of the orthogonality of the vector $\mathbf{Q}^{(3)}$ and the eigenvector $\boldsymbol{\psi}_c$ of the problem that is conjugate to set (15):

$$(\boldsymbol{\psi}_c\mathbf{Q}^{(3)}) = 0. \tag{20}$$

The vector $\boldsymbol{\psi}_c$ is found from the equation

$$\hat{D}^T \cdot \boldsymbol{\psi}_c = 0,$$

where the superscript T means the transposition of the matrix. Solving this equation with allowance for both expression (18) for ε_0^2 and inequalities (8), we represent $\boldsymbol{\psi}_c$ in the form

$$\boldsymbol{\psi}_c \approx \begin{pmatrix} 1 \\ q/k_x \end{pmatrix}. \tag{21}$$

Let us substitute the components of the vectors $\boldsymbol{\psi}^{(1)}$ and $\boldsymbol{\psi}_c$ into Eq. (20). Neglecting the terms on the order of smallness of $k^2/q^2 \ll 1$ and $\lambda\delta' \ll 1$ and using relation $k_x^2 = k^2/2$, we arrive at the following equation for a:

$$(2f_1 + f_2)E_2 - \left[\frac{9}{16}\frac{q^4}{k^2} + \frac{9}{128}(2f_1 + f_2)\varepsilon_0^2\right]a^2 = 0.$$

Multiplying both sides of this equation by ζ^2, we obtain

$$[\psi_1^{(1)}\zeta]^2\left[\frac{9}{16}\frac{q^4}{k^2} + \frac{9}{128}(2f_1 + f_2)\varepsilon_0^2\right] = (2f_1 + f_2)(\varepsilon^2 - \varepsilon_0^2). \tag{22}$$

We separate the expression for $\psi_1^{(1)}\zeta$ from Eq. (22). Taking into account inequalities (8) and the estimates

$$\varepsilon_0^2 \sim \frac{k_0^2}{2f_1 + f_2}, \quad \varepsilon_0^2\frac{(2f_1 + f_2)k^2}{q^4} \sim \left(\frac{k}{q_0}\right)^4 \ll 1,$$

we arrive at the expression for $\psi_1^{(1)}\zeta$ in the form

$$\psi_1^{(1)}\zeta = \sqrt{\frac{4(3+\lambda)}{9}}\frac{k_0^2}{q_0^2}f(s, \delta, \xi),$$

where

$$f(s, \delta, \xi) = \left\{(1-\delta)\xi\left[s^2 + \frac{\delta}{1-\delta} - \frac{\xi^2 + 1}{2\xi(1-\delta)}\right]\right\}^{1/2}; \tag{23}$$

$\xi = k^2/k_0^2$ is the ratio squared of the wave number of the structure to the wave number of the stretched layer structure; $s = \varepsilon/\varepsilon_{th}$; and ε_{th} is the value of ε_0 that is minimal in k and is determined by the formula

$$\varepsilon_{th} = \left[\frac{(3+\lambda)k_0^2}{2(2f_1 + f_2)}(1-\delta)\right]^{1/2},$$

this value being reached at $k = k_0$.

The amplitudes of the angles θ and φ in the first approximation in ζ take the form

$$\theta_0 = \theta_0(k) \approx \psi_1^{(1)}\zeta = \sqrt{\frac{4(3+\lambda)}{9}}\frac{k_0^2}{q^2}f(s, \delta, \xi) = \frac{2\sqrt{2\lambda}}{3}\frac{P_0}{h}f(s, \delta, \xi),$$
$$\varphi_0 = \varphi_0(k) \approx \psi_2^{(1)}\zeta = \sqrt{\frac{2(3+\lambda)}{9}}\frac{k_0}{q}f(s, \delta, \xi) = \left[\frac{4\sqrt{2\lambda(3+\lambda)}}{9}\frac{P_0}{h}\right]^{1/2}f(s, \delta, \xi). \tag{24}$$

The ratio of the amplitudes θ_0 and φ_0 is equal to $\theta_0/\varphi_0 = [2\lambda(3+\lambda)P_0^2/h^2]^{1/4}$. In a layer with a small helix pitch, this ratio is small, which justifies the simplifications used in the derivation of Eq. (5) for the elastic energy.

Let us analyze the results obtained above. The distortion of the structure corresponds to the real values of the function $f(s, \delta, \xi)$. Using a simple estimate $f^2(s, \delta, \xi) \geq k^2/k_0^2(1-\delta)(s^2-1) \geq 0$, we determine the condition of the appearance of stationary distortions in the CLC layer under the effect of ultrasound:

$$\varepsilon \geq \varepsilon_{th}.$$

Hence, the value

$$\varepsilon_{th} = \left[\frac{3+\lambda}{2(2f_1 + f_2)}k_0^2(1-\delta)\right]^{1/2}$$

has the meaning of the threshold compression of the CLC layer in the sound field. The geometry of the structure formed in this case is determined by the wave number k_0, and the size of domains $d = \pi\sqrt{2}/k$ is equal to the size of domains $d_0 = \pi\sqrt{2}/k_0$ that occur under a static tension of the layer. These threshold parameters coincide with the results of previous calculations reported in [12, 13].

Beyond the threshold, where the inequality $s > 1$ ($\varepsilon > \varepsilon_{th}$) is valid, the distortions of the structure are represented by a spectrum of wave numbers k lying in the range

$$s^2(1-\delta) + \delta - \sqrt{[s^2(1-\delta) + \delta]^2 - 1} < \frac{k}{k_0} < s^2(1-\delta) + \delta + \sqrt{[s^2(1-\delta) + \delta]^2 - 1}.$$

Assuming that, in the experiment, one observes the distortions with the amplitude that is maximal in k, which is reached at a wave number k_{max} equal to

$$k_{max} = k_0\sqrt{s^2(1-\delta) + \delta}, \tag{25}$$

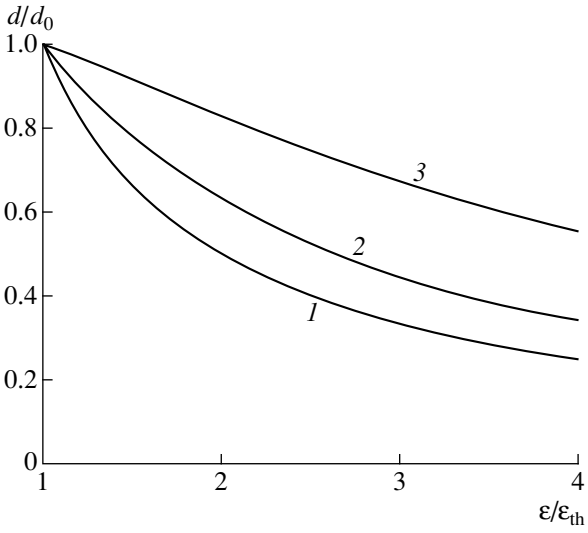

Fig. 1. Dependence of the reduced domain size d/d_0 on the amplitude of compression in the ultrasonic field for different elongations of the CLC layer: δ = (*1*) 0, (*2*) 0.5, and (*3*) 0.85.

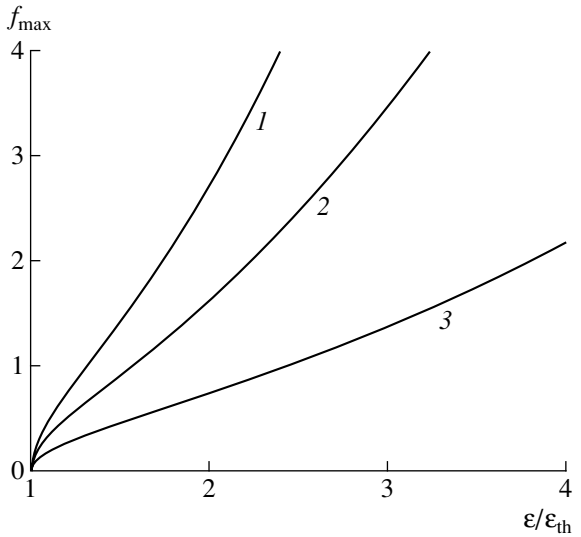

Fig. 2. Dependence of the reduced amplitude of the crystal deformation, $f_{max} = 3h/(2\sqrt{2\lambda}\,P_0)\theta_0$, on the amplitude of compression in the ultrasonic field for different elongations of the CLC layer: δ = (*1*) 0, (*2*) 0.5, and (*3*) 0.85.

we determine the deformation of the structure as before, by Eqs. (24), in which for the function $f(s, \delta, \xi)$ we take its maximal value in k, f_{max}:

$$f_{max} = f(s, \delta, s^2(1-\delta)+\delta) = \left\{\frac{1}{2}[(s^2(1-\delta)+\delta)^2 - 1]\right\}^{1/2}. \quad (26)$$

In this case, the size of domains d is determined by the formula

$$d = \frac{\pi\sqrt{2}}{k_{max}} = \frac{\pi\sqrt{2}}{k_0\sqrt{s^2(1-\delta)+\delta}} = \frac{d_0}{\sqrt{s^2(1-\delta)+\delta}}. \quad (27)$$

The size of domains d and the amplitudes of the structure deformation θ_0 and φ_0 depend on the relative compression of the CLC in the sound wave $s = \varepsilon/\varepsilon_{th}$ and the preliminary elongation δ of the cholesteric layer through the scaling combination $[s^2(1-\delta)+\delta]$. The results of numerical calculations for d and f_{max} are shown in Figs. 1 and 2. Figure 1 represents the reduced size of the domain structure, d/d_0, as a function of the compression amplitude in the ultrasonic wave. The curves are obtained by formula (27) for different values of the layer elongation. The theoretical curves demonstrate a decrease in the size of domains with an increase in the intensity of ultrasound beyond the threshold of the effect. This result correlates with the data reported in [14], where a decrease in the domain size with ultrasonic intensity growing above the threshold was observed in the experiment.

From the form of the curves obtained for $f_{max} = f(s, \delta, \xi_{max})$, which are plotted in Fig. 2 for different values of the layer elongation δ, it follows that, as δ increases, the rate of deformation growth in the domains with growing $s = \varepsilon/\varepsilon_{th}$ decreases. This result means that the role of ultrasound in the formation of the domain structure is reduced when the layer is preliminarily stretched.

The dependence of the amplitude of the CLC deformation on the compression in the sound wave, $\theta_0 \sim \varphi_0 \sim \sqrt{\varepsilon^2 - \varepsilon_{th}^2}$, is similar to the dependence of the parameter of the phase transition on the distance to the transition temperature in the Landau theory of second-order phase transitions. In the system under consideration, the analog of temperature is the inverse intensity of ultrasound: $J^{-1} \sim \varepsilon^{-2}$.

Let us consider the dynamics of the distortions of the cholesteric structure. Assuming that the coefficients ψ_1 and ψ_2 are time dependent, we transform the set of equations (11) to the form

$$\frac{\gamma}{K_{33}}\frac{d}{dt}\boldsymbol{\psi} + \hat{D}\cdot\boldsymbol{\psi} = \mathbf{Q}, \quad (28)$$

where the matrix $\hat{D}$ and the vector $\mathbf{Q}$ are determined by formulas (12) and (13).

As before, we represent the vector ψ as an expansion

$$\boldsymbol{\psi} = \zeta\boldsymbol{\psi}^{(1)} + \zeta^2\boldsymbol{\psi}^{(2)} + \zeta^3\boldsymbol{\psi}^{(3)} + \ldots,$$

and we introduce different scales for the dependence of the deformation angles on time by expanding the time derivative in powers of ζ:

$$\frac{d}{dt} = \frac{\partial}{\partial t_0} + \zeta\frac{\partial}{\partial t_1} + \zeta^2\frac{\partial}{\partial t_2} + \ldots.$$

Separating the terms with different powers of ζ from set (28), we obtain the equations

$$\frac{\gamma}{K_{33}}\frac{\partial}{\partial t_0}\boldsymbol{\psi}^{(1)} + \hat{D}\cdot\boldsymbol{\psi}^{(1)} = 0, \tag{29}$$

$$\frac{\gamma}{K_{33}}\frac{\partial}{\partial t_0}\boldsymbol{\psi}^{(2)} + \hat{D}\cdot\boldsymbol{\psi}^{(2)} = -\frac{\gamma}{K_{33}}\frac{\partial}{\partial t_1}\boldsymbol{\psi}^{(1)}, \tag{30}$$

$$\frac{\gamma}{K_{33}}\frac{\partial}{\partial t_0}\boldsymbol{\psi}^{(3)} + \hat{D}\cdot\boldsymbol{\psi}^{(3)} = -\frac{\gamma}{K_{33}}\frac{\partial}{\partial t_2}\boldsymbol{\psi}^{(1)} - \frac{\gamma}{K_{33}}\frac{\partial}{\partial t_1}\boldsymbol{\psi}^{(2)} + Q^{(3)}. \tag{31}$$

…

Representing the time dependence of $\boldsymbol{\psi}^{(1)}$ by the exponent $\boldsymbol{\psi}^{(1)} \sim e^{i\nu t_0}$, where $\mathrm{Im}\nu = 0$, we reduce Eq. (29) to the equation

$$\frac{i\gamma\nu}{K_{33}}\boldsymbol{\psi}^{(1)} + \hat{D}\cdot\boldsymbol{\psi}^{(1)} = 0, \tag{32}$$

which, for a real value of ε, has a solution only at $\nu = 0$. The solution to Eq. (32) and its conjugate is again determined by formulas (19) and (21), and the eigenvalue, by formula (18).

From the solvability condition for set (30),

$$\left(\boldsymbol{\psi}_c\cdot\frac{\gamma}{K_{33}}\frac{\partial}{\partial t_1}\boldsymbol{\psi}^{(1)}\right) + (\boldsymbol{\psi}_c\cdot\hat{D}\cdot\boldsymbol{\psi}^{(1)})$$

$$= \left(\boldsymbol{\psi}_c\cdot\frac{\gamma}{K_{33}}\frac{\partial}{\partial t_1}\boldsymbol{\psi}^{(1)}\right) = \frac{\gamma}{K_{33}}\left(1 + \frac{q^2}{k_x^2}\right)\frac{\partial a}{\partial t_1} = 0,$$

it follows that the amplitude a and, hence, the vector $\boldsymbol{\psi}^{(1)}$ do not depend on time t_1. In this case, the right-hand side of Eq. (30) becomes equal to zero and the equation has a zero solution $\boldsymbol{\psi}^{(2)} = 0$.

The solvability condition for the set of equations (31) with allowance for inequalities (8) can be reduced to the form

$$\left(\boldsymbol{\psi}_c\cdot\left[-\frac{\gamma}{K_{33}}\frac{\partial}{\partial t_2}\boldsymbol{\psi}^{(1)} - \frac{\gamma}{K_{33}}\frac{\partial}{\partial t_1}\boldsymbol{\psi}^{(2)} + \mathbf{Q}^{(3)}\right]\right)$$
$$\approx -\frac{2\gamma q_0^2}{K_{33}k^2}\frac{\partial a}{\partial t_2} + (2f_1 + f_2)E_2 a - \frac{9q^4}{16k^2}a^3 = 0. \tag{33}$$

Determining, as before, the deformation amplitude by the first approximation in ζ, $\theta_0 = \theta_0(t, k) \approx \zeta a$, and introducing the notation

$$\tau_s^{-1} = \frac{(2f_1 + f_2)K_{33}k^2}{\gamma q_0^2}(\varepsilon^2 - \varepsilon_0^2)$$
$$= \frac{(3+\lambda)K_{33}k_0^4}{4\gamma q_0^2}f^2(s, \delta, \xi) \tag{34}$$
$$= \frac{2\lambda K_{33}k_z^2}{\gamma}f^2(s, \delta, \xi),$$

we derive from Eq. (33) the following equation for the evolution of the amplitude θ_0:

$$\frac{d\theta_0}{dt} - \frac{\theta_0}{2\tau_s}\left[1 - \frac{\theta_0^2}{\theta^2(k)}\right] = 0. \tag{35}$$

The solution to Eq. (35) has the form

$$\theta_0(t, k) = \theta_0(k)\left\{1 + \left[\frac{\theta_0^2(k)}{\theta_{00}^2} - 1\right]e^{-t/\tau_s}\right\}^{-1/2}, \tag{36}$$

where θ_{00} is the angle of the initial deviation of the director from the xy plane. The parameter $\tau_s = \tau_s(k)$ plays the role of the settling time of perturbations with the wave number k. According to formula (34), this time is minimal for the wave number $k = k_{\max}$. When $t \longrightarrow \infty$, formula (36) passes into the first of Eqs. (24).

Let us determine the limits of applicability of the results obtained above from the viewpoint of the intensity of the external action. Formulas (24) and (27) were derived under the assumption that

$$k \ll q_0, \quad \theta_0 \ll \varphi_0 \ll 1.$$

Using expression (25) for $k_{\max}$ and formulas (24) for φ_0 and θ_0, in which $f = f_{\max}$, we obtain the following limitation for the parameter s determining how far we have gone beyond the threshold:

$$s = \varepsilon/\varepsilon_{\mathrm{th}} < \left\{\left(\sqrt{\frac{9}{\sqrt{2\lambda(3+\lambda)}}\frac{h}{P_0} + 1} - \delta\right)(1-\delta)^{-1}\right\}^{1/2}.$$

For the value $\lambda = 0.028$, which was used in [12, 13], this inequality is reduced to

$$s = \varepsilon/\varepsilon_{\mathrm{th}} < \left\{\frac{4.7\sqrt{h/P_0} - \delta}{1-\delta}\right\}^{1/2}.$$

ACKNOWLEDGMENTS

This work was supported by the Russian Foundation for Basic Research, project no. 00-02-17732.

REFERENCES

1. A. P. Kapustin and O. A. Kapustina, *Acoustics of Liquid Crystals* (Nauka, Moscow, 1986), p. 247 [in Russian].
2. *Pattern Formation in Liquid Crystals*, Ed. by A. Buka and L. Kramer (Springer, New York, 1996).
3. *Physical Properties of Liquid Crystals*, Ed. by D. Demus *et al.* (Wiley, Weinheim, 2000), Vol. 1, pp. 447–466.
4. O. S. Tarasov, A. P. Krechov, and L. Kramer, cond-mat/0205399 (2003).
5. E. N. Kozhevnikov, Zh. Éksp. Teor. Fiz. **92**, 1306 (1987) [Sov. Phys. JETP **65**, 731 (1987)].
6. S. J. Hogan, T. Mullen, and P. Woodford, Proc. R. Soc. London, Ser. A **441**, 559 (1993).
7. A. P. Krekhov, T. Borsonyi, P. Totch, *et al.*, Phys. Rep. **337**, 171 (2000).
8. H. Moritake, T. Seike, and K. Toda, Jpn. J. Appl. Phys. **38**, 3076 (1999).
9. M. Inoue, H. Moritake, and K. Toda, Jpn. J. Appl. Phys. **39**, 3125 (2000).
10. M. J. Stephen and J. P. Straley, Rev. Mod. Phys. **46**, 617 (1974).
11. P. de Gennes, *The Physics of Liquid Crystals* (Clarendon Press, Oxford, 1974; Mir, Moscow, 1977).
12. E. N. Kozhevnikov, Akust. Zh. **47**, 553 (2001) [Acoust. Phys. **47**, 430 (2001)].
13. E. N. Kozhevnikov, Akust. Zh. **48**, 777 (2002) [Acoust. Phys. **48**, 687 (2002)].
14. I. N. Gurova and O. A. Kapustina, Akust. Zh. **43**, 338 (1997) [Acoust. Phys. **43**, 290 (1997)].
15. E. N. Kozhevnikov, Akust. Zh. **42**, 800 (1996) [Acoust. Phys. **42**, 705 (1996)].
16. L. D. Landau and E. M. Lifshitz, *Course of Theoretical Physics*, Vol. 7: *Theory of Elasticity*, 4th ed. (Nauka, Moscow, 1987; Pergamon, New York, 1986).

Translated by E. Golyamina

Acoustical Physics, Vol. 50, No. 5, 2004, pp. 571–574. Translated from Akusticheskiĭ Zhurnal, Vol. 50, No. 5, 2004, pp. 666–670.

Acoustical Method for Measuring the Gas Content in Bottom Sediments

N. N. Komissarova and A. V. Furduev

Andreev Acoustics Institute, Russian Academy of Sciences, ul. Shvernika 4, Moscow, 117036 Russia

e-mail: bvp@akin.ru

Received December 25, 2003

Abstract—Gas bubbles in the bottom of shallow-water seas and freshwater basins lead to a substantial decrease in the sound speed. The gas content in the bottom changes because of the variability of the biological activity and water contamination, therefore serving as an indicator of the environmental equilibrium in the basin. It is proposed to monitor the gas content in bottom sediments by measuring the frequency spectrum of the bottom reflection coefficient in a broad frequency band. The data of calculations are presented for the sound speed in gas-containing sediments and for the values of the bottom reflection coefficient. A method is proposed for monitoring the gas content by measuring the frequency and angular characteristics of the natural ambient noise. © *2004 MAIK "Nauka/Interperiodica".*

In the acoustical monitoring of the state and variability of seas and freshwater basins, it is insufficient to monitor only the water surface and the water bulk. It is important to develop methods for monitoring the physical state of the bottom and the biological activity in it. The frequency-angular spectrum of the sound reflection coefficient of the bottom carries information on the sediment structure and biological activity. It is well known that gas inclusions (in the form of small gas bubbles) exist in the bottom sediments of sea shelves, harbors, lakes, and shallow seas [1–4]. The gas-saturated layer usually has a thickness of several meters. This layer is produced by the activity of methane-generating bacteria and by oxidation–reduction chemical reactions. The gas content can serve as an indicator of the environmental equilibrium of the waters, and acoustical methods for measuring the gas content are most advantageous. Actually, the sound speed sharply decreases in the presence of gas bubbles, from 1600 m/s in the liquid seafloor to 50 m/s in the gas-saturated sediments. The following sound speeds in bottom sediments were experimentally measured: 70–90 m/s in the Baltic Sea [3], 200–250 m/s in the Ivan'kovskoe man-made lake (the data of the authors), and 500 m/s at the African shelf of the Atlantic Ocean [2]. As the experiments [5, 6] show, the gas bubbles in the bottom are stable because of the films covering them, have mean dimensions of 0.01 to 0.1 mm, and fill the pores in the bottom sediments.

The following formula can be used to calculate the sound speed in three-phase bottom sediments:

$$c = (\rho\beta)^{-0.5}, \quad \rho = \sum_{i=1}^{i=3} \alpha_i \rho_i, \quad \beta = \sum_{i=1}^{i=3} \alpha_i/(\rho_i c_i),$$

where ρ is the density, β is the compressibility, α_i is the volume fraction of each component, and ρ_i and c_i are the densities and sound speeds in the components, respectively. For the gas component, $\rho_g = \rho_0(1 + 0.1h)$ and $\alpha_g = \alpha_0(1 - 0.1h)$, where ρ_0 and α_0 are the density and volume fraction at the atmospheric pressure and h is the sea depth.

Figure 1 shows the profiles of the sound speed in the bottom. These profiles are calculated according to the geological data [1–4]. The existence of the "soft" bottom leads to a change in the time and mode structure of the signal propagating over the bottom [7] and also to a change in the bottom reflection coefficient.

The idea of monitoring the thickness of the gas-saturated layer and the sound speed in it consists in measuring the spectrum of the sound reflection coefficient with the use of the anisotropy characteristic of ambient

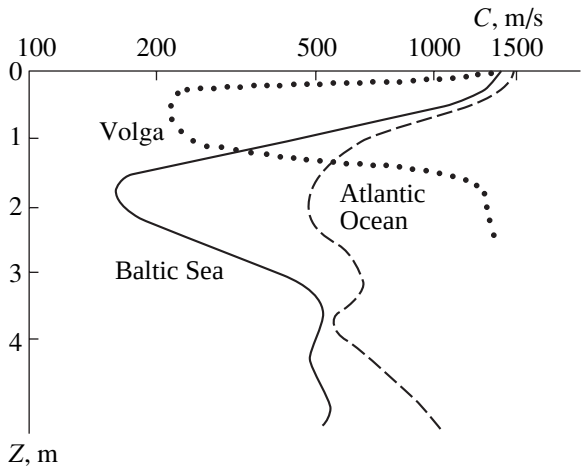

Fig. 1. Sound speed profiles in the gas-containing bottom.

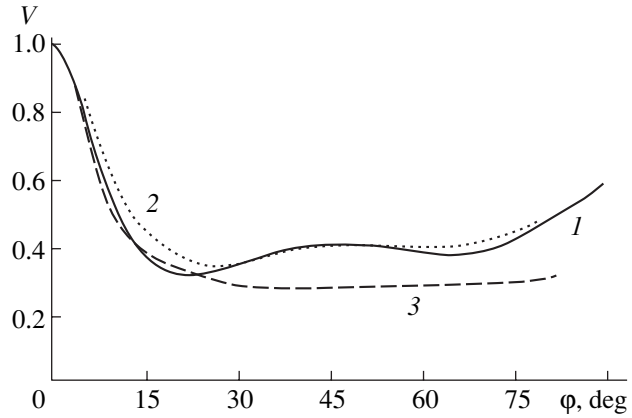

Fig. 2. Angular dependences of the bottom reflection coefficient. Simultaneous measurements with the use of the noise field at the frequencies of (*2*) 1 (dotted curve) and (*3*) 3 kHz and (*1*) by the conventional method at the frequency of 1 kHz.

noise [8]. The bottom reflection coefficient can be measured by a vertical antenna array that has two lobes in its directivity pattern. Within one of the lobes, the noise $I_{-\varphi}$ from the bottom is received, the other one serving to receive the noise $I_{+\varphi}$ from the surface. The bottom reflection coefficient $V_\partial(\varphi)$ (for sound pressure) can be calculated as

$$V_\partial^2(\varphi) = \frac{I_{-\varphi}}{I_{+\varphi}}\exp[\gamma(R_1 - R_0)], \qquad (1)$$

where φ is the grazing angle near the bottom, R_1 is the distance along the ray from the array to the first contact with the surface, R_0 is the length of the ray cycle, and γ is the absorption coefficient for the water.

Figure 2 illustrates the feasibility of the method. Similar data form the basis for the technique of monitoring the spectrum of the bottom reflection coefficient.

The reflection coefficient of the bottom in which a gas-saturated layer exists has a number of interesting features. Figure 3 shows the calculated dependences of the modulus $|V|$ of the reflection coefficient on the angle of incidence ϑ and the frequency f for the following medium model. The water half-space, with the density ρ_w and sound speed c_w, is bounded from below by the gas-saturated layer with the thickness g and the parameters ρ_g and c_g. In turn, the gas-saturated layer is bounded from below by a layer of sand of thickness d_s, which lies on an elastic half-space. Let us introduce the following notation: ρ_s and c_s for the density and sound speed in the sand and ρ_b, c_b, and c_t for the density and the velocities of the longitudinal and transverse waves, respectively, in the elastic half-space. In addition, let us introduce the impedances of the media: $Z = \rho_w c_w/\cos\vartheta$ for the water; $Z_g = \rho_g c_g/\cos\vartheta_g$ for the gas-saturated layer; $Z_s = \rho_s c_s/\cos\vartheta_s$ for the sand; and $Z_{bt} = Z_b\cos^2 2\vartheta_t + Z_t\sin^2 2\vartheta_t$ for the elastic half-space, where $Z_b = \rho_b c_b/\cos\vartheta_b$ and $Z_t = \rho_t c_t/\cos\vartheta_t$. The angles of incidence in the layers are governed by the Snell law:

$$k\sin\vartheta = k_g\sin\vartheta_g = k_s\sin\vartheta_s = k_b\sin\vartheta_b = k_t\sin\vartheta_t,$$

where $k = \omega/c_w$, $k_g = \omega/c_g$, $k_s = \omega/c_s$, $k_b = \omega/c_b$, and $k_t = \omega/c_t$.

In calculating the reflection coefficient V, we used the formulas of monograph [9] for layers lying on an elastic half-space:

$$V = (U_{wg} + V_{gs}e^{2i\varsigma_g g})/(1 + U_{wg}V_{gs}e^{2i\varsigma_g g}), \qquad (2)$$

where $\varsigma_g = k_g\cos\vartheta_g$; U_{wg} is the coefficient of reflection in the water from a half-space whose parameters are those of the gas-saturated layer,

$$U_{wg} = (Z_g - Z)/(Z_g + Z); \qquad (3)$$

and V_{gs} is the reflection coefficient for the wave that propagates in the half-space with the parameters of the gas-saturated layer and is reflected from the sand overlying the elastic half-space,

$$V_{gs} = (U_{gs} + V_{sb}e^{2i\varsigma_s d_s})/(1 + U_{gs}V_{sb}e^{2i\varsigma_s d_s}). \qquad (4)$$

Here, $\varsigma_s = k_s\cos\vartheta_s$ and $U_{gs} = (Z_s - Z_g)/(Z_s + Z_g)$ is the reflection coefficient for the wave that propagates in the medium with the parameters of the gas-saturated layer and is reflected from a half-space with the parameters of the sand. In turn, for the wave that propagates in the half-space of sand and is reflected from the elastic half-space, the reflection coefficient is given by the expression $V_{sb} = (Z_{bt} - Z_s)/(Z_{bt} + Z_s)$.

Equation (2) leads to a well-known property of the reflection coefficient for a half-wavelength layer: when the thickness g of the gas-saturated layer satisfies the equation $\varsigma_g g = m\pi$ (m is an integer number), the reflection in the water from the boundary between two layers occurs in the same way as the reflection from the sand layer lying on the elastic half-space (without the gas-saturated layer).

The results of the calculations are shown in Fig. 3a (for the man-made lake, see Fig. 1). The following parameters were specified in the calculations: $c_g = 200$ m/s, $\rho_g = 1.1$ g/cm^3, and $g = 1$ m for the gas-saturated layer; $c_s = 1700(1 - 0.018i)$ m/s, $\rho_s = 1.7$ g/cm^3, and $d_s = 100$ m for the sand layer; and $c_b = 6000(1 - 0.002i)$ m/s, $c_t = 3000(1 - 0.01i)$ m/s, and $\rho_b = 3$ g/cm^3 for the elastic half-space (basalt). The frequencies used in the calculations were much lower than the resonant frequencies of the gas bubbles.

The calculations reveal a number of features in the dependence of the reflection coefficient V on the angle ϑ and frequency f. Such features cannot be observed in the absence of the gas-saturated layer.

(i) The modulus of the reflection coefficient is close to unity elsewhere except for a narrow frequency band near its minimum.

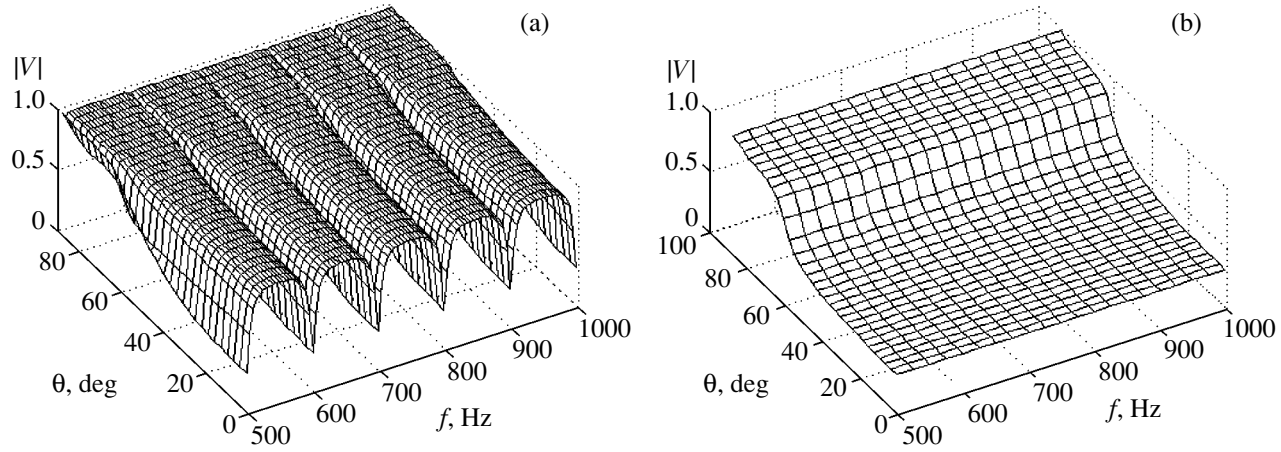

Fig. 3. Modulus of the reflection coefficient as a function of the angle of incidence and the frequency: (a) in the presence of the gas-saturated layer with the sound speed c_g = 200 m/s and (b) in the absence of the gas-saturated layer.

(ii) The dependence of $|V|$ on the angle ϑ manifests itself only in the vicinity of the minima of the modulus of the reflection coefficient.

(iii) The dependence of the reflection coefficient on frequency is close to a periodic one.

(iv) The frequency f at which $|V|$ reaches its minimum weakly depends on the angle of incidence ϑ.

For the sake of comparison, Fig. 3b presents the dependences of the modulus of the reflection coefficient on angle and frequency for the case without the gas-saturated layer. The calculation shows that the resonant properties of the sand layer manifest themselves only at low frequencies, and, therefore, $|V|$ is frequency independent in Fig. 3b (f > 500 Hz). The comparison of Figs. 3a and 3b shows how strongly the gas-saturated layer influences the bottom reflection.

All the aforementioned features of the reflection coefficient are caused by the fact that the sound speed in a gas-saturated medium is much lower than in water. From the Snell law $\sin\vartheta_g = (c_g/c_w)\sin\vartheta$, it follows that the angle ϑ_g is always small in the gas-saturated layer. In particular, for the example of Fig. 3a, the maximal value of this angle is 7.7° for the wave propagating from the water to the gas-saturated layer. Therefore, the condition $Z \gg Z_g$ is satisfied in a wide range of angles ϑ, and, according to Eq. (3), the reflection from the half-space with the parameters of the gas-saturated layer is approximately equivalent to the reflection from a pressure-release boundary ($U_{wg} \approx -1$). Furthermore, according to Eq. (2), the reflection from the layered medium with the gas-saturated upper layer is analogous to that from a pressure-release interface ($V \approx -1$).

Thus, the reflection coefficient of the bottom containing the gas-saturated layer is equal to –1 for a wide range of angles of incidence in the water. The only exception is the case when $\varsigma_g g = m\pi$. In this case, the modulus of the reflection coefficient reaches its minimal value, which is equal to the reflection coefficient of the bottom without the gas-saturated layer. This statement is confirmed by Fig. 3a (f = 500 Hz, the first curve).

The main feature of the coefficient of reflection from the bottom with the gas-saturated layer is its frequency dependence. According to Fig. 3a, $|V|$ is a nearly periodic function of frequency with the period $\Delta f \approx c_g/(2g)$, which is equal to 100 Hz in our case. The frequency f_m corresponding to the m-yth minimum in the modulus of the reflection coefficient is expressed as

$$f_m = \frac{mc_g}{2g}\Big/\sqrt{1-\left(\frac{c_g}{c_w}\sin\vartheta\right)^2}. \qquad (5)$$

This frequency is nearly independent of the angle of incidence ϑ of the wave. Again, such an independence is a consequence of the smallness of the ratio (c_g/c_w). By expanding the right-hand side of Eq. (5) into a series in terms of the small parameter (c_g/c_w), we arrive at the approximate expression

$$f_m \approx f_{m0}(1 + 0.5(c_g/c_w)^2\sin^2\vartheta),$$

where $f_{m0} = mc_g(2g)$ denotes the frequency that corresponds to the minimum in the modulus of the reflection coefficient at normal incidence (ϑ = 0). The frequency f_m calculated at the incidence angle $\vartheta = \pi/2$ differs from f_{m0} by a value not exceeding $\delta f_m = 0.5(c_g/c_w)^2 f_{m0}$. For the calculations illustrated in Fig. 3a, the value of δf_m is as low as 10 Hz for $f_m \sim 1$ kHz. That is why the position of the minimum of $|V|$ is nearly independent of the angle of incidence.

A change in the parameters of the gas-saturated layer leads to a change in the frequency dependence of the reflection coefficient. Figure 4 shows the dependence of the modulus of the reflection coefficient on the incidence angle and on the frequency for the gas-saturated layer with the sound speed c_g = 400 m/s (other parameters are the same as in Fig. 3a). The period of the

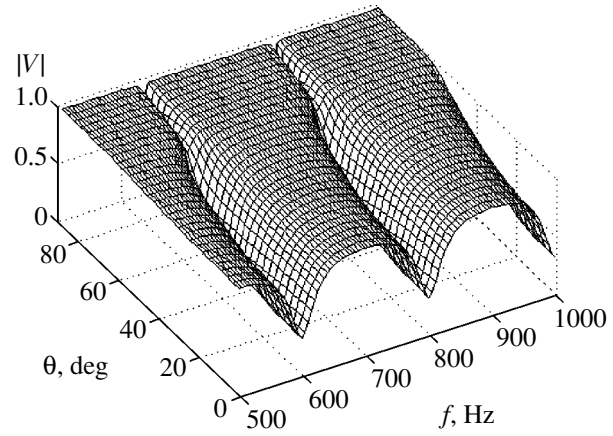

Fig. 4. Modulus of the reflection coefficient as a function of the angle of incidence and the frequency in the presence of the gas-saturated layer with the sound speed $c_g = 400$ m/s.

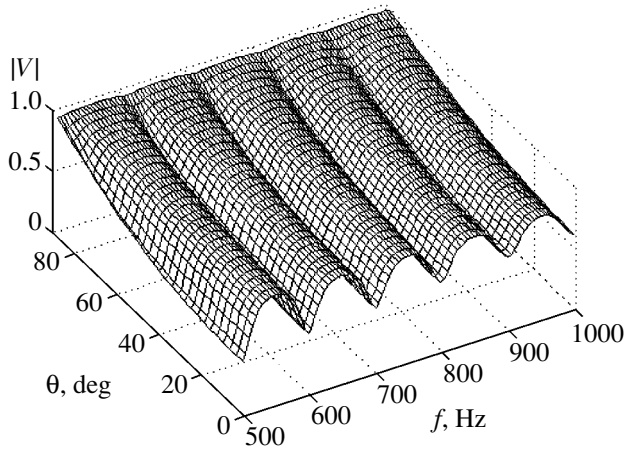

Fig. 5. Modulus of the reflection coefficient as a function of the angle of incidence and the frequency in the presence of the gas-saturated layer with sound absorption: $c_g = 200(1 - 0.02i)$ m/s.

frequency dependence of $|V|$, $\Delta f \approx c_g/(2g)$, is directly proportional to the sound speed c_g in the gas-saturated layer and inversely proportional to its thickness g.

In all our calculations, the sound absorption in the medium of the gas-saturated layer was ignored. Figure 5 illustrates the effect of absorption on the reflection coefficient. These data are calculated for $c_g = 200(1 - 0.01i)$ m/s. The comparison of Figs. 5 and 3a shows that the introduction of absorption leads to a decrease in the value of the reflection coefficient but does not change its frequency dependence.

Thus, the gas-saturated layer causes a substantial increase in the modulus of the bottom reflection coefficient and a periodic frequency dependence of this coefficient. This fact allows one to monitor the gas content of the bottom by measuring the frequency and angular dependences of the bottom reflection coefficient for the natural ambient noise produced by surface sources. For this purpose, one can use a rather simple technique [8] based on sensing the vertical directivity of the noise field in the basin. This technique has the following advantages: (i) it does not need any artificial sound sources; (ii) the ambient noise has a broad frequency band, which is required for obtaining the spectrum of the reflection coefficient; and (iii) no strict requirements are imposed on the sharpness of the main lobe of the vertical antenna array used to measure the anisotropy of the noise field. Actually, according to Figs. 3–5, the gas features are retained in the bottom in a wide range of angles, and, therefore, the array can be short with a broad main lobe of its directivity pattern.

To conclude with, we note that the results of the mathematical modeling and the aforementioned ideas concerning the measurement technique allow one to develop methods for an acoustical monitoring of the gas content in bottom sediments. However, the acoustical methods cannot serve to determine the composition of the gases, their origin, and the factors governing the variability in the gas content. Such questions can be answered by simultaneously studying each specific basin with biological, chemical, and acoustical methods to determine the criteria and thresholds for the environmentally oriented significance of the data obtained from the acoustical monitoring of the region.

ACKNOWLEDGMENTS

This work was supported by Russian Foundation for Basic Research, project no. 03-02-16565.

REFERENCES

1. A. A. Geodekyan, Yu. M. Berlin, *et al.*, in *Geochemistry of Waters of the Bottom Sediments in the Baltic Sea* (Inst. Okeanol. Ross. Akad. Nauk, Moscow, 1997), pp. 19–30.
2. A. M. Bol'shakov, in *Biogeochemistry of Boundary Regions of the Atlantic Ocean*, Ed. by E. A. Romankevich (Nauka, Moscow, 1994), pp. 353–359.
3. V. A. Kononov and M. M. Domanov, Okeanologiya (Moscow) **39** (3), 370 (1999).
4. V. N. Moskalenko, W. C. Pitman, and W. B. F. Ryan, Okeanologiya **36** (3), 462 (1996).
5. T. N. Gardner and G. C. Sills, J. Acoust. Soc. Am. **110**, 1878 (2001).
6. T. N. Gardner, J. Acoust. Soc. Am. **107**, 163 (2000).
7. A. V. Furduev, in *Proceedings of Conference on Applied Technologies of Hydroacoustics and Hydrophysics* (Morfizpribor, St. Petersburg, 2000), p. 147.
8. A. A. Aredov and A. V. Furduev, Akust. Zh. **40**, 200 (1994) [Acoust. Phys. **40**, 176 (1994)].
9. L. M. Brekhovskikh, *Waves in Layered Media*, 2nd ed. (Nauka, Moscow, 1973; Academic, New York, 1980).

Translated by E. Kopyl

Acoustical Physics, Vol. 50, No. 5, 2004, pp. 575–579. Translated from Akusticheskiĭ Zhurnal, Vol. 50, No. 5, 2004, pp. 671–675.

The Angular Dependence of the Coefficient of Sound Reflection from Anisotropic Volume Inhomogeneities of the Ocean

E. A. Kopyl and Yu. P. Lysanov

Andreev Acoustics Institute, Russian Academy of Sciences, ul. Shvernika 4, Moscow, 117036 Russia

e-mail: bvp@akin.ru

Received September 4, 2003

Abstract—The small perturbation method is used to consider the scattering of sound by random volume inhomogeneities of the ocean. The inhomogeneities are assumed to be horizontally anisotropic with their horizontal dimensions far exceeding the vertical ones. Expressions are obtained for the angular dependence of the scattering coefficient. Vertical and horizontal sections of the scattering pattern are presented, and the angular widths of its maxima are analytically estimated. © *2004 MAIK "Nauka/Interperiodica".*

The sound scattering is an important factor affecting the acoustic field formation in the ocean. Because of scattering, additional multipath propagation arises, space-time fluctuations of propagating waves appear, and the signal coherence decreases or completely disappears. The scattered fields are the main reason for sea reverberation, which reduces the operational efficiency of hydroacoustic systems of various purposes. On the other hand, the scattered signals contain useful information on the inhomogeneous parameters, which can be extracted by solving inverse problems of the scattering theory. Depending on the special situation, one or another scattering mechanism predominates. When sound propagates in the deep-water sound channel, random volume inhomogeneities of the water column are advanced to the foreground. Due to the volume scattering, part of the waves leak out of the channel, which considerably affects the laws of the sound intensity decay with distance and leads to an additional attenuation of the acoustic field in the water medium.

In our previous paper [1], we considered the sound scattering by oceanic volume inhomogeneities with spatial anisotropy of various types and analyzed the frequency dependences of the low-frequency reflection coefficient. In the present paper, we consider the angular dependences of the low-frequency volume scattering coefficient. In so doing, we restrict ourselves to not the most general but the quite realistic case of horizontally anisotropic inhomogeneities that are large-scale (relative to the sound wavelength) in the horizontal plane and small-scale in depth. Such a model corresponds to the modern representations of the volume inhomogeneities of the ocean as "lenses" or even "cakes" of shapes, for which the ratio of the horizontal scale to the vertical one is 10^2–10^3. According to [2], a considerable part of the fine-structured stratification of oceanic waters is formed by such diverse lenses. The highly anisotropic character of spatial fluctuations of the sound velocity in the ocean is confirmed by the field measurement data [3, 4].

Random inhomogeneities in the atmosphere and in the underwater bottom are of the same character.

The volume inhomogeneities of the ocean are "weak" ones: the mean square values of the refractive index fluctuations, $\langle\mu^2\rangle$, measured in various regions of the ocean vary from 1×10^{-10} to 8.4×10^{-8} [5]. In the case of weak inhomogeneities, the volume scattering coefficient can be calculated in the first approximation of the small perturbation method [6]:

$$m_v = 2\pi k^4 G(\mathbf{q}), \tag{1}$$

where $G(\mathbf{q})$ is the power spectrum of the refractive index fluctuations; $\mathbf{q} = \{\mathbf{q}_\perp, q_z\} = \mathbf{k} - \mathbf{k}_0$; $\mathbf{k}_0$ and $\mathbf{k}$ are the wave vectors of the incident and scattered waves, respectively; $k = |\mathbf{k}|$; and $\mathbf{q}_\perp = \{q_x, q_y\}$ and q_z are the components of the vector $\mathbf{q}$ in the horizontal plane and in the vertical direction (in depth).

As in [1], the correlation function of the refractive index fluctuations is given in the factorized form:

$$B(\rho) = \langle\mu^2\rangle N_1(\xi) N_2(\eta), \tag{2}$$

where $N_1(\xi)$ and $N_2(\eta)$ are the correlation coefficients in the horizontal plane and along the vertical, respectively; $\xi = \{\xi_x, \xi_y\}$ is the separation of the observation points along the horizontal axes x and y; and η is the separation in the depth. Such a representation of the correlation function corresponds to the above-mentioned features of the fluctuation field of the refractive index in the ocean and, in addition, considerably facilitates the calculations. Relationship (2) corresponds to the spectrum that is also represented as the product

$$G(\kappa_\perp, \kappa_z) = \langle\mu^2\rangle G_1(\kappa_\perp) G_2(\kappa_z) \tag{3}$$

of the horizontal $G_1(\kappa_\perp)$ and vertical $G_2(\kappa_z)$ spectra of the refractive index fluctuations with the horizontal

wave number $\kappa_\perp = \{\kappa_x, \kappa_y\}$ and the vertical wave number κ_z.

To describe the horizontal correlation, we assume the formula

$$N_1(X) = \frac{1}{2^{\nu-1}\Gamma(\nu)} X^\nu K_\nu(X), \quad (4)$$

where $K_\nu(X)$ is the Macdonald function of the order ν, $\Gamma(\nu)$ is the gamma function, $X = [(\xi_x/\xi_{0x})^2 + (\xi_y/\xi_{0y})^2]^{1/2}$ is the dimensionless argument, and ξ_{0x} and ξ_{0y} are the correlation scales (radii) along the horizontal axes. The corresponding spatial spectrum has the form [1]

$$G_1(\kappa_\perp) = \frac{\nu\xi_{0x}\xi_{0y}}{\pi(1 + \xi_{0x}^2\kappa_x^2 + \xi_{0y}^2\kappa_y^2)^{\nu+1}}. \quad (5)$$

Note that the correlation functions and the spectra of the form given by Eqs. (4) and (5) were successfully used in the theory of turbulence [7] and in treating the sound scattering by a layered bottom of the ocean [8]. The choice of the value of the free parameter, i.e., the index ν of the Macdonald function, allows us to approximate the correlation function or the spectrum of inhomogeneities that were measured experimentally in a finite interval of wave numbers κ.

In accordance with the above-described features of oceanic volume inhomogeneities, we assume that the latter are small-scale along the vertical: $\eta_0 q_z \ll 1$, where η_0 is the vertical correlation radius of fluctuations. In this case, the form of the vertical correlation coefficient is insignificant and the vertical spectral density at the resonance value of the vertical wave number of the inhomogeneities does not depend on q_z [1]:

$$G_2(q_z) \approx \frac{\eta_0}{\pi}. \quad (6)$$

Eventually, substituting Eqs. (5) and (6) at $\kappa_\perp = \mathbf{q}_\perp$ into expression (1), we obtain the following expression for the scattering coefficient:

$$m_\nu = \frac{2\nu}{\pi}\langle\mu^2\rangle \frac{\xi_{0x}\xi_{0y}\eta_0 k^4}{(1 + \xi_{0x}^2 q_x^2 + \xi_{0y}^2 q_y^2)^{\nu+1}}. \quad (7)$$

For the large-scale inhomogeneities in the horizontal plane, where $(\xi_{0i}q_i)^2 \gg 1$, $i = x, y$, such a scattering coefficient has the asymptotic $m_\nu \sim k^{-2\nu+2}$. Note that, in this limiting case, the angular and frequency dependences of the scattering coefficient are separated. Therefore, the sound attenuation coefficient β that appears because of the sound scattering by volume inhomogeneities in the underwater sound channel has the same frequency dependence as that of m_ν. For $\nu = 0.25$, this frequency dependence has the form $\beta \sim k^{3/2}$, which corresponds to the data of field measurements. The fact that the horizontal spectrum of inhomogeneities for such a value of ν asymptotically follows the power law with the nonintegral exponent may point to the fractal character of the inhomogeneities. This fact was first noted in [9] for the case of horizontally isotropic fluctuations of the refractive index.

In considering the angular dependences of the scattering coefficient, we divide both parts of expression (7) by factors independent of the angular variables and introduce the following notation for the scattering pattern:

$$\tilde{m}_\nu \equiv m_\nu \frac{\pi}{2\nu\langle\mu^2\rangle\xi_{0x}\xi_{0y}\eta_0 k^4}. \quad (8)$$

Now in the expression for $\tilde{m}_\nu$, we pass to angular variables according to the formulas $q_x = k(\cos\chi\cos\varphi - \cos\chi_0\cos\varphi_0)$ and $q_y = k(\cos\chi\sin\varphi - \cos\chi_0\sin\varphi_0)$, where χ_0, χ and φ_0, φ are the grazing and azimuth angles that characterize the directions of incidence and scattering (the values $\varphi_0 = 0$ and $\varphi = 0$ correspond to the direction of the x axis).

Analyzing the vertical angular dependence, we limit our consideration to the case $\varphi = \varphi_0 = 0$. In the plane of incidence ($\varphi = \varphi_0$), the scattering pattern has two maxima at $\mathbf{q}_\perp = 0$, which correspond to the directions of incidence and specular reflection from the horizontal plane. This fact was noted in [9] for the case of horizontally isotropic inhomogeneities, as well as in [10], where the scattering by fine-structured inhomogeneities of the ocean were analyzed. Figure 1 shows vertical sections of the scattering pattern by the plane of incidence, which were calculated for the grazing angle $\chi_0 = 6°$ of the incident wave for the value $\nu = 0.25$, which corresponds to the aforementioned 3/2-power law. The parameter of the curves is the longitudinal scale of inhomogeneities, $k\xi_{0x}$, whose values are indicated in the plots. The selected values of this parameter (100, 200, and 300) correspond to the case of large-scale inhomogeneities for a sound frequency of several hundred hertz. (For example, for the size of the inhomogeneities $\xi_{0x} = 150$ m, which is close to experimental estimates, these values correspond to sound frequencies of 159, 317, and 476 Hz, respectively.) As one would expect, the narrower the maxima of the pattern, the greater the longitudinal scale of inhomogeneities (in the case under consideration, $\varphi = \varphi_0 = 0$ and the value of $\tilde{m}_\nu$ does not depend on the transverse correlation radius ξ_{0y}).

The vertical sections of the scattering pattern are shown in Fig. 2 for the same value $\nu = 0.25$ at $k\xi_{0x} = 300$. The parameter of these curves is the grazing angle χ_0 of the incident radiation. The greater the grazing angle, the narrower the maxima of the scattering pattern. Two maxima merge into one at the horizontal incidence of sound on the inhomogeneities (at $\chi_0 = 0$).

In the limiting case $(\xi_{0i}q_i)^2 \gg 1$, $i = x, y$, the effective half-width $\Delta\chi$ of the maxima shown in Figs. 1 and 2 can

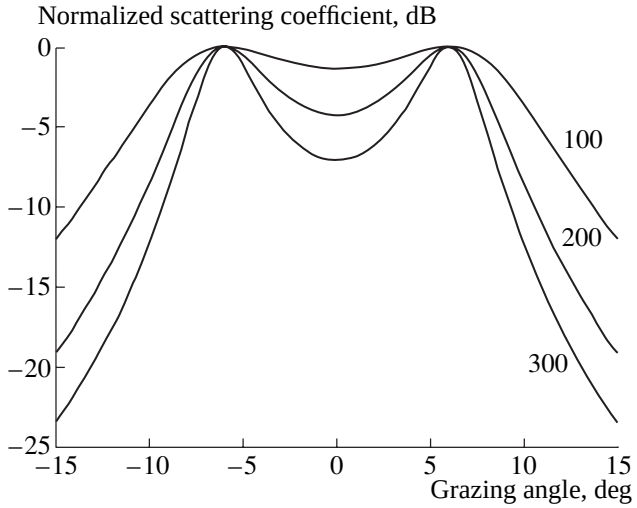

Fig. 1. Vertical sections of the scattering pattern by the plane of incidence at the grazing angle of the incident wave $\chi_0 = 6°$ and at $\nu = 0.25$. The parameter of the curves is the longitudinal wave size of inhomogeneities $k\xi_{0x}$ (indicated in the plot).

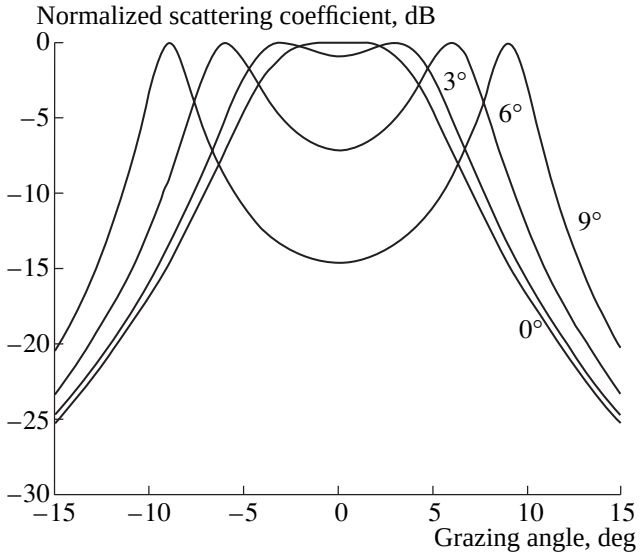

Fig. 2. Vertical sections of the scattering pattern at $\nu = 0.25$ and $k\xi_{0x} = 300$. The parameter of the curves is the grazing angle χ_0 of the incident radiation (shown in the plot).

be estimated analytically. From the twofold decrease in the scattering coefficient, it is found to be

$$\Delta\chi = \varepsilon^{1/2}[k\sin\chi_0(\xi_{0x}^2\cos^2\varphi_0 + \xi_{0y}^2\sin^2\varphi_0)^{1/2}]^{-1} \quad (9)$$

for $k\xi_0\sin\chi_0 \gg 1$ and

$$\Delta\chi = (4\varepsilon)^{1/4}[k^{1/2}(\xi_{0x}^2\cos^2\varphi_0 + \xi_{0y}^2\sin^2\varphi_0)^{1/4}]^{-1} \quad (10)$$

for $\chi_0 = 0$. In these formulas, as previously, $\varphi = \varphi_0$, while the quantity $\varepsilon = 2^{1/(\nu+1)}$ is determined by the value of the index ν. The values of the scattering coefficient at two maxima are the same and equal to

$$m_\nu = (2\nu/\pi)\langle\mu^2\rangle\xi_{0x}\xi_{0y}\eta_0 k_0^4. \quad (11)$$

In the case of horizontally isotropic inhomogeneities ($\xi_{0x} = \xi_{0y} = \xi_0$), estimates (9) and (10) coincide with those obtained in [1]: $\Delta\chi = \varepsilon^{1/2}/(k\xi_0\sin\chi_0)$ for $k\xi_0\sin\chi_0 \gg 1$ and $\Delta\chi = (4\varepsilon)^{1/4}(k\xi_0)^{-1/2}$ at $\chi_0 = 0$, and the value of the maxima is $m_\nu = (2\nu/\pi)\langle\mu^2\rangle\xi_0^2\eta_0 k_0^4$. The ratio of the maxima for horizontally isotropic and anisotropic inhomogeneities equals $\xi_0^2/(\xi_{0x}\xi_{0y})$; this ratio varies from 1 at $\xi_{0x} = \xi_{0y} = \xi_0$ to $\xi_{0x}/\xi_{0y} \gg 1$ for highly anisotropic inhomogeneities ($\xi_{0y} \ll \xi_{0x}$).

The half-width values of the maxima of the vertical section of the scattering pattern, which are given by Eq. (9), are shown in Fig. 3 versus the grazing angle χ_0 of the incident acoustic wave. As previously, we assume that $\nu = 0.25$ and $k\xi_{0x} = 300$ (at such values of the longitudinal size of inhomogeneities, the condition $k\xi_0\sin\chi_0 \gg 1$ is valid for the whole range of values of χ_0 that are specific for long-range sound propagation in the deep-water sound channel). Because, in obtaining Eq. (9), the value of the azimuth angle φ_0 was not fixed (this angle serves as a parameter for the curves in Fig. 3), the pattern width is determined by both scales ξ_{0x} and ξ_{0y}, or, to be more exact, by their ratio $\alpha = \xi_{0y}/\xi_{0x}$. The latter may be called the coefficient of horizontal anisotropy of inhomogeneities. Figure 3 shows the dependences that were obtained for $\alpha = 0.5$ (the

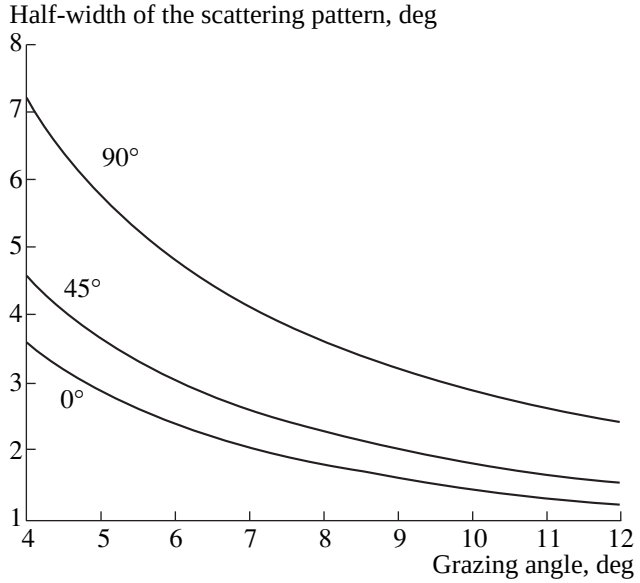

Fig. 3. Half-width (by the level of 0.5) of the maxima of the vertical section of the scattering pattern versus the grazing angle χ_0 of the incident acoustic wave for $\nu = 0.25$, $k\xi_{0x} = 300$, and $\alpha = \xi_{0y}/\xi_{0x} = 0.5$. The parameter of the curves is the azimuth angle φ_0 (shown in the plot).

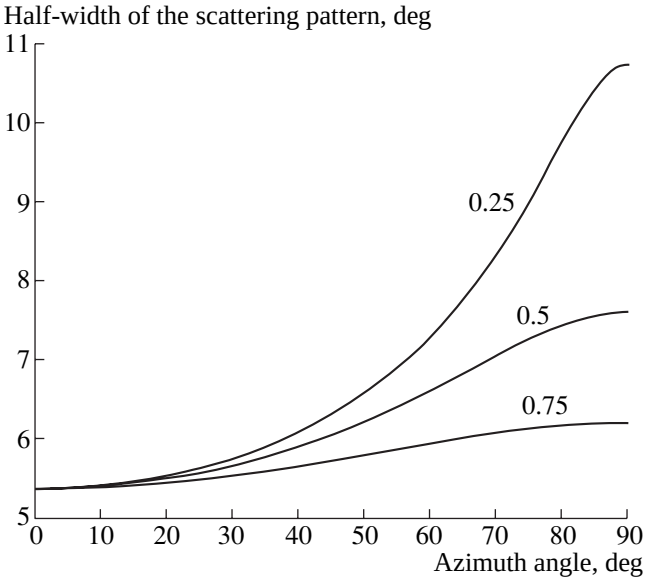

Fig. 4. Half-width (by the level of 0.5) of the maxima of the vertical section of the scattering pattern at horizontal incidence of sound ($\chi_0 = 0$) versus the azimuth angle φ_0 for $\nu = 0.25$ and $k\xi_{0x} = 300$. The parameter of the curves is the coefficient of horizontal anisotropy α (shown in the plot).

transverse size of inhomogeneities is two times smaller than the longitudinal one).

Figure 4 shows the half-width of scattering pattern maxima given by Eq. (10) for the horizontal sound incidence on the inhomogeneities. The values of ν and $k\xi_{0x}$ are the same as above. The azimuth angle φ_0 is represented by the abscissa, and the parameter of the curves is the coefficient of horizontal anisotropy α. It is seen that approximate values of the half-widths of maxima of the vertical section of the scattering pattern, which are presented in Figs. 3 and 4, agree well with the calculation results shown in Figs. 1 and 2.

Figure 5 exhibits the normalized scattering coefficients $\tilde{m}_\nu$ depending on the azimuth angle of scattering φ, which were calculated for the case of horizontal incidence of acoustic waves ($\chi_0 = 0$) in the direction of the x axis ($\varphi_0 = 0$) on large-scale inhomogeneities ($k\xi_{0x} = 300$) for $\nu = 0.25$. The parameter of the curves is the coefficient of horizontal anisotropy α (shown in the plots). It is seen that the azimuth dependences are very narrow, since the inhomogeneities are large-scale in the horizontal plane. The narrower these dependences, the less the inhomogeneities are elongated along the propagation track at a fixed longitudinal wave size $k\xi_{0x}$.

The same angular dependences are shown in Fig. 6 for the fixed value of the coefficient of anisotropy $\alpha = 0.5$ for three different values of the longitudinal wave size of inhomogeneities: $k\xi_{0x} = 100$, 200, and 300. The rest of the parameters are the same as in Fig. 5. As follows from the plots shown in Fig. 6, at a fixed ratio of the longitudinal and transverse correlation radii of inhomogeneities, the greater the wave size of inhomogeneities in the direction of incidence, the narrower the azimuth dependence.

The results of calculations presented above show which values can be reached by the angles of deviation of the sound trajectories in the ocean with anisotropic volume inhomogeneities. The relation of the angular

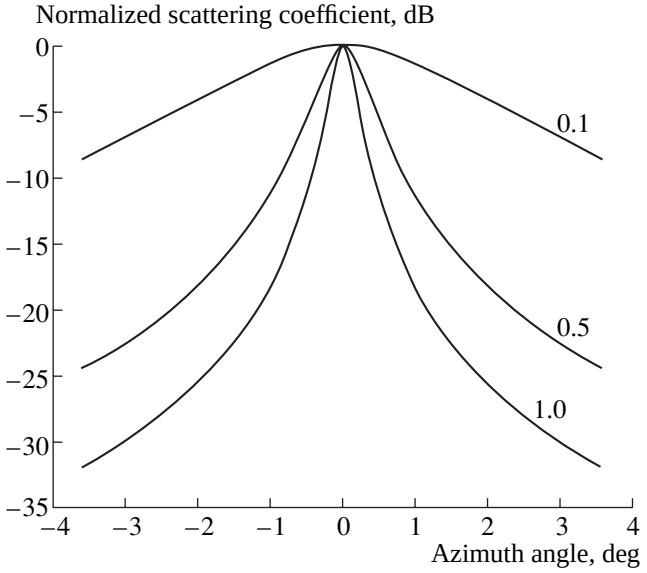

Fig. 5. Horizontal sections of the scattering pattern at horizontal incidence ($\chi_0 = 0$) of the acoustic wave versus the azimuth angle for $\varphi_0 = 0$, $\nu = 0.25$, and $k\xi_{0x} = 300$. The parameter of the curves is the coefficient of horizontal anisotropy α (shown in the plot).

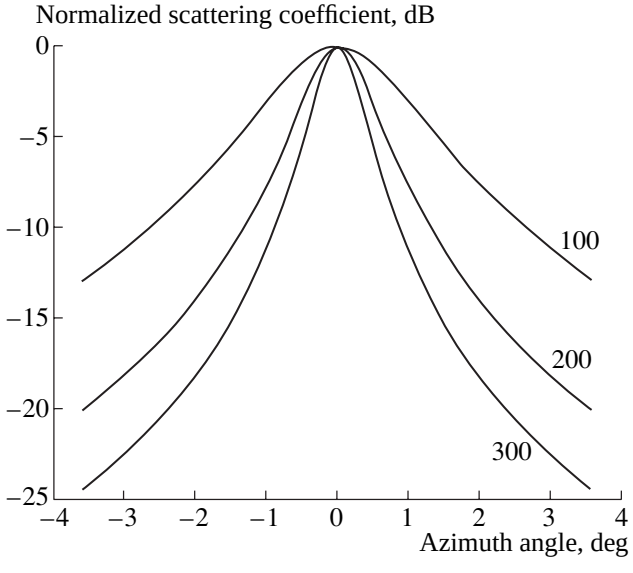

Fig. 6. Horizontal sections of the scattering pattern at horizontal incidence ($\chi_0 = 0$) of the acoustic wave for $\varphi_0 = 0$, $\nu = 0.25$, and $\alpha = 0.5$. The parameter of the curves is the longitudinal wave size $k\xi_{0x}$ of inhomogeneities (shown in the plot).

parameters of the scattering pattern (directions and widths of its maxima) and the limiting angles of rays trapped by the underwater sound channel can be used for estimating the part of the energy of acoustic waves that leaks from the channel under the influence of volume scattering. This leads to additional attenuation in the long-range sound propagation in the ocean.

In conclusion, we note that the work on the estimating the effects of sound scattering by inhomogeneities of the fractal type was initiated by L.M. Lyamshev, who, unfortunately, recently passed away [1, 9].

ACKNOWLEDGMENTS

This work was supported by the Russian Foundation for Basic Research, project no. 01–05–64711.

REFERENCES

1. E. A. Kopyl, Yu. P. Lysanov, and L. M. Lyamshev, Akust. Zh. **48**, 517 (2002) [Acoust. Phys. **48**, 453 (2002)].
2. K. D. Sabinin and M. G. Deev, Okeanologiya (Moscow) **31**, 714 (1991).
3. V. S. Gostev and R. F. Shvachko, in *Problems in the Ocean Acoustics*, Ed. by L. M. Brekhovskikh and I. B. Andreeva (Nauka, Moscow, 1984), pp. 153–164.
4. V. S. Gostev, N. G. Potylitsin, and R. F. Shvachko, in *Proceedings of XI All-Union Acoustical Conference* (Akust. Inst. Akad. Nauk SSSR, Moscow, 1991), Sect. D, p. 109.
5. *Acoustics of the Ocean*, Ed. by L. M. Brekhovskikh (Nauka, Moscow, 1974), Part 1 [in Russian].
6. L. M. Brekhovskikh and Yu. P. Lysanov, *Fundamentals of Ocean Acoustics*, 2nd ed. (Gidrometeoizdat, Leningrad, 1991; Springer, Berlin, 1991).
7. V. I. Tatarskiĭ, *Wave Propagation in a Turbulent Atmosphere* (Nauka, Moscow, 1967) [in Russian].
8. D. Li, G. V. Frisk, and D. Tang, J. Acoust. Soc. Am. **109**, 1384 (2001).
9. Yu. P. Lysanov and L. M. Lyamshev, Dokl. Akad. Nauk **366** (1), 36 (1999) [Dokl. Phys. **44**, 264 (1999)].
10. V. S. Gostev and R. F. Shvachko, Akust. Zh. **47**, 623 (2001) [Acoust. Phys. **47**, 540 (2001)].

Translated by Yu. Lysanov

Acoustical Physics, Vol. 50, No. 5, 2004, pp. 580–584. Translated from Akusticheskiĭ Zhurnal, Vol. 50, No. 5, 2004, pp. 676–681.

Analysis of Tracheal Noise of Forced Human Expiration According to Clinical Experimental Data

V. I. Korenbaum and I. A. Pochekutova

Il'ichev Pacific Oceanological Institute, Far East Division, Russian Academy of Sciences, ul. Baltiĭskaya 43, Vladivostok, 690041 Russia

e-mail: v-kor@poi.dvo.ru

Received November 18, 2002

Abstract—The analysis of tracheal noise of forced expiration is one of the promising methods for the diagnosis of bronchial patency disorders, which are a sign of such widespread diseases as bronchial asthma and chronic obstructive bronchitis. The aim of this study is the verification and refinement of the acoustic model of forced expiration (Korenbaum *et al.*, 1998) on the basis of a statistical analysis of clinical experimental data. A sample of 127 volunteers (from 18 to 74 years old) is used as an experimental statistical model: 34 persons suffering from bronchial asthma, 21 persons suffering from chronic obstructive bronchitis, 29 healthy persons, and 43 persons liable to developing the aforementioned diseases. The following parameters are analyzed: the total duration of noise of forced expiration at the trachea, the duration of wheeze of forced expiration with frequencies from 400 to 600 Hz, and the presence of narrowband high-frequency (over 600–700 Hz) spectral components at the end of forced expiration and during the whole expiration process. Reliable differences in the parameters of tracheal noise are revealed in the groups under study. The high prognostic value (a sensitivity of 89% and a specificity of 86%) of the parameters of tracheal noise of forced expiration, which were suggested *a priori* as the diagnostic parameters on the basis of the acoustic model (Korenbaum *et al.*, 1998), indirectly confirms the adequacy of this model. The biomechanical-pathophysiological interpretation of the occurrence of acoustic deviations in the experimental sample groups provides an opportunity to relate the parameters of tracheal noise of forced expiration to the degree of mechanical nonuniformity of the lungs. *© 2004 MAIK "Nauka/Interperiodica".*

INTRODUCTION

The auscultation of respiratory sounds is a traditional and highly efficient instrument for lung examination. Regretfully, it is still impossible to make it objective, i.e., to replace it by hardware acoustic means of examination, which prevents its implementation in modern evidence-based medical science. One of the versions of objective acoustic investigation of respiratory sounds is the analysis of tracheal noise. Opportunities for revealing bronchial patency disorders, which are a sign of such widespread diseases as bronchial asthma or chronic obstructive bronchitis, on the basis of tracheal noise analysis with the use of forced expiration as a provocative tool have been discussed for years. The potential simplicity, convenience, and safety of the method inspired many researchers, but it has turned out to be impossible to develop a reliable diagnostic procedure up to now. According to many authors, this situation is connected with insufficient understanding of the origin of tracheal noise of forced expiration, its connection with respiration biomechanics and clinical physiology/pathophysiology.

STATE OF THE ART

From the point of view of acoustics, the most probable mechanism of main tracheal noise is the turbulence of the air flow in the trachea and large bronchi [1–3]. Charbonneau *et al.* [4] and Soufflet *et al.* [5] have empirically determined that the flow rate in the range up to 2 l/s is connected functionally with the average amplitude and average frequency of the spectrum of tracheal noise. According to clinicians [6], lung sounds are also transmitted to a large extent to the trachea along the airways and walls of the bronchial tree. In particular, Takezawa *et al.* [7] arrived at a conclusion that wheezes at the trachea can be considered as a superposition of sounds from both lungs. At the same time, Mussel *et al.* [8] demonstrated that the sounds detected at the trachea and chest of healthy adults at flow rates of 1.6–2.6 l/s are independent biological signals with a small overlapping of spectral characteristics. Pasterkamp *et al.* [9], Sanchez *et al.* [10], and Kraman *et al.* [11] determined the influence of the resonances of the central respiratory tract on tracheal sounds in the case of a quiet breathing.

Tracheal noise accompanying forced expiration differs from the noise of quiet breathing in the higher intensity of the wideband component of the noise and the appearance of narrowband components, i.e., wheezes of forced expiration. While the rise of the wideband component is evidently connected with the increase in the turbulence of the air flow, opinions on the wheezes of forced expiration differ. Forgacs [12]

supposed that the wheezes of forced expiration are connected with vibrations of the walls of the respiratory tract. Analyzing the quantitative contents of the wheezes of forced expiration, Kraman [13] connected their origin with the large bronchi and the position of the equal pressure point. Charbonneau *et al.* [14] determined that the wheezes of forced expiration of healthy people manifest themselves after attaining the maximum flow rate. Gavriely *et al.* [15] made a conclusion that the wheezes of forced expiration are the manifestation of restriction of the air flow and do not differ in frequency from the wheezes observed in the case of obstructive lung disorders. Beck and Gavriely [16] demonstrated a high repeatability of the presence of the wheezes of forced expiration for healthy people (95%) and a similarity of the basic frequencies of the wheezes of forced expiration under equal conditions. Gavriely [17] noted that, for the generation of the wheezes of forced expiration, not only the restriction of the air flow is necessary, but the airway downstream from the compression point must be buckled but not completely collapsed, so that the opposing airway walls are close to each other but do not touch. This brings closer the opposite walls of the respiratory tract and, in the case of a preset flow rate, increases the linear velocity of the air flow. Both effects increase the Bernoulli forces and the probability of the appearance of wall vibrations of the respiratory tract. The establishment of these vibrations is the result of interaction between the forces generated by the gas flow, the static pressure drop, the elastic forces of the respiratory tract walls, and the longitudinal stress. The wall vibrations are considered as the source of the wheezes of forced expiration. The vortex shedding [18, 19] or the dynamic flutter [20] can be the mechanism responsible for the appearance of wall vibrations of the respiratory tract. It is still impossible to make a final decision in favor of one or another mechanism [21].

The imperfection of the aforementioned model concepts is confirmed by rather contradictory results of clinical experimental studies. For example, King *et al.* [22] and Schreur *et al.* [23] demonstrated that the phenomenon of the wheezes of forced expiration is observed not only for unhealthy patients but also for healthy people. At the same time, Ishikawa *et al.* [24] determined that the power maximum of the wheezes of forced expiration for healthy people is concentrated in the range of 300–500 Hz, while, for patients suffering from bronchial asthma, the second maximum is observed in the range of 1.3–1.5 kHz. Fiz *et al.* [25] noted the difference in the wheezes of forced expiration for patients suffering from bronchial asthma or chronic obstructive bronchitis and healthy people.

Earlier, we proposed a semiempirical model of noise generation at the trachea during forced expiration [26]. On the basis of this model, we determined the acoustic parameters of tracheal noise that are presumably significant for the diagnosis of bronchial patency disorders. The aim of the present work is to verify and refine the model [26] on the basis of a statistical analysis of clinical experimental data on the diagnosis of bronchial patency disorders.

ACOUSTIC MODEL

According to the physical model [26] of the trachea, the noises of a turbulent flow with wideband spectral peaks in the frequency ranges around 200 Hz (trachea, f_1) and 300–400 Hz (primary bronchi, f_2) are separated at the start of forced expiration. In the case of the development of a functional expiratory stenosis accompanying forced expiration, the wheezes of forced expiration (admittedly, a vortex shedding) are observed in the form of a "track" of intense narrowband spectral peaks f_3 in the frequency range of 400–600 Hz. Other observed tracks of narrowband spectral peaks f_4–f_7 (wheezes) are self-induced vibrations connected with the modulation of the air flow due to the wall vibrations of the respiratory tract. It is possible to distinguish the low-frequency "tracks" f_4 (lower than approximately 100 Hz), the mid-frequency "tracks" f_5 (100–400 Hz), and the high-frequency ones (over 600–700 Hz): f_6 at the end of expiration and f_7 at the start of expiration or during the whole length of forced expiration, $f_7 \longrightarrow f_6$. The acoustic parameters presumably important for the diagnosis of bronchial patency disorders are separated on the basis of the model. These are the time parameters, i.e., the total duration of the noise process T, the duration of the wheezes of forced expiration t, and the presence/absence of the narrowband spectral components f_6 and $f_7 \longrightarrow f_6$.

MATERIALS AND METHODS

A sample of 127 volunteers, males and females from 18 to 74 years old, was used as an experimental statistical model: 34 patients suffering from bronchial asthma, 21 patients suffering from chronic obstructive bronchitis, 29 healthy persons, and 43 persons liable to developing bronchial asthma or chronic obstructive bronchitis. The reference diagnosis of bronchial patency disorders was performed using computer spirography.

The recording and analysis of forced expiration noise (a sitting patient, a nasal clamp) were performed by an informational-measuring system [27]. The hardware of the system contained an acoustic sensor installed at the outer wall of the trachea (an electret microphone with a stethoscope head), a small tape recorder (the dynamic range was 46 dB and the system of automated level control was switched off), and a personal computer with a data acquisition board (the dynamic range was 72 dB). The software consisted of the TFGTEST application package. The sampling frequency of the recorded digital files was 8 kHz. Taking into account the insufficient stationarity of respiratory noise of forced expiration, as the major means of spectral evaluation of the signal we used a relief (waterfall)

Acoustic parameters of tracheal noise of forced expiration in the groups under examination

Groups	T (s)	T (s)	Occurrence of spectral components f_6 and/or $f_7 \longrightarrow f_6$ (%)
Patients suffering from bronchial asthma	1.4 (1.13; 1.76)* $n = 34$	0.97 (0.79; 1.41)* $n = 31$	74*
Patients suffering from chronic obstructive bronchitis	1.52 ± 0.42* $n = 21$	1.08 ± 0.32* $n = 20$	81*
Persons liable to developing bronchial asthma or chronic obstructive bronchitis	0.96 (0.83; 1.15)* $n = 43$	0.77 (0.62; 0.9)* $n = 38$	88*
Healthy people	0.81 ± 0.24 $n = 29$	0.49 ± 0.17 $n = 26$	38

* Reliability of differences ($p < 0.01$) is indicated with respect to the healthy group. The values of T and t for samples with a normal distribution are given in the form of ($M \pm \sigma$) and, for samples with the distribution different from normal, in the form of Me(Q25; Q75). The number n is the amount of sampling.

spectrum of the noise process, which provides an opportunity to divide the whole realization into quasi-stationary samples. A periodogram algorithm of the FFT was used for signal transformation at each interval. In the case of the FFT, signal subsamples with a length of 1024 points were transformed into 512 spectral readings. The averaging of subsample spectra within each sample was performed with a 50% overlapping. Weighing was performed by a Hamming window. The normalization of the relief spectrum with respect to the amplitude maximum was used. The dynamic range of representation of the relief spectrum was selected to be linear as a rule. The time parameters T and t were determined with the help of the cursor (the start and the end were determined by the level approaching the background). The spectral components f_6 and f_7 were identified by the user subjectively, by the appearance of characteristic "tracks," i.e., by the presence of the spectral peaks at subsequent time intervals with a no less than twofold excess over the level of the nearby background. In some cases, when the decision on the presence or absence of the "tracks" f_6 and f_7 seemed questionable because of the smallness of their amplitudes, a logarithmic scale was used for viewing (not greater than –24 dB of the maximum).

In connection with the problem of a correct performance of forced expiration, which is analogous to the one existing in spirography, for the analysis we selected the attempt with the maximum value of T from two or three records of forced expiration made for each patient.

The evaluation of the short-term reproducibility of acoustic time parameters was performed. For this purpose, in a group of three persons, 87 examinations were carried out during four weeks. The average variation coefficients were 10.4% for T and 19.7% for t.

In the statistical analysis (Statistica 5.0, StatSoft Inc.) of acoustic parameters, the normality of samples was determined according to the W-criterion by Shapiro and Wilk. If normal, the samples were characterized by the mean (M) and the standard deviation (σ). In the case of a distribution different from normal, the median (Me) and quartiles ($Q25$ and $Q75$) were used. A two-sided heteroskedastic t-test was used to evaluate the validity of the differences in the samples in the case of their normality. In the case of a distribution different from normal, the U-test by Mann and Whitney was applied. The significance level of differences between two values in percent was evaluated on the basis of the one-sided t-test.

RESULTS

The statistical results of examination of the experimental sample groups are given in the table. The results demonstrate the presence of reliable differences in the parameters between healthy people and patients suffering from bronchial asthma or chronic obstructive bronchitis, as well as between healthy people and persons liable to developing these disorders.

The acoustic diagnostic criteria for bronchial patency disorders, which were developed according to the groups of knowingly ill patients (who had independently confirmed bronchial patency disorders) and healthy people, are used further as an instrument of statistical modeling.

The probabilistic boundaries between the norm and pathology for the time parameters of noise were determined in the healthy group at the level $M + 1.65\sigma$ ($p < 0.05$). The corresponding threshold value of the parameter T was 1.199 s, and that of the parameter t, 0.773 s. Thus, the acoustic diagnostic criteria for bronchial patency disorders should be $T \geq 1.2$ s and/or $t \geq 0.78$ s.

The widespread occurrence of high-frequency spectral components f_6 and $f_7 \longrightarrow f_6$ in the groups of sick people and the relatively low occurrence of these components in the healthy group (see table) allowed us to develop an additional combined criterion. Analyzing the operating characteristic of detection, we determined that, in the presence of these components, the threshold

value of the parameter t can be reduced to 0.55–0.7 s. Taking into account the fact that the group of sick people was more representative than the healthy group, the decisive boundary was chosen to be at the upper limit of this interval. Thus, the third combined criterion was formulated: the presence of the high-frequency spectral components f_6 and/or $f_7 \longrightarrow f_6$ with $t > 0.7$ s.

The application of the set of the aforementioned acoustic diagnostic criteria (logical unification) provides a sensitivity (the probability of a correct detection of bronchial patency disorders) of 94% in the group of patients suffering from chronic obstructive bronchitis, 85% in the group of patients suffering from bronchial asthma, and 89% in the group of persons with the obstructive pathology on the whole (bronchial asthma and chronic obstructive bronchitis). The specificity (the probability of false detection of bronchial patency disorders in the healthy group) is 86%. From the comparison of the sensitivity of the analysis of tracheal noise of forced expiration with the sensitivity of computer spirography for persons with confirmed bronchial patency disorders, it was found that the method of studying the tracheal noise for patients suffering from bronchial asthma is 1.3 times more sensitive than spirography (85% vs. 65%, $p = 0.03$). In the case of patients suffering from chronic obstructive bronchitis, the sensitivities of the two methods cannot be reliably distinguished (95% vs. 100%, $p = 0.15$).

The relatively high operational characteristics revealed by analyzing the results for healthy and sick people with confirmed bronchial patency disorders allowed us to proceed to the acoustic examination of the group of persons liable to developing bronchial asthma or chronic obstructive bronchitis. This is most important for medical application, because the main problem of a timely detection of these lung diseases is the diagnosis of the initial bronchial patency disorders. Proceeding from the data of clinical examination, one could suspect the presence of initial bronchial patency disorders for some of the people from the group at risk of becoming ill. The acoustic examination of this group revealed its nonuniformity, which was not detected by computer spirography. The acoustic diagnostic criteria of bronchial patency disorders were detected for 23 persons from the group at risk (53%).

DISCUSSION

It is necessary to note that the very high (according to the medical criteria) prognostic significance (a sensitivity of 89% and a specificity of 86%) of identifying the knowingly sick (with independently confirmed bronchial patency disorders) and healthy persons in the experimental sample, which was achieved with the above acoustic model [26] using the parameters of tracheal noise of forced expiration proposed *a priori* as the diagnostic ones, indirectly confirms the adequacy of the model in use.

The data of the statistical modeling is also evidence of the fact that the occurrence of the proposed acoustic diagnostic criteria depends on the degree of bronchial patency disorders: 89% in the group of knowingly sick people, 53% in the risk group, and only 14% in the healthy group. Taking into account the biomechanical-pathophysiological concepts [28], the experimental results can be interpreted as follows.

It is known that tracheal noise is a superposition of sounds generated in both lungs [6, 7]. Even in the norm, lungs are characterized by a certain mechanical nonuniformity connected with the irregularity of emptying the lung units. Structural changes in the bronchial wall in the cases of bronchial asthma and chronic obstructive bronchitis lead to the formation of sections with increased resistance to air flow in the respiratory tract [28]. Most probably, the intense sounds of forced expiration are produced exactly in these sections of the bronchial tree due to the turbulence and viscoelastic interactions of the flow with the walls of the respiratory tract.

Wheezes of forced expiration for healthy people start approximately from the moment of the establishment of the maximum resistance zone (and the equal pressure point) in the lower part of the trachea, which is caused by the flow restriction in the case of a functional expiratory stenosis accompanying forced expiration. Further, the region of maximum resistance to the flow moves deeper into the bronchial tree, a uniform zone of maximum resistance of the respiratory tract being formed, probably, in the norm due to the automated synchronization of emptying parallel airways (the mechanism of equalization of the elastic recoil). In the case of pathology, the synchronization is violated and resistance maxima and, hence, intense sound effects are observed in many restricted sections of the bronchial tree. This is what leads to the prolongation of the wheezes of forced expiration (t) in full agreement with the acoustic model described above [26].

The high-frequency spectral components f_6 are formed when the integral air flow is already small and the local rate in the lung units with increased resistance to the air flow is still significant.

The appearance of the spectral component $f_7 \longrightarrow f_6$ can be connected with changes in the large respiratory pathways [19]. However, another mechanism is also possible. Since, in the case of bronchial patency disorders, the zone of establishment of the equal pressure point shifts to the peripheral parts of the bronchial tree, its pathologically changed sections can be compressed at the very start of forced expiration and produce wheezes lasting from the start to the end of the maneuver. This means that, in this case, the spectral component f_6 seems to shift to the start of forced expiration.

The increase in the total duration of the noise process (T) for sick people also can be caused by a delay in emptying the lung units with increased resistance to the air flow but at local rates smaller than in the case of f_6.

Taking into account the above consideration, the experimentally established fact of the much greater occurrence of the acoustic diagnostic criteria in the group of sick people with confirmed bronchial patency disorders in comparison with the risk group and especially the healthy group can be explained by the more pronounced and more extended structural changes in the walls of respiratory pathways of the bronchial tree, and, therefore, also greater mechanical nonuniformity of the lungs.

CONCLUSIONS

(1) The high prognostic validity of the parameters of tracheal noise of forced expiration, which were proposed *a priori* as the diagnostic ones on the basis of the acoustic model [26], indirectly confirms the adequacy of the model.

(2) The biomechanical-pathophysiological interpretation of the occurrence of the acoustic diagnostic criteria in the experimental sample groups provides an opportunity to connect the parameters of tracheal noise of forced expiration with the degree of mechanical nonuniformity of the lungs.

REFERENCES

1. J. Hardin and J. Patterson, Acta Astronaut. **6**, 1137 (1979).
2. D. E. Olson, D. Hartig, A. Taleb, and J. R. Hammersley, in *ILSA Proceedings* (Winnipeg, 1989), www.ilsa.cc.
3. I. V. Vovk, K. É. Zalutskiĭ, and L. G. Krasnyĭ, Akust. Zh. **40**, 762 (1994) [Acoust. Phys. **40**, 676 (1994)].
4. G. Charbonneau, M. Sudraud, and G. Soufflet, Bull. Eur. Physiopathol. Respir. **23** (3), 265 (1987).
5. G. Soufflet, G. Charbonneau, M. Polit, *et al.*, IEEE Trans. Biomed. Eng. **37** (4), 384 (1990).
6. U. H. Cegla, Prog. Respir. Res. **11** (10), 235 (1979).
7. Y. Takezawa, F. Shirai, S. Savaki, *et al.*, in *ILSA Proceedings* (London, 1980), p. 30, www.ilsa.cc.
8. M. J. Mussell and Y. Miyamoto, Front. Med. Biol. Eng. **4** (2), 73 (1992).
9. H. Pasterkamp, W. Wiebicke, and D. Daien, in *ILSA Proceedings* (Paris, 1987), p. 18, www.ilsa.cc.
10. I. Sanchez, R. E. Powell, and H. Pasterkamp, in *ILSA Proceedings* (Helsinki, 1992), p. 20, www.ilsa.cc.
11. S. S. Kraman, H. Pasterkamp, M. Kompis, *et al.*, Respir. Physiol. **111** (3), 295 (1998).
12. P. Forgacs, Chest **73**, 399 (1978).
13. S. S. Kraman, Respiration **44** (3), 189 (1983).
14. G. Charbonneau, N. Meslier, J. L. Racineux, *et al.*, in *ILSA Proceedings* (Cincinnati, 1984), p. 15, www.ilsa.cc.
15. N. Gavriely, K. B. Kelly, J. B. Grotberg, and S. H. Loring, J. Appl. Physiol. **62**, 2398 (1987).
16. R. Beck and N. Gavriely, Am. Rev. Respir. Dis. **141**, 1418 (1990).
17. N. Gavriely, in *ILSA Proceedings* (Helsinki, 1992), p. 40, www.ilsa.cc.
18. Y. Ploysongsang, R. P. Baughman, R. G. Loudon, and M. C. Rashkin, Respiration **54** (1), 50 (1988).
19. M. Mori, M. Ono, T. Hisada, *et al.*, Respiration **54** (2), 78 (1988).
20. N. Gavriely and J. B. Grotberg, J. Appl. Physiol. **64** (1), 17 (1988).
21. Y. Shabtai-Musih, J. B. Grotberg, and N. Gavriely, J. Appl. Physiol. **72**, 629 (1992).
22. D. K. King, B. T. Thompson, and D. C. Johnson, Ann. Intern. Med. **110**, 451 (1989).
23. H. J. Schreur, J. Vanderschoot, A. H. Zwinderman, *et al.*, Chest **106** (1), 91 (1994).
24. S. Ishikawa, H. Beauchamp, L. Kenney, *et al.*, in *ILSA Proceedings* (1993), www.ilsa.cc.
25. J. A. Fiz, R. Jane, A. Homs, *et al.*, Chest **122** (1), 186 (2002).
26. V. I. Korenbaum, A. A. Tagiltsev, Ju. V. Kulakov, *et al.*, J. Sound Vibr. **213** (2), 377 (1998).
27. Yu. V. Kulakov, A. A. Tagil'tsev, V. I. Korenbaum, and S. A. Kirichenko, Med. Tekh., No. 5, 20 (1995).
28. P. T. Macklem, Am. J. Crit. Care Med. **157**, 88 (1998).

Translated by M. Lyamshev

Acoustical Physics, Vol. 50, No. 5, 2004, pp. 585–595. Translated from Akusticheskiĭ Zhurnal, Vol. 50, No. 5, 2004, pp. 682–692.

Rayleigh Wave Attenuation Due to the Scattering by Two-Dimensional Irregularities of the Walls of an Empty Borehole

G. A. Maximov*, E. Ortega, E. V. Pod"yachev*, and M. R. Chillemi****

**Moscow Engineering Physics Institute, Kashirskoe sh. 31, Moscow, 115409 Russia*
e-mail: maximov@dpt39.mephi.ru
***Universitad Nacional de San Juan, Argentina*
Received September 19, 2003

Abstract—Attenuation of the Rayleigh waves propagating along an irregular surface of an empty borehole is investigated. This problem generalizes the problem on the attenuation of Rayleigh waves by an irregular boundary of a half-space. The technique used to evaluate the attenuation coefficient is based on the perturbation method and the mean field method. As a result, an expression is obtained that relates the partial attenuation coefficients of the surface Rayleigh wave to the scattering by the irregular surface of an empty borehole into the bulk longitudinal and transverse waves (the $R \longrightarrow P$ and $R \longrightarrow S$ processes) and into the surface Rayleigh waves (the $R \longrightarrow R$ processes). The frequency-dependent behavior of the partial attenuation coefficients is analyzed for different correlation functions of irregularities. *© 2004 MAIK "Nauka/Interperiodica".*

The theory of attenuation and dispersion of surface Rayleigh waves due to the scattering by surface irregularities is the subject of numerous publications [1–18]. In addition to theoretical aspects, the interest in this problem is governed by the fact that surface waves are currently used in different fields of science, for example, in geophysics and microelectronics. Most of the papers deal with Rayleigh waves traveling along surfaces that are on average flat. The attenuation coefficient and the phase velocity dispersion of the Rayleigh waves were studied in detail for the limiting cases of irregularities with small heights [1–3, 5–12, 14–17] and small curvatures [4, 8]. For the Rayleigh wave scattering by irregularities with heights small in comparison with the wavelength, the main result consists in that the forward scattering amplitude is equal to zero [1–3, 5–12, 14–17]. Therefore, the behavior of the frequency-dependent attenuation coefficient of the Rayleigh waves is governed by the correlation function of the irregular surface. In the case of correlation lengths small in comparison with the wavelength, this frequency-dependent behavior appears to be proportional to ω^4 [12–15] for two-dimensional surface irregularities and ω^5 [17] for three-dimensional irregularities.

At the same time, Rayleigh waves can travel not only along flat surfaces but also along curvilinear surfaces, in particular, along cylindrical ones. This particular case is of importance in borehole geophysics, where a surface Rayleigh wave may travel along an empty borehole. In the case of a fluid-filled borehole, the quasi-Rayleigh modes in the borehole are accompanied by a Stoneley wave whose properties—in particular, attenuation—are used to evaluate the filtration capacity characteristics of the surrounding medium [19]. The attenuation of eigenmodes traveling along the borehole can be caused not only by the fluid viscosity and fluid flows through the borehole walls but also by the scattering by the irregular surface of the borehole. Such a formulation of the problem is quite justified, because geophysical explorations of boreholes are usually carried out before the borehole is cased, and, in this situation, the borehole walls are always irregular.

Thus, the question arises as to how to correctly interpret the data on the borehole eigenmode attenuation in the presence of different physical mechanisms of attenuation.

In this paper, we consider a Rayleigh wave traveling along an empty borehole and evaluate its attenuation due to the scattering by irregularities of the borehole walls.

The mathematical formulation of the problem can be as follows. Consider an empty infinite borehole with irregular walls in an elastic medium (Fig. 1). We assume that the irregular surface of the borehole is spherically symmetric and can be described by the function $r = R + \eta(z)$, where R is the mean radius of the borehole and $\eta(z)$ is the random function specifying the borehole radius as a function of the coordinate along the borehole axis. The average height of irregularities $\sigma = \sqrt{\langle \eta^2(z) \rangle}$ is assumed to be small in comparison

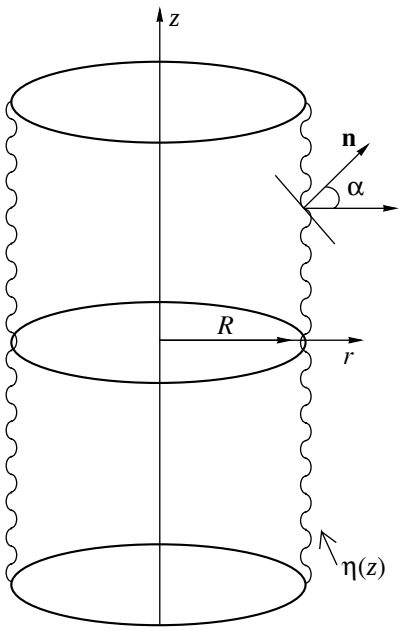

Fig. 1. Geometry of the problem.

with the wavelength λ: $\sigma/\lambda \ll 1$. The vector of the local normal to the surface has the form

$$\mathbf{n} = (\cos\alpha, \sin\alpha) = \left(1, -\frac{\partial\eta(z)}{\partial z}\right)\Big/\sqrt{1+\left(\frac{\partial\eta(z)}{\partial z}\right)^2}, \quad (1)$$

where α is the angle between vector **n** and the normal to the mean surface $\langle\mathbf{n}\rangle$.

Two types of waves can propagate in an elastic medium: longitudinal and transverse waves described by scalar (φ) and vector (**ψ**) potentials, respectively. Thus, the combined displacement of points in the medium **U** can be represented in the form $\mathbf{U} = \mathrm{grad}\,\varphi + \mathrm{curl}\,\boldsymbol{\psi}$, where φ and **ψ** are the scalar and vector potentials satisfying the wave equations

$$\begin{cases} \Delta\varphi - \dfrac{1}{c_l^2}\dfrac{\partial^2\varphi}{\partial t^2} = 0 \\ \Delta\boldsymbol{\psi} - \dfrac{1}{c_s^2}\dfrac{\partial^2\boldsymbol{\psi}}{\partial t^2} = 0 \end{cases}; \quad (2)$$

here, c_l and c_s are the longitudinal and transverse velocities of sound.

Consider the problem on the propagation of a Rayleigh wave along an empty borehole whose walls are characterized by a cylindrically symmetric (two-dimensional) irregularity. In this case, we deal with a cylindrically symmetric problem independent of azimuth and can describe the vector potential in terms of the azimuth component $\boldsymbol{\psi} = (0, \psi, 0)$ alone. The latter assumes that we consider only the waves polarized in the vertical direction.

The system of wave equations (2) can be represented in the cylindrical coordinate system in the form

$$\begin{aligned} &\left[\frac{1}{r}\frac{\partial}{\partial r}r\frac{\partial}{\partial r} + \frac{\partial^2}{\partial z^2} - \frac{1}{c_l^2}\frac{\partial^2}{\partial t^2}\right]\varphi(r,z,t) = 0 \\ &\left[\frac{1}{\partial r}\frac{1}{r}\frac{\partial}{\partial r}r + \frac{\partial^2}{\partial z^2} - \frac{1}{c_s^2}\frac{\partial^2}{\partial t^2}\right]\psi(r,z,t) = 0. \end{aligned} \quad (3)$$

The boundary conditions at the irregular borehole surface $r = R + \eta(z)$ are formulated as the absence of forces acting on this surface:

$$\begin{cases} \sigma_{rr}n_r + \sigma_{rz}n_z = 0 \\ \sigma_{zr}n_r + \sigma_{zz}n_z = 0, \end{cases} \quad (4)$$

where σ_{ij} is the stress tensor. At infinity ($r \longrightarrow \infty$), the wave field must satisfy the radiation condition. In terms of the potentials of longitudinal and transverse waves, the components of the stress tensor in the cylindrical coordinate system have the form

$$\begin{aligned} \sigma_{rr} &= 2\mu\left(\frac{\partial^2\varphi}{\partial r^2} - \frac{\partial^2\psi}{\partial r\partial z}\right) + \frac{\lambda}{c_l^2}\frac{\partial^2\varphi}{\partial t^2}, \\ \sigma_{rz} &= \mu\left(2\frac{\partial^2\varphi}{\partial r\partial z} + \frac{1}{c_s^2}\frac{\partial^2\psi}{\partial t^2} - 2\frac{\partial^2\psi}{\partial z^2}\right), \\ \sigma_{zz} &= 2\mu\left(\frac{\partial^2\varphi}{\partial z^2} + \frac{1}{r}\frac{\partial\psi}{\partial z} + \frac{\partial^2\psi}{\partial r\partial z}\right) + \frac{\lambda}{c_l^2}\frac{\partial^2\varphi}{\partial t^2}, \end{aligned} \quad (5)$$

where μ and λ are the Lamé coefficients and the second derivatives with respect to radius are expressed through Eqs. (3).

Using Eqs. (4), (5), and (1), we represent the boundary conditions in the form

$$\begin{aligned} &2\frac{\partial^2\varphi}{\partial r\partial t} - 2\frac{\partial^2\psi}{\partial z^2} + \frac{1}{c_s^2}\frac{\partial^2\psi}{\partial t^2} \\ &= -\left[\frac{\mu+\lambda}{c_l^2\mu}\frac{\partial^2\varphi}{\partial t^2} + \frac{1}{r}\left(\frac{\partial\psi}{\partial z} - \frac{\partial\varphi}{\partial r}\right)\right]\sin 2\alpha, \end{aligned} \quad (6a)$$

$$\begin{aligned} &2\frac{\partial^2\psi}{\partial r\partial z} + 2\frac{\partial^2\varphi}{\partial z^2} + \frac{2}{r}\frac{\partial\varphi}{\partial r} - \frac{1}{c_l^2}\frac{\partial^2\varphi}{\partial t^2} \\ &= -2\left[\frac{\lambda+\mu}{\mu c_l^2}\frac{\partial^2\varphi}{\partial t^2} + \frac{1}{r}\left(\frac{\partial\psi}{\partial z} - \frac{\partial\varphi}{\partial r}\right)\right]\sin^2\alpha. \end{aligned} \quad (6b)$$

Assuming that the wall irregularity is weak, we expand the boundary conditions in a series near the mean radius of the borehole $r = R$:

$$f(r = R + \eta(z)) = f(r = R) + \frac{\partial f}{\partial r}\Big|_{r = R} \eta(z) + \ldots.$$

Retaining only the first-order terms in $\eta(z)$ and its derivatives, we reduce the system of equations (6a), (6b) to the form

$$2\frac{\partial^2\varphi}{\partial r\partial z} - 2\frac{\partial^2\psi}{\partial z^2} + \frac{1}{c_2^2}\frac{\partial^2\psi}{\partial t^2}$$

$$= \left(-2\frac{\partial^3\varphi}{\partial r^2\partial z} + 2\frac{\partial^3\psi}{\partial r\partial z^2} - \frac{1}{c_s^2}\frac{\partial^3\psi}{\partial t^2\partial r}\right)\eta(z)$$

$$+ 2\left[\frac{\mu + \lambda}{c_l^2\mu}\frac{\partial^2\varphi}{\partial t^2} + \frac{1}{R}\left(\frac{\partial\psi}{\partial z} - \frac{\partial\varphi}{\partial r}\right)\right]\frac{\partial\eta}{\partial z}, \qquad (7)$$

$$2\frac{\partial^2\psi}{\partial r\partial z} + 2\frac{\partial^2\varphi}{\partial z^2} + \frac{2}{R}\frac{\partial\varphi}{\partial r} - \frac{1}{c_l^2}\frac{\partial^2\varphi}{\partial t^2}$$

$$= \left(-2\frac{\partial^3\psi}{\partial r^2\partial z} - 2\frac{\partial^3\varphi}{\partial r\partial z^2} - \frac{2}{R}\frac{\partial^2\varphi}{\partial r^2} + \frac{2}{R^2}\frac{\partial\varphi}{\partial r}\right)\eta(z).$$

As a result, we obtained the problem on the wave propagation along an empty borehole with regular walls but with complex random boundary conditions.

The solution to the problem can be sought by applying the Fourier transformation with respect to time ($t \Leftrightarrow \omega$) and axial coordinate z ($z \Leftrightarrow k$). In this case, wave equations (3) are reduced to the Helmholtz equations

$$\left(\frac{1}{r}\frac{\partial}{\partial r}r\frac{\partial}{r} - \nu_l^2\right)\varphi(r, k, \omega) = 0,$$
$$\left(\frac{\partial}{\partial r}\frac{1}{r}\frac{\partial}{\partial r}r - \nu_s^2\right)\psi(r, k, \omega) = 0, \qquad (8)$$

where $\nu_j = \sqrt{k^2 - k_j^2}$ for $|k| \geq \frac{\omega}{c_j}$ and $\nu_j = i\sqrt{k_j^2 - k^2}$ for $|k| \leq \frac{\omega}{c_j}$; here, $j = l, s$.

The general-form solutions to Eqs. (8) that satisfy the radiation condition at infinity $r \longrightarrow \infty$ have the form

$$\varphi(r, k, \omega) = C_1K_0(\nu_l r),$$
$$\psi(r, k, \omega) = C_2K_1(\nu_s r), \qquad (9)$$

where $K_0(z)$ and $K_1(z)$ are the zero- and first-order Macdonald functions, respectively, and C_1 and C_2 are arbitrary constants. Applying the above Fourier transformations to boundary conditions (7), we rewrite them in the form

$$2ik\frac{\partial\varphi}{\partial r} + \Omega_s\psi = \frac{1}{2\pi}\int_{-\infty}^{+\infty} dk'\eta(k')\left[-2i\tilde{k}\frac{\partial^2\tilde{\varphi}}{\partial r^2} - \tilde{\Omega}_s\frac{\partial\tilde{\psi}}{\partial r}\right.$$
$$\left. + \left(-(k_s^2 - k_l^2)\tilde{\varphi} + \frac{1}{R}\left(i\tilde{k}\tilde{\psi} - \frac{\partial\tilde{\varphi}}{\partial r}\right)\right)2ik'\right],$$
$$2ik\frac{\partial\psi}{\partial r} - \Omega_s\varphi + \frac{2}{R}\frac{\partial\varphi}{\partial r} = \frac{1}{2\pi}\int_{-\infty}^{+\infty} dk'\eta(k')\left[-2i\tilde{k}\frac{\partial^2\tilde{\psi}}{\partial r^2}\right. \qquad (10)$$
$$\left. + \tilde{\Omega}_s\frac{\partial\tilde{\varphi}}{\partial r} - \frac{2}{R}\frac{\partial^2\tilde{\varphi}}{\partial r^2} + \frac{2}{R^2}\frac{\partial\tilde{\varphi}}{\partial r}\right],$$

where we introduced the following designations:

$$\tilde{k} = k - k'; \quad \Omega_s = 2k^2 - k_s^2;$$
$$\tilde{\Omega}_s = 2\tilde{k}^2 - k_s^2; \quad \tilde{\nu}_j^2 = \tilde{k}^2 - k_j^2;$$

the tilde over a function means that we deal with a function of argument $\tilde{k}$, and the function

$$\eta(k) = \int_{-\infty}^{+\infty} dz e^{-ikz}\eta(z)$$

is the Fourier spectrum of the boundary profile.

Substituting solutions (9) into boundary conditions (10), we obtain a homogeneous system of integral linear boundary equations for the coefficients C_1 and C_2:

$$L_0(k)\mathbf{C}(k) = \frac{1}{2\pi}\int_{-\infty}^{+\infty} dk'\eta(k')L_1(k, \tilde{k})\mathbf{C}(\tilde{k}), \qquad (11)$$

where

$$\mathbf{C}(k) = \begin{pmatrix} C_1 \\ C_2 \end{pmatrix}$$

is the vector of coefficients,

$$L_0(k) = \begin{pmatrix} \left(\Omega_sK_0^l + \frac{2}{R}\nu_lK_1^l\right) & 2ik\left(\nu_sK_0^s + \frac{1}{R}K_1^s\right) \\ -2ik\nu_lK_1^l & \Omega_sK_l^s \end{pmatrix} \qquad (12)$$

is the matrix operator, and

$$L_1(k, \tilde{k}) = \begin{pmatrix} L_{11} & L_{12} \\ L_{21} & L_{22} \end{pmatrix} \qquad (13)$$

is the matrix operator whose components are

$$L_{11} = \left(\tilde{\nu}_l \tilde{K}_1^l \left(\tilde{\Omega}_s + \frac{4}{R^2}\right) + \frac{2}{R}\tilde{\nu}_l^2 \tilde{K}_0^l\right);$$

$$L_{12} = 2i\tilde{k}\left(\tilde{K}_1^s\left(\tilde{\nu}_s^2 + \frac{2}{R^2}\right) + \frac{1}{R}\tilde{\nu}_s \tilde{K}_0^s\right)$$

$$L_{21} = -2i\tilde{k}\left(\tilde{\nu}_l^2 \tilde{K}_0^l + \frac{\tilde{\nu}_l}{R}\tilde{K}_1^l\right) \tag{14}$$

$$-\frac{2ik'}{R}\tilde{\nu}_l \tilde{K}_1^l + 2ik'(k_s^2 - k_l^2)\tilde{K}_0^l;$$

$$L_{22} = \tilde{\Omega}_s\left(\tilde{\nu}_l \tilde{K}_0^s + \frac{\tilde{K}_1^s}{R}\right) - \frac{2}{R}k'\tilde{k}\tilde{K}_1^s.$$

For short, in Eqs. (13) and (14), we used the following designations of the Macdonald functions:

$$K_n(\nu_l R) = K_n^l, \quad K_n(\nu_s R) = K_n^s, \quad n = 0, 1.$$

Equation for the mean field. The integral matrix equation (11) can be solved by the mean field method. To this end, we represent the total field of coefficients **C** as the sum of the mean and random fields

$$\mathbf{C} = \langle \mathbf{C} \rangle + \mathbf{C}', \quad \langle \mathbf{C}' \rangle = 0 \tag{15}$$

and rewrite Eq. (11) in the symbolic form

$$L_0(k)\mathbf{C}(k) = L_1^*(k, k')\mathbf{C}(k'), \tag{16}$$

where we introduced the integral operator $L_1^* = \frac{1}{2\pi}\int_{-\infty}^{+\infty} dk' \eta(k') L_1(k, k')$.

Substituting expression (15) for the total field into Eq. (16) and averaging the result, in view of the fact that $\langle L_1^* \rangle = 0$ and $\langle \mathbf{C}' \rangle = 0$, we obtain

$$L_0(k)\langle \mathbf{C}(k) \rangle = \langle L_1^* \mathbf{C}' \rangle. \tag{17}$$

If we subtract Eq. (17) from the exact equation (16) for **C**', we find that the random component **C**' satisfies the equation

$$L_0 \mathbf{C}' = L_1^* \langle \mathbf{C} \rangle + (-\langle L_1^* \mathbf{C}' \rangle + L_1^* \mathbf{C}'). \tag{18}$$

Note that the term in parentheses can be small if either $\|L_0\| \gg \|L_1^*\|$ and the incoherent component of the field is small in comparison with the coherent component $|\mathbf{C}'| \ll |\langle \mathbf{C} \rangle|$ or the distances between the points at which the main portion of random field **C**' is rescattered are shorter than the correlation radius of the irregularities.

Neglecting in Eq. (18) the terms in parentheses and substituting the resulting random component **C**' into Eq. (17), we obtain the equation for the mean field

$$L_0(k)\langle \mathbf{C}(k) \rangle - \langle L_1^*(k, \tilde{k}) L_0^{-1}(\tilde{k}) L_1^*(\tilde{k}, \tilde{k}') \rangle \langle \mathbf{C}(\tilde{k}') \rangle = 0. \tag{19}$$

In the context of this approximation, the source of the random field is the scattered mean field and the source of the mean field is the scattered random field, which forms a self-consistent problem on the propagation of both mean and random fields.

Calculating the average operator $\langle L_1^*(k, \tilde{k}) L_0^{-1}(\tilde{k}) L_1^*(\tilde{k}, \tilde{k}') \rangle$, we obtain the equation for the mean field in the explicit form

$$[L_0(k) - \sigma^2 L_2]\langle \mathbf{C} \rangle = 0, \tag{20}$$

where $L_2 = \frac{1}{2\pi}\int_{-\infty}^{+\infty} dk' W(k') L_1^*(k, \tilde{k}) L_0^{-1}(\tilde{k}) L_1^*(\tilde{k}, k)$ and $W(k)$ is the Fourier spectrum of the correlation function $W(z)$: $\sigma^2 W(z - z') = \langle \eta(z)\eta(z') \rangle$.

Attenuation coefficient of the Rayleigh wave. Solutions satisfying the homogeneous matrix equation (20) correspond to the eigenmodes that can propagate along an empty borehole with irregular walls. The condition for the existence of these modes follows from the solution of the dispersion equation

$$\det[L_0(k) - \sigma^2 L_2] = 0, \tag{21}$$

which is the requirement that the determinant of the matrix in Eq. (20) be equal to zero. The second term of this equation is small ($\sigma/\lambda \ll 1$), so that we can expand Eq. (21) in this parameter to reduce it to the form

$$\det L_0(k) - \sigma^2 H(k) = 0, \tag{22}$$

where

$$H(k) = \frac{1}{2\pi}\int_{-\infty}^{+\infty} dk' W(k') \frac{M(k, \tilde{k})}{\det L_0(\tilde{k})},$$

$$M(k, \tilde{k}) = \sum_{i \neq j} (L_{0ii}(k) L_{2jj}(k, \tilde{k}) - L_{0ij}(k) L_{2ji}(k, \tilde{k})), \tag{23}$$

$$L_2(k, \tilde{k}) = L_1^*(k, \tilde{k}) L_0^{-1}(\tilde{k}) L_1^*(\tilde{k}, k).$$

In the case of weak scattering, condition $\|L_0\| \gg \|L_2\|$ holds, and we can solve the dispersion equation (22) by the perturbation method. The solution can be represented as $k = k_R + \delta k$, where δk is a small cor-

rection and k_R is the solution to the dispersion equation for the borehole with regular walls, $\det L_0(k) = 0$:

$$\det L_0(k) = K_1^l K_1^s \left(\Omega_s^2 \frac{K_0^l}{K_1^l} - 4k^2 \nu_l \nu_s \frac{K_0^s}{K_1^s} - \frac{2}{R} \nu_l k_s^2 \right). \quad (24)$$

This dispersion equation is well known [20]; it functionally depends on k^2, in which it has a sole real-valued root existing for frequencies exceeding certain critical cutoff frequency ω_0 [20]. Thus, two roots of the dispersion equation $k = \pm k_R(\omega)$, where $k_R = \omega/c_R(\omega)$, correspond to the Rayleigh waves propagating in opposite directions along an empty borehole with frequency-dependent velocity $c_R(\omega)$. In the case of large ratios of the borehole radius to the wavelength ($R/\lambda \gg 1$), the properties of the Rayleigh wave traveling along the borehole approach the properties of the Rayleigh wave on a flat surface, $c_R(\omega \longrightarrow \infty) \longrightarrow c_R$. In the vicinity of the cutoff frequency ω_0, the velocity of the Rayleigh wave tends to the velocity of the transverse wave: $c_R(\omega \longrightarrow \omega_0) \longrightarrow c_s$.

Substituting expression $k = k_R + \delta k$ in Eq. (22) and expanding operators L_0 and H around k_R, we obtain

$$\left.\frac{\partial \det L_0}{\partial k}\right|_{k = k_R} \delta k - \sigma^2 H(k_R) - \sigma^2 \left.\frac{\partial H(k)}{\partial k}\right|_{k = k_R} \delta k = 0. \quad (25)$$

The last term in Eq. (25) has the next order of smallness in comparison with the other two terms; consequently, we can neglect it. Thus, the correction to the wave number of the Rayleigh wave because of the scattering is given by the expression

$$\delta k = \sigma^2 \frac{H(k_R)}{\left.\dfrac{\partial \det L_0(k)}{\partial k}\right|_{k_R}}. \quad (26)$$

The real and imaginary parts of the wave number determine the phase velocity $c(\omega)$ and the attenuation coefficient $\alpha(\omega)$ of the wave:

$$k(\omega) = \frac{\omega}{c(\omega)} + i\alpha(\omega).$$

Since the unperturbed Rayleigh wave traveling along an empty borehole possesses a dispersion property but shows no attenuation, our main interest lies in the imaginary part of the wave number, which is responsible for the attenuation of the wave:

$$\alpha(\omega) = \mathrm{Im}\,\delta k = \sigma^2 \mathrm{Im} \frac{H(k_R)}{\left.\dfrac{\partial \det L_0(k)}{\partial k}\right|_{k_R}}. \quad (27)$$

To analyse Eq. (27), we introduce dimensionless variables by specifying the dimensionless wave number x as $k = k_s x$, where $k_s = \omega/c_s$ is the wave number of the transverse wave. With this substitution in operators $L_0(k)$ and $L_1^*(k, \tilde{k})$ given by Eqs. (12) and (13), the expression for the attenuation coefficient, after factoring out the factors K_1^l and K_1^s, takes the form

$$\alpha(\omega) = \sigma^2 k_s^4 \mathrm{Im} \frac{H(x_R)}{\left.\dfrac{\partial \det L_0(x)}{\partial k}\right|_{x = x_R}}, \quad (28)$$

where $k_R = k_s x_R$ and the operators appearing in Eq. (23) are expressed as

$$L_0 = \left(\frac{\omega}{c_s}\right)^2 \begin{pmatrix} \Omega_s^s \dfrac{K_0^l}{K_1^l} + \dfrac{2\nu_l^s}{r_s} & 2ix\left(\nu_s^s \dfrac{K_0^s}{K_1^s} + \dfrac{1}{r_s}\right) \\ -2ix\nu_l^s & \Omega_s^s \end{pmatrix};$$

$$\det L_0 = k_s^4 \left(\Omega_s^2 \frac{K_0^l}{K_1^l} - 4k^2 \nu_l^s \nu_s^s \frac{K_0^s}{K_1^s} - \frac{2}{r_s} \nu_l^s \right),$$

$$L_1(k, \tilde{k}) = \left(\frac{\omega}{c_s}\right)^3 \begin{pmatrix} L_{11} & L_{12} \\ L_{21} & L_{22} \end{pmatrix},$$

$$L_{11} = \tilde{\nu}_l \left(\tilde{\Omega}_s^s + \frac{2}{r_s}\left(\tilde{K}_l + \frac{1}{r_s}\right)\right),$$

$$L_{12} = 2i\tilde{x}\left(\tilde{\nu}_s^{s2} + \frac{\nu_s^s \tilde{K}_0^s}{r_s \tilde{K}_1^s} + \frac{2}{r_s^2} \right),$$

$$L_{12} = -2i\left(\tilde{x}\tilde{\nu}_l^s \tilde{K}_l + x'\left(\left(1 - \frac{c_s^2}{c_l^2}\right)\frac{\tilde{K}_0^l}{\tilde{K}_1^l} - \frac{\tilde{\nu}_l^s}{r_s} \right)\right),$$

$$L_{22} = \tilde{\Omega}_s^s \tilde{K}_s - \frac{2x'\tilde{x}}{r_s},$$

where

$$\nu_i^s = \sqrt{x^2 - \frac{c_s^2}{c_i^2}}, \quad \Omega_s^s = 2x^2 - 1, \quad r_s = Rk_s,$$

$$K_s = \frac{K_0^s}{K_1^s}\nu_s^s + \frac{1}{r_s}, \quad K_l = \frac{K_0^l}{K_1^l}\nu_l^s + \frac{1}{r_s}.$$

The imaginary part in the correction to the wave number appears due to the following singularities in the integrand of Eq. (23): (i) the Rayleigh poles $\tilde{k} = \pm k_R$, which are the roots of the dispersion equation $\det \det L_0(\tilde{k}) = 0$, and (ii) the branching points $|k| \le \dfrac{\omega}{c_l}$ and $|k| \le \dfrac{\omega}{c_s}$, which produce their contributions along the edges of the cut. According to these singularities, the attenuation coefficient can be represented as the sum of

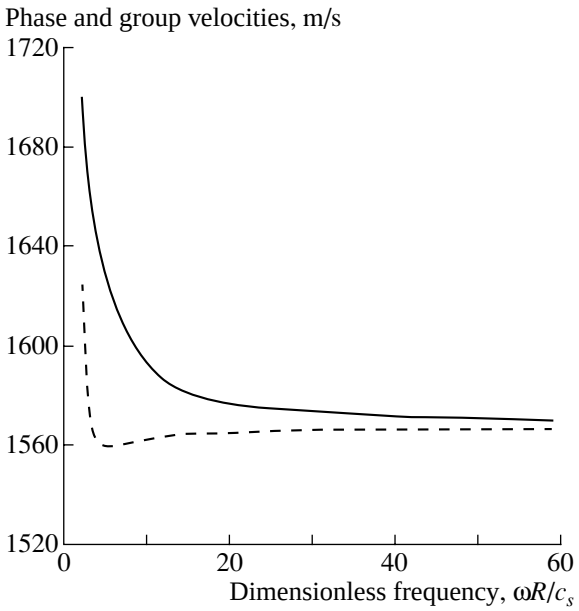

Fig. 2. Frequency-dependent phase (the solid line) and group (the dashed line) velocities of the Rayleigh wave traveling along the borehole.

partial attenuation coefficients $\alpha = \alpha_R + \alpha_l + \alpha_s$ caused by the scattering of the Rayleigh waves into the secondary Rayleigh waves (the R ⟶ R process), the bulk longitudinal waves (the R ⟶ P process), and the bulk transverse waves (the R ⟶ S process).

Consider the Rayleigh wave attenuation caused by the R ⟶ R process, i.e., by the scattering into the secondary Rayleigh waves. Here, we must take into account the waves scattered both forwards and backwards. In this case, the integral can be calculated by the residue theorem, and we can give an analytical expression for the attenuation coefficient α_R:

$$\alpha_R(\omega) = \frac{\sigma^2}{\left(\left.\frac{\partial \det L_0(x)}{\partial x}\right|_{x_R}\right)^2} \times k_s^4\{W(0)M(x_R, x_R) + W(2k_R)M(x_R, -x_R)\}. \quad (29)$$

The first term in the braces corresponds to the forward scattering of the Rayleigh wave, while the second term corresponds to the backscattering. Note that, in contrast to the case of a flat surface, the forward scattering coefficient is nonzero in the general case, which gives rise to certain specific features of the Rayleigh wave attenuation along the borehole in comparison with the case of a half-space.

If the spectrum of the correlation function is descending and the correlation lengths are sufficiently long, from Eq. (29) it follows that the main contribution to attenuation is made by the forward scattering and the attenuation coefficient α_R does not depend on the form of the correlation function.

Consider now the Rayleigh wave attenuation caused by the scattering into the bulk longitudinal and transverse waves (the R ⟶ P and R ⟶ S processes):

$$\alpha_\nu(\omega) = \frac{\sigma^2}{2\pi}\frac{k_s^4}{\left.\frac{\partial \det L_0(k)}{\partial k}\right|_{k = k_R}} \times \mathrm{Im}\int\limits_{c_s/c_R - 1}^{c_s/c_R + 1} dx' W(x' k_s)\frac{M(x, \tilde{x})}{\det L_0(\tilde{x})}, \quad (30)$$

where c_R is the velocity of the Rayleigh wave for the flat boundary.

In the region $x' \in \left[\frac{c_s}{c_R} - 1; \frac{c_s}{c_R} - \frac{c_s}{c_l}\right] \cup \left[\frac{c_s}{c_R} + \frac{c_s}{c_l}; \frac{c_s}{c_R} + 1\right]$, only the scattered transverse waves contribute to the attenuation, while, in the region $x' \in \left[\frac{c_s}{c_R} - \frac{c_s}{c_l}, \frac{c_s}{c_R} + \frac{c_s}{c_l}\right]$, mainly longitudinal waves contribute.

In view of the one-dimensional nature of the Rayleigh wave propagation along the borehole, we might expect that the low-frequency behavior of attenuation is described, as follows from Eqs. (29) and (30), by the function ω^4. However, the existence of a cutoff frequency below which no Rayleigh wave propagates along the borehole causes certain specific features not only in the R ⟶ R scattering processes but also in the R ⟶ P and R ⟶ S scattering processes. Moreover, in contrast to the problem with the half-space, where the sole parameter with the dimension of length was the correlation length of irregularities a, the case of the borehole is additionally characterized by a second parameter, namely, the borehole radius R. This fact determines a more variable behavior of the attenuation coefficient, depending on the relationship between these and other parameters of the problem. Below, we illustrate the frequency-dependent behavior of the partial attenuation coefficients for several specific cases taken as examples. We consider three correlation functions of different forms, whose spatial spectra radically differ in the short-wave region:

(i) the Gaussian correlation function $W(x) = \exp(-x^2/a^2)$, $W(k) = a\sqrt{\pi}\exp(-(ka)^2/4)$;

(ii) the exponential correlation function $W(x) = \exp(-|x|/a)$, $W(k) = a/((ka)^2 + 1)$; and

(iii) the quasi-periodic correlation function $W(x) = \exp(-|x|/a) + \sin\frac{|x|}{a}$, $W(k) = 4a/((ka)^4 + 1)$.

For all above correlation functions, the parameter a is the characteristic correlation length.

Numerical calculations were carried out for an elastic medium with parameters c_l = 3 km/s, c_s = 1.7 km/s, and ρ = 2 g/cm^3 and a borehole radius R = 8 cm, with the use of the three above correlation functions for different ratios a/R. Figure 2 shows the results calculated with these parameters for the frequency-dependent phase $c_R^{ph}(\omega)$ and group $c_R^{gr}(\omega)$ velocities of the Rayleigh wave, which are determined by the relationships

$$c_R^{ph}(\omega) = \frac{\omega}{k_R(\omega)}; \quad c_R^{gr}(\omega) = \frac{1}{\dfrac{\partial k_R(\omega)}{\partial \omega}}.$$

The curves in Fig. 2 show that, in the high-frequency limit ($\omega R/c_s \geq 1$), the phase velocity tends to the velocity of the Rayleigh wave traveling along a plane boundary of the elastic half-space. In the low-frequency limit, the phase velocity tends to the velocity of the transverse wave in the elastic medium.

To analyze the relationship between the contributions of forward and backward scattering in the R ⟶ R scattering processes, Fig. 3 shows the curves $M(x_R, x_R)$ and $M(x_R, -x_R)$ on the linear and logarithmic scales. Figure 3a shows that, for high frequencies, when the wavelength is small in comparison with the borehole radius, the amplitude of the forward scattering $M(x_R, x_R)$ tends to zero, as is the case for the flat surface. Figure 3b shows that this amplitude decays according to the power law $(\omega R/c_s)^{-4}$.

Figures 4–6 show the characteristic frequency-dependent behavior of the normalized partial attenuation coefficient α_R calculated for the R ⟶ R scattering processes with the use of the three above correlation functions and three characteristic correlation lengths for each of them. The attenuation coefficient is normalized by the dimensionless factor $(\sigma^2 a/R^3)$; in addition, we use here the dimensionless frequency $(\omega R/c_s)$. These variables are convenient for analyzing the frequency-dependent attenuation coefficient as a function of the correlation radius a of irregularities.

Comparing the curves shown in Figs. 3–6, one can easily see that frequency-dependent behaviors of the attenuation coefficients appear to be qualitatively different for different correlation functions, especially in the high-frequency region. These differences are related to the backscattering, whose contribution to Eq. (29) at higher frequencies is proportional to the Fourier spectrum of the correlation function. The contribution of the forward scattering does not depend on the form of the correlation function and appears to be the same, correct to a normalizing factor, for all cases considered (the dashed line). Thus, if the Fourier spectrum of the correlation function decays faster than k^{-4} in the high-frequency region (correspondingly, for short correlation lengths), then the high-frequency behavior of the attenuation coefficient is governed by the forward scattering contribution (Fig. 4); otherwise, it is governed by the backscattering contribution (Fig. 5); and only in the intermediate case of the asymptotic behavior precisely proportional to k^{-4} does it depend on both contributions (Fig. 6). Basically, this feature offers a possibility to distinguish the contributions of the backscattering and the forward scattering from the frequency-dependent behavior of the coefficient $\alpha_R(\omega)$, thus obtaining more detailed information about the correlation properties of irregularities.

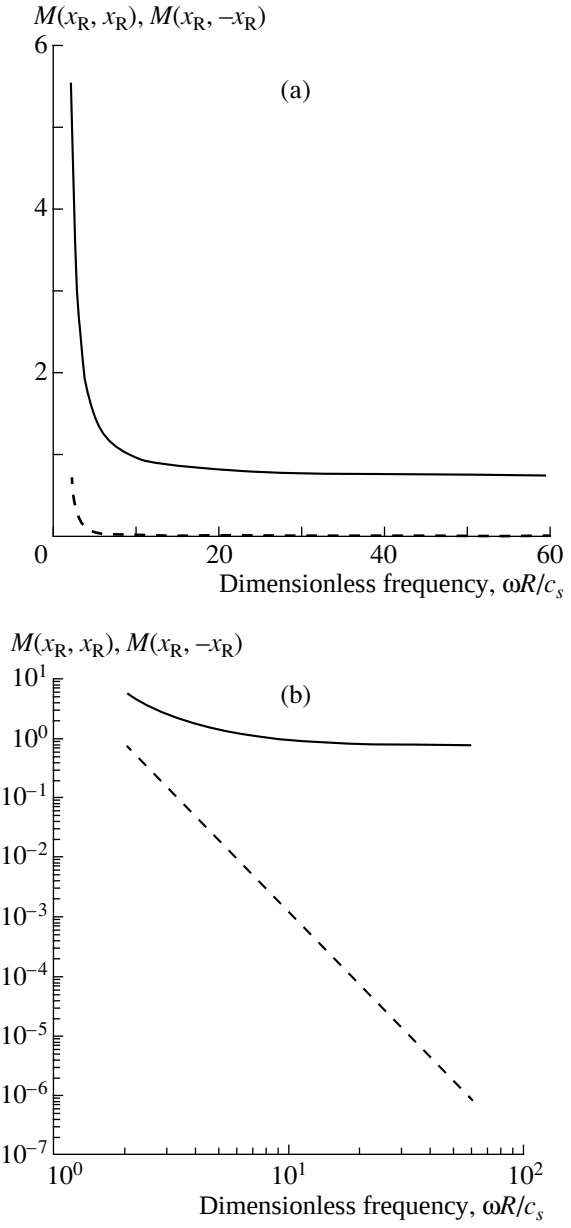

Fig. 3. Frequency-dependent forward scattering (the dashed line) and backscattering (the solid line) amplitudes on the (a) linear and (b) logarithmic scales.

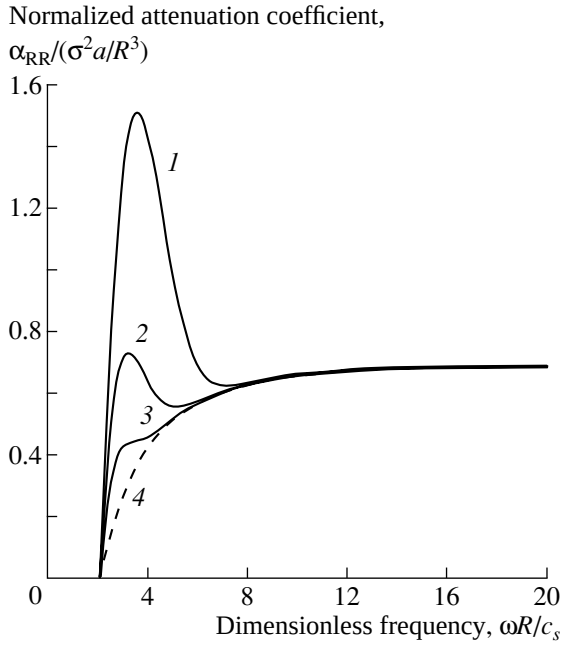

Fig. 4. Frequency-dependent partial attenuation coefficient α_{RR} for the Gaussian correlation function and different correlation lengths: a/R = (*1*) 0.4, (*2*) 0.5, and (*3*) 0.6. (*4*) The dashed line corresponds to the contribution of forward scattering.

Figures 7–9 show the relationship between the partial contributions of the R ⟶ R, R ⟶ P, and R ⟶ S scattering processes for the Gaussian correlation function with different correlation lengths. For the exponential correlation function, similar results are given in Figs. 10–12. In all cases, the partial contribution to the attenuation coefficient from the scattering into longitudinal waves (the R ⟶ S process) exceeds the contribution from the scattering into transverse waves (the R ⟶ P process); in the case of the Gaussian correlation function, the excess is most substantial. The ratio between the partial attenuation coefficients due to the scattering into volume waves and due to the scattering into the Rayleigh wave depends on both the form of the correlation function and the ratio between the correlation radius and the borehole radius. On the whole, the relative contribution of the scattering into the Rayleigh wave to the total attenuation coefficient increases with increasing ratio a/R. This behavior corresponds to an increase in the contribution of the forward scattering with increasing ratio a/R and reflects the adiabatic behavior of this scattering process. However, for higher frequencies, the predominance of the contributions of either scattering into bulk waves or scattering into Rayleigh waves depends on the form of the correlation function. For example, in the case of the Gaussian correlation function, the attenuation caused by the scattering into the Rayleigh wave begins to prevail as the ratio a/R increases (Fig. 9), while, in the case of the exponential correlation function, the scattering into bulk waves gives the predominant contribution at higher frequencies (Fig. 12).

Conclusions. In conclusion, we briefly formulate the main results obtained in the paper.

We analyzed the features of the Rayleigh waves traveling along the irregular boundary of an empty

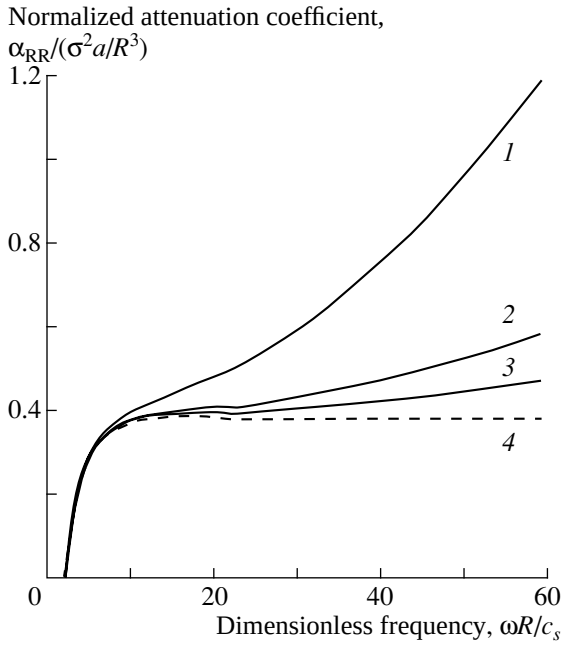

Fig. 5. Same as in Fig. 4, but for the exponential correlation function and different correlation lengths: a/R = (*1*) 5, (*2*) 10, and (*3*) 15.

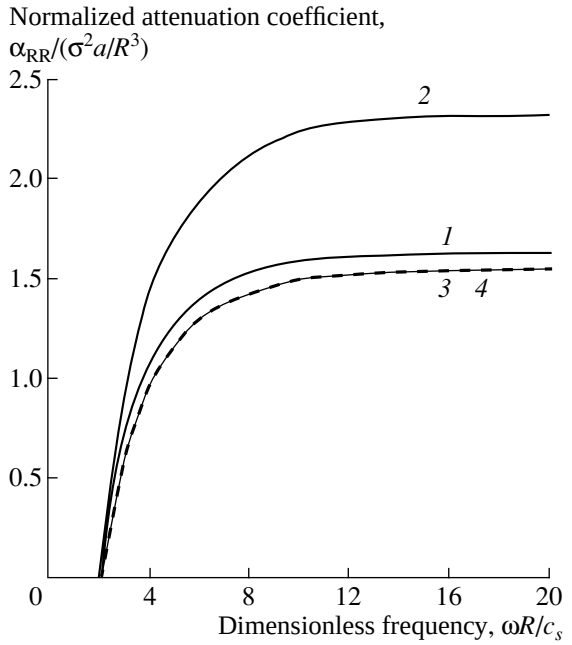

Fig. 6. Same as in Fig. 4, but for the quasi-periodic correlation function and different correlation lengths: a/R = (*1*) 0.5, (*2*) 1, and (*3*) 1.5.

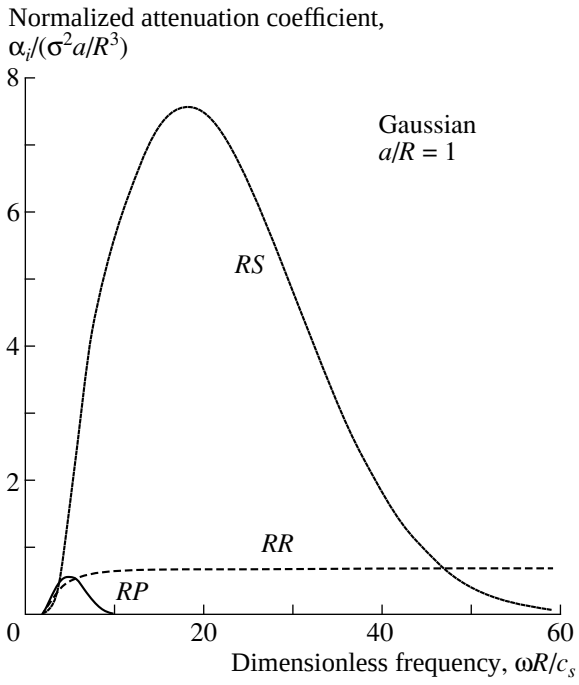

Fig. 7. Frequency-dependent partial attenuation coefficients of the Rayleigh wave because of the scattering processes *RR*, *RS*, and *RP* for the Gaussian correlation function with the ratio $a/R = 1$.

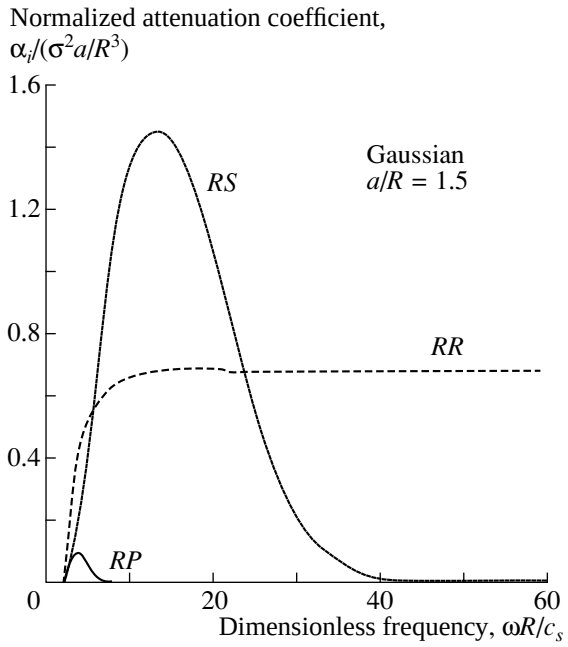

Fig. 8. Same as in Fig. 7, but for $a/R = 1.5$.

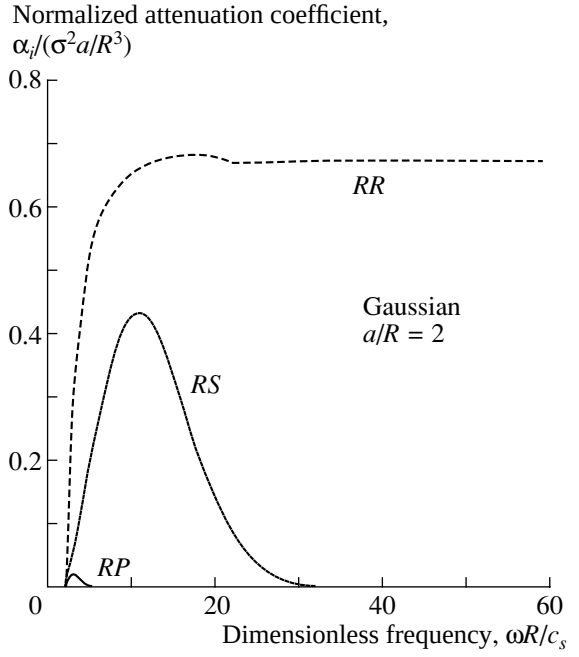

Fig. 9. Same as in Fig. 7, but for $a/R = 2$.

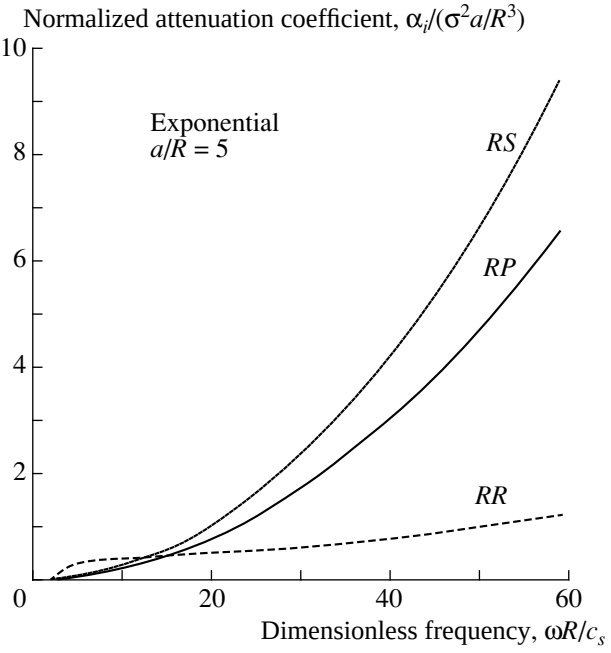

Fig. 10. Same as in Fig. 7, but for the exponential correlation function at $a/R = 5$.

borehole. The solution to the problem was obtained within the framework of the perturbation method and the mean field method.

We derived the dispersion equation describing the propagation of the Rayleigh waves along a borehole with irregular walls. We obtained the correction to the

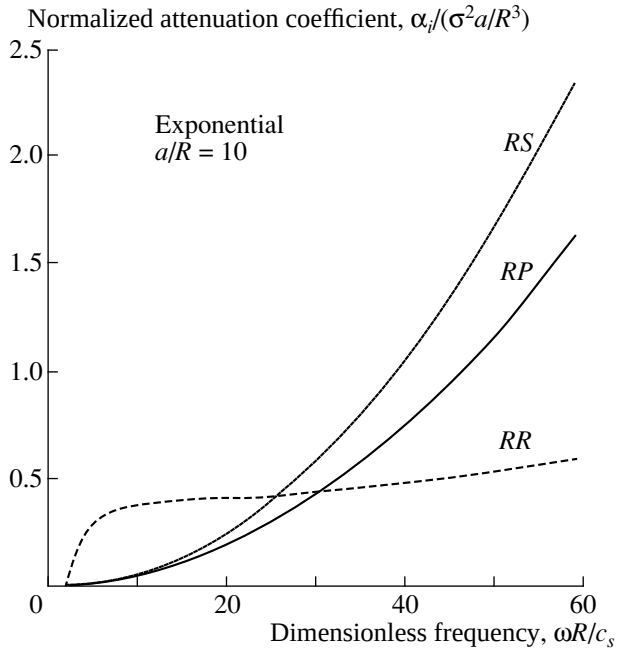

Fig. 11. Same as in Fig. 10, but for $a/R = 10$.

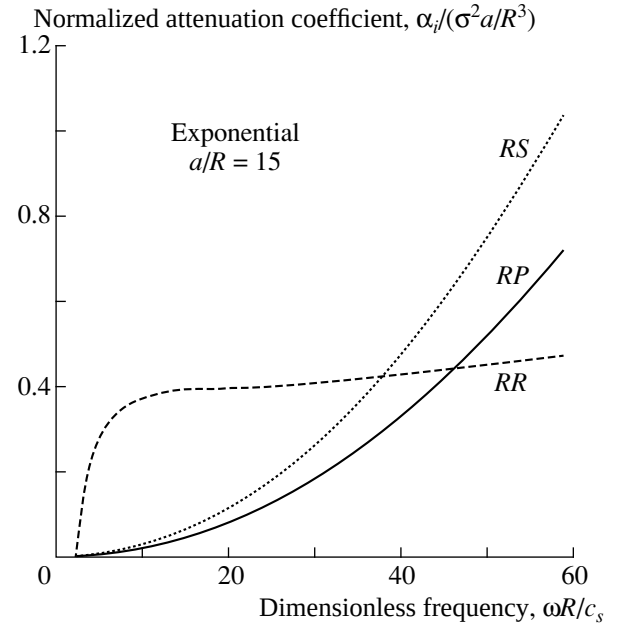

Fig. 12. Same as in Fig. 10, but for $a/R = 15$.

wave number caused by the scattering by irregularities of the boundary. The imaginary and real parts of this correction describe the attenuation and the dispersion of waves, respectively.

We showed that the total attenuation coefficient is representable in the form of the sum of partial attenuation coefficients caused by the scattering into secondary surface and bulk waves. Unlike the case of a plane boundary, the partial attenuation coefficient caused by the scattering into the Rayleigh wave depends not only on the backscattering but also on the forward scattering. Either the backscattering contribution or the forward scattering contribution may prevail in the partial attenuation coefficient α_R, depending on the ratio a/R and the form of the correlation function.

We calculated frequency-dependent partial attenuation coefficients for different correlation lengths by using three characteristic forms of correlation functions differing in the asymptotic behavior of their Fourier spectra in the short-wave region.

We showed that the behavior of the attenuation coefficient qualitatively depends on the form of the correlation function and the ratio of the correlation length to the borehole radius a/R. For short correlation lengths $a/R \le 1$, the attenuation caused by the scattering into the bulk (predominantly transverse) waves prevails. In this case, the frequency-dependent behavior of the attenuation coefficient is governed by the form of the correlation function. As the correlation length increases, the attenuation coefficient begins to depend mainly on the contribution of the scattering into the surface Rayleigh wave, which in this case is governed by the forward scattering.

REFERENCES

1. L. M. Brekhovskikh, Akust. Zh. **5**, 282 (1959) [Sov. Phys. Acoust. **5**, 288 (1959)].
2. F. Gilbert and L. Knopoff, J. Geophys. Res. **65**, 3437 (1960).
3. J. Hudson and L. Knopoff, Bull. Seismol. Soc. Am. **57** (1), 83 (1967).
4. A. D. Lapin, Akust. Zh. **15**, 387 (1969) [Sov. Phys. Acoust. **15**, 336 (1969)].
5. E. I. Urazakov and L. A. Fal'kovskiĭ, Zh. Éksp. Teor. Fiz. **63**, 2297 (1972) [Sov. Phys. JETP **36**, 1214 (1972)].
6. E. I. Urazakov, Fiz. Tverd. Tela (Leningrad) **18** (1), 47 (1976) [Sov. Phys. Solid State **18**, 26 (1976)].
7. A. A. Maradudin and D. L. Milles, Ann. Phys. (N.Y.) **100**, 262 (1976).
8. V. V. Krylov and V. E. Lyamov, Zh. Tekh. Fiz. **49**, 2514 (1979) [Sov. Phys. Tech. Phys. **24**, 1424 (1979)].
9. N. E. Glass, R. London, and A. A. Maradudin, Phys. Rev. B **24**, 6843 (1981).
10. V. G. Polevoĭ, Akust. Zh. **29**, 91 (1983) [Sov. Phys. Acoust. **29**, 52 (1983)].
11. N.-V. Chong, Ukr. Fiz. Zh. **28**, 1699 (1983).
12. A. G. Eguiluz and A. A. Maradudin, Phys. Rev. B **28**, 728 (1983).
13. Yu. Yu. Popov, Akust. Zh. **31**, 823 (1985) [Sov. Phys. Acoust. **31**, 506 (1985)].

14. X. Huang and A. A. Maradudin, Phys. Rev. B **36**, 7827 (1987).
15. S. Z. Dunin and G. A. Maksimov, Preprint No. 032-88, MIFI (Moscow Inst. of Engineering Physics, Moscow, 1988).
16. S. Z. Dunin and G. A. Maksimov, in *Abstracts of XIV All-Union Conference on Acoustic Electronics and Physical Acoustics of Solids* (Chisinau, 1989), p. 70.
17. V. V. Kosachev and A. V. Shchegrov, Ann. Phys. (N.Y.) **240** (2), 225 (1995).
18. F. Luzon, F. J. Sanchez-Sesma, J. L. Rodriguez-Zuniga, *et al.*, Geophys. J. Int. **129**, 571 (1997).
19. K. Tezuka, C. H. Cheng, and X. M. Tang, Geophysics **62**, 1047 (1997).
20. G. I. Petrashen', L. A. Molotkov, and P. V. Krauklis, *Waves in Layered-Homogeneous Isotropic Elastic Media* (Nauka, Leningrad, 1985), Vol. 2 [in Russian].

Translated by A. Vinogradov

Acoustical Physics, Vol. 50, No. 5, 2004, pp. 596–601. Translated from Akusticheskiĭ Zhurnal, Vol. 50, No. 5, 2004, pp. 693–699.

Diffraction Focusing of the Sound Field of a Vertical Antenna Array in a Range-Dependent Shallow Sea

Yu. V. Petukhov

Institute of Applied Physics, Russian Academy of Sciences, ul. Ul'yanova 46, Nizhni Novgorod, 603600 Russia
e-mail: petukhov@hydro.appl.sci-nnov.ru

Received August 4, 2003

Abstract—Using the adiabatic approximation for the mode representation of the sound field, it is shown that the efficiency of the diffraction focusing grows when the thickness of the isovelocity water layer increases with distance. © *2004 MAIK "Nauka/Interperiodica".*

The main features characterizing the formation of the zones of diffraction-caused focusing of sound fields in range-independent oceanic waveguides are considered in detail in [1–7], both analytically and numerically. However, for waveguides smoothly varying with distance, only general relations are obtained [8] for estimating the effect of horizontal inhomogeneities on the position and width of the focusing zones, as well as on the variations in the focusing efficiency. However, as in [1–7], the results of numerical modeling of sound propagation in specific ocean environments are important for smoothly varying waveguides as well. This importance is related to the need for a quantitative determination of the intensities of sound fields and their transformations in the diffraction-focusing zones as functions of the extent of horizontal inhomogeneity of the waveguide characteristics.

In view of the aforementioned facts, this work, which is actually an extension of [8], presents the results of a numerical modeling of the process of the diffraction-focusing zone formation in the simplest case: a Pekeris model waveguide with the depth of the water layer increasing with distance. The main objective of this study is the verification and quantitative description of the phenomenon predicted in [8], which consists in the enhancement of the focusing efficiency for the sound fields in oceanic waveguides whose vertical scale of inhomogeneity increases along the path.

As in [8], let us use the adiabatic approximation for the mode representation of the sound field in a waveguide smoothly varying with distance (the validity conditions [9, 10] of such an approximation are assumed to be met). Then, the dependence of the intensity $J(r, z)$ of the sound field on horizontal distance r and reception depth z can be expressed as follows:

$$J(r,z) = 2\pi p_0^2 \frac{R_0^2}{r} \times \left\{ \sum_{l=1}^{L} |A_l(r,z)|^2 + \sum_{l \neq l'}^{L} \sum_{l'=1}^{L} A_l(r,z) A_{l'}(r,z) \cos\left[\frac{2\pi r}{\bar{R}_{l,l'}} \right] \right\}. \quad (1)$$

Here,

$$A_l(r,z) = \psi_l(z_s,0)\psi_l(z,r)/\sqrt{k_l(r)} \quad (2)$$

is the amplitude of the lth mode, $k_l(r)$ is its horizontal wave number, $\psi_l(z, r)$ is the mode's orthonormal eigenfunction defined for the reference waveguide, $L = \max\{l\}$ is the number of the excited modes at the cyclic frequency of radiation ω, z_s is the source depth, and p_0 is the amplitude of the pressure perturbation produced by a point source in the corresponding homogeneous medium on a spherical surface of radius R_0. Expression (1) also involves the quantity

$$\bar{R}_{l,l'}(r) = r/\int_0^r \frac{dr}{R_{l,l'}(r)}, \quad (3)$$

which corresponds to the spatial interference scale for the modes of ordinal numbers l and l', where

$$R_{l,l'}(r) = \frac{2\pi}{k_l(r) - k_{l'}(r)}. \quad (4)$$

To proceed with the considerations, note an important fact concerning the most informative representation of the results of the numerical modeling. In describing the process of the diffraction-focusing zone formation in range-independent oceanic waveguides, the emphasis was always [1–7] made on the behavior of the wave front in the spatial distribution of the sound

field intensity, $J_0(r, z) = \frac{r}{R_0} J(r, z)/p_0^2$, normalized to the geometrical (cylindrical) spread. In studying the diffraction focusing in oceanic waveguides smoothly varying with distance, the additional geometrical spread (or the focusing) of the wave front, as compared to the cylindrical law, should be considered, this spread being caused by the change in the vertical scale of inhomogeneity with distance [10]. The additional variations of the wave front are fully governed by the amplitudes of the modes excited. Therefore, to solve the problem stated, it is advantageous to normalize the intensity of the sound field as follows:

$$J_H(r, z) = \frac{r}{p_0^2 R_0} S(r) J(r, z), \tag{5}$$

where

$$S(r) = \Phi(r = 0)/\Phi(r), \quad \Phi(r) = \frac{1}{H}\sum_{l=1}^{L}\int_0^H |A_l(r, z)|^2 dz, \tag{6}$$

and $H(r)$ is the varying thickness of the water layer. The comparison of Eqs. (1), (5), and (6) shows that the quantity $J_H(r, z)$ describes the sound field intensity normalized to its incoherent component averaged over the depth of the water layer.

In view of the aforementioned relations, let us consider the specific phenomena accompanying the diffraction-caused focusing of the sound field in waveguides smoothly varying along the path. For this purpose, the results of numerical modeling of the spatial distribution of the sound field intensity can be used for the Pekeris waveguide with increasing thickness of the water layer:

$$H(r) = \begin{cases} H_0, & 0 \le r \le r_0 \\ H_0\left(1 + \dfrac{r - r_0}{R_H}\right), & r_0 \le r \le r_s \\ H_s, & r \ge r_s. \end{cases} \tag{7}$$

Here, H_0 is the thickness of the water layer at the homogeneous and relatively shallow-water part of the waveguide, which is limited by r_0 in distance; H_s is the thickness of the homogeneous and relatively deep-water part of the waveguide, which begins from the distance r_s; and

$$R_H = \frac{r_s - r_0}{H_s - H_0}. \tag{8}$$

To more clearly define the zones of the diffraction focusing, let us assume that, as in [6, 7], tone sound signals are generated by a vertical antenna array with an aperture h, positioned at the depth $z_0 = H/2$ and distance $r = 0$. In the waveguide at hand, the diffraction-focusing zones are mainly produced by modes with low ordinal numbers (see [3]). Therefore, let us assume that there is no phase distribution of the excitation factor over the aperture, and, for the sake of simplicity, let us assume that the amplitude distribution is constant.

Then, the mode amplitude appearing in Eq. (1) can be expressed as

$$A_l(r, z) \Rightarrow \frac{A_l(r, z)}{\sin(kz_s\xi_l)} B_l(z_0, h). \tag{9}$$

Here, the amplitude $A_l(r, z)$, Eq. (2), corresponding to the point source is defined by the eigenfunctions of the reference waveguide:

$$\psi_l(z, r) = \frac{\sin(kz\xi_l)}{\sqrt{H F_l}}, \qquad F_l = \left\{1 + \frac{1}{b}\left(\frac{\varepsilon}{\chi_l}\right)^2 \frac{\sin^2\chi_l}{\sqrt{\varepsilon^2 - \chi_l^2}}\right\}^{1/2}. \tag{10}$$

For the mode of a certain ordinal number, the directivity pattern $B_l(z_0, h)$ of the array can be written as

$$B_l(z_0, h) = \frac{1}{k_0 h \xi_l(0)}\left\{\cos\left[k_0 z_0 \xi_l(0)\left(1 - \frac{h}{2z_0}\right)\right] - \cos\left[k_0 z_0 \xi_l(0)\left(1 + \frac{h}{2z_0}\right)\right]\right\}. \tag{11}$$

The following dimensionless quantities are introduced into Eqs. (9)–(11):

$$\xi_l(r) = \sqrt{1 - \left(\frac{k_l}{k}\right)^2}, \quad \chi_l(r) = kH\xi_l, \quad b = \rho_g/\rho_0, \qquad \varepsilon = kH(1 - n_g^2), \quad n_g = c_0/c_g, \tag{12}$$

where c_0 and c_g are the sound speeds in the water layer and liquid bottom and ρ_0 and ρ_g are the densities of these media, respectively. The horizontal wave numbers of the modes should be determined from the dispersion equation for the reference waveguide [9]:

$$\frac{b\chi_l}{\tan\chi_l} + \sqrt{\varepsilon^2 - \chi_l^2} = 0. \tag{13}$$

Note that, in the situation considered (see [7]), the additional ("purely" geometrical) spread of the mode wave fronts, which is caused by the increase in the water layer thickness with distance within $r_0 \le r \le r_s$, follows a similar "cylindrical" law, $1/\sqrt{H}$, for the modes of relatively low numbers and $l/kH \ll 1$. This conclusion can be easily drawn from Eq. (10) on the assumption that the bottom is perfectly rigid ($1/b = 0$, $F_l = 1$). Therefore, Eq. (6) yields the approximate dependence $S(r) \approx H/H_0$

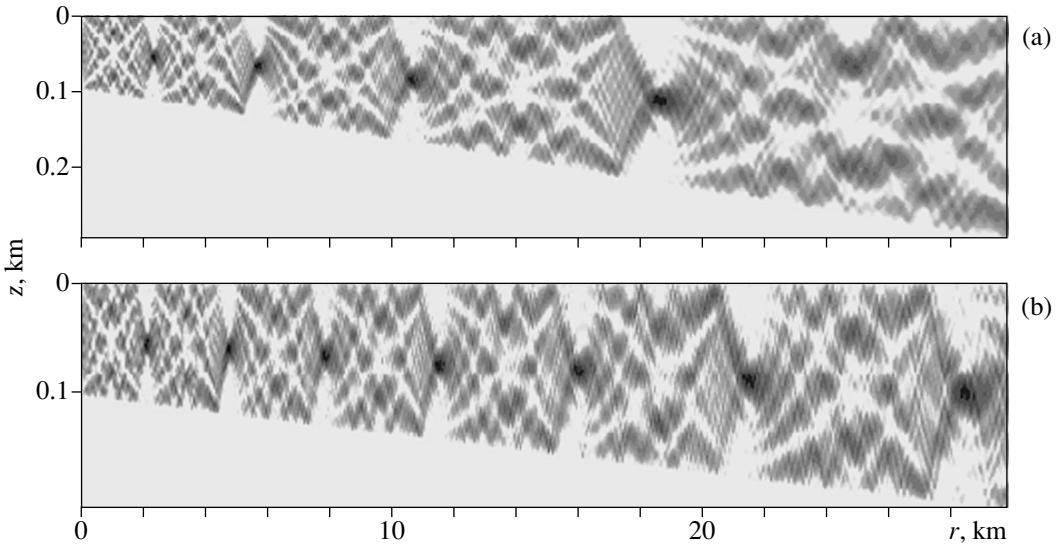

Fig. 1. Spatial dependences of the normalized intensity $J_H(r, z)$, Eq. (5), shown by the shades of gray, with a dynamic range of 16 dB for $h/\lambda = 3$ and H_s = (a) 300 and (b) 200 m.

if only modes of relatively low grazing angles are taken into account, i.e., the modes that mainly contribute to the formation of the diffraction-focusing zones in the waveguide at hand.

Evidently, the function $F_l > 1$ characterizes the diffraction-caused spread of the wave field of each mode. This spread is governed by propagation of the corresponding part of the mode's energy in the liquid bottom, by analogy with the effects observed in the case of a total internal reflection of sound beams from the interface between two liquid media [11, 12]. The changes in the diffraction-caused spread $F_l(r)$ of the mode's wave field are caused by the changes in the angle of incidence of the corresponding plane wave on the bottom's surface.

For the sake of compatibility of the results presented here and in [1–7], the following values of the parameters characterizing the sound signal and the oceanic waveguide (in Eq. (7)) were specified in the numerical calculations: $f = 3 \times 10^2$ Hz, $h/\lambda = 3$–3.6, $\lambda = c/f$, $z_0 =$ 50 m, $R_0 = 1$ m, $r_0 = 0$, $H_0 = 10^2$ m, $H_s = 200$–300 m, $r_s = 3 \times 10^4$ m, $c = 1.5 \times 10^3$ m/s, $c_g = 1.7 \times 10^3$ m/s, and $b = 1.6$.

Figure 1 shows the dependences $J_H(r, z)$. With the specified conditions of sound radiation, the diffraction-focusing zones are at the middle depth, $z = H/2$, of the water layer. The characteristic distances between the adjacent zones increase and are equal to the fourth part

$$R_1(r) = \frac{1}{4}\bar{R}_{\max}(r) \tag{14}$$

of the distance

$$\bar{R}_{\max}(r) = \max\{\bar{R}_g(l, l'; n, n'; r)\}, \tag{15}$$

where

$$\bar{R}_g(l, l'; n, n'; r) = r/\left|\int_0^r \frac{dr}{R_g(l, l'; n, n'; r)}\right|. \tag{16}$$

The quantity $\bar{R}_{\max}$ characterizes the maximal spatial scale of the diffraction focusing for the oceanic waveguides smoothly varying with distance [8]. The quantity

$$R_g(l, l'; n, n'; r) = \frac{R_{l,l'}(r)R_{n,n'}(r)}{|R_{l,l'}(r) - R_{n,n'}(r)|} \tag{17}$$

appearing in Eq. (16) can be interpreted as the period of rearrangement of the interference structure for the pairs of modes with the numbers l and l', and n and n' in the reference waveguide.

According to [7], Eq. (14) is a consequence of the fact that the diffraction-focusing zones are produced by modes of the same parity, the odd-number modes in our case.

Figures 2 and 3 illustrate the phenomenon of enhancement of the focusing effect for increasing vertical scales of range-dependent waveguide inhomogeneity, which in the case under study is the thickness of the water layer. In Figs. 2 and 3, the range dependences

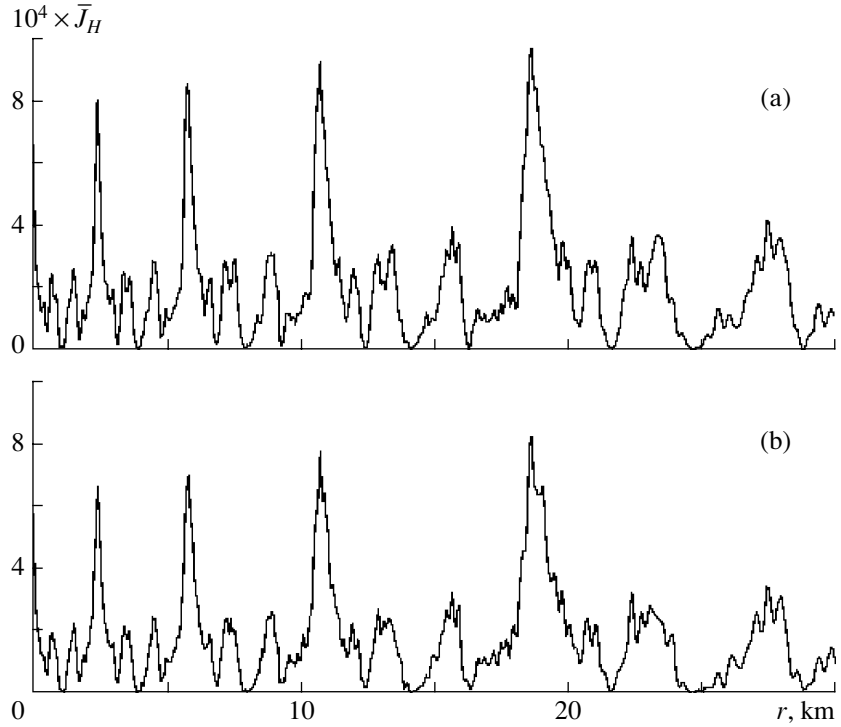

Fig. 2. Normalized intensity $\bar{J}_H$, Eq. (18), versus horizontal distance r for H_s = 300 m and h/λ = (a) 3 and (b) 3.6.

of the normalized intensity averaged over the depth correspond to $z = H/2$ and have the form

$$\bar{J}_H\left(r, z = \frac{H}{2}\right) = \frac{1}{\Delta z}\int_{z_1}^{z_2} J_H(r, z)\,dz, \tag{18}$$

where $\Delta z = H_s/20$, $z_1 = \frac{H}{2} - \Delta z/2$, and $z_2 = \frac{H}{2} + \Delta z/2$. In accordance with the results of analytical studies [8], the increase in the diffraction focusing within the inhomogeneous part of the waveguide becomes more pronounced as R_H defined by Eq. (8) decreases (see Figs. 2, 3).

It is also worth mentioning that an increase in the aperture of the transmitting array leads to a decrease in the efficiency of the diffraction focusing in the inhomogeneous part of the waveguide (see Figs. 2, 3). This phenomenon can be explained as follows. As h increases, the excitation factor of the array,

$$G_l = \left|\psi_l(z_s, 0)\frac{B_l(z_0, h)}{\sin(kz_s\xi_l)}\right|, \tag{19}$$

decreases more strongly for modes of relatively high numbers. According to [8], the greater the thickness of the water layer, the stronger the effect produced by these modes on the process of the diffraction-focusing zone formation. Thus, these modes govern the change in the efficiency of the diffraction focusing in the inhomogeneous part of the waveguide.

It is advantageous to use the model (7) of a shallow-water oceanic waveguide to consider how the sound attenuation in the bottom influences the diffraction zones.

If the absorbing properties of the bottom are characterized by a number α, which is usually much smaller than unity ($\alpha = 10^{-3}$ to 10^{-2}, see [13]), it is possible to add an imaginary component to the wave number k_g of the wave propagating in the seafloor:

$$k_g = kn_g\left(1 + i\frac{\alpha}{2}\right). \tag{20}$$

Then, in the framework of perturbation theory, the following expression can be obtained [13] for the mode attenuation coefficient in the reference waveguide:

$$\gamma_l(r) = \frac{\alpha}{H}bn_g^2\xi_l^2\frac{k}{k_l}/\eta_l\left[\eta_l^2 + (b\xi_l)^2 + \frac{b}{kH\eta_l}(1 - n_g^2)\right], \tag{21}$$

where

$$\eta_l = \sqrt{(k_l/k)^2 - n_g^2}. \tag{22}$$

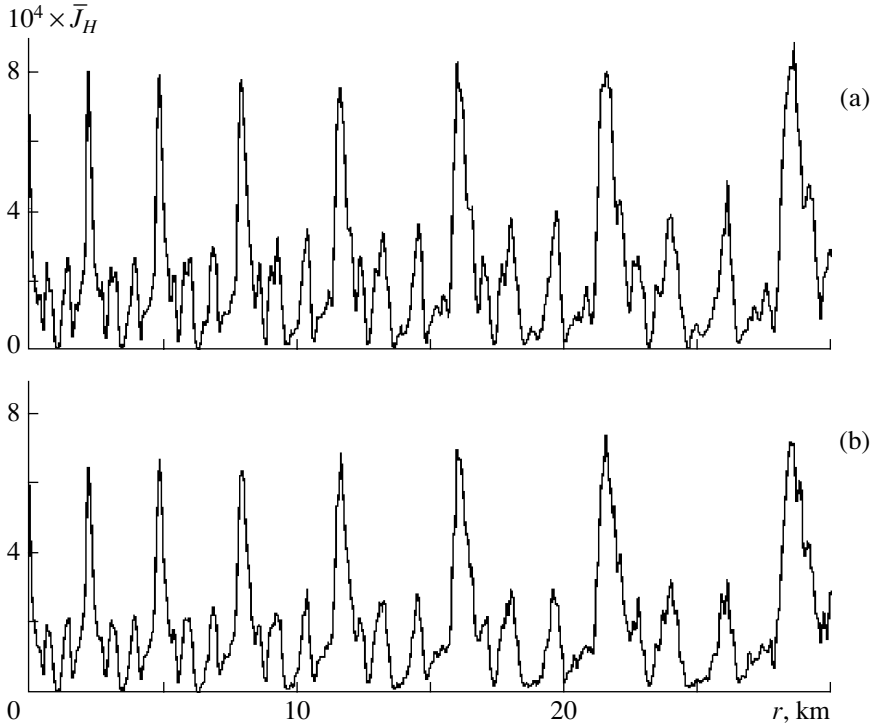

Fig. 3. Normalized intensity $\bar{J}_H(r, z = H/2)$, Eq. (18), versus horizontal distance r for H_s = 200 m and h/λ = (a) 3 and (b) 3.6.

Naturally, in view of the attenuation, the mode amplitude will be described by Eq. (9) multiplied by the corresponding exponential factor:

$$A_l(r, z) \Rightarrow A_l(r, z)\exp\left(-\int_0^r \gamma_l(r)dr\right). \qquad (23)$$

It is known [13] that, in a range-independent Pekeris waveguide, the attenuation coefficient of the modes sharply increases as the mode number grows, namely, it follows the quadratic law, $\gamma_l \sim l^2$, for modes of relatively low ordinal numbers. Therefore, in our case described by Eq. (7), the attenuation of modes can substantially weaken the manifestation of the effect of enhancement of the diffraction focusing in the inhomogeneous part of the waveguide. If the homogeneous part r_0 of the waveguide is sufficiently long, the modes with relatively high numbers are substantially lower in their amplitudes in comparison with the modes with relatively low numbers. Hence, the high-number modes cannot affect the process of the diffraction-focusing zone formation in the waveguide part with increasing thickness of the water layer and, hence, cannot lead to a noticeably enhanced diffraction focusing.

However, if the transmitting array is positioned near an inhomogeneous waveguide fraction whose length is sufficiently great, i.e., $r_0 = 0$, the influence of the mode attenuation can lead to a suppression of the enhancement of the diffraction focusing within certain range intervals where the contribution of the modes with relatively high numbers can be neglected. In contrast to the aforementioned case, the mode attenuation will now more weakly influence the process of the diffraction-focusing zone formation, because the quantity γ_l sharply decreases as the thickness of the water layer increases. This decrease obeys the law $\gamma_l \sim (H_0/H)^{3+\alpha_1}$, where $\alpha_1 = 0$ for modes of relatively low numbers and $\alpha_1 \sim (H_0/H)^{\alpha_2}$ $(2 < \alpha_2 < 3)$ for modes of relatively high numbers.

The above inferences are confirmed by Fig. 4, which shows the dependences $\bar{J}_H(r)$ obtained in view of the attenuation with $\alpha = 0.006$ in the bottom, this value corresponding to a sound attenuation coefficient of 30 dB/km. The steeper the increase in the thickness of the water layer within the fixed part of the waveguide, the more pronounced the diffraction focusing. This is explained by the faster decrease in the value of the ratio $\bar{R}_g(l, l', n, n'; r)/\bar{R}_{\max}(r)$ (see Eqs. (15) and (16)) and in the attenuation coefficient γ_l (see Eq. (21)).

Thus, the numerical modeling of the spatial distribution of the sound field intensity (Eq. (5)) normalized to the geometrical spread of the wave front in the Pekeris waveguide with the thickness of the water layer increasing with distance clearly confirms the conclusion that was analytically derived in [8]; namely, the diffraction focusing of the sound field is more efficient

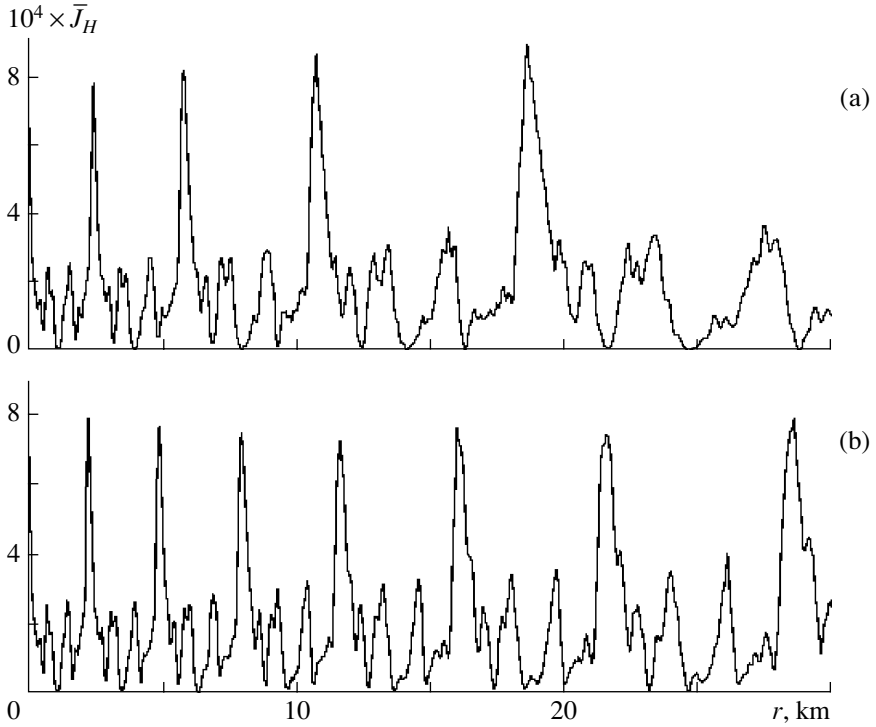

Fig. 4. Changes in the dependence of the normalized intensity $\bar{J}_H(r, z = H/2)$, Eq. (18), on distance r with a sound attenuation in the bottom for $h/\lambda = 3$ and H_s = (a) 300 and (b) 200 m.

for oceanic waveguides with an inhomogeneity whose vertical scale increases with distance. In such waveguides, the normalized intensity of the sound field in the diffraction-focusing zones proves to be increased in spite of the increase in the distance to the respective zones.

ACKNOWLEDGMENTS

This work was supported by the Russian Foundation for Basic Research, project no. 00-05-64604.

REFERENCES

1. Yu. V. Petukhov, Akust. Zh. **46**, 384 (2000) [Acoust. Phys. **46**, 327 (2000)].
2. D. I. Abrosimov and Yu. V. Petukhov, Akust. Zh. **46**, 149 (2000) [Acoust. Phys. **46**, 113 (2000)].
3. D. I. Abrosimov and Yu. V. Petukhov, Akust. Zh. **46**, 5 (2000) [Acoust. Phys. **46**, 1 (2000)].
4. E. L. Borodina and Yu. V. Petukhov, Akust. Zh. **47**, 313 (2001) [Acoust. Phys. **47**, 262 (2001)].
5. E. L. Borodina and Yu. V. Petukhov, Akust. Zh. **47**, 451 (2001) [Acoust. Phys. **47**, 384 (2001)].
6. E. L. Borodina and Yu. V. Petukhov, Akust. Zh. **47**, 590 (2001) [Acoust. Phys. **47**, 511 (2001)].
7. E. L. Borodina and Yu. V. Petukhov, Preprint No. 555, IPF RAN (Nizhni Novgorod Inst. of Applied Physics, Russian Academy of Sciences, 2001); Akust. Zh. **48**, 602 (2002) [Acoust. Phys. **48**, 529 (2002)].
8. Yu. V. Petukhov, Preprint No. 571, IPF RAN (Nizhni Novgorod Inst. of Applied Physics, Russian Academy of Sciences, 2001); Akust. Zh. **50** (2) (2004) (in press).
9. L. M. Brekhovskikh and Yu. P. Lysanov, *Fundamentals of Ocean Acoustics* (Gidrometeoizdat, Leningrad, 1982; Springer, New York, 1991).
10. R. Burridge and H. Weinberg, in *Wave Propagation and Underwater Acoustics*, Ed. by J. B. Keller and J. S. Papadakis (Springer, New York, 1977; Mir, Moscow, 1980).
11. L. M. Brekhovshikh, *Waves in Layered Media*, 2nd ed. (Nauka, Moscow, 1973; Academic, New York, 1980).
12. C. T. Tindle and D. E. Weston, J. Acoust. Soc. Am. **67**, 1614 (1980).
13. B. G. Katsnel'son and V. G. Petnikov, *Acoustics of a Shallow Sea* (Nauka, Moscow, 1997).

Translated by E. Kopyl

Acoustical Physics, Vol. 50, No. 5, 2004, pp. 602–611. Translated from Akusticheskiĭ Zhurnal, Vol. 50, No. 5, 2004, pp. 700–709.

Localization of a Transverse Elastic Wave in a Semibounded Acoustic Superlattice of Ferrimagnetic and Superconducting Layers: 1. Slip Boundary

O. S. Tarasenko, C. V. Tarasenko, and V. M. Yurchenko

Galkin Physicotechnical Institute, National Academy of Sciences of Ukraine, ul. R. Lyuksemburg 72, Donetsk, 83114 Ukraine

e-mail: tarasen@host.dipt.donetsk.ua

Received August 20, 2003

Abstract—On the basis of the effective medium method, which correctly takes into account the dynamic interaction of the spin and elastic subsystems, the effect of gyrotropy on the conditions of propagation of a shear elastic wave in a semibounded magnetic superlattice consisting of ferrimagnetic and superconducting layers is studied both near the point of magnetic compensation of the ferrimagnetic medium and away from it.

Studies of wave properties generally and acoustic properties specifically in composite structures that possess additional translational symmetry in one, two, or three dimensions (phononic crystals) are a rapidly progressing field of modern physical acoustics [1–3]. An example of a one-dimensional phononic crystal may be an acoustic superlattice, which in the simplest case is two-component and consists of equidistant identical elastically isotropic layers of thickness d_1 (medium 1) acoustically coupled with layers of medium 2, each of which has a thickness d_2. From the viewpoint of applications, objects of special interest are acoustic magnetic superlattices, because, owing to the magnetoelastic interaction, their elastic dynamics can be controlled by an external magnetic field.

A real two-component magnetic superlattice consisting of alternating equidistant acoustically coupled magnetic and nonmagnetic layers is an example of a phononic–photonic crystal [4], and a theoretical description of its dynamics must be based on a simultaneous consideration of the magnetoelastic and magnetodipole interactions. However, even for a semibounded acoustic magnetic superlattice, the calculation of the spectrum of normal elastic SH waves by the transfer matrix method with allowance for the magnetoelastic and magnetodipole interactions in the presence of gyrotropy requires the use of matrices with a dimension of no less than 4×4 [5]. At the same time, if we limit our consideration to the region of relatively small wave numbers (a fine-layered superlattice), the spectrum of collective excitations arising in the acoustic magnetic superlattice can be analyzed on the basis of the effective medium method [6]. In addition, if the nonmagnetic medium included in such a superlattice is a perfect diamagnet, e.g., a superconductor ($2\lambda/t \longrightarrow 0$, where λ is the London penetration depth and t is the thickness of a superconducting layer), this structure can be considered as a one-dimensional magnetic phononic crystal, because, in this case, the only mechanism forming the collective excitation spectrum is the acoustic interlayer interaction [7]. Today, the class of one-dimensional magnetic phononic crystals often used for investigation are ferrimagnet–superconductor acoustic superlattices. As a rule, these objects are studied from the viewpoint of the coexistence of the magnetic and superconducting types of ordering [8]. At the same time, a simple comparison of the conditions of propagation of a shear elastic wave in an easy-axis ferrimagnet at the point of magnetic compensation ($\nu = 0$) and away from it ($\nu \gg 1$) shows that they should be noticeably different even without taking into account the boundary conditions, because, in a zero external magnetic field, a homogeneously magnetized easy-axis ferromagnet ($\nu \gg 1$), unlike an easy-axis antiferromagnet ($\nu = 0$), possesses an acoustic gyrotropy [9]. The presence of an acoustic gyrotropy in the crystal under consideration is of the same origin as that in a single-sublattice ferromagnet [9]: it is related to the presence of an uncompensated magnetic moment (in the given case, $\mathbf{L} = \mathbf{M}_1 - \mathbf{M}_2 \neq 0$), which is an axial vector, even in an unbounded homogeneously magnetized sample. As a result, at a fixed excitation frequency ω, the value of the wave number will be different for the left-handed and right-handed polarized normal magnetoelastic waves propagating collinear with the vector $\mathbf{L}$, which gives rise to the acoustic Faraday effect. Another equally important manifestation of acoustic gyrotropy is that, even in an unbounded homogeneously magnetized easy-axis (the *OZ* axis) and elastically isotropic ferro- or ferrimagnet, only one geometry allows the propagation of a normal shear magnetoelastic SH wave with a wave vector $\mathbf{k}$ noncoincident with the easy axis-direc-

tion: $\mathbf{k} \perp OZ \parallel \mathbf{u}$ (where $\mathbf{u}$ is the vector of elastic displacements of the lattice) [9]. However, at present, the effect of gyrotropy on the reflection and localization of a shear elastic wave near the surface of a superlattice of the magnet–perfect diamagnet type remains an issue open to question.

In this connection, the purpose of the study described in this paper is, on the basis of the effective medium method, to reveal the features induced by the gyrotropy of the magnetic medium in the propagation and localization of an elastic SH wave traveling along a mechanically free surface of an acoustic superlattice of the easy-axis ferrimagnet–perfect superconductor type.

Structurally, the study consists of several sections, the first of which presents the basic relations necessary for the solution of the stated problem in terms of the effective medium method for the cases of an unbounded and a semibounded acoustic magnetic superlattice of the ferrimagnet–superconductor type. The following section presents the results of classification according to the frequency ω and wave number $k_\perp$ of the possible types of shear elastic SH waves propagating along the surface of the given lattice. In a separate section, with allowance for the gyrotropy, we analytically study the spectrum of surface shear elastic vibrations localized near the slip boundary between a semibounded magnetic superlattice and a semibounded perfect superconductor. The next to last section is devoted to the analysis of the relation between the spectrum of the surface SH wave types found with allowance for the gyrotropy and the character of reflection of a shear elastic bulk wave from the surface of the magnetic superlattice. The same section considers the effect of gyrotropy on the Schoch effect for a beam of bulk SH waves incident from the depth of the magnetic superlattice on its surface. The closing section presents the conclusions derived from the results of the study.

BASIC RELATIONS

Let us consider a magnetic superlattice in the form of a system of equidistant ferrimagnetic layers (medium 1) of thickness d_1 each, which are acoustically coupled through identical layers of a perfect superconductor (medium 2) of thickness d_2 each (we assume that, in the superconductor, the London penetration depth λ satisfies the condition $2\lambda \ll d_2$ to a good accuracy).

As an example of a magnetic medium, we consider a two-sublattice ($\mathbf{M}_{1,2}$ are the magnetizations of the sublattices) model of an easy-axis (the OZ easy axis) ferrimagnet [10] and assume that both magnetic and nonmagnetic media are isotropic in their elastic and magnetoelastic properties. In this case, the magnetoelastic dynamics of the magnet model under consideration is described by the set of equations

$$-\frac{\nu}{gM_0}l_t = \left[l, \left(2\nu h_m - \frac{\alpha}{c^2}l_{tt} - \frac{1}{2M_0^2}\frac{\partial W}{\partial l}\right)\right] + \frac{2}{\delta}(h_m l)[h_m l] + \frac{1}{gM_0}[(h_m)_t - 2l_t(h_m l) - l(h_m l_t)], \quad (1)$$

$$M = \nu L + \frac{1}{g\delta L^2}[LL_t] + \frac{H_m}{\delta} - \frac{L}{\delta L^2}(H_m L), \quad h_m \equiv H_m/(2M_0), \quad (2)$$

$$\mathrm{div}H_m = -4\pi \mathrm{div}M, \quad \mathrm{curl}H_m = 0, \quad (3)$$

$$\rho_1 \frac{\partial^2 u_i}{\partial t^2} = \frac{\partial^2 W}{\partial x_k \partial u_{ik}}, \quad (4)$$

$$W = -0.5bl_z^2 + 0.5\lambda_1 u_{ii}^2 + \mu_1 u_{ik}^2 + Bl_i l_k u_{ik}. \quad (5)$$

Here, $A_t \equiv \partial A/\partial t$; $\nu \equiv (M_1^2 - M_2^2)/2M_0|L|$; $M_0^2 \equiv (M_1^2 + M_2^2)/2$; $\mathbf{l} \equiv \mathbf{L}/|\mathbf{L}|$, where $\mathbf{L} \equiv \mathbf{M}_1 - \mathbf{M}_2$ ($|\mathbf{L}|$ is the total magnetization of the easy-axis two-sublattice ferrimagnet); λ_1 and μ_1 are the Lame constants of the magnetic medium; u_{ik} is the elastic strain tensor; $\mathbf{H}_m$ is the magnetodipole field; $M \equiv M_1 + M_2$; $\delta > 0$ is the intersublattice exchange constant; $b > 0$ is the easy-axis anisotropy constant; ρ_1 is the density of the magnetic medium; and B is the magnetoelastic interaction constant. In the set of dynamic equations (1)–(5), Eqs. (1) and (2) are obtained in [10] from the Landau–Lifshits equations under the condition that $|\mathbf{M}| \ll |\mathbf{L}|$ and describe the low-frequency ($\omega \ll \omega_E \equiv \delta g M_0$) dynamics of the spin subsystem of the two-sublattice ferrimagnet both near the magnetic compensation point ($\nu = 0$) and away from it ($\nu \gg 1$). Equations (3) and (4) are the equations of magnetostatics and mechanics of a continuous medium, respectively, and Eq. (5) describes the density of the thermodynamic potential of the ferrimagnet model under consideration [10]. If $\nu = 0$, from Eqs. (1)–(5), we obtain a set of equations describing the magnetoelastic dynamics of an easy-axis two-sublattice antiferromagnet, while, in the limit $\delta \longrightarrow \infty$, Eqs. (1)–(5) yield a set of equations describing the magnetoelastic dynamics of an easy-axis one-sublattice ferromagnet with the magnetization $\mathbf{M}_f \equiv 2\nu M_0 l$. The dynamics of the nonmagnetic elastically isotropic (superconducting) medium (medium 2; λ_2 and μ_2 are the Lame constants) is determined by Eqs. (4) and (5) with the following substitutions: $\rho_1 \longrightarrow \rho_2$, $\lambda_1 \longrightarrow \lambda_2$, $\mu_1 \longrightarrow \mu_2$, and $b = B = 0$. From Eqs. (1)–(5) it follows that, since $\mathbf{L} \parallel OZ$ in the equilibrium state, the dispersion law for the normal SH wave propagating with $\mathbf{u} \parallel \mathbf{L} \parallel OZ$ and

$k \in XY$ in an unbounded easy-axis two-sublattice ferrimagnet can be represented in the form ($s_t^2 \equiv \mu_1/\rho_1$)

$$\omega^2 = s_t^2 \eta (k_x^2 + k_y^2), \tag{6}$$

$$\eta = 1 - \frac{\omega_{me}^2(\omega_0^2 + \omega_{me}^2 - \omega^2)}{D}, \tag{7}$$

$$D \equiv (\omega_0^2 + \omega_{me}^2 - \omega^2)^2 - \nu^2 \omega_E^2 \omega^2.$$

Note that, for the given geometry of propagation, the following effective elastic moduli are formed under the effect of magnetoelastic interaction:

$$\tilde{c}_{44} = \tilde{c}_{55} = \eta \mu_1, \quad \tilde{c}_{45} = -\tilde{c}_{54} = \eta_* \mu_1,$$

$$\eta_* \equiv \frac{\nu \omega_E \omega_{me}^2 \omega}{D}. \tag{8}$$

Since we consider a magnetic superlattice of the magnet–nonmagnet type, the acoustic continuity requirement for the hybrid structure under study leads to the following conditions at the boundaries between the magnetic (subscript 1) and nonmagnetic (subscript 2) layers ($N = 0, 1, \ldots$, and ξ is the running coordinate along the boundary between magnetic and nonmagnetic layers in the superlattice) [11]:

$$u_i^{(1)} = u_i^{(2)}, \quad \xi = d_1 + N(d_1 + d_2), \quad N(d_1 + d_2), \tag{9}$$

$$\sigma_{ik}^{(1)} n_k^{(1)} = \sigma_{ik}^{(2)} n_k^{(2)}, \quad \xi = d_1 + N(d_1 + d_2), \quad N(d_1 + d_2). \tag{10}$$

Assuming that the superconducting medium is a perfect diamagnet, we can represent the corresponding electrodynamic boundary conditions at the boundary between magnetic and nonmagnetic layers in the form [11]

$$Bn = 0, \quad \xi = d_1 + N(d_1 + d_2), \quad N(d_1 + d_2). \tag{11}$$

Thus, in the given superlattice, the only mechanism forming the collective excitation spectrum is the indirect interlayer interaction through the phonon field (i.e., such a superlattice represents one of the versions of a magnetic phononic crystal).

Since, even in the model of an unbounded easy-axis ferrimagnet given by Eqs. (1)–(5), the propagation of a shear linearly polarized elastic wave is possible only under the condition that its wave vector is orthogonal to the easy axis and $\mathbf{u} \parallel \mathbf{L} \parallel OZ$ (Eqs. (6) and (7)), in the following consideration we assume that, first, $k \in XY$; second, the equilibrium magnetization directions in all magnetic layers of the easy-axis (OZ axis) ferrimagnet–superconductor superlattice are collinear and orthogonal to the normal to the boundary between the two media n; and, third, by virtue of the isotropy of the magnet properties in the XY plane, the normal to the layer boundary can be considered to be $\mathbf{n} \parallel OX$ without lack of generality.

As a result, from the viewpoint of elastic dynamics, in the absence of an external magnetic field, two fundamentally different types of equilibrium magnetic configurations are possible in the superlattice under consideration: collinear (the directions of vectors **L** of any pair of neighboring ferrimagnet layers are parallel; we call it configuration *A*) and anticollinear (vectors **L** for any pair of neighboring ferrimagnetic layer are antiparallel; we call it configuration *B*). With respect to translational symmetry, these structures are different, because, in configuration *A*, the period of the magnetic superlattice under study D_A consists of two layers: a ferrimagnetic layer (with a thickness d_1) and a superconducting layer (with a thickness d_2), i.e., $D_A = d_1 + d_2$, whereas, in configuration *B*, the elementary period of the superlattice D_B consists of four layers: two ferrimagnetic layers (with a thickness d_1 each) and two superconducting layers acoustically coupled with them (with a thickness d_2 each), i.e., $D_B = 2D_A$. As was noted above, we limit our consideration to the region of frequencies ω and wave numbers $k_\perp$ in which the superlattice under study can be considered as fine-layered [6]. Then, the component of the wave vector of the shear elastic wave that is normal to the surface is much smaller than the inverse thickness of the corresponding layer (d_1, d_2) in each of the layers forming the superlattice period, both magnetic ($k_{\parallel 1}$) and superconducting ($k_{\parallel 2}$) ones:

$$k_{\parallel 1} d_1 \ll 1, \quad k_{\parallel 2} d_2 \ll 1. \tag{12}$$

As a result, such an acoustic lattice, in both configurations *A* and *B*, can be considered as an effective spatially homogeneous medium, which is characterized by the elastic stress and strain tensor components averaged over the period of the superlattice (D_A in the case of configuration *A* and $D_B = 2D_A$ for a superlattice with configuration *B*): σ_i ($\langle \sigma_i \rangle$) and u_i ($\langle u_i \rangle$).

The corresponding calculation was performed for a lattice model more general than that considered in this paper, and, hence, the results for the magnetic superlattice under study with an equilibrium configuration of type *A* or *B* are obtained as particular cases.

Let us consider an acoustic superlattice whose elementary period D consists of four layers, two of which (we denote them by the letters *a* and *b*) are acoustically gyrotropic ($c_{44}^{(a)} = c_{55}^{(a)}$, $c_{45}^{(a)} = -c_{54}^{(a)}$, $c_{44}^{(b)} = c_{55}^{(b)}$, $c_{45}^{(b)} = -c_{54}^{(b)}$) with thicknesses d_a and d_b; these layers are separated by acoustically nongyrotropic ($c_{44}^{(2)} = c_{55}^{(2)}$, $c_{44}^{(4)} = c_{55}^{(4)}$) layers (we denote them by the numbers 2 and 4) with thicknesses d_2 and d_4. Then, a physical quantity P averaged over the elementary period of this lattice $D = d_a + d_2 + d_b + d_4$ has the form

$$\langle P\rangle = [f_a P_a + f_2 P_2 + f_b P_b + f_4 P_4],$$
$$f_a \equiv \frac{d_a}{D}; \quad f_b \equiv \frac{d_b}{D}; \quad f_{1,2} \equiv \frac{d_{1,2}}{D}. \tag{13}$$

The relation between the averaged (with allowance for the acoustic continuity of the layered structure under study, i.e., the continuity of σ_{ix} and u_i at the boundaries between adjacent layers) components of the elastic stress tensor $\langle\sigma_{ik}\rangle$ and elastic strain tensor $\langle u_{ik}\rangle$ is determined by the corresponding effective elastic moduli $\bar{c}_{ik}$. Thus, for the chosen geometry of the propagation of an elastic SH wave (**u** ∥ *OZ*, $k \in XY$; **n** ∥ *OX*), the tensor components $\langle\sigma_i\rangle$ and $\langle u_i\rangle$ should satisfy the conditions

$$\langle\sigma_4\rangle = [f_a\sigma_4^{(a)} + f_2\sigma_4^{(2)} + f_b\sigma_4^{(b)} + f_4\sigma_4^{(4)}],$$
$$\langle\sigma_5\rangle = \sigma_5^{(a)} = \sigma_5^{(b)} = \sigma_5^{(2)} = \sigma_5^{(4)},$$
$$\langle u_4\rangle = u_4^{(a)} = u_4^{(b)} = u_4^{(2)} = u_4^{(4)}, \tag{14}$$
$$\langle u_5\rangle = [f_a u_4^{(a)} + f_2 u_4^{(2)} + f_b u_4^{(b)} + f_4 u_4^{(4)}].$$

As a result, for such an acoustic superlattice whose period *D* is formed by two acoustically gyrotropic layers (*a* and *b*) and two acoustically nongyrotropic layers (2 and 4), we can determine the effective elastic moduli $\bar{c}_{44}$, $\bar{c}_{55}$, $\bar{c}_{45}$, and $\bar{c}_{54}$ as follows:

$$\langle\sigma_5\rangle = \bar{c}_{55}\langle u_5\rangle + i\bar{c}_{54}\langle u_4\rangle,$$
$$\langle\sigma_4\rangle = \bar{c}_{44}\langle u_4\rangle - i\bar{c}_{45}\langle u_5\rangle, \tag{15}$$

where

$$\bar{c}_{55} = c_{55}^{(A)}c_{55}^{(B)}\Delta_*^{-1}, \quad \Delta_* \equiv F_B c_{55}^{(A)} + F_A c_{55}^{(B)},$$
$$\bar{c}_{45} = [F_A c_{45}^{(A)} c_{55}^{(B)} + F_B c_{55}^{(A)} c_{45}^{(B)}]\Delta_*^{-1},$$
$$\bar{c}_{44} = F_A c_{44}^{(A)} + F_B c_{44}^{(B)} - [c_{45}^{(A)} - c_{45}^{(B)}]^2\Delta_*^{-1}, \tag{16}$$
$$F_A \equiv (d_a + d_2)/D, \quad F_B \equiv (d_b + d_4)/D.$$

In relations (16),

$$c_{55}^{(A)} = c_{55}^{(a)}c_{55}^{(2)}\Delta_A^{-1}, \quad \Delta_A \equiv f_2 c_{55}^{(a)} + c_{55}^{(2)} f_a,$$
$$c_{45}^{(A)} = [f_a c_{45}^{(a)} c_{55}^{(2)} + f_2 c_{55}^{(a)} c_{45}^{(2)}]\Delta_A^{-1},$$
$$c_{44}^{(A)} = f_a c_{44}^{(a)} + f_2 c_{44}^{(2)} - f_a f_2 [c_{45}^{(a)} - c_{45}^{(2)}]^2\Delta_A^{-1}, \tag{17}$$
$$f_2 \equiv d_a/(d_a + d_2); \quad f_2 \equiv d_2/(d_a + d_2),$$
$$c_{55}^{(B)} = c_{55}^{(b)}c_{55}^{(4)}\Delta_B^{-1}, \quad \Delta_B \equiv f_4 c_{55}^{(b)} + c_{55}^{(4)} f_b,$$
$$c_{45}^{(B)} = [f_b c_{45}^{(b)} c_{55}^{(4)} + f_4 c_{55}^{(b)} c_{45}^{(4)}]\Delta_B^{-1},$$
$$c_{44}^{(B)} = f_b c_{44}^{(b)} + f_4 c_{44}^{(4)} - f_b f_4 [c_{45}^{(b)} - c_{45}^{(4)}]^2\Delta_B^{-1}, \tag{18}$$
$$f_b \equiv d_b/(d_b + d_4); \quad f_4 \equiv d_4/(d_b + d_4).$$

Returning to the description of the two-layer acoustic superlattice of the ferrimagnet–superconductor type in the framework of the effective medium method, we use relations (14)–(18) and set $d_a = d_b = d_1$ and $d_2 = d_4$. In this case, for the chosen geometry of propagation of the elastic SH wave (**l** ∥ **u** ∥ *OZ*, $k \in XY$; **n** ∥ *OX*), irrespective of the magnetic configuration of the superlattice under study (configuration *A* or *B*), the desired components of the effective moduli $\bar{c}_{44}$, $\bar{c}_{55}$, $\bar{c}_{45}$, and $\bar{c}_{54}$ will be determined by relations (15)–(18). With allowance for the notation given by formulas (7) and (8), for the acoustic superlattice of the easy-axis ferrimagnet–superconductor type in configuration *A*, we should use Eqs. (15)–(18) with

$$c_{44}^{(a)} = c_{44}^{(b)} = c_{55}^{(a)} = c_{55}^{(b)} = \eta\mu_1,$$
$$c_{45}^{(a)} = c_{45}^{(b)} = -c_{54}^{(a)} = -c_{54}^{(b)} = \eta_*\mu_1,$$
$$c_{44}^{(2)} = c_{55}^{(2)} = c_{44}^{(4)} = c_{55}^{(4)} = \mu_2, \tag{19}$$
$$c_{45}^{(2)} = c_{54}^{(2)} = c_{45}^{(4)} = c_{54}^{(4)} = 0,$$

while, for the same magnetic superlattice in configuration *B*, in Eqs. (15)–(18) we should set

$$c_{44}^{(a)} = c_{44}^{(b)} = c_{55}^{(a)} = c_{55}^{(b)} = \eta\mu_1,$$
$$c_{45}^{(a)} = -c_{45}^{(b)} = -c_{54}^{(a)} = c_{54}^{(b)} = \eta_*\mu_1,$$
$$c_{44}^{(2)} = c_{55}^{(2)} = c_{44}^{(4)} = c_{55}^{(4)} = \mu_2, \tag{20}$$
$$c_{45}^{(2)} = c_{54}^{(2)} = c_{45}^{(4)} = c_{54}^{(4)} = 0.$$

Since we consider the elastic dynamics of the acoustic superlattice of the magnet–perfect diamagnet type in terms of the effective field method, condition (11) is assumed to be satisfied for thickness in each of the magnetic and superconducting plates forming the superlattice. As a result, the inclusion of magnetodipole interaction in this region of wave numbers gives no additional (compared to magnetoelastic) mechanisms for the formation of the temporal dispersion of elastic moduli (14)–(18). For the chosen geometry of propagation ($k \in XY$, **L** ∥ **u** ∥ *OZ*), the effect of this interaction will be reduced to only the renormalization of the uniaxial magnetic anisotropy constant: $b \longrightarrow b - 4\pi$. In what follows, we assume that the densities and shear moduli of the magnetic (ρ_1, μ_1) and nonmagnetic (ρ_2, μ_2) media forming the superlattice under study satisfy the equalities $\rho_1 = \rho_2 = \rho$ and $\mu_1 = \mu_2 = \mu$. Then, in terms of the effective medium method, the spectrum of the elastic SH wave propagating in an unbounded acoustic superlattice of the easy-axis ferromagnet–perfect superconductor type with $k \in XY$ and **u** ∥ *OZ*, with allowance for the magnetoelastic and magnetodipole

interactions for both magnetic configurations, is determined by the relation ($s_t^2 \equiv \mu/\rho$)

$$\omega^2 = s_t^2(c_\perp k_y^2 + c_\parallel k_x^2). \quad (21)$$

For configuration *A*, in relation (21) we have

$$c_\parallel = \bar{c}_{55}/\mu = \frac{(\omega_{1+}^2 - \omega^2)(\omega_{1-}^2 - \omega^2)}{(\omega_{2+}^2 - \omega^2)(\omega_{2-}^2 - \omega^2)},$$

$$c_\perp = \bar{c}_{44}/\mu = \frac{(\omega_{4+}^2 - \omega^2)(\omega_{4-}^2 - \omega^2)}{(\omega_{2+}^2 - \omega^2)(\omega_{2-}^2 - \omega^2)}, \quad (22)$$

$$c_* = \bar{c}_{54}/\mu = \frac{\nu\omega_E\omega_{me}^2\bar{f}_1}{(\omega_{2+}^2 - \omega^2)(\omega_{2-}^2 - \omega^2)}.$$

Here, $\omega_{1\pm}$ are the positive roots of the biquadratic equation for ω: $(\omega_0^2 + \omega_{me}^2 - \omega^2)(\omega_0^2 - \omega^2) - \nu^2\omega_E^2\omega^2 = 0$; $\omega_{2\pm}$ are the positive roots of the biquadratic equation for ω: $(\omega_0^2 + \omega_{me}^2 - \omega^2)(\omega_0^2 + \bar{f}_1\omega_{me}^2 - \omega^2) - \nu^2\omega_E^2\omega^2 = 0$; $\omega_{4\pm}$ are positive roots of the biquadratic equation for ω: $\omega_0^2 + \omega_{me}^2 - \omega^2)(\omega_0^2 - \omega^2) - \nu^2\omega_E^2\omega^2 + \bar{f}_1\bar{f}_2\omega_{me}^4 = 0$; $\bar{f}_1 = d_1/(d_1 + d_2)$; and $\bar{f}_2 = d_2/(d_1 + d_2)$. In addition, for any $k_\perp$, the following relation is valid: $\omega_{1-} < \omega_{4-} < \omega_{2-} < \omega_{4+} < \omega_{1+} < \omega_{2+}$.

For configuration *B*, in Eq. (21), we have

$$c_\parallel = \bar{c}_{55}/\mu = \frac{(\omega_{1+}^2 - \omega^2)(\omega_{1-}^2 - \omega^2)}{(\omega_{2+}^2 - \omega^2)(\omega_{2-}^2 - \omega^2)},$$

$$c_\perp = \bar{c}_{44}/\mu = \frac{(\omega_{3+}^2 - \omega^2)(\omega_{3-}^2 - \omega^2)}{(\omega_{1+}^2 - \omega^2)(\omega_{1-}^2 - \omega^2)}, \quad (23)$$

$$\bar{c}_{45} = \bar{c}_{54} = 0.$$

Here, $\omega_{3\pm}$ are the positive roots of the biquadratic equation for ω: $(\omega_0^2 - \omega^2)(\omega_0^2 + \bar{f}_2\omega_{me}^2 - \omega^2) - \nu^2\omega_E^2\omega^2 = 0$. In this case, for any $k_\perp$, when $d_1 < d_2$, the relation $\omega_{3-} < \omega_{1-} < \omega_{2-} < \omega_{3+} < \omega_{1+} < \omega_{2+}$ is satisfied, while, when $d_1 > d_2$, we have $\omega_{3-} < \omega_{1-} < \omega_{3+} < \omega_{2-} < \omega_{1+} < \omega_{2+}$.

Thus, effective moduli (22) and (23) obtained for the acoustic magnetic superlattice, in contrast to the corresponding effective elastic moduli of an unbounded ferrimagnet ($\mathbf{l} \parallel OZ$) that were calculated without taking into account the magnetodipole interaction (c_{44}, c_{55}, c_{45}, and c_{54} given by Eqs. (8)), not only possess a temporal dispersion but also noticeably depend on the relative thicknesses of the magnetic and nonmagnetic layers ($d_{1,2}$).

From Eqs. (21)–(23), it follows that, if $k_\perp = 0$, the propagation of a shear magnetoelastic wave occurs normally to the boundary between the layers of the magnetic superlattice under study. In this case, irrespective of the type of equilibrium magnetic configuration (*A* or *B*), the frequencies $\omega_{1\pm}$ and $\omega_{2\pm}$ correspond to the frequencies of a homogeneous ($k_\perp = 0$) magnetic resonance for the model under study representing a fine-layered superlattice of the easy-axis two-sublattice ferrimagnet–perfect superconductor type under the condition that they are calculated by ignoring ($\omega_{1\pm}$) and by taking into consideration ($\omega_{2\pm}$) the dynamic magnetoelastic interaction. If $k_\parallel = 0$ in Eq. (21), then, according to Eqs. (22) and (23), a shear magnetoelastic wave propagates along the boundary between the layers of the magnetic superlattice. In this case, $\omega_{4\pm}$ and $\omega_{2\pm}$ for configuration *A* and $\omega_{3\pm}$ and $\omega_{1\pm}$ for configuration *B* correspond to the frequencies of a homogeneous magnetic resonance for the model of a fine-layered superlattice of the easy-axis two-sublattice ferrimagnet–perfect superconductor type under the condition that they are calculated by ignoring ($\omega_{3\pm}$, $\omega_{4\pm}$) and by taking into account ($\omega_{2\pm}$, $\omega_{1\pm}$) the dynamic magnetoelastic interaction.

It should be noted that, although the acoustic magnetic superlattice under study is formed by gyrotropic (ferrimagnetic) layers, the corresponding hypothetical spatially homogeneous elastic medium given by Eqs. (14)–(18) may possess (configuration *A*, $\bar{c}_{54} = -\bar{c}_{45} \neq 0$, Eqs. (22)) or lack gyrotropic properties (configuration *B*, $\bar{c}_{54} = -\bar{c}_{45} = 0$, Eqs. (23)).

One can easily verify that, without taking into account the magnetoelastic interaction (by a formal passage to the limit $B \longrightarrow 0$ in Eqs. (22) and (23)), the effective elastic moduli determined by Eqs. (22) and (23) coincide with the corresponding effective elastic moduli of a two-layer nonmagnetic superlattice [6].

From Eqs. (21)–(23), it follows that, irrespective of the type of equilibrium magnetic configuration of the superlattice (*A* or *B*), the shear elastic wave of interest, with allowance for the magnetoelastic and magnetodipole interactions, represents an excitation of a one-partial type; i.e., for this wave, we have

$$\langle u_z \rangle = A\exp(ik_\parallel x)\exp(ik_\perp y - i\omega t). \quad (24)$$

The case $k_\parallel^2 > 0$ corresponds to a traveling bulk (trigonometric) elastic SH wave, while, when $k_\parallel^2 < 0$, only a hyperbolic shear elastic wave can propagate along the surface of the magnetic superlattice under study, for which we can write

$$\langle u_z \rangle \longrightarrow 0 \text{ as } x \longrightarrow \infty \quad (25)$$

if the superlattice occupies the upper half-space $x \geq 0$.

If in relations (21)–(23) ω and $k_\perp$ are considered as preset external parameters, we can specify the conditions at which the propagating shear elastic wave can be localized near the surface of the magnetic superlattice.

The calculation shows that the necessary conditions for the formation of a shear surface acoustic wave (a SAW of the SH type) depend on the type of equilibrium

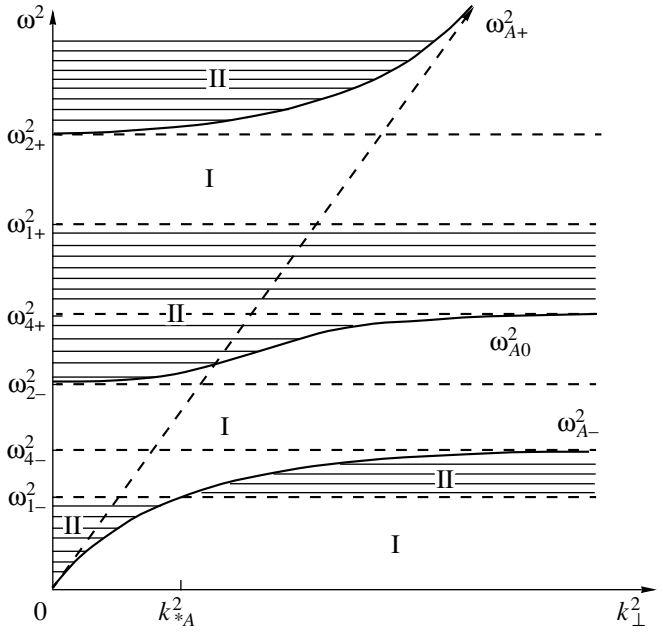

Fig. 1. Regions of the possible existence of traveling surface elastic SH waves (in Eq. (24), $k_\parallel^2 \equiv -\alpha^2 k_\perp^2$; $\alpha^2 > 0$) in an easy-axis ferrimagnet–perfect superconductor superlattice with configuration *A* for $\mathbf{k}_\perp \parallel OY$, $\mathbf{u} \parallel \mathbf{l} \parallel OZ$, $\mathbf{n} \parallel OX$.

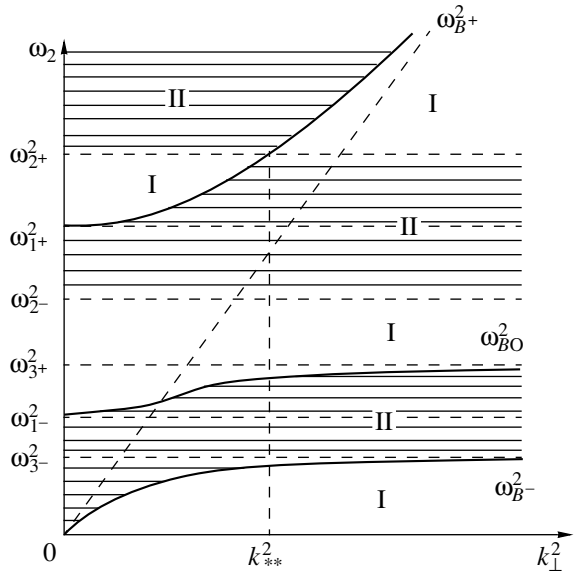

Fig. 2. Regions of the possible existence of travelling surface elastic SH waves (in Eq. (24), $k_\parallel^2 \equiv -\alpha^2 k_\perp^2$; $\alpha^2 > 0$) in an easy-axis ferrimagnet–perfect superconductor superlattice with configuration *B* for $\mathbf{k}_\perp \parallel OY$, $\mathbf{u} \parallel \mathbf{l} \parallel OZ$, $\mathbf{n} \parallel OX$; $d_1 > d_2$.

magnetic configuration of the lattice (see Figs. 1–3). In the case of a magnetic superlattice with configuration *A*, the existence of a propagating surface (hyperbolic) one-partial SH elastic wave described by formulas (21)–(23) and (25) is possible only when $\alpha^2 > 0$ ($k_\parallel^2 \equiv -\alpha^2 k_\perp^2$), i.e., if its frequency ω and wave number $k_\perp$ satisfy one of the following relations (region *I*):

$$\begin{gathered}
\omega_{1+}(k_\perp) < \omega < \omega_{A+}(k_\perp), \\
k_\perp > k_{*A}; \quad \omega_{A-}(k_\perp) < \omega < \omega_{A0}(k_\perp), \\
k_\perp < k_{*A}; \quad \omega_{1-}(k_\perp) < \omega < \omega_{A0}(k_\perp), \\
k_\perp > k_{*A}; \quad \omega < \omega_{1-}(k_\perp), \\
k_\perp < k_{*A}; \quad \omega < \omega_{A-}(k_\perp).
\end{gathered} \tag{26}$$

Here, $\omega_{A\pm}(k_\perp)$ and $\omega_{A0}(k_\perp)$ are real positive roots of the cubic equation for ω^2: $\omega^2(\omega_{2+}^2 - \omega^2)(\omega_{2-}^2 - \omega^2) = s_t^2 k_\perp^2 (\omega_{4+}^2 - \omega^2))(\omega_{4-}^2 - \omega^2)$. In this case, for any k_{*A} and $k_\perp \omega_{A+}(k_\perp) > \omega_{A0}(k_\perp) > \omega_{A-}(k_\perp)$, the wave number k_{*A} is determined by the condition $\omega_{A-}(k_{*A}) = \omega_{1-}(k_{*A})$.

For the acoustic magnetic superlattice with equilibrium configuration *B*, the formation of a propagating one-partial shear SAW (in Eq. (24), $k\|^2 = -\alpha^2 k_\perp^2$, $\alpha^2 > 0$) is possible only when one of the following relations is satisfied (region *I*):

$$\begin{gathered}
d_1 < d_2 \\
k_\perp > k_{**}; \quad \omega_{2+}(k_\perp) < \omega < \omega_{B+}(k_\perp), \\
k_\perp < k_{**}; \quad \omega_{B+}(k_\perp) < \omega < \omega_{2+}(k_\perp), \\
k_\perp > k_{*B}; \quad \omega_{2-}(k_\perp) < \omega < \omega_{B0}(k_\perp), \\
k_\perp < k_{*B}; \quad \omega_{B0}(k_\perp) < \omega < \omega_{2-}(k_\perp), \\
\omega < \omega_{B-}(k_\perp);
\end{gathered} \tag{27}$$

$$\begin{gathered}
d_1 > d_2 \\
k_\perp > k_{**}; \quad \omega_{2+}(k_\perp) < \omega < \omega_{B+}(k_\perp), \\
k_\perp < k_{**}; \quad \omega_{B+}(k_\perp) < \omega < \omega_{2+}(k_\perp), \\
\omega_{B0}(k_\perp) < \omega < \omega_{2-}(k_\perp), \\
\omega < \omega_{B-}(k_\perp).
\end{gathered} \tag{28}$$

Here, $\omega_{B\pm}(k_\perp)$ and $\omega_{B0}(k_\perp)$ are real positive roots of the cubic equation for ω^2: $\omega^2(\omega_{2+}^2 - \omega^2)(\omega_{2-}^2 - \omega^2) = s_t^2 k_\perp^2 (\omega_{3+}^2 - \omega^2))(\omega_{3-}^2 - \omega^2)$. In this case, for any $k_\perp$, $\omega_{B+}(k_\perp) > \omega_{B0}(k_\perp) > \omega_{B-}(k_\perp)$.

In the case under consideration, in formulas (27) and (28), the wave number k_{**} is determined by the condition $\omega_{2+}(k_{**}) = \omega_{B+}(k_{**})$ and the wave number k_{*B} is the root of the equation $\omega_{2-}(k_{*B}) = \omega_{B0}(k_{*B})$.

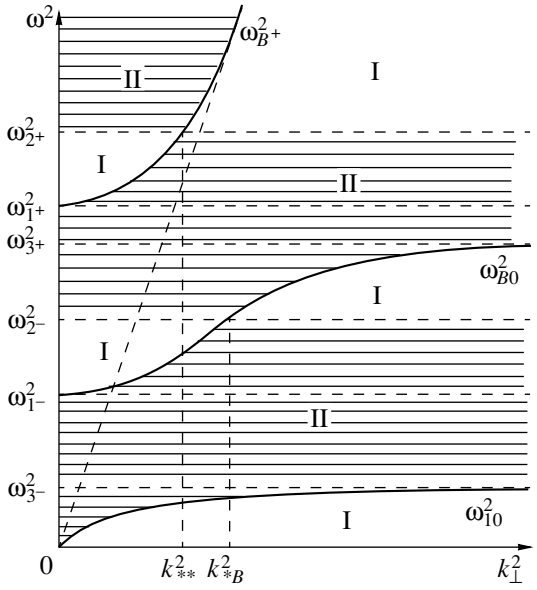

Fig. 3. Regions of the possible existence of traveling surface elastic SH waves (in Eq. (24), $k_\parallel^2 \equiv -\alpha^2 k_\perp^2$; $\alpha^2 > 0$) in an easy-axis ferrimagnet–perfect superconductor superlattice with configuration *B* for $\mathbf{k}_\perp \parallel OY$, $\mathbf{u} \parallel \mathbf{l} \parallel OZ$, $\mathbf{n} \parallel OX$; $d_1 < d_2$.

For ω and $k_\perp$ that do not satisfy relations (26) or (27) and (28), the localization of a shear bulk elastic wave near the surface of the magnetic superlattice under study is impossible (in Eq. (24), $k_\parallel^2 > 0$).

However, relations (26) or (27) and (28) provide the realization of only the necessary conditions for the formation of a surface elastic SH wave in a given magnetic configuration. The dispersion law for this wave is determined from the boundary conditions at the surface of the superlattice as the condition for the existence of a nontrivial solution to the corresponding boundary-value problem for an arbitrary amplitude of the elastic wave *A* involved in Eq. (24).

Let the surface $x = 0$ of the effective medium (the fine-layered magnetic superlattice) occupying the upper half-space $x > 0$ be a slip boundary with a perfect superconductor occupying the lower half-space ($x < 0$). Then, for $\mathbf{u} \parallel OZ$ and $\mathbf{k}_\perp \parallel OY$, we have

$$\langle \sigma_{zx} \rangle = 0, \quad x = 0. \tag{29}$$

The calculation with allowance for relations (21)–(25) shows that, under these conditions, a shear SAW can be formed near the surface of the acoustic magnetic superlattice of the ferrimagnet–superconductor type only if the superlattice possesses an acoustic gyrotropy ($c_* \neq 0$), i.e., if it has the equilibrium magnetic configuration of type *A*. The corresponding dispersion equation with allowance for Eq. (22) can be represented in the form

$$k_\perp^2 = \omega^2 [(c_\perp - c_\parallel \alpha^2) s_t^2]^{-1}; \quad \alpha \equiv \sigma c_* / c_\parallel;$$

$$\sigma \equiv k_\perp / |k_\perp|, \quad c_\parallel = \frac{(\omega_{1+}^2 - \omega^2)(\omega_{1-}^2 - \omega^2)}{(\omega_{2+}^2 - \omega^2)(\omega_{2-}^2 - \omega^2)}, \tag{30}$$

$$c_\perp = \frac{(\omega_{4+}^2 - \omega^2)(\omega_{4-}^2 - \omega^2)}{(\omega_{2+}^2 - \omega^2)(\omega_{2-}^2 - \omega^2)},$$

$$c_* = \frac{\nu \omega_E \omega_{me}^2 \omega \bar{f}_1}{(\omega_{2+}^2 - \omega^2)(\omega_{2-}^2 - \omega^2)}.$$

From Eq. (30), it follows that the spectrum of the shear SAW of interest is characterized by a nonreciprocity with respect to the inversion of the propagation direction: $\omega(k_\perp) \neq \omega(-k_\perp)$. In this case, for a fixed magnitude of the wave number $k_\perp$, the degree of localization of elastic vibrations near the mechanically free surface of the superlattice proves to be different: in Eq. (24), $|k_\parallel(k_\perp)| \neq |k_\parallel(-k_\perp)|$. When $\sigma = -1$, the SAW under consideration has one branch and its dispersion law (denote it as $\Omega_{A0}(k_\perp)$) satisfies the condition $\omega_{1-} < \Omega_{A0}(k_\perp) < \omega_{1+}$ for any $k_\perp$. The corresponding dispersion curve begins at $k_\perp = 0$ at the point $\omega = \omega_{1-}$ and, as $k_\perp$ increases, asymptotically tends to the frequency $\Omega_{A0}(\infty)$, which, in the elastostatic limit, with allowance for the notation introduced in Eqs. (22), is determined as the root of the following equation for frequency ω:

$$c_* + c_\parallel \sqrt{\frac{c_\perp}{c_\parallel}} = 0. \tag{31}$$

When $\sigma = 1$, the dispersion curve of the shear SAW (Eq. (30)) has two branches (the low-frequency $\Omega_{A-}(k_\perp)$ and high-frequency $\Omega_{A+}(k_\perp)$ ones). The low-frequency branch lies in the frequency range $\Omega_{A-} < \omega_{A-}(k_\perp)$ for $k_\perp < k_{*A}$ and satisfies the condition $\Omega_{A-}(k_\perp) < \omega_{1-}$ for $k_\perp > k_{*A}$. Its dispersion curve begins at the point $\omega = 0$, $k_\perp = 0$ and, as the wave number increases, tends to the frequency $\Omega_{A-}(\infty)(\Omega_{A-}(\infty) < \omega_{1-})$, which, in the elastostatic limit ($\omega/(s_t k_\perp) \longrightarrow 0$), with allowance for the notation introduced in Eqs. (22), is determined by the relation

$$-c_* + c_\parallel \sqrt{\frac{c_\perp}{c_\parallel}} = 0. \tag{32}$$

The dispersion law of the high-frequency branch of the spectrum of the SAW under consideration satisfies the condition $\Omega_{A+}(k_\perp) > \omega_{1+}$ for $\sigma = 1$ and any $k_\perp$. The corresponding dispersion curve begins at $k_\perp = 0$ at the point

$\omega = \omega_{1+}$ and, as $k_\perp$ increases, asymptotically tends from below to the line

$$\omega^2 = s_t^2 k_\perp^2 c_\perp. \quad (33)$$

Since all aforementioned branches of the surface elastic SH wave (30) possess only long-wave end points and no short-wave ones, they can be ascribed to the shear SAWs of type *I* in terms of the polariton dynamics [12].

It is easy to verify that, in the limit $d_2/d_1 \longrightarrow 0$, dispersion relation (30) coincides with the expression for the dispersion law of the Parek wave formed in this geometry for a semibounded two-sublattice ferrimagnet under the condition that, in this expression, a formal passage to the limit $4\pi \longrightarrow 0$ is preliminarily performed (this corresponds to the neglect of magnetodipole interaction):

$$k_\perp^2 = \omega^2[(1-\alpha^2)s_t^2]^{-1},$$
$$\alpha \equiv \frac{\sigma\nu\omega_E\omega_{me}^2\omega}{(\omega_0^2+\omega_{me}^2-\omega^2)(\omega_0^2-\omega^2)-\nu^2\omega_E^2\omega^2}. \quad (34)$$

Now, let us proceed to studying the relation between the conditions of the existence of the SAW localized near the surface of the acoustic magnetic sublattice under study and the conditions of the reflection of a bulk elastic wave with the same polarization that is incident on the surface of the sublattice from its depth (**u** || *OZ*, $k \in XY$; **n** || *OX*).

FEATURES OF THE REFLECTION OF A BULK ELASTIC SH WAVE FROM THE SURFACE OF A MAGNET–SUPERCONDUCTOR ACOUSTIC SUPERLATTICE

Calculations show that, in the framework of the effective medium method, for an acoustically continuous boundary ($x = 0$) between two half-spaces given by Eqs. (2) and (3) and occupied by the magnetic superlattice ($x > 0$) and a superconductor ($x < 0$), respectively, the coefficient of reflection R of a bulk transverse SH wave polarized normally to the plane of incidence (**u** || *OZ*) and incident from the magnetic superlattice on its surface can be represented in the following form, depending on the equilibrium magnetic configuration (*A* or *B*) of the superlattice and with allowance for Eqs. (22) and (23) ($\tilde{k}_\parallel^2 \equiv -q^2 k_\perp^2$):

$$R = \frac{c_\parallel k_\parallel + ic_*\sigma k_\perp}{c_\parallel k_\parallel - ic_*\sigma k_\perp}, \text{ of the } A\text{–}S \text{ structure}; \quad (35)$$

$$c_\parallel = \frac{(\omega_{1+}^2-\omega^2)(\omega_{1-}^2-\omega^2)}{(\omega_{2+}^2-\omega^2)(\omega_{2-}^2-\omega^2)},$$

$$c_\perp = \frac{(\omega_{4+}^2-\omega^2)(\omega_{4-}^2-\omega^2)}{(\omega_{2+}^2-\omega^2)(\omega_{2-}^2-\omega^2)},$$

$$c_* = \frac{\nu\omega_E\omega_{me}^2 f_1\omega}{(\omega_{2+}^2-\omega^2)(\omega_{2-}^2-\omega^2)},$$

$$R = 1, \text{ of the } B\text{–}S \text{ strucuture}. \quad (36)$$

Here and below, the notation *A*–*S* and *B*–*S* means an acoustically free boundary between a semibounded superconductor (*S*) and a semibounded magnetic superlattice with an equilibrium configuration of the *A* or *B* type, respectively.

In particular, from Eqs. (35) and (36), it follows that, if between the half-spaces under consideration (the magnetic superlattice and the superconductor) the boundary $x = 0$ is a slip boundary, for configuration *B* (Eq. (36)), at any angle of incidence of the bulk shear elastic wave on the surface of the superlattice, we obtain $R = 1$. For the lattice with magnetic configuration *A* (Eq. (35)), at any angle of incidence, a bulk elastic wave experiences a total internal reflection, $|R| = 1$. In this case, the reflected bulk SH wave acquires an additional gyrotropy-induced phase shift, $R = \exp(i\phi)$:

$$\tan(\phi/2) = \frac{\sigma\omega\omega_{me}^2 \bar{f}_1\omega_E}{(\omega_{1+}^2-\omega^2)(\omega_{1-}^2-\omega^2)}\left(\frac{k_\perp}{k_\parallel}\right). \quad (37)$$

It should also be noted that, for magnetic configuration *A* and preset values of ω and $|k_\perp|$, the phase shift ϕ determined from Eq. (37) possesses a nonreciprocity with respect to the substitution $k_\perp \longrightarrow -k_\perp$ ($\sigma \equiv k_\perp/|k_\perp|$).

From Eq. (35), it follows that, at $k_\parallel = 0$, $R = -1$, which means that the propagation of a homogeneous bulk shear SH wave along the mechanically free boundary between the *A*-type superlattice and the superconductor ($x = 0$) is impossible. This effect is caused by the presence of gyrotropy and occurs only for configuration *A*. According to the general theory of wave processes [13], with allowance for the substitution $k_\parallel \longrightarrow i\alpha k_\perp$, the reflection coefficient R given by Eq. (35) may have a pole on the $\omega, k_\perp$ plane and this pole corresponds to the dispersion law determined above for SH SAWs (Eq. (30)), which propagate in these geometries along the mechanically free boundary between the superlattice and the superconductor with **n** || *OX*, **u** || *OZ*, $\mathbf{k}_\perp$ || *OY* (for the equilibrium magnetic configuration *A*).

Under the conditions of total internal reflection in Eq. (35), a beam of shear elastic waves that is incident from the depth of the ferrimagnet–superconductor superlattice on its mechanically free surface not only acquires a phase shift ϕ upon reflection but also experiences a longitudinal displacement $\Delta \equiv -\partial\phi/\partial k_\perp$ along

the boundary (the Schoch effect) [13]. With allowance for Eq. (37), we have

$$\Delta = \frac{-2k_\parallel}{k_\parallel^2 + \kappa^2 k_\perp^2}\left[\frac{\kappa c_\perp k_\perp^2}{c_\parallel k_\parallel^2} + \kappa\right];$$
$$\kappa \equiv \frac{c_* \sigma}{c_\parallel}; \quad k_\parallel^2 > 0; \quad k_\parallel^2 = \left(\frac{\omega^2}{s_t^2} - c_\perp k_\perp^2\right)\frac{1}{c_\parallel}. \tag{38}$$

Hence, in the case of an acoustically gyrotropic medium (Eq. (35)), an additional feature of the Schokh effect is the dependence of the sign of the longitudinal displacement of the reflected acoustic beam Δ (for preset values of ω and $|k_\perp|$) on the sign of the projection of the wave vector onto the direction of propagation of the incident SH wave: $\Delta(k_\perp) \neq \Delta(-k_\perp)$.

If the medium in which the incident bulk SH wave propagates is acoustically nongyrotropic (configuration *B*), the beam of bulk SH waves reflected under the conditions of total internal reflection will experience no longitudinal displacement ($\Delta > 0$). If the incident bulk shear wave propagates in an acoustically gyrotropic medium (configuration *A*), the beam of SH waves reflected under the conditions of total internal reflection may experience a negative longitudinal displacement ($\Delta < 0$) along the outer surface of the superlattice. A similar correlation between the signs of ϕ and Δ and the frequency range of one-partial SAW propagation is characteristic of other types of SAWs (e.g., Bleustein–Gulyaev waves in piezoelectric crystals [14]).

CONCLUSIONS

Thus, in this paper, on the basis of a simultaneous consideration of magnetoelastic and magnetodipole interactions, in the framework of the effective medium method, we studied the propagation of a shear elastic wave along a slip boundary between a semibounded perfect diamagnet and a semibounded acoustic superlattice of the easy-axis ferrimagnet–perfect superconductor type. The analysis was performed for the cases of parallel (configuration *A*) and antiparallel (configuration *B*) orientations of equilibrium magnetic moments of the neighboring tangentially magnetized ferrimagnetic layers of the superlattice. Although, in the Voigt geometry, an unbounded ferrimagnetic medium possesses a gyrotropy, in the case of the magnetic superlattice with a fixed geometry of elastic wave propagation, the first of the aforementioned magnetic configurations possesses a "macroscopic" acoustic gyrotropy (configuration *A*) and the second (configuration *B*) possesses no such gyrotropy, at least in the long-wave limit. As a result, for the given values of frequency ω and wave number $k_\perp$, the conditions of propagation of the SH wave along the mechanically free surface of the magnetic acoustic superlattice under consideration noticeably vary depending on the type of equilibrium magnetic configuration. In particular, in the case of a magnetic superlattice with configuration *A*, the presence of the acoustic gyrotropy for the mechanically free surface leads to

(i) the formation of a shear SAW of the first kind (with only a long-wave end point of the spectrum), whose spectrum is nonreciprocal;

(ii) to the impossibility of a slip along the surface of the magnetic superlattice under study for a homogeneous bulk SH wave;

(iii) to the effect of a total internal reflection for a shear bulk wave incident from the depth of the magnetic superlattice on its surface and to a phase shift of the reflected SH wave; and

(iv) to the formation of the Schoch effect under the conditions of total internal reflection for a beam of shear bulk SH waves incident from the depth of the magnetic superlattice on its surface.

All effects listed above, because of the gyrotropy, possess a nonreciprocity with respect to the change of sign of the projection of the wave vector of an elastic SH wave onto the surface of the superlattice.

We revealed the relation between the sign of the longitudinal displacement of the acoustic SH beam in the Schoch effect and the presence of acoustic gyrotropy in the medium.

In the case of the equilibrium magnetic configuration *B*, all effects listed above are impossible for the magnetic superlattice under consideration with a mechanically free outer surface.

The characteristic features of the propagation of a shear acoustic wave in the case when the outer surface of the superlattice under study has a continuous acoustic contact with a superconducting coating will be studied in another paper.

ACKNOWLEDGMENTS

One of the authors (S.V.T.) is grateful to I.E. Dikshtein for supporting the idea of this study and for useful discussions.

REFERENCES

1. R. Sainidou, N. Stefanou, and A. Modinos, Phys. Rev. B **66**, 212301 (2002).
2. J. O. Vasseur, P. A. Deymier, B. Chenni, *et al.*, Phys. Rev. Lett. **86**, 3012 (2001).
3. S. Yang, J. H. Page, L. Zhengyou, *et al.*, Phys. Rev. Lett. **88**, 104301 (2002).
4. A. M. Kosevich and M. A. Mamaluĭ, Zh. Éksp. Teor. Fiz. **122**, 897 (2002) [JETP **95**, 777 (2002)].
5. M. G. Cottam and D. R. Tilley, *Introduction to Surface and Superlattice Excitations* (Cambridge Univ. Press, Cambridge, 1989).
6. S. M. Rytov, Akust. Zh. **2**, 72 (1956) [Sov. Phys. Acoust. **2**, 68 (1956)].
7. S. M. Rytov, Zh. Éksp. Teor. Fiz. **29**, 605 (1955) [Sov. Phys. JETP **2**, 466 (1956)].

8. Yu. A. Izyumov, Yu. N. Proshin, and M. G. Khusainov, Usp. Fiz. Nauk **172** (2), 113 (2002) [Phys. Usp. **45**, 109 (2002)].

9. A. G. Gurevich and G. A. Melkov, *Magnetic Oscillations and Waves* (Nauka, Moscow, 1994) [in Russian].

10. B. A. Ivanov and A. L. Sukstanskiĭ, Zh. Éksp. Teor. Fiz. **84** (1), 370 (1983) [Sov. Phys. JETP **57**, 214 (1983)].

11. V. I. Al'shits, A. S. Gorkunova, and A. L. Shuvalov, Zh. Éksp. Teor. Fiz. **110**, 924 (1996) [JETP **83**, 509 (1996)].

12. *Surface Polaritons: Electromagnetic Waves at Surfaces and Interfaces*, Ed. by V. M. Agranovich and D. L. Mills (North-Holland, Amsterdam, 1982; Nauka, Moscow, 1985).

13. L. M. Brekhovskikh, *Waves in Layered Media*, 2nd ed. (Nauka, Moscow, 1973; Academic, New York, 1980).

14. M. K. Balakirev and I. A. Gilinskiĭ, *Waves in Piezoelectric Crystals* (Nauka, Novosibirsk, 1982) [in Russian].

Translated by E. Golyamina

Acoustical Physics, Vol. 50, No. 5, 2004, pp. 612–613. Translated from Akusticheskiĭ Zhurnal, Vol. 50, No. 5, 2004, pp. 710–711.

SHORT COMMUNICATIONS

On the Determination of the Phase of a Plane Sound Wave Transmitted through a Layer

M. V. Lobur and Ya. P. Kosobutskiĭ

Institute of Computer Sciences and Information Technologies, Lvivska Politekhnika National University, ul. S. Banderi 12, Lviv-13, 79646 Ukraine

e-mail: pet_kos@LITech.lviv.ua

Received November 1, 2002

It is well known that both amplitude and phase of a sound wave reflected from a plane-parallel layer or transmitted through it are determined by the phase–amplitude relations at the interfaces and by the effect of multipath interference inside the layer. This problem has been much investigated in both acoustics and optics, and the results of multiple publications devoted to it were generalized in monographs (see, e.g., [1, 2]). However, today, these studies continue attracting considerable interest [3, 4].

In the corresponding experiments, it is important to know not only the energy reflection and energy transmission coefficients of a wave but also the character of its phase variation. In this paper, we show that the phase of a sound wave reflected from or transmitted through a plane-parallel layer can be expressed in terms of the experimental value of the reflection coefficient at a specific frequency. The essence of the proposed approach is as follows.

According to [1], for a wave reflected from a symmetric three-layer structure of the air–layer–air type, the resulting amplitude reflection coefficient calculated with allowance for the multipath interference has the form

$$\tilde{r}_{13} = \frac{-\sigma(1-\exp(-i\delta))}{1-\sigma^2\exp(-i\delta)}. \quad (1)$$

Here, $\sigma = \dfrac{Z_1+Z_2}{Z_1-Z_2}$, where $Z_s = \rho_j c_j$ (j = 1, 2, 3) represents the impedances for a plane wave in media characterized by the densities ρ_j and propagation velocities c_j; $\delta = 2k_2 d$ has the meaning of the phase shift acquired by the plane wave in the course of its propagation in the layer, where $k_2 = 2\pi\nu/c_2$ is the wave number in it [3] and the symmetry of the structure is taken into account, i.e., $Z_1 = Z_3$. For plane sound waves, the specific acoustic impedance $\rho_j c_j$ is a real quantity. Then, according to Eq. (1), the real and imaginary parts of the complex amplitude $\tilde{r}_{13}$ can be expressed by the formulas

$$\begin{aligned}\mathrm{Re}\tilde{r}_{13} &= \frac{-2\sigma(1+\sigma^2)\sin^2\frac{\delta}{2}}{(1-\sigma^2)^2+4\sigma^2\sin^2\frac{\delta}{2}},\\ \mathrm{Im}\tilde{r}_{13} &= \frac{-\sigma(1+\sigma^2)\sin\delta}{(1-\sigma^2)^2+4\sigma^2\sin^2\frac{\delta}{2}}.\end{aligned} \quad (2)$$

Relations (2) determine the reflection coefficient

$$R = \mathrm{Re}^2\tilde{r}_{13} + \mathrm{Im}^2\tilde{r}_{13}$$

and the phase shift

$$\tan\phi = \frac{\mathrm{Im}\tilde{r}_{13}}{\mathrm{Re}\tilde{r}_{13}}$$

with the use of the corresponding hodograph technique [5].

However, from these relations, it also follows that, if we introduce the functions $S = \dfrac{2\sigma}{1+\sigma^2}\cos\dfrac{\delta}{2}$ and $P = \dfrac{2\sigma}{1-\sigma^2}\sin\dfrac{\delta}{2}$, the tangent of the phase can be expressed through these functions as

$$\tan\phi = \frac{S}{P} = \frac{1-\sigma^2}{1+\sigma^2}\cot\frac{\delta}{2}.$$

Hence, expressing the energy reflection coefficient $R = \tilde{r}_{13}\tilde{r}_{13}^*$ in terms of the functions S and P, we obtain the expression

$$\begin{aligned}R &= (\mathrm{Re}\tilde{r}_{13})^2(1+\tan^2\phi) = \frac{P^2}{1+P^2}\\ &= \frac{R_{\max}-S^2}{1-S^2},\end{aligned} \quad (3)$$

1063-7710/04/5005-0612$26.00 © 2004 MAIK “Nauka/Interperiodica”

where $\mathrm{Re}\tilde{r}_{13} = -\frac{R}{\sqrt{R_{\max}}}$.

Thus, if a sound wave is reflected from or transmitted through a plane-parallel medium, the energy reflection coefficient of this wave and its phase are related by a simple formula:

$$R = R_{\max}\frac{P^2}{1+P^2} = \frac{R_{\max}}{1+\tan^2\phi}, \quad (4)$$

where $R_{\max} = \left(\frac{2\sigma}{1+\sigma^2}\right)^2$. From Eq. (4), correct to a full period 2π, we obtain

$$\tan\phi = \sqrt{\frac{R_{\max}}{R} - 1}. \quad (5)$$

Then, the resulting amplitude transmission coefficient $\tilde{t}_{13}$ of the wave has the form [1]

$$\tilde{t}_{13} = \frac{-\frac{4Z_1Z_2}{(Z_1-Z_2)^2}\exp(-i\delta/2)}{1-\sigma^2\exp(-i\delta)}. \quad (6)$$

The reflecting or transmitting medium is transparent, and, therefore, the energy transmission and energy reflection coefficients are related by the formula [2]

$$T = \frac{1}{1+P^2} = \frac{R_{\max}}{1-S^2}. \quad (7)$$

We check that the tangent of the phase of both transmitted and reflected waves is expressed through S and P as

$$\tan\varphi = \frac{\mathrm{Im}\tilde{t}_{13}}{\mathrm{Re}\tilde{t}_{13}} = -\frac{1+\sigma^2}{1-\sigma^2}\tan\frac{\delta}{2} = -\frac{P}{S}. \quad (8)$$

The correctness of the results obtained above is confirmed by the fact that, for a symmetric medium, the following known [3] relationship between the phases of the reflected and transmitted waves is satisfied:

$$\phi - \varphi = \arctan\left(\frac{S}{P}\right) + \arctan\left(\frac{S}{P}\right) = \frac{\pi}{2}.$$

REFERENCES

1. L. M. Brekhovskikh, *Waves in Layered Media*, 2nd ed. (Nauka, Moscow, 1973; Academic, New York, 1980).
2. M. Born and E. Wolf, *Principles of Optics*, 5th ed. (Pergamon, Oxford, 1975; Nauka, Moscow, 1976).
3. V. V. Efimov and D. I. Sementsov, Akust. Zh. **47**, 789 (2001) [Acoust. Phys. **47**, 695 (2001)].
4. S. A. Afanas'ev, V. V. Efimov, and D. I. Sementsov, Opt. Spektrosk. **76**, 475 (1994) [Opt. Spectrosc. **76**, 425 (1994)].
5. P. S. Kosobuts'kiĭ and M. S. Segeda, *Complex Values in Problems of Physics* (Lvivska Politekhnika, Lviv, 2000), p. 193.

Translated by E. Golyamina

Acoustical Physics, Vol. 50, No. 5, 2004, pp. 614–620. Translated from Akusticheskiĭ Zhurnal, Vol. 50, No. 5, 2004, pp. 712–718.

INVITATION TO DISCUSSION

Development of an Acoustical-Mathematical Model of a Human Heart for a Fast Diagnosis of Preinfarction Angina by Pulse

V. P. Glotov, R. A. Vadov, and P. A. Kolobaev

Andreev Acoustics Institute, Russian Academy of Sciences, ul. Shvernika 4, Moscow, 117036 Russia

e-mail: vadov@akin.ru

Received May 16, 2002

Abstract—An approximate model for nonlinear self-induced vibrations of a myocardium pump which involves in situ experiments on evaluation of the resonance, Q-factor, and elastic parameters of a cardiac circuit (cavity) in the frequency range of 0.1–15 Hz is presented. A concept of a fast diagnosis of human preinfarction angina by the pulse at the wrist is proposed. *© 2004 MAIK "Nauka/Interperiodica".*

Cardiovascular diseases (cardiac infarction, heart failure, arrhythmia, fibrillation, cardiac arrest, aortic rupture, etc.) are at the first place among human illnesses. They are difficult to predict and unexpectedly affect not only sick people but also healthy subjects, such as sportsmen whose hearts seem to be well trained. A wave of lethal cases is steadily moving from west to east as a consequence of civilization (stresses), unhealthy environment, and extreme way of life.

A great number of heart models are described in the literature [1]. However, none of them contributes to solving the aforementioned problem, because they do not take into account some most important factors, namely, the abnormally large values of the dielectric constant and electrostriction of a live tissue (deformation up to 30–40%) and the intense nonlinear resonance at a frequency of ~1 Hz (up to 90% of vibration energy), which is observed experimentally on the human heart in the process of its vital activity.

Our model is targeted first of all at the development of a technique for continuous heart diagnostics and a timely warning about an approaching illness. An acoustic test bench that allows the detection of amplitude–frequency characteristics of pulsed vibrations of the heart according to the pulse by a wide-band microphone in the frequency range of 0.1–15 Hz was developed along with three models of the heart: mechanical, analog, and digital. The models are developed for the extrapolation of results obtained at rest to the mode corresponding to heavy physical loading, when experiments with humans are life-threatening.

Pulsation-type natural vibrations of a human heart, which is represented as a three-dimensional circuit acoustically matched to the aorta, with one degree of freedom, and with effective parameters including mass and elasticity, are considered. We assume that the basic elements of the heart are the strong left ventricle shaped as a spherical shell with a certain thickness (myocardium) and the aorta in the form of a thin-walled cylindrical tube. This idealization is quite possible in our opinion, because the length of a pulsation wave is large in comparison with the radii of the sphere and the cylinder. Since the whole system is filled with an incompressible fluid (blood), radial heart pulsation is possible only because of the presence of escape valves. Within this problem formulation, we try to investigate the natural mechanism of heart operation in a sufficiently complete form that combines the electromagnetic impulsation by a sin-node, the elastic properties of a shell, the natural vibrations of an elastic pendulum with a cubic (in particular) nonlinearity analogous to a radio-engineering characteristic [2, 3], and the amplitude–phase regeneration of the excitation of a three-dimensional circuit:

$$\ddot{x} + 2\lambda\dot{x} + \omega_0^2 x + \beta x^3 = f(t)/M, \qquad (1)$$

where x is the radial displacement of the shell; ω_0 is the natural resonance frequency; λ is the loss factor in the circuit, which is equal to $\omega_0/2Q$ (Q is the Q-factor); β is the coefficient connected with the vibration anharmonicity; M is the myocardium mass; $f(t) = F(t) = F\sum_{i=-\infty}^{\infty}\delta(t - i\tau)$ is the excitation force (F is the acoustic amplitude of the pulse and δ is the delta function); and τ is the length of the interval between the pulses. Equation (1) follows from the Lagrangian taking into account the kinetic energy of the myocardium

1063-7710/04/5005-0614$26.00 © 2004 MAIK "Nauka/Interperiodica"

($\sim M\dot{x}^2$) and the potential energy of its symmetric radial extension in the linear ($\sim\omega_0^2 x^2$) and nonlinear ($\sim\beta x^4$) approximations in the case of pulsation vibrations of a large amplitude. The cubic nonlinearity in Eq. (1) arises at an ordinary (real) physical activity of the human body with a power of up to 0.5 hp. In the case of a forced activity (over 0.5 hp), it is necessary to take into account the quadratic nonlinearity as well. We restrict our consideration to ordinary physical loading.

A pulse emitted by the sin-node has an electric amplitude $V = 90$ mV ~ 0.1 V, a duration $\tau_0 \sim 0.001$ s, and an interval between pulses $\tau \sim 1$ s (pulse of 60 beats per minute). According to common concepts, the origin of pulses is apparently a synchronous discharge of cells of a charged (polarized) membrane with the thickness $d = 10^{-8}$ m and an electric field strength up to $\sim 10^5$ V/cm [4].

Acoustic (striction) excitation of the shell is performed by the three-dimensional Helmholtz ponderomotive forces acting on the tissues of the shell, along which a pulse moves with a velocity of up to 30 m/s and excites a depolarization wave within it [5]:

$$F_0 = \frac{1}{4\pi}[E(\partial\varepsilon/\partial p)_t \mathrm{grad}E - \mathrm{grad}\varepsilon] \text{ dyn/cm}^3, \quad (2)$$

where ε is the dynamic dielectric constant of the live tissue, ρ is its density, t is the body temperature (36.5°C), and E is the transverse electric field of the pulse ($E = V_{\text{volt}}/300h$, where h is the effective myocardium thickness).

Equation (2) can be also represented in the form of $\mathrm{grad}\zeta$, where ζ is the chemical potential of a substance, which was introduced by Landau, or in the form of a tensor of the Maxwell ponderomotive forces [5]. Using the Lorentz–Lorentz formula [6] for the dielectric constant of a water-like medium (live tissue), we obtain $d\varepsilon/d\rho \cong \varepsilon^2/3\rho$. Using Eq. (2), it is possible to evaluate the density of the ponderomotive forces causing internal mechanical stress σ in the myocardium live tissue. The stress, in turn, is connected with the blood pressure P within the cavity by the Laplace law (spherical cavity):

$$\sigma = F_0 h = PR/(2h_0), \quad (3)$$

where R is the cavity radius and h_0 is the epicardium thickness (a collagenic shell [8]), or, in the case of equilibrium, in the form

$$P = \text{const} + P_{\text{st}}, \quad (3')$$

where $P_{\text{st}} = (\partial\varepsilon/\partial p)_t E^2\rho/8\pi$ is the electrostriction pressure [5]. Assuming that $E = 0$ in the intervals between the excitation pulses, we obtain from Eq. (3') the value of the constant, which we interpret as a diastolic pressure. In this case, P_{st} corresponds to systolic pressure. Equations (2) and (3) make it possible to evaluate the human ponderomotive forces from the measured drop between the systolic and diastolic pressures by the Korotkov's method [7].

The pressure P within the heart cavity and in the radial artery is measured by the Korotkov experimental method and also by the pulse at the wrist or at a finger tip. The pressure estimation by Eqs. (2) and (3) provides a satisfactory agreement with the systolic pressure in order of magnitude because of the striction "compression" of the substance.

Equation (1) has an analog in radio engineering that is implemented in the Thomson generator [9], where $f(t)$ is formed in the feedback unit by automated differentiation of the anode voltage of an electronic tube [10]. Therefore the Thomson generator and the heart cavity are self-oscillating systems with one degree of freedom and operate without external energy supply. The natural frequency of a heart cavity as a system with lumped parameters can be represented in the form

$$\omega_0 = \sqrt{\kappa/M}, \quad (4)$$

where κ is the coefficient of tissue elasticity and M is the effective myocardium mass (the basic contribution). The parameter κ is determined from the equality of the radial force and the shell tension force. It is equal (per unit area) to [11]

$$\kappa = h_0\frac{E_1}{(1-\nu^2)R^2} \text{ (artery)}, \qquad \kappa = h_0\frac{2E_1}{(1-\nu)R^2} \text{ (spherical cavity)}, \quad (5)$$

where E_1 is Young's modulus of the live tissue and ν is the Poisson ratio.

In the case of live (water-like or rubber-like) tissues, $\nu \sim 0.5$ and $E_1 \sim \mu$, where μ is the shear modulus. If the radius of the heart cavity ($R \sim 3$–3.5 cm), the epicardium thickness ($h_0 \sim 0.02$ cm [8]), and the experimental resonance frequency ω_0 are known, it is easy to estimate the shear modulus μ. It is equal to $\sim 10^3$ Pa, which is close to the value in fish tissues.

At rest, Eq. (1) in the linear approximation has a well known form in the case of harmonic excitation $f(t) = F_m\cos(\omega t)$, for example, fibrillation at the tone with a frequency of ~2.5 Hz (pulse of 150 beats per minute). As is known, in the case of ventricular fibrillation, the human heart gives up ordinary impulsation and changes to a narrowband sinusoidal mode, in which case the blood flow to the brain and other

organs almost stops and a lethal outcome occurs in several minutes.

At resonance, we have

$$|X| = \frac{F_m}{2M\omega_0\lambda}, \tag{6}$$

where X is the amplitude of radial vibrations of the shell (heart).

In the case of nonstationary excitation by an infinite sequence of short pulses, it is necessary to reduce the problem to the preceding case, i.e., to determine the effective amplitude $(F_m)_{\text{eff}}$. Considering the frequency spectrum of this nonstationary excitation, i.e., the comb spectrum that is well known in the theory of information processing [12], and transmitting it through a circuit with one degree of freedom, we obtain an analytical form for $(F_m)_{\text{eff}}$:

$$(F_m)_{\text{eff}} = \omega\tau_0 F_m/\pi, \tag{7}$$

where $\omega = \pi\Pi/30$ is the excitation frequency, Π is the pulse frequency (unit/min), and τ_0 is the pulse length. Thus, the amplitude of heart excitation is equal to

$$\begin{aligned} |X|_{\text{eff}} &= F_m \frac{\omega\tau_0}{2\pi M_0\omega_0\lambda} \\ &= F_m \frac{\tau_0}{2\pi M\lambda} \quad (\text{at } \omega \longrightarrow \omega_0). \end{aligned} \tag{8}$$

At rest, it does not depend on the resonance frequency, but it strongly depends on frequency in the cases of bradycardia ($\omega < \omega_0$) and tachycardia ($\omega > \omega_0$).

Expressing the amplitude F_m through the pressure within the heart (artery) cavity, we finally obtain at the resonance

$$|X|_{\text{eff}} = 2P\frac{R^2\tau_0}{M\lambda}, \tag{9}$$

where P is pressure and R is the cavity radius.

Assuming that $P \sim 10^4$ Pa (average per pulse), R = 3 cm, M = 600 g, τ_0 = 0.001 s, and λ = 3 (Q = 1–1.5 according to experimental data), we obtain $|X|_{\text{eff}} \sim$ 1 cm. Thus the volume of blood ejection per one pulsation by the left and right ventricles reaches more than 200 cm^3, which agrees well with medical data [1, 4].

Moreover, the theoretical heart power in systole is equal to 1–5 W and the efficiency is $\eta_{\text{mech}} \sim 0.99$–0.98, which also coincides with medical data. Taking into account the known efficiency of a live cell $\eta_{\text{biol}} \sim$ 0.50–0.55, we obtain the resulting efficiency of the heart $\eta = \eta_{\text{biol}}\eta_{\text{mech}} \simeq \eta_{\text{biol}}$, and the shell deformation is $s = |X|_{\text{eff}}/R \approx 0.3$ (see Fig. 1a).

In the case of a noticeable deviation from nonlinearity (physical and psychological activities), i.e., taking into account the cubic nonlinearity, it is necessary (as in the radio-engineering case) to replace the elasticity coefficient by the effective value $\kappa_{\text{eff}} = \kappa + \text{const}A^2$, where A is the resulting amplitude of vibrations. As is demonstrated in [2, 3], this substitution leads to a shift of the resonance frequency of the circuit:

$$\omega_{\text{rez}} = \omega_0 + \kappa_1 A^2, \tag{10}$$

where ω_0 is the resonance frequency at rest and κ_1 is the coefficient of phase anharmonicity of vibrations.

In the case of forced activity, when the impulsation frequency is too high, analogously to the preceding case, we introduce the regeneration of the excitation amplitude, which is equivalent to the regular expansion of the cavity volume:

$$F_{\text{eq}} = F(0) + \kappa_2 A^2, \tag{11}$$

where $F(0)$ is the amplitude at rest and κ_2 is the coefficient of amplitude anharmonicity of vibrations that characterizes additional "compression" of the myocardium thickness by ponderomotive forces. This anharmonicity leads to vanishing effective losses in the circuit, $\lambda \longrightarrow \lambda_{\text{eff}} \longrightarrow 0$ ($Q > \infty$), and is a consequence of mergence of single muscle contractions (the so-called state of long contraction) at pulse acceleration under loading (Eq. (10), [1]). It is necessary to note that, when only the phase anharmonicity of the nonlinear circuit (κ_1) is taken into account, the maximum amplitude is limited by the inherent loss λ [3], and the limiting cycle is stable [13].

With allowance for the anharmonicity of natural vibrations, the solution to Eq. (1) has three real roots, which leads to a dynamic instability of vibrations, blood ejection into the aorta and brain (preinfarction state of a healthy heart), and also to infarction and myocardium rupture. The frequency characteristic of the heart cavity extends into a loop figure (see Fig. 2b), where the region of dynamic instability of vibrations (three real roots) is hatched. A further increase in the pulse frequency in the case of physical activity leads to a single real root with the minimal amplitude of vibrations. Blood ejection (mainly into the brain) is sharply reduced. The lack of oxygen leads to the loss of consciousness and cardiac infarction or myocardium rupture if the regeneration of vibration amplitude is considerable ($Q \gg 1$), which corresponds (theoretically) to expansion of the heart volume by 5%.

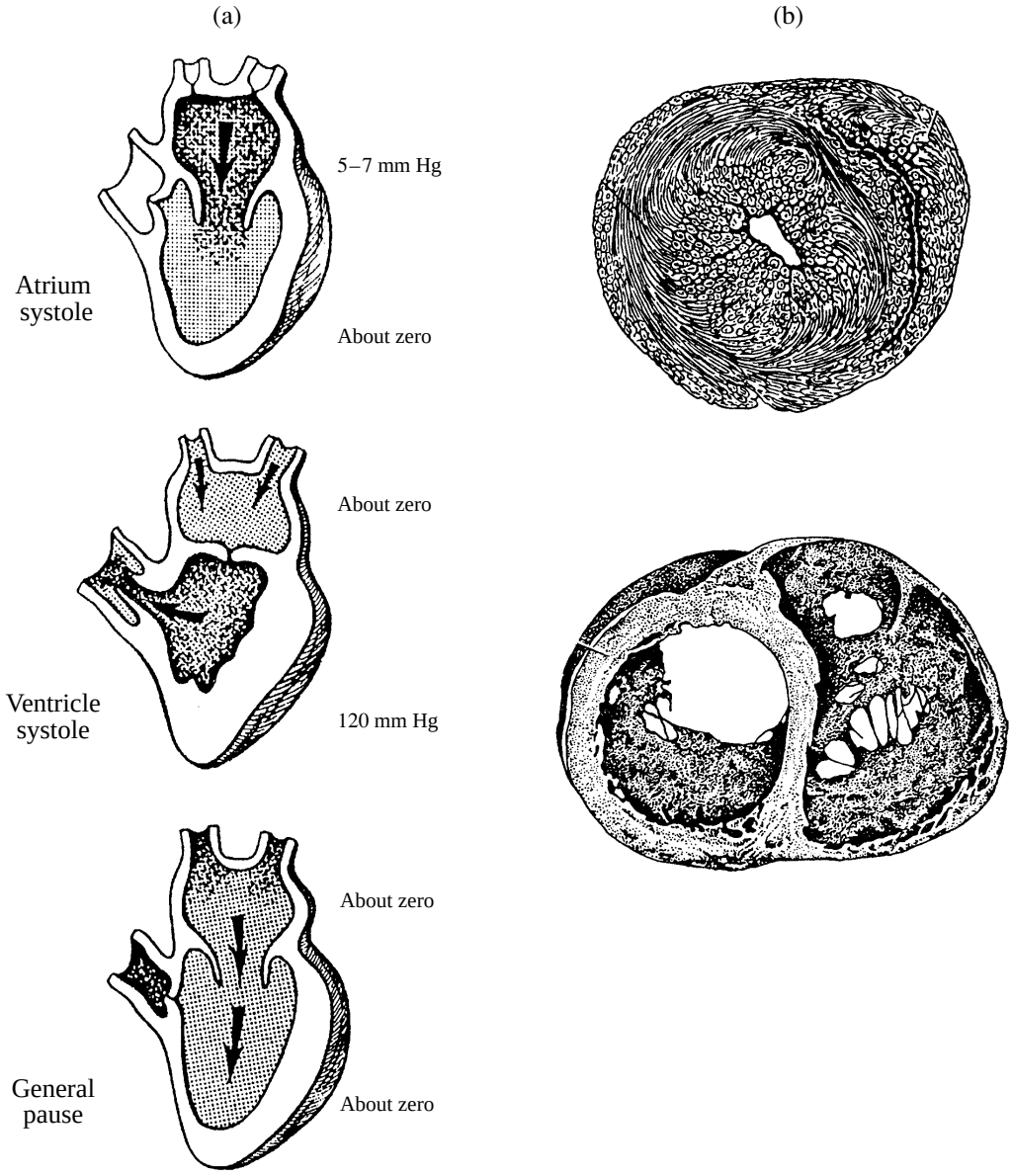

Fig. 1. (a) Schematic diagram of radial vibrations of the left (forced) ventricle with the atrium. Hatching shows the mechanism of blood ejection into the human body [4]. (b) Transverse section of the ventricle that demonstrates the full blood "ejection" into pulsation, $\Delta V/V_0 \sim 1$, where ΔV is the change in the ventricle volume in the process of compression and V_0 is the initial volume (the deformation is $s = 1/\pi \cong 0.3$).

Dynamic equation (1) provides an opportunity, as in other technological problems [9], to proceed to the statistic mechanism of circuit excitation, i.e., from the coherent operation of the sin-node to the incoherent operation. A definite (during a person's life) rhythm of the sin-node (regular pulse) is considerably violated, and it gradually passes to the statistic mode of operation; i.e., the emission of pulses occurs irregularly in time (incoherently), which, in turn, causes irregular operation of the myocardium (extrasystoles, arrhythmias, etc.). The development of this process leads to an incurable heart disease, i.e., cardiac fibrillation with a very large possibility of infarction.

Figure 2a presents the dependence of the extension force on the deformation of a live shell, which consists of elastic and collagen cells, according to the known Hill model [1]. One can see that, at small loads, the elastic cells are "streched" (Hooke's law $\tan(\varphi) = M\omega_0^2$). In the case of high loads, the collagen cells become involved. As a result, the natural frequency of the heart cavity increases (see Eq. (10)), which is appar-

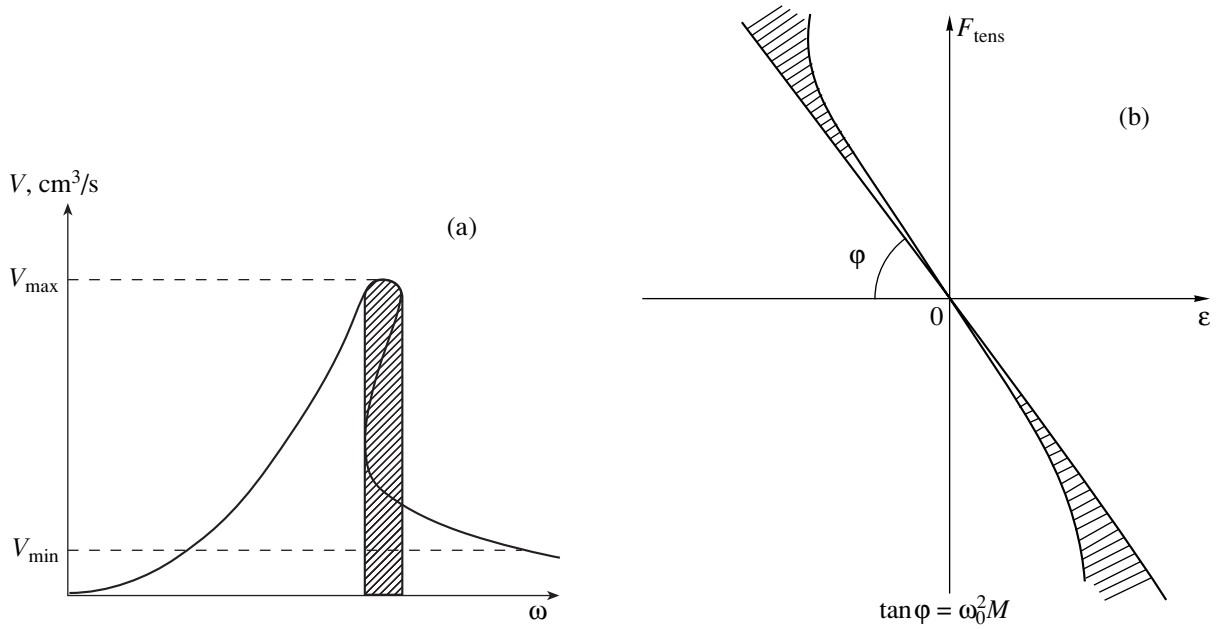

Fig. 2. (a) Assumed dependence of the myocardium tension force on the volumetric deformation of the heart. The hatched area corresponds to the cubic nonlinearity (collagen fibers). (b) Nonlinear frequency characteristic of a three-dimensional circuit with a cubic nonlinearity. The hatched area corresponds to the region of existence of three real roots; V_{max} and V_{min} are the rates of blood ejection from the heart ventricles.

ently a natural phenomenon for automated "tuning" of the myocardium into the resonance for the case of physical activity of a human (running, weightlifting, etc.) and leads to a proportional pulse acceleration [1].

Radial vibrations of a left (power) ventricle with an atrium are displayed in Fig. 1a. Figure 1b gives the transverse section of the ventricle in the case of its pulsation, where blood ejection is observed: $\Delta V/V \sim 1$ ($\Delta V \sim 4\pi R^2|X|_{\text{eff}}$, i.e., $s \sim |X|_{\text{eff}}/R \sim 1/\pi \sim 30\%$).

One can see that the atrium and the ventricle operate quite effectively, but in this case the process of "compression" (blood ejection) is asymmetric with respect to the extension, which is visual evidence of the nonlinearity of natural vibrations of the heart cavity.

Figure 3 shows the frequency spectra on the pulse of (a) a healthy and (b) ill human at rest. The realization length in both cases was 10–15 s. One can see that a healthy heart has a well-developed structure (up to 12 harmonics) with a large excess over the incoherent background. The circle denotes the harmonic dominant in amplitude, with a frequency of ~1 Hz. The contribution of other harmonics is important only for the pulsation timbre and other purposes [14, 15] but is inessential for our problem. A pulse cardiogram has a basic advantage over an electrocardiogram, because it carries direct information on the true pulsation of the myocardium pump and not indirect information (according to the wave of electric depolarization), which is not always adequate to the pump function (blocks of His bundles and other heart diseases) and, hence, may lead to an erroneous diagnosis.

In the case of an ill heart, cardiac fibrillation is observed. According to the model, violation of the sin-node function occurs (pulses arise randomly). In this case, surgical implantation of an artificial sin-node (pacing lead) is necessary, otherwise a lethal outcome may occur unexpectedly [4, 16]. Figure 3b shows the pulsation spectrum for a relatively young recipient several months before a lethal outcome. The diagnosis is well confirmed by the proposed model, but the model provides an opportunity to evaluate the risk of infarction expeditiously, within only ten seconds, and in an automated mode with the help of personal devices whose development is quite feasible, since their possible design is based on already existing industrial technologies [17].

In conclusion, it is necessary to note that, despite the use of a simplified model, we managed to substantiate a series of medical facts concerning cardiology: the nonlinear dependence of systolic "ejection," the linear dependence of human pulse on physical activity [1], the extremely large radial displacement of the myocardium, and the previously unknown values of the shear modulus of a live myocardium tissue and its low-frequency resonance (~1 Hz); we formulated a hypothesis on the real risk of rupture for the myocardium (the aorta and the brain vessels) because of intense self-induced vibration

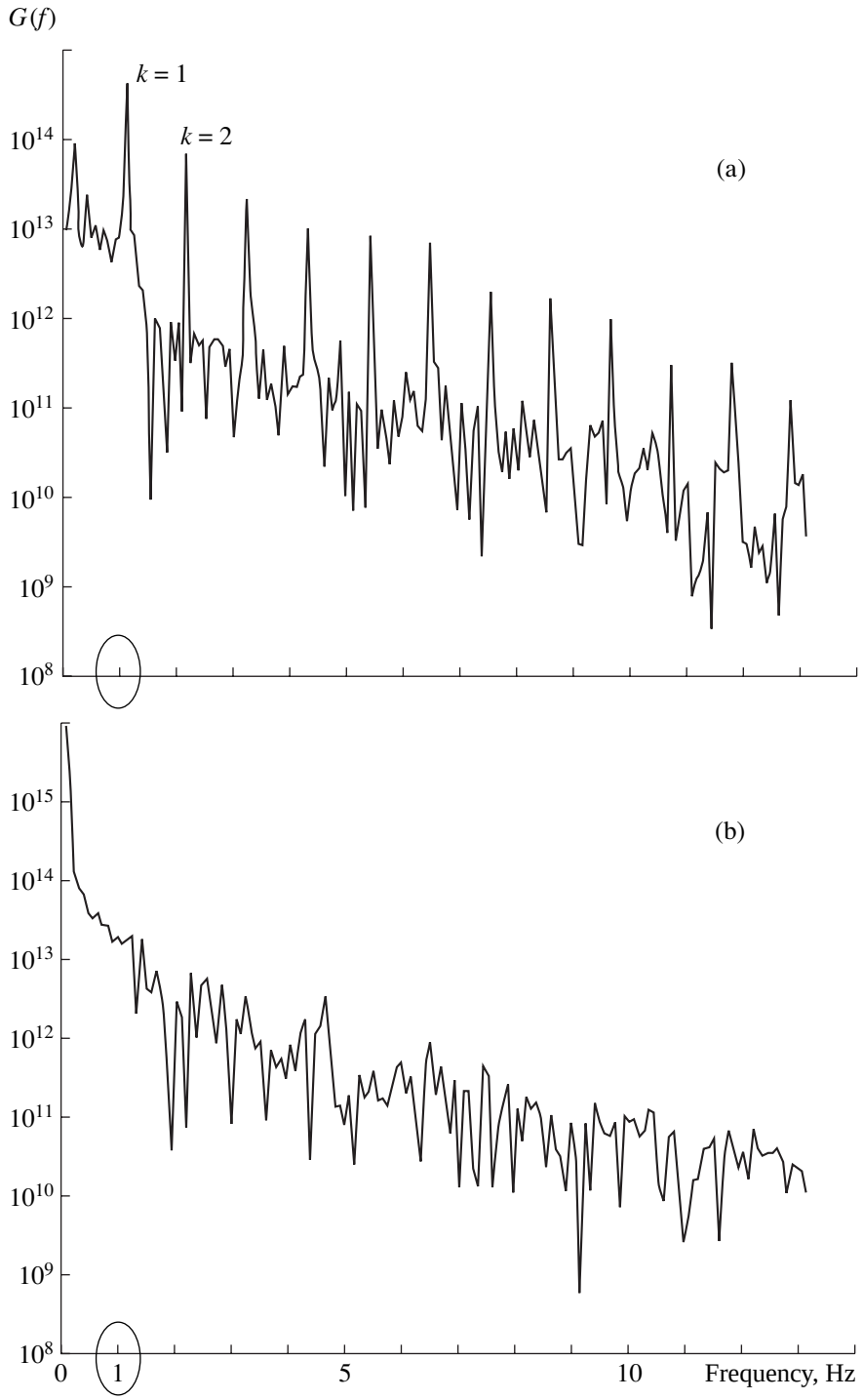

Fig. 3. (a) Pulsation spectrum for a healthy heart (coherent excitation). (b) Pulsation spectrum for an ill heart (incoherent excitation). The abscissa axis represents the frequency in hertz (the circle indicates the natural frequency; the radial resonance $k = 1$).

of the heart cavity in the case of a violation of the regular functions of the sin-node (human pulse [18]).

CONCLUSIONS

An effective technique for the diagnosis of preinfarction angina is developed. Its main advantage over the conventional clinical methods (electrocardiogram, ultrasonic testing, tomography, etc.) is the opportunity for a patient to perform an expeditious monitoring of the true pump function of the heart in the deep infrasound region, where the pulsation is inaudible.

The devices to be designed can be used together with clinical devices (ECG, etc.) in the aftertreatment of patients with infarction (stroke) in a continuous independent mode during medical procedures (the level of loading), drug intake (rapidness of their effect), sleep (a trend to cardiac arrest), and so on.

ACKNOWLEDGMENTS

We are grateful to Academician K.V. Frolov and Professor A.I. Korendyasev for their attention and interest in this work.

REFERENCES

1. V. V. Parin, *Handbook on Physiology: Physiology of Circulation. Heart Physiology* (Nauka, Leningrad, 1980) [in Russian].
2. A. A. Andronov, A. A. Vitt, and S. E. Khaĭkin, *Theory of Oscillations* (Fizmatgiz, Moscow, 1959; Pergamon Press, Oxford, 1966).
3. L. D. Landau and E. M. Lifshitz, *Course of Theoretical Physics*, Vol. 1: *Mechanics* (Nauka, Moscow, 1958; Pergamon Press, Oxford, 1965).
4. E. I. Chazov, *Diseases of Circulation Organs* (Meditsina, Moscow, 1997) [in Russian].
5. L. D. Landau and E. M. Lifshitz, *Course of Theoretical Physics*, Vol. 8: *Electrodynamics of Continuous Media*, 2nd ed. (Nauka, Moscow, 1982; Pergamon, New York, 1984).
6. G. S. Landsberg, *Optics* (Tekhteorlit, Moscow, 1954) [in Russian].
7. K. Yu. Bogdanov, *Physics as a Guest of Biologists* (Nauka, Moscow, 1986) [in Russian].
8. Yu. I. Afanas'eva and N. A. Yurina, *Histology* (Meditsina, Moscow, 1989) [in Russian].
9. S. M. Rytov, *Introduction to Statistical Radio Physics* (Nauka, Moscow, 1966) [in Russian].
10. G. S. Gorelik, *Oscillations and Waves* (Fizmatlit, Moscow, 1959) [in Russian].
11. M. A. Isakovich, *General Acoustics* (Nauka, Moscow, 1973) [in Russian].
12. A. A. Kharkevich, *Suppression of Interferences* (Nauka, Moscow, 1965) [in Russian].
13. G. A. Rakcheeva, V. V. Smolyaninov, and I. S. Yavelov, in *Proceedings of II Meeting of Biophysicists of Russia* (1999), Vol. 2, p. 442.
14. T. J. Royston, Y. Yazicioglu, and F. Loth, J. Acoust. Soc. Am. **113**, 1109 (2003).
15. E. V. Bukhman, S. G. Gershman, V. D. Svet, and G. N. Yakovenko, Akust. Zh. **41**, 50 (1995) [Acoust. Phys. **41**, 41 (1995)].
16. R. A. Miller, *How to Live with a Heart Attack: and How to Avoid One* (Chilton, Radnor, 1973; Kron-Press, Moscow, 1996).
17. V. Efremov and Yu. Shiaptsov, Modelist–Konstruktor, No. 10, 9 (1982); Élektronika, No. 5, 6 (1979); Élektronika, No. 9, 11 (1977).
18. V. P. Glotov, R. A. Vadov, and P. A. Kolobaev, in *Proceedings of XIII Session of the Russian Acoustical Society* (GEOS, Moscow, 2003), Vol. 3, p. 224.

A paper by V. P. Glotov, R. A. Vadov, and P. A. Kolobaev "Development of an Acoustical-Mathematical Model of a Human Heart for a Fast Diagnosis of Preinfarction Angina by Pulse" considers the simplest model of vibrations of the heart as a nonlinear resonator. It is proposed to describe specific features of the heart behavior in the state of preinfarction angina in the framework of a second-order ordinary differential equation containing a cubic nonlinear term. Analyzing the solution to this equation, the authors demonstrate the results testifying to a qualitative agreement of the proposed approach with the data of clinical observations of healthy and ill hearts. Despite the fact that the paper ignores basic electrophysiological and biomechanical properties of the heart muscle and contains no statistical data that seem to be necessary in this case, the editorial board of *Acoustical Physics* decided to publish this paper in the section "Invitation to Discussion." Probably, the discussion of this paper in the journal will attract the attention of researchers to solving such important problem as the development of acoustic methods for the diagnosis of cardiovascular diseases.

Translated by M. Lyamshev

Acoustical Physics, Vol. 50, No. 5, 2004, pp. 621–622. Translated from Akusticheskiĭ Zhurnal, Vol. 50, No. 5, 2004, pp. 719–720.

INFORMATION

Information on the Activities of the St. Petersburg Seminar on Computational and Theoretical Acoustics of the Scientific Council on Acoustics of the Russian Academy of Sciences in 2003

In 2003, the St. Petersburg Seminar on Computational and Theoretical Acoustics proceeded with its regular activities. Twenty sessions were held. In addition to the papers concerned with acoustics alone, some papers were devoted to wave mechanics and to the development of the mathematical techniques used in acoustics.

G.D. Izak described the main methods of calculating the acoustic characteristics of auditoriums. As an example, he described the design and the results of measuring the acoustic characteristics of the theater hall belonging to the Culture Palace in Kirishi.

Two papers presented by É.P. Babaĭlov were concerned with the energy concept of free oscillations of shells in an acoustic medium. He used the relation between the complex frequency of shell oscillations and the energy loss in the surrounding medium. He analyzed the behavior of the complex natural frequencies of a spherical shell as functions of the shell parameters and the parameters of the environment.

A.V. Shanin considered the diffraction of a plane acoustic wave by an infinitely thin plane obstacle with a smooth boundary. He showed that the spatial pattern of the scattered field can be represented as an integral of the product of two directional patterns for the edge Green's function (the so-called "splitting formula").

V.D. Luk'yanov and G.L. Nikitin obtained and studied an exact analytical solution to the problem of normal wave reflection from a semi-infinite periodic system of baffles in a waveguide. The baffles were assumed to be identical and had the form of rigid diaphragms with holes closed by moving valves. The valves were assumed to be elastically connected with the diaphragms and able to perform translational motions.

The paper presented by A.P. Kiselev, V.O. Yarovoĭ, and E.A. Vsemirnova considered the deviations of the properties of an elastic wave field from those predicted by the simplest models. The authors proposed a method of numerical modeling of the polarization anomalies of nonstationary fields near caustics and in the half-shadow zone on the basis of using both the principal and the correction terms of asymptotic formulas.

A.P. Kiselev revealed the possibility for the existence of a specific Rayleigh wave on the surface of a homogeneous elastic half-space. The amplitude of this wave varies along the wave front as a linear function of coordinate.

A Rayleigh-type wave propagating at the surface of an elastic half-space that is covered with an elastic layer characterized by high velocities of elastic wave propagation was considered in the paper by G.V. Filippenko and D.P. Kouzov. This wave is undamped below a certain cutoff frequency. At higher frequencies, the wave number of this wave is complex because of the radiation loss. The loss appears to be very large at the beginning, but it decreases as the frequency grows. Today, studies of vibration-insulating properties of trenches attract considerable interest in different countries. The aforementioned result shows that, in the layered structure described above, at some frequencies an increase in the width of a trench may reduce the vibration insulation caused by it.

Using the "spectral functions" method developed by G. Lebeau, V.V. Kamotskiĭ proved the existence and uniqueness theorems for the problem of diffraction of a plane elastic wave in an elastic wedge.

E.A. Ivanova presented the derivation of the bar vibration equations using P.A. Zhilin's version, according to which the definition of the structure of stiffness tensors and the derivation of the general equations are based on the fundamental laws of mechanics. In this approach, specific equations of the elasticity theory for the material of the bar, as well as the shape of its cross section, are used only at the terminal stage of consideration.

I.V. Andronov studied the scattering of a flexural plane wave from a reinforced weld of two semi-infinite plates. The problem was reduced to a set of integral equations for which an asymptotic solution was constructed.

S.N. Gavrilov considered a nonstationary motion of a material point along a string with an elastic base. He showed that the character of the motion is such that the material point seems to acquire an additional velocity-dependent mass.

E.V. Shishkina applied the method of a direct separation of motions, which is conventionally used in vibration mechanics, for calculating distributed systems. The study was performed using transverse vibra-

1063-7710/04/5005-0621$26.00 © 2004 MAIK "Nauka/Interperiodica"

tions of a beam loaded with a harmonically varying longitudinal force as an example. For a hinged beam, it was shown that, under the effect of vibration, the stability of the structure increases, because the beam acquires an additional effective stiffness.

Li Yen Kwan (from Korea) studied the effect of parametric resonance in some distributed systems on the basis of the computational techniques developed by himself.

Two papers presented by V.V. Alekseev considered the stability of a boundary layer on a flexible surface under small perturbations in the form of traveling waves. To describe a liquid flow, the author used a three-layer model of a boundary layer with a self-induced pressure. The flexible surface was modeled by a thin plate lying on an elastic base. It was shown that two types of stability loss are possible in this model: the Tollmien–Schlichting instability and the instability caused by the effect of hydrodynamic pressure on the surface contacting the flow.

Some problems of the theory of gravity surface waves in a liquid were considered in two papers by O.V. Motygin. He studied the spectrum of the Steklov problem of free oscillations of a liquid placed under a rigid cover with slots and also studied the localized modes for steady-state motions of an unbounded incompressible liquid with a free surface in the presence of partially or completely submerged bodies. In particular, the author proved the presence of such modes for an arbitrary number (>1) of partially submerged bodies.

V.D. Luk'yanov proposed a new algorithm for calculating the experimental dependences with allowance for the possible presence of false data among the experimental results ("the weighted least squares method"). In this approach, each result of measurement is given a certain weighting factor that takes into account the degree of deviation of this result from all other results.

V.É. Petrov introduced a new class of integral transformations for a finite segment, this class being related to orthogonal polynomials. He derived the corresponding inversion formulas and convolution theorems.

The seminars are held in the assembly hall of the Institute for Problems of Mechanical Engineering, Russian Academy of Sciences (Vasil'evskiĭ Ostrov, Bol'shoĭ pr. 61, St. Petersburg), Tuesdays at 18:30.

More detailed authors' abstracts of papers and other information on the seminar can be obtained on the web site:

http:/mph.phys.spb.ru/~george/seminar.html

Applications for papers can be forwarded by e-mail:

kouzov@alfa.ipme.ru or george@GF4663.spb.edu

and also by phone to the seminar head D.P. Kouzov (812)312-3530 or the seminar secretary G.V. Filippenko (812)143-2323.

D.P. Kouzov

Translated by E. Golyamina